

The Hemisphere-Cylinder at an Angle of Attack

by

Ngoc T. Hoang

Dissertation submitted to the Faculty of the

Virginia Polytechnic Institute and State University

in partial fulfillment of the requirements for the degree of

Doctor of Philosophy

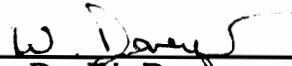
in

Engineering Mechanics

APPROVED:



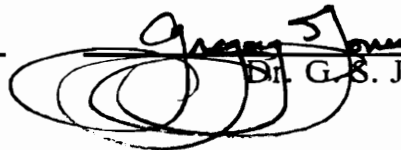
Dr. D. P. Telionis, Chairman



Dr. W. Davenport



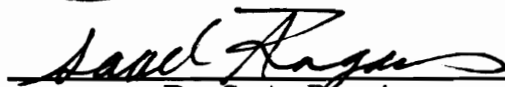
Dr. S. L. Hendricks



Dr. G. S. Jones



Dr. D. H. Morris



Dr. S. A. Ragab

December, 1991

Blacksburg, Virginia

The Hemisphere-Cylinder at an Angle of Attack

by

Ngoc T. Hoang

Dr. D. P. Telionis, Chairman

Engineering Mechanics

(ABSTRACT)

An experimental investigation was carried out of the flow over a hemisphere-cylinder at angles of attack $\alpha = 0^\circ$ to 90° . Visualizations of skin-friction lines were conducted and were focused mainly on the development of the laminar separation bubble as a function of angle of attack, the conditions under which open and closed separation exist and the interaction between the separation bubble and the leeward vortices. A digital processing method was developed to convert flow visualizations to numerical data. Static pressure measurements over a large range of Reynolds numbers were obtained for two models with different sizes and the same length-to-diameter ratios. Detailed velocity fields, mapped out by a seven hole probe and a laser-Doppler velocimeter (LDV) probe, were carefully examined to provide information on the development of vortical structures on the surface of the model. Comparisons were made of the results obtained using these two instruments. The flowfield in the wake of the hemisphere-cylinder was also examined at an angle of attack $\alpha = 30^\circ$. A small bead was strategically placed near the nose to force vortex asymmetry. Different sizes of bead were also tested to investigate the effectiveness on the asymmetric pattern. Hot-wire anemometers and a dynamic signal analyzer were employed to study the unsteady motion of leeward vortices.

Acknowledgements

Words cannot adequately express my appreciation to Dr. Demetri Telionis for his support and guidance throughout the course of my studies. I owe him special gratitude for the completion of my graduate work.

I am grateful to the members of my dissertation committee, Dr. Davenport, Dr. Hendricks, Dr. Jones, Dr. Morris and Dr. Ragab, for their time in reviewing this manuscript. I would like express my keen admiration for Dr. Ragab for having such a positive influence in my academic career.

This research effort was undertaken with the support of the NASA-Langley Experimental Methods Branch and Theoretical Aerodynamics Branch, Grant#NGT-50144 and Grant#NAS1-18471. A special thanks is given to Mr. M. Salas and Dr. G. S. Jones.

To my friends and colleagues, Terry Martin, Mr. and Mrs. Nelson Martin, Othon Rediniotis, Mike Wilder, Norman Scheaffler, Matt Pesce, Erik Panzer and Sandie Klute, I thank them for their friendship. Gratitude is also extended to Air Force Lt. William Gideon for digitizing the flow visualization pictures.

I would like to thank my parents, Mr. and Mrs. Suy Van Hoang, my brothers and sisters, Chi Ti, Anh Triem, Chi Be, Chut, Xiu, Xec, Teo and To, and all my nieces and

nephew for their unfailing support and love. I also wish to thank my parents-in-law, Mr. and Mrs. Chuc Tran, brothers- and sisters-in-law, Anh Tam, Hiep, Truc, Son and Ha for their encouragement throughout my entire education.

Finally, my most sincere appreciation goes to my wife, Lan, for her love, patience and understanding, especially when my Ph.D. program consumed most of our precious time together as a family.

Table of Contents

Chapter 1: Introduction 1

Chapter 2: Facilities and Experimental Methods 12

 2.1 Introduction 12

 2.2 ESM Wind Tunnel 13

 2.3 VPI Stability Wind Tunnel 13

 2.4 Velocity Measurement Using LDV 17

 Introduction 17

 Two-Component LDV Fiber-optic Probe System 17

 Theory Of Operation 20

 Seeding Techniques 28

 Signal Processing and Data Reduction 29

 Uncertainty Analysis 31

 2.5 Static Pressure Measurement 33

 Introduction 33

 Instrumentation 33

 2.6 Velocity Measurement Using a Seven-Hole Probe 37

Introduction	37
Calibration Procedure Using The Gallington's Method	39
Calibration Procedure Using The Zilliac's Method	45
Comparison Between The Two Calibration Methods	48
2.7 Hot-Wire Anemometry	49
2.8 Flow Visualization And Digital Processing	49
Introduction	49
Flow Visualization Techniques	50
Setup Of The Instrumentation	50
Chapter 3: Low-Reynolds Number Measurements	52
3.1 Introduction	52
3.2 Experimental Setup	60
3.3 Experimental Conditions	63
3.4 Results and Discussion	64
Flow Visualization	64
Pressure Measurements	78
Velocity Measurements	108
Chapter 4: High-Reynolds Number Measurements	128
4.1 Introduction	128
4.2 Experimental Setup	130
4.3 Experimental Conditions	134
4.4 Results and Discussion	136
Flow Visualization and Digitization	136
Pressure Measurements	148
Velocity Measurements	174

Chapter 5: Unsteady Flow **210**

 5.1 Introduction 210

 5.2 Experimental Setup 214

 5.3 Results and Discussion 216

 (i) $\alpha = 90^\circ$ Case 216

 (ii) $\alpha = 0^\circ - 85^\circ$ Case 231

Chapter 6: Conclusions and Recommendations **240**

References **245**

Appendix: Data Acquisition and Reduction Programs **252**

Vita **302**

 Personal 302

 Education 302

List of Illustrations

Figure 1.1. Flow over various axisymmetric bodies (a) the prolate spheroid (b) the ogive-cylinder and (c) the hemisphere-cylinder.	4
Figure 1.2. (a) Maskell's sketches of vortex separation and (b) bubble separation. .	5
Figure 2.1. The ESM Wind Tunnel.	14
Figure 2.2. The VPI Stability Wind Tunnel.	15
Figure 2.3. A layout of an LDV fiber-optic probe system.	18
Figure 2.4. Heterodyne detection methods (a) reference beam system (b) dual scattered system (c) dual beam system.	22
Figure 2.5. Definition of coordinates.	25
Figure 2.6. Interference pattern of two point light sources.	26
Figure 2.7. Seeding system configuration.	30
Figure 2.8. A schematic diagram of instrumentation for pressure measurements in the ESM Wind Tunnel.	34
Figure 2.9. A schematic diagram of instrumentation for pressure measurements in the VPI Stability Tunnel.	36
Figure 2.10. (a) Probe geometry and (b) flow angle definition.	38
Figure 2.11. Flow over the probe at high angles of attack.	41
Figure 2.12. Division of the calibration domain (a) seven main sectors (b) twenty sub-sectors.	46
Figure 3.1. Skin-friction patterns over a hemisphere-cylinder at various incidences. .	54
Figure 3.2. (a) Lines of separation and (b) topological structure for flow over a hemisphere-cylinder at a moderate incidence.	56

Figure 3.3. Models with (a) forebody strakes and (b) three different configurations - ogive, elliptical and chined bodies.	59
Figure 3.4. (a) Definition of coordinates and (b) seven-hole probe experimental setup.	61
Figure 3.5. Surface flow visualizations at $\alpha = 0^\circ$ and $Re = 27000$ (a) $\phi = 180^\circ$ (b) $\phi = 90^\circ$	65
Figure 3.6. Surface flow visualizations at $\alpha = 5^\circ$ and $Re = 27000$ (a) $\phi = 180^\circ$ (b) $\phi = 90^\circ$	67
Figure 3.7. Surface flow visualizations at $\alpha = 10^\circ$ and $Re = 27000$ (a) $\phi = 180^\circ$ (b) $\phi = 120^\circ$ (c) $\phi = 90^\circ$	68
Figure 3.8. Surface flow visualizations at $\alpha = 15^\circ$ and $Re = 27000$ (a) $\phi = 180^\circ$ (b) $\phi = 120^\circ$ (c) $\phi = 90^\circ$	70
Figure 3.9. Surface flow visualizations at $\alpha = 20^\circ$ and $Re = 27000$ (a) $\phi = 180^\circ$ (b) $\phi = 120^\circ$ (c) $\phi = 90^\circ$	71
Figure 3.10. Surface flow visualizations at $\alpha = 25^\circ$ and $Re = 27000$ (a) $\phi = 180^\circ$ (b) $\phi = 120^\circ$ (c) $\phi = 90^\circ$	73
Figure 3.11. Surface flow visualizations at $\alpha = 30^\circ$ and $Re = 27000$ (a) $\phi = 180^\circ$ (b) $\phi = 120^\circ$ (c) $\phi = 90^\circ$	74
Figure 3.12. Surface flow visualizations at $\alpha = 35^\circ$ and $Re = 27000$ (a) $\phi = 180^\circ$ (b) $\phi = 120^\circ$ (c) $\phi = 90^\circ$	75
Figure 3.13. Surface flow visualizations at $\alpha = 40^\circ$ and $Re = 27000$ (a) $\phi = 180^\circ$ (b) $\phi = 120^\circ$ (c) $\phi = 90^\circ$	76
Figure 3.14. Surface flow visualizations at $\alpha = 45^\circ$ and $Re = 27000$ (a) $\phi = 180^\circ$ (b) $\phi = 120^\circ$ (c) $\phi = 90^\circ$	77
Figure 3.15. Pressure distributions on the ESM Wind Tunnel wall when the hemisphere-cylinder model is placed at various angles of attack.	79
Figure 3.16. Axial pressure distributions on a hemisphere-cylinder at $\phi = 180^\circ$ and $\alpha = 20^\circ$ in two different wind tunnels.	80
Figure 3.17. Axial pressure distributions on a hemisphere-cylinder at $\alpha = 0^\circ$ and two different Reynolds numbers.	82
Figure 3.18. Axial pressure distributions on a hemisphere-cylinder at $\alpha = 10^\circ$ and $Re = 15000$ with added constants.	83
Figure 3.19. Pressure coefficient contours on a hemisphere-cylinder at $\alpha = 10^\circ$ and $Re = 15000$	85

Figure 3.20. Circumferential pressure distributions on a hemisphere-cylinder at $\alpha = 10^\circ$ and $Re = 15000$	86
Figure 3.21. Axial pressure distributions on a hemisphere-cylinder at $\alpha = 10^\circ$ and $Re = 27000$ with added constants.	87
Figure 3.22. Pressure coefficient contours on a hemisphere-cylinder at $\alpha = 10^\circ$ and $Re = 27000$	88
Figure 3.23. Circumferential pressure distributions on a hemisphere-cylinder at $\alpha = 10^\circ$ and $Re = 27000$	89
Figure 3.24. Axial pressure distributions on a hemisphere-cylinder at $\alpha = 20^\circ$ and $Re = 15000$ with added constants.	90
Figure 3.25. Pressure coefficient contours on a hemisphere-cylinder at $\alpha = 20^\circ$ and $Re = 15000$	92
Figure 3.26. Circumferential pressure distributions on a hemisphere-cylinder at $\alpha = 20^\circ$ and $Re = 15000$	93
Figure 3.27. Axial pressure distributions on a hemisphere-cylinder at $\alpha = 20^\circ$ and $Re = 27000$ with added constants.	94
Figure 3.28. Pressure coefficient contours on a hemisphere-cylinder at $\alpha = 20^\circ$ and $Re = 27000$	95
Figure 3.29. Circumferential pressure distributions on a hemisphere-cylinder at $\alpha = 20^\circ$ and $Re = 27000$	96
Figure 3.30. Axial pressure distributions on a hemisphere-cylinder at $\alpha = 30^\circ$ and $Re = 15000$ with added constants.	98
Figure 3.31. Pressure coefficient contours on a hemisphere-cylinder at $\alpha = 30^\circ$ and $Re = 15000$	99
Figure 3.32. Circumferential pressure distributions on a hemisphere-cylinder at $\alpha = 30^\circ$ and $Re = 15000$	100
Figure 3.32. Continued	101
Figure 3.32. Continued	102
Figure 3.33. Axial pressure distributions on a hemisphere-cylinder at $\alpha = 30^\circ$ and $Re = 27000$ with added constants.	103
Figure 3.34. Pressure coefficient contours on a hemisphere-cylinder at $\alpha = 30^\circ$ and $Re = 27000$	104
Figure 3.35. Circumferential pressure distributions on a hemisphere-cylinder at $\alpha = 30^\circ$ and $Re = 27000$	105

Figure 3.35. Continued	106
Figure 3.35. Continued	107
Figure 3.36. Velocity field at $\alpha = 20^\circ$ and $Re = 27000$ with no bead.	109
Figure 3.37. Velocity field at $\alpha = 30^\circ$ and $Re = 27000$ with no bead.	110
Figure 3.38. Axial velocity component contours at $\alpha = 30^\circ$ and $Re = 27000$ with no bead.	111
Figure 3.39. Velocity field and vorticity contours at $\alpha = 30^\circ$ and $Re = 27000$ with bead#1 at $\phi = 30^\circ$ and $x/R = 0.5$.	112
Figure 3.40. Velocity field and vorticity contours at $\alpha = 30^\circ$ and $Re = 27000$ with bead#1 at $\phi = 70^\circ$ and $x/R = 0.5$.	114
Figure 3.41. Velocity field and vorticity contours at $\alpha = 30^\circ$ and $Re = 27000$ with bead#1 at $\phi = 90^\circ$ and $x/R = 0.5$.	115
Figure 3.42. Velocity field and vorticity contours at $\alpha = 30^\circ$ and $Re = 27000$ with bead#1 at $\phi = 120^\circ$ and $x/R = 0.5$.	116
Figure 3.43. Axial velocity component contours at $\alpha = 30^\circ$ and $Re = 27000$ with bead#1 at $\phi = 120^\circ$ and $x/R = 0.5$.	117
Figure 3.44. Velocity field and vorticity contours at $\alpha = 30^\circ$ and $Re = 27000$ with bead#1 at $\phi = 150^\circ$ and $x/R = 0.5$.	118
Figure 3.45. Velocity field and vorticity contours at $\alpha = 30^\circ$ and $Re = 27000$ with bead#1 at $\phi = 120^\circ$ and $x/R = 1.8$.	120
Figure 3.46. Velocity field and vorticity contours at $\alpha = 30^\circ$ and $Re = 27000$ with bead#1 at $\phi = 120^\circ$ and $x/R = 2.5$.	121
Figure 3.47. Velocity field and vorticity contours at $\alpha = 30^\circ$ and $Re = 27000$ with bead#1 at $\phi = 280^\circ$ and $x/R = 0.5$.	122
Figure 3.48. Velocity field and vorticity contours at $\alpha = 30^\circ$ and $Re = 27000$ with bead#2 at $\phi = 120^\circ$ and $x/R = 0.5$.	123
Figure 3.49. Flow patterns over a sharp-nosed ogive cylinder at (a) low incidence (b) moderate incidence.	124
Figure 3.50. Skin-friction patterns over a hemisphere-cylinder with a bead mounted near the nose (leeward view).	127
Figure 4.1. (a) The hemisphere-cylinder model showing windows for LDV measurements (b) cross-section of the traversing mechanism shown inside the model.	131

Figure 4.2. The traversing mechanism.	133
Figure 4.3. The seven-hole probe experimental setup.	135
Figure 4.4. Surface flow visualization at $\alpha = 0^\circ$ and $Re = 2.9 \times 10^5$	137
Figure 4.5. Surface flow visualization at $\alpha = 20^\circ$ and $Re = 2.9 \times 10^5$ (a) $\phi = 180^\circ$ (b) $\phi = 90^\circ$	139
Figure 4.6. Side view of digitized skin-friction lines for $\alpha = 20^\circ$ and $Re = 2.9 \times 10^5$ (a) actual view (b) unwrapped view.	140
Figure 4.7. Surface flow visualization at $\alpha = 20^\circ$ and $Re = 4.2 \times 10^5$ (a) $\phi = 180^\circ$ (b) $\phi = 90^\circ$	142
Figure 4.8. Side view of digitized skin-friction lines for $\alpha = 20^\circ$ and $Re = 4.2 \times 10^5$ (a) actual view (b) unwrapped view.	143
Figure 4.9. Surface flow visualization at $\alpha = 30^\circ$ and $Re = 2.9 \times 10^5$ (a) $\phi = 180^\circ$ (b) $\phi = 90^\circ$	144
Figure 4.10. Side view of digitized skin-friction lines for $\alpha = 30^\circ$ and $Re = 2.9 \times 10^5$ (a) actual view (b) unwrapped view.	145
Figure 4.11. Surface flow visualization at $\alpha = 30^\circ$ and $Re = 4.2 \times 10^5$ (a) $\phi = 180^\circ$ (b) $\phi = 90^\circ$	146
Figure 4.12. Side view of digitized skin-friction lines for $\alpha = 30^\circ$ and $Re = 4.2 \times 10^5$ (a) actual view (b) unwrapped view.	147
Figure 4.13. Pressure distributions on the VPI Stability Wind Tunnel wall when the hemisphere-cylinder model is placed at various angles of attack.	149
Figure 4.14. Axial pressure distributions on a hemisphere-cylinder at $\alpha = 0^\circ$ and $Re = 2.9 \times 10^5$	150
Figure 4.15. Axial pressure distributions on a hemisphere-cylinder at $\alpha = 0^\circ$ and three different Reynolds numbers.	151
Figure 4.16. Axial pressure distributions on a hemisphere-cylinder at $\alpha = 0^\circ$ and various Reynolds numbers.	153
Figure 4.17. Axial pressure distributions on a hemisphere-cylinder at $\alpha = 0^\circ$ and various Reynolds numbers with added constants.	154
Figure 4.18. Axial pressure distributions on a hemisphere-cylinder at $\alpha = 10^\circ$ and $Re = 2.9 \times 10^5$ with added constants.	155
Figure 4.19. Pressure coefficient contours on a hemisphere-cylinder at $\alpha = 10^\circ$ and $Re = 2.9 \times 10^5$	156

Figure 4.20. Circumferential pressure distributions on a hemisphere-cylinder at $\alpha = 10^\circ$ and $Re = 2.9 \times 10^5$	157
Figure 4.21. Axial pressure distributions on a hemisphere-cylinder at $\alpha = 10^\circ$ and $Re = 4.2 \times 10^5$ with added constants.	159
Figure 4.22. Pressure coefficient contours on a hemisphere-cylinder at $\alpha = 10^\circ$ and $Re = 4.2 \times 10^5$	160
Figure 4.23. Circumferential pressure distributions on a hemisphere-cylinder at $\alpha = 10^\circ$ and $Re = 4.2 \times 10^5$	161
Figure 4.24. Axial pressure distributions on a hemisphere-cylinder at $\alpha = 10^\circ$ and various Reynolds numbers.	162
Figure 4.25. Axial pressure distributions on a hemisphere-cylinder at $\alpha = 10^\circ$ and various Reynolds numbers with added constants.	163
Figure 4.26. Axial pressure distributions on a hemisphere-cylinder at $\alpha = 20^\circ$ and $Re = 2.9 \times 10^5$ with added constants.	164
Figure 4.27. Pressure coefficient contours and digitized skin-friction patterns on a hemisphere-cylinder at $\alpha = 20^\circ$ and $Re = 2.9 \times 10^5$	165
Figure 4.28. Circumferential pressure distributions on a hemisphere-cylinder at $\alpha = 20^\circ$ and $Re = 2.9 \times 10^5$	166
Figure 4.28. Continued.	167
Figure 4.29. Axial pressure distributions on a hemisphere-cylinder at $\alpha = 20^\circ$ and $Re = 4.2 \times 10^5$ with added constants.	169
Figure 4.30. Pressure coefficient contours and digitized skin-friction patterns on a hemisphere-cylinder at $\alpha = 20^\circ$ and $Re = 4.2 \times 10^5$	170
Figure 4.31. Circumferential pressure distributions on a hemisphere-cylinder at $\alpha = 20^\circ$ and $Re = 4.2 \times 10^5$	171
Figure 4.32. Circumferential pressure distributions on a hemisphere-cylinder at $\alpha = 20^\circ$ and $Re = 4.2 \times 10^5$	172
Figure 4.32. Continued.	173
Figure 4.33. Axial pressure distributions on a hemisphere-cylinder at $\alpha = 20^\circ$ and various Reynolds numbers.	175
Figure 4.34. Axial pressure distributions on a hemisphere-cylinder at $\alpha = 20^\circ$ and various Reynolds numbers with added constants.	176
Figure 4.35. Axial pressure distributions on a hemisphere-cylinder at $\alpha = 30^\circ$ and $Re = 2.9 \times 10^5$ with added constants.	177

Figure 4.36. Pressure coefficient contours and digitized skin-friction patterns on a hemisphere-cylinder at $\alpha = 30^\circ$ and $Re = 2.9 \times 10^5$	178
Figure 4.37. Circumferential pressure distributions on a hemisphere-cylinder at $\alpha = 30^\circ$ and $Re = 2.9 \times 10^5$	179
Figure 4.37. Continued.	180
Figure 4.38. Axial pressure distributions on a hemisphere-cylinder at $\alpha = 30^\circ$ and $Re = 4.2 \times 10^5$ with added constants.	181
Figure 4.39. Pressure coefficient contours and digitized skin-friction patterns on a hemisphere-cylinder at $\alpha = 30^\circ$ and $Re = 4.2 \times 10^5$	182
Figure 4.40. Circumferential pressure distributions on a hemisphere-cylinder at $\alpha = 30^\circ$ and $Re = 4.2 \times 10^5$	183
Figure 4.40. Continued.	184
Figure 4.41. Pressure distributions on a hemisphere-cylinder at $\alpha = 0^\circ$ with the seven-hole probe mounted at different radial locations and $\phi = 90^\circ$	185
Figure 4.42. Pressure distributions on a hemisphere-cylinder at $\alpha = 30^\circ$ with the seven-hole probe at (a) $\phi = 90^\circ$ (b) $\phi = 170^\circ$	187
Figure 4.43. Seven-hole probe velocity vector fields along a normal plane at $x/R = 5.8$, $\alpha = 20^\circ$, and $Re = 1.5 \times 10^5$	188
Figure 4.44. Seven-hole probe velocity vector fields along a normal plane at $x/R = 6.1$, $\alpha = 20^\circ$, and $Re = 1.5 \times 10^5$	189
Figure 4.45. Seven-hole probe velocity vector fields along a normal plane at $x/R = 8.1$, $\alpha = 20^\circ$, and $Re = 1.5 \times 10^5$	190
Figure 4.46. Seven-hole probe velocity vector fields along a normal plane at $x/R = 8.4$, $\alpha = 20^\circ$, and $Re = 1.5 \times 10^5$	191
Figure 4.47. Seven-hole probe velocity vector fields along a normal plane at $x/R = 9.7$, $\alpha = 20^\circ$, and $Re = 1.5 \times 10^5$	192
Figure 4.48. Seven-hole probe velocity vector fields along a normal plane at $x/R = 10.0$, $\alpha = 20^\circ$, and $Re = 1.5 \times 10^5$	193
Figure 4.49. LDV and seven-hole probe circumferential velocity profiles at $x/R = 5.8$, $\alpha = 20^\circ$ (a) $\phi = 147^\circ$ (b) $\phi = 154^\circ$ (c) $\phi = 161^\circ$	197
Figure 4.50. LDV and seven-hole probe axial velocity profiles at $x/R = 5.8$, $\alpha = 20^\circ$ (a) $\phi = 147^\circ$ (b) $\phi = 154^\circ$ (c) $\phi = 161^\circ$	198
Figure 4.51. LDV and seven-hole probe circumferential velocity profiles at $x/R = 9.7$, $\alpha = 20^\circ$ (a) $\phi = 119^\circ$ (b) $\phi = 140^\circ$ (c) $\phi = 161^\circ$	199

Figure 4.52. LDV and seven-hole probe axial velocity profiles at $x/R = 9.7$, $\alpha = 20^\circ$ (a) $\phi = 119^\circ$ (b) $\phi = 140^\circ$ (c) $\phi = 161^\circ$	200
Figure 4.53. LDV and seven-hole probe circumferential velocity profiles at $x/R = 10.0$, $\alpha = 20^\circ$ (a) $\phi = 119^\circ$ (b) $\phi = 140^\circ$ (c) $\phi = 161^\circ$	201
Figure 4.54. LDV and seven-hole probe axial velocity profiles at $x/R = 10.0$, $\alpha = 20^\circ$ (a) $\phi = 119^\circ$ (b) $\phi = 140^\circ$ (c) $\phi = 161^\circ$	202
Figure 4.55. Seven-hole probe velocity vector fields along a normal plane at $x/R = 5.8$, $\alpha = 30^\circ$, for $Re = 1.5 \times 10^5$	203
Figure 4.56. Seven-hole probe velocity vector fields along a normal plane at $x/R = 6.1$, $\alpha = 30^\circ$, and $Re = 1.5 \times 10^5$	204
Figure 4.57. Seven-hole probe velocity vector fields along a normal plane at $x/R = 8.1$, $\alpha = 30^\circ$, and $Re = 1.5 \times 10^5$	205
Figure 4.58. Seven-hole probe velocity vector fields along a normal plane at $x/R = 8.4$, $\alpha = 30^\circ$, and $Re = 1.5 \times 10^5$	206
Figure 4.59. LDV and seven-hole probe circumferential velocity profiles at $x/R = 5.8$, $\alpha = 30^\circ$ (a) $\phi = 140^\circ$ (b) $\phi = 168^\circ$ (c) $\phi = 175^\circ$	207
Figure 4.60. LDV and seven-hole probe axial velocity profiles at $x/R = 5.8$, $\alpha = 30^\circ$ (a) $\phi = 140^\circ$ (b) $\phi = 168^\circ$ (c) $\phi = 175^\circ$	208
Figure 4.61. LDV and seven-hole probe profiles at $x/R = 8.1$, $\phi = 160^\circ$, $\alpha = 30^\circ$ and $Re = 1.5 \times 10^5$	209
Figure 5.1. (a-f) The position of the models in the wind tunnel (g) definition of coordinates and positioning of the hot wires.	215
Figure 5.2. (a) Two-dimensional von Karman vortex shedding over an infinite cylinder and (b) periodic motion of the leeward vortices of an inclined hemisphere-cylinder.	217
Figure 5.3. Velocity power spectra in the wake of an infinite circular-cylinder at free-stream velocities of (a) 24.3 ft/sec and (b) 33.8 ft/sec.	219
Figure 5.4. The Strouhal number downstream of the models of Figure 5.1 at different elevation from their bottom.	220
Figure 5.5. Magnitude and phase of cross spectrum of two hot wires positioned in the wake of a semi-infinite hemisphere-cylinder at z/l of (a) 0.3 (b) 0.75 (c) 0.9.	221
Figure 5.6. Time records obtained with two hot wires positioned in the wake of a semi-infinite hemisphere-cylinder at $z/l = 0.3$	223

Figure 5.7. Magnitude and phase of cross spectrum of two hot wires positioned in the wake of a semi-infinite flat top cylinder at z/l of (a) 0.5 (b) 0.8 (c) 0.95.	224
Figure 5.8. Magnitude and phase of cross spectrum of two hot wires positioned in the wake of a semi-infinite nose cone cylinder at $z/l = 0.5$	226
Figure 5.9. Magnitude and phase of cross spectrum of two hot wires positioned at $z/l = 0.5$ in the wake of a finite (a) hemisphere-cylinder (b) flat top cylinder.	227
Figure 5.10. Magnitude and phase of cross spectrum of two hot wires positioned in the wake of a finite hemisphere-cylinder at $z/l = 0.5$	228
Figure 5.11. The hemisphere-cylinder model with a plate mounted near the top. .	229
Figure 5.12. Magnitude and phase of cross spectrum of two hot wires positioned in the wake of a semi-infinite hemisphere-cylinder (with a plate mounted near the top) at $z/l = 0.5$	230
Figure 5.13. Magnitude and phase of cross spectrum of two hot wires when the model at an angle of attack of (a) 20° (b) 25° (c) 30° (d) 40° (e) 45° (f) 80°	232
Figure 5.14. Strouhal number obtained at different angles of attack.	233
Figure 5.15. Magnitude and phase of cross spectrum of two hot wires at a vertical distance of (a) $0.060D$ (b) $0.303D$ (c) $0.606D$ (d) $0.909D$ (e) $1.212D$ from each other.	236
Figure 5.16. The hemisphere-cylinder model with a splitter plate mounted in the leeward plane of symmetry.	237
Figure 5.17. Velocity spectrum of the hot wires positioned in the wake of the hemisphere-cylinder with a splitter plate at α of (a) 20° (b) 25° (c) 40° . .	238
Figure 5.18. Magnitude and phase of cross spectrum of the hot wires positioned in the wake of the hemisphere-cylinder at high Re and α of (a) 30° (b) 35° . .	239

Chapter 1: Introduction

Three-dimensional flows over axisymmetric bodies at an angle of attack have received considerable attention in the last decade. It has been known that the wake of an axisymmetric body at an incidence is organized in the form of two vortices, nearly aligned with the direction of the free-stream velocity. In practice, these types of flows are commonly displayed over the forebody of aircrafts or missiles at an angle of attack. The requirement to enhance maneuverability of these vehicles during flight at high incidence has motivated researchers to seek a better understanding of vortex development and formation. As a result, a good number of careful investigations, both experimental and numerical, have been carried out for flow about bodies of revolution.

The numerical difficulties encountered by many investigators are considerable. The problem is extremely complex due to a large turbulent wake. In addition, the lines of separation can not be easily defined on a three-dimensional body. Purely theoretical methods for prediction of the separation lines and the effect of separated flow on a three-dimensional body are not presently available. A more serious problem is a lack of computers that can perform fast calculations and are capable of handling mass storage. Only recently some interesting information on the development of three-dimensional

separation has emerged with the help of rapid progress in numerical methods and computer hardware. Boundary-layer calculations have clearly demonstrated that the difficulties of the problem center mostly about the proper choice of the grid shape and the marching process (Blottner and Ellis, 1973; Geissler, 1974; Patel and Choi, 1979). Approximate methods have been attempted, such as integral methods or streamline methods (Stock, 1980; Tai, 1981); however, the validity of the results is still questionable. Full Navier-Stokes calculations are available and it appears that a fine grid is required in the vicinity of separation in order to model the phenomenon correctly (Zilliac, 1986; Shirayama and Kuwahara, 1987; Hsieh, 1981; Ying, 1986, 1987).

Early experimental efforts on flows over axisymmetric bodies were inspired by the theoretical arguments on "open" and "closed" separation. Flow diagnostic techniques were confined to static pressure measurements, surface flow visualization and three-hole probe measurements (Han and Patel, 1974; Wang, 1975; Hsieh, 1975, 1976, 1977; Meier and Kreplin, 1980; Ramaprian et al., 1981; Kreplin et al., 1982). The effects of transition on the development of flow separation were also examined in these studies. Experimentalists moved further to document the development of vortex sheets which roll over the axisymmetric bodies to form a pair of leeward vortices. These were achieved by laser-Doppler velocimeter (LDV), five-hole probes and flow visualization (Meier et al., 1981; Telionis and Costis, 1983; Costis et al., 1989). A very surprising fact is the difficulty experimentalists meet with sharp-nosed axisymmetric bodies. Intuition would lead us to expect that the leeward vortices would be symmetric over an axisymmetric body. In fact, this is not necessarily the case. The flow is extremely sensitive to many parameters; even local microscopic disturbances on the surface of the model can cause asymmetric flow pattern. Therefore, the conditions of the experimental setup can not be exactly duplicated, causing numerous discrepancies and inconsistencies between results of different researchers.

The basic fluid mechanic issues of interest in flows over axisymmetric bodies are the development of the three-dimensional separation, the formation of leeward vortices and the characteristics of natural unsteadiness. Three configurations were adopted by many investigators to examine the fundamental physics of such flows: the prolate spheroid, the ogive-cylinder and the hemisphere-cylinder (Figure 1.1). The hemisphere-cylinder is chosen for the present study. This research effort was undertaken with the support of the NASA-Langley Fluid Mechanics Branch and the Theoretical Aerodynamics Branch to investigate experimentally the flow over a hemisphere-cylinder at an angle of attack. The results are used for code validation and also to compare with experimental data conducted by the Fluid Mechanics Branch on an identical model.

Historically, the prolate spheroid emerged first as an appropriate configuration for three-dimensional studies of flow separation. Ambitious analytical and experimental efforts were launched in the 1970's to solve this difficult problem. Patel and Baek [1983], Ericsson and Reding [1986] and Hoang et al. [1990] published the most complete list of references on the topic. Maskell [1955] was the first to identify the fact that separation in three dimensions could follow a distinct pattern that has no counterpart in two dimensions. He recognized that a separation vortex sheet could have a beginning (point B in Figure 1.2a) and, thus, the oncoming stream could reach both its sides from the upstream attachment point. He also identified a more conventional pattern whereby skin-friction lines emanating from the stagnation point could not reach behind the separating vortex sheet. He coined the terms "vortex separation" and "bubble separation" for the two patterns, respectively, and he accompanied his discussion by the sketches shown in Figure 1.1. Numerical investigation of the topology of limiting streamline patterns was initiated by Wang [1975] who introduced the alternative terms of "open separation" and "closed separation".

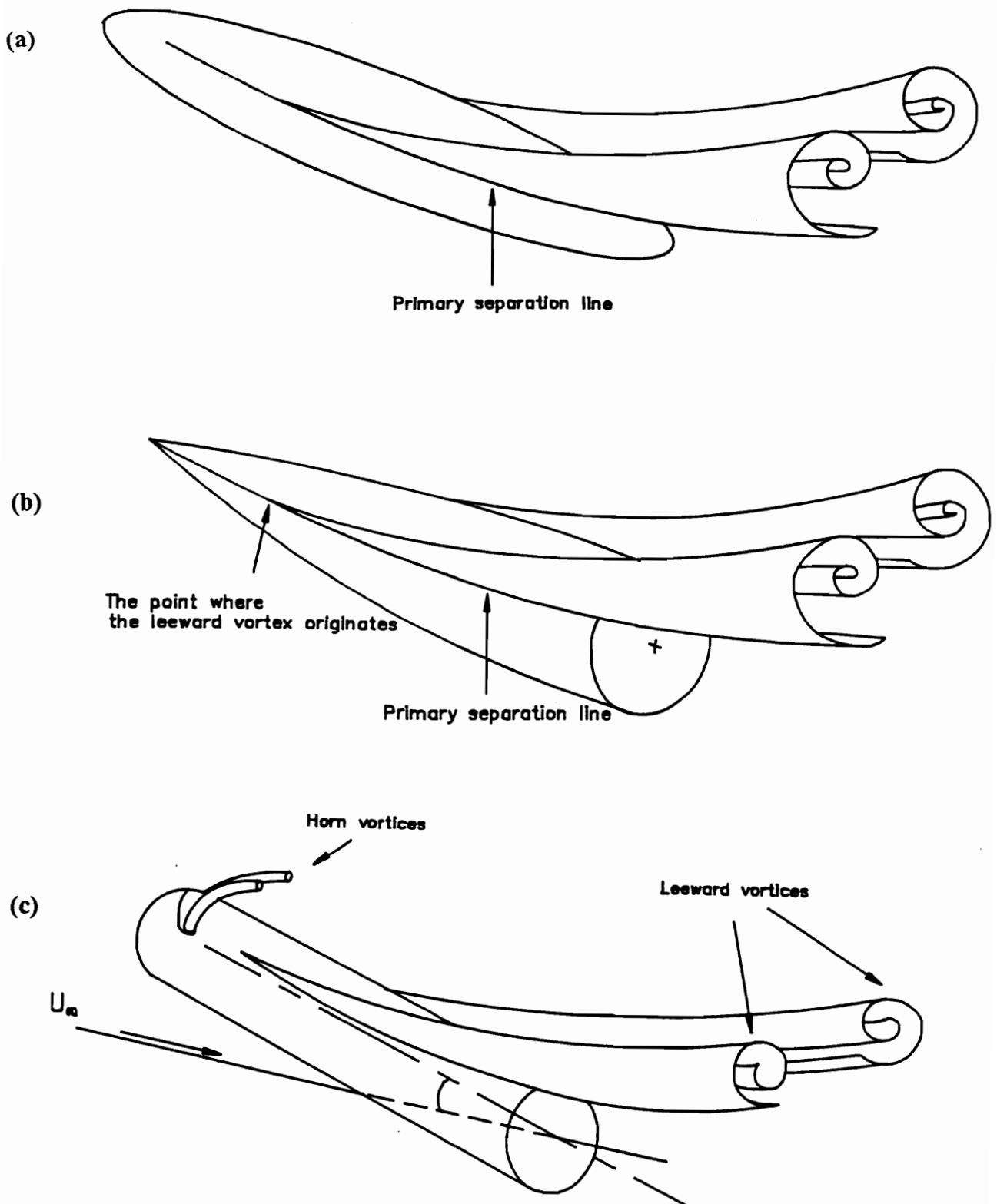
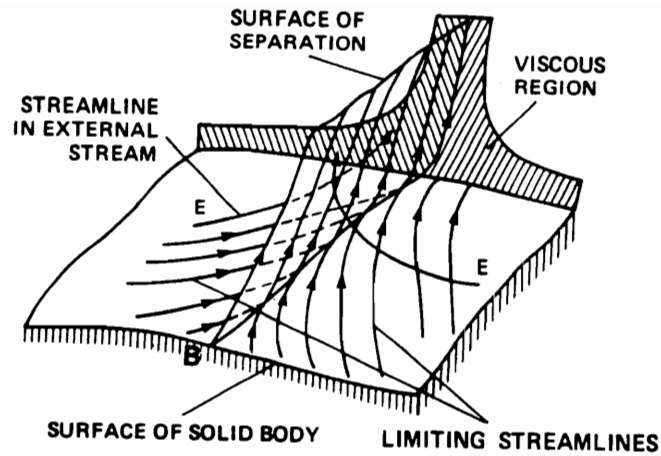
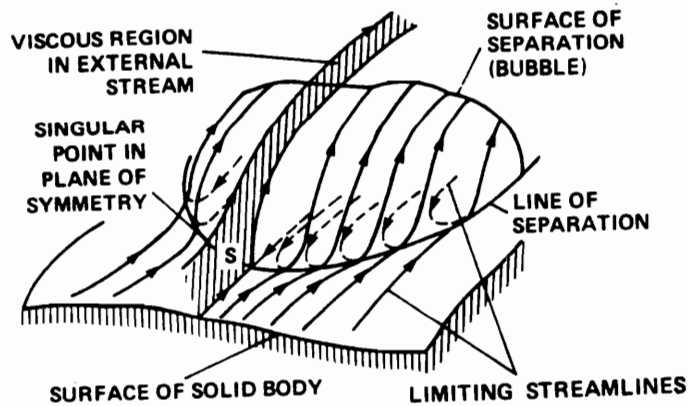


Figure 1.1. Flow over various axisymmetric bodies (a) the prolate spheroid (b) the ogive-cylinder and (c) the hemisphere-cylinder.



(a)



(b)

Figure 1.2. (a) Maskell's sketches of vortex separation and (b) bubble separation.

Similar to the prolate spheroid, open and closed separations also exist for flow over a hemisphere-cylinder at an angle of attack. In addition, the flow exhibits another type of peculiarity; a laminar separation bubble and a pair of concentrated vortex filaments or "horn vortices" that form on top of the hemispherical cap. Hsieh [1977] identified both the separation bubble and the horn near the tip of the model at an angle of attack $\alpha = 19^\circ$ and Mach number $M_\infty \geq 0.8$. The axes of the horn vortices are first perpendicular to the body surface and are convected downstream above the body. Wang [1982] used the limiting streamline patterns over a hemisphere-cylinder model at high Mach numbers to compare certain basic concepts about open and closed separations with the prolate spheroid. Meade and Schiff [1987] provided extensive surface pressure distributions and oil-flow visualizations at a Mach number $M_\infty = 1.2$. The results from this study were used to validate the topology rules of three-dimensional separation proposed by Tobak and Peake [1979, 1982].

Past experimental efforts on the hemisphere-cylinder have concentrated exclusively on the visualization of skin-friction lines and static pressure measurements at very high Mach numbers. The present work reported here is undertaken with the purpose of shedding some light on the peculiar structure of three-dimensional separation over the hemisphere-cylinder at low Mach numbers ($M_\infty \leq 0.25$) and for a wide range of Reynolds numbers, namely from $Re = 10^4$ to 10^6 . Visualization of skin friction lines were conducted to gain qualitative information regarding the overall flow behavior. The experiments focused mainly on the development of the laminar separation bubble and horn vortices as a function of angle of attack, the conditions under which open and closed separation exist and the interaction between the separation bubble and the leeward vortices. A digital processing method was developed to convert flow visualizations to numerical data. Such data offer quantitative information and can be used in direct comparison with analytical results. Static pressure measurements over a large

range of Reynolds numbers were obtained for two models with different sizes and the same length-to-diameter ratios. This gives the most comprehensive set of pressure data ever attempted. Surface pressure distributions were used to check against respective skin-friction line visualization photographs, regarding the position of the separation bubble and also the approximate location of the leeward vortices. In addition, the relative strength of these vortices could also be determined as functions of angle of attack and Reynolds number.

There is a definite void in the area of velocity measurements over a axisymmetric bodies and in particular the hemisphere-cylinder. This is due to the difficulty in measuring two or three velocity components and traversing probes in three-dimensional space. In the present contribution, detailed velocity fields were mapped out by a seven hole probe and a fiber-optic laser-Doppler velocimeter (LDV) probe. Data were carefully examined to provide information on the development of vortical structures on the surface of the model. Comparisons were made on the results obtained by using these two instruments.

Many flight vehicles have axisymmetric forebodies with pointed nose. Side forces were first reported in the early 1950's on aircraft and missile configurations at zero sideslip and $\alpha > 30^\circ$ (Hunt, 1982). At that time, it was thought that the problem is of academic interest only, since there was little practical application in flight at high angles of attack. Not until the mid-1960's, the problem re-surfaced, when flight regimes of modern aircraft and missile have been extended to include high incidences. Consequently, a great deal of experimental effort has been concentrated on the study of flows around ogive-cylinders and cone-cylinders at large incidences. Most recently, investigators became more interested in the wake, and in particular the development of asymmetric vortex structures. Flow diagnostic techniques commonly used to study vortex

asymmetry are flow visualization, hot-wire anemometry and static and dynamic pressure measurements.

For an ogive-cylinder or cone-cylinder at angles of attack less than 30° , strong crossflow causes the boundary-layer to separate. Consequently, a steady and symmetrical pair of vortices forms on the leeside of the body (Klopfer and Nielsen, 1980; Wardlaw and Yanta, 1982; Moskovitz et al., 1989). The separated region is dominated by the axial flow. The model does not exhibit any measurable side force and tests can be accurately repeated for all roll angles. The strength of the vortices continue to increase with increasing angle of attack. The vortex pattern, when an angle of attack is between 30° and 50° , can exist in any number of states from nearly symmetric to highly asymmetric. These states are triggered by irregularities in the vicinity of the nose, surface roughness, total body length, slenderness of the nose, angle of attack, free-stream turbulence and Reynolds number (Hall, 1987). Moskovitz et al. [1989] had shown that the degree of asymmetry is highly dependent on the location and size of the surface roughness and machining imperfections at the nose of the model. The overall flowfield becomes more sensitive as the disturbances (machining imperfections and surface roughness) get closer to the apex. Degani and Tobak [1991] observed a change in the asymmetric flow pattern due to fingerprints left on the model's tip. Zilliac et al. [1990] found that microscopic dust particles, in the order of a few microns in diameter, accumulated near the nose of the model during the experiment, can trigger a vortex asymmetry pattern at all angles of attack greater than 30° . Therefore, the side force could change over a period of time during the experiment. After cleaning the nose of the model with lens tissue, the side force returned to its original value. They also observed that smoke particles, used for flow visualization, could have similar effect if the smoke stream were allowed to hit the tip. Therefore, there is no unique description of the overall flowfield regardless of care taken in conducting the experiment and con-

structing the model. The asymmetric vortical structure results in side forces on the model even at zero degree sideslip. The side force can be detected at every roll angle ranging from very high to very low depending on the degree of asymmetry. The magnitude of the side force or degree of asymmetry is a function of roll angle. The maximum value of side force occurs when the vortex pattern has the highest degree of asymmetry and is unique at a given angle of attack.

At angles of attack from 50° to 65° , the leeward vortices over pointed-nose axisymmetric bodies can exist only in the form of two stable and highly asymmetric orientations. At incidences higher than 65° , three distinct vortex shedding formations have been identified by Zilliac et al. [1990]. Near the base of the model, the vortices shed alternately resembling the von Karman vortex shedding on a two-dimensional circular cylinder. The axes of the vortices are aligned with the model's axis of symmetry. In the mid-section of the model, the vortices continue to shed as before but the axis of shedding is inclined to the model's axis. A pair of stationary and steady tip vortices are formed near the nose tip. The axes of these vortices are nearly parallel to the direction of the oncoming flow. The mean side force remains constant at these incidences and no longer depends on the roll angle. As the angle of attack approaches 90° , the mean side force progressively approaches zero.

Many investigators, both experimentalists and numerical analysts have chosen the round-nosed ogive-cylinder to study the flowfield of a blunt-nosed body. These type of models, which evolved from the pointed-nosed ogive-cylinder, have the advantage of increasing lateral stability at high incidences. They do not display any vortex asymmetry pattern even at angles of attack up to $\alpha = 45^\circ$; therefore, no noticeable side force can be detected. The blunt-nosed model that has not received much attention is the hemisphere-cylinder; although its body geometry is quite simple and can be accurately machined. In addition, it has been widely adopted as the standard configuration for flow

measuring devices such as the pitot static tube and the three- and five-hole probes. Similar to other axisymmetric slender bodies, the flow on the leeside of a hemisphere-cylinder at an incidence also separates and rolls up to form a pair of symmetric vortices. These vortices originate near the junction of the hemisphere with the circular cylinder. Unlike the ogive-cylinder, where the vortices align themselves almost parallel to the axis of the model at moderate incidences, these vortices form further from the model surface (Wardlaw and Yanta, 1982).

For the first time, the flowfield in the wake of a hemisphere-cylinder was considered experimentally in this study. The intention was to investigate natural asymmetry exhibited by a blunt-nose axisymmetric body at angles of attack up to 30° . It was not at all a surprise when the results showed no asymmetry. A small bead was then placed near the nose to force vortex asymmetry at an angle of attack $\alpha = 30^\circ$. The bead was strategically placed on the model to reveal the mechanisms that trigger vortex asymmetry. The degree of asymmetry was very sensitive to both the location and size of the bead. Different sizes of beads were also tested to investigate the effectiveness on the asymmetric pattern.

Very little is known about the unsteady behavior of the vortices at all angles of attack. It is often assumed that the vortices are steady up to an angle of attack, beyond which von Karman vortex shedding begins. A closer examination of the results by Wardlaw and Yanta [1982] for flow over an ogive-cylinder indicated that large velocity fluctuations occur in portions of the flow field for angle of attack greater than 30° . The fluctuations are the results of vortex interaction and high frequency shear-layer unsteadiness. In the present effort, different patterns of vortex shedding are identified for flow over a hemisphere-cylinder. In fact, a new mode of periodic vortex shedding is discovered. This involves a periodic heaving of leeward vortices. Hot-wire anemometers and a dynamic signal analyzer were employed to study the phenomenon of vortex

heaving and shedding at angles of attack $\alpha = 0^\circ$ up to 90° . An extensive investigation was carried out at $\alpha = 90^\circ$ for a cylinder, a hemisphere-cylinder and a cone-cylinder models with one and two free-ends. Various shedding frequencies were detected along the body of these models.

The material of the dissertation is arranged as follows. The experimental methods and facilities described in Chapter 2 include: fiber-optic laser-Doppler velocimetry, static pressure measurements, seven-hole probe measurements, hot-wire anemometry, flow visualization and also a description of the ESM Wind Tunnel and the VPI Stability Wind Tunnel. Flow visualization, wake velocity measurements and static pressure measurements at low and high Reynolds numbers are discussed in Chapter 3 and 4, respectively. The main objective of Chapter 3 is to examine the development of symmetric and asymmetric leeward vortices, the horn vortices and the separation bubble on the hemisphere-cylinder. The focus of Chapter 4 is the separated region as well as the evaluation and testing of new tools, a fiber-optic LDV probe and a seven-hole probe. Chapter 5 includes the unsteady flow around the hemisphere-cylinder at angles of attack $\alpha = 0^\circ$ to 90° . Von Karman vortex shedding and leeward vortex heaving were carefully documented. Conclusions and recommendations are drawn in Chapter 6.

Chapter 2: Facilities and Experimental Methods

2.1 Introduction

Measurement techniques employed primarily in the ESM Wind Tunnel and VPI Stability Wind Tunnel are discussed in this chapter. These include : laser-Doppler velocimetry (LDV), static pressure measurements, seven-hole probe measurements, hot-wire anemometry and flow visualization and digitization. Special emphasis will be placed on the calibration of the seven-hole probe. Detailed discussion on the theories of operation for both LDV and hot-wire anemometry is beyond the scope of this dissertation. Therefore, only brief introductions to these techniques are mentioned. The interested reader should consult Richards [1976], Durst et al. [1981], Holman [1984] and TSI notes for short courses on data analysis and laser velocimetry [1987] for additional information.

2.2 ESM Wind Tunnel

The ESM Wind Tunnel is an open-circuit low-speed tunnel (Figure 2.1). A honeycomb and five nylon screens are placed inside the settling chamber, near the entrance of the tunnel, to reduce the turbulence level. The contraction ratio after the settling chamber is 5 to 1. A 0.51 x 0.51 x 1.27 meter test section is made out of plexiglass that allows flow visualization. A two-dimensional traversing mechanism, mounted underneath the test section, is controlled by a laboratory computer. The model mounting sting is bolted to the floor of the building; independent of the wind tunnel. Therefore, it does not receive vibration generated by the wind tunnel fan. The diffuser has an area ratio of about 3.7 and an angle of 5°. The tunnel axial fan is driven by a 5 hp dc motor. The velocity can range from 4 m/sec up to 20 m/sec and is very stable over time. The noise and vibration level increase significantly when the tunnel is operated at the upper velocity limit. However, they do not add any disturbances to the flow because the axial fan and motor-generator are mounted on an isolated concrete foundation. The turbulence level does not exceed 0.51% at a free-stream velocity of 8 m/sec except in small regions very close to the tunnel walls. The flow across the test section is sufficiently uniform with a variation of speed smaller than 2.5%. Further information on the design, construction and calibration of the ESM Wind Tunnel can be found in the report by G. Seider [1984].

2.3 VPI Stability Wind Tunnel

The VPI Stability Wind Tunnel, originally the NACA Stability Tunnel of Langley Field, is a continuous, closed-loop, single-return, subsonic wind tunnel (Figure 2.2). The

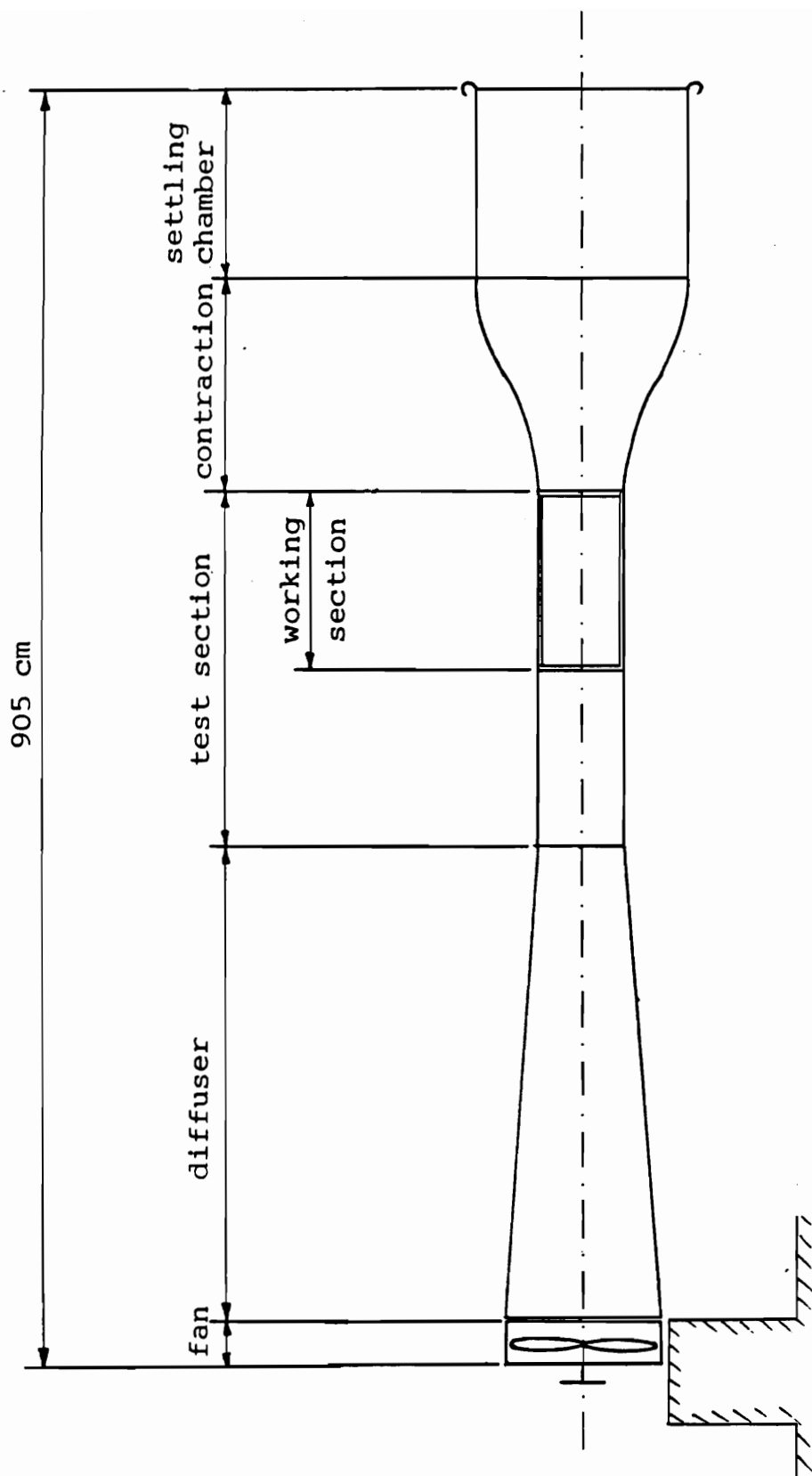


Figure 2.1. The ESM Wind Tunnel.

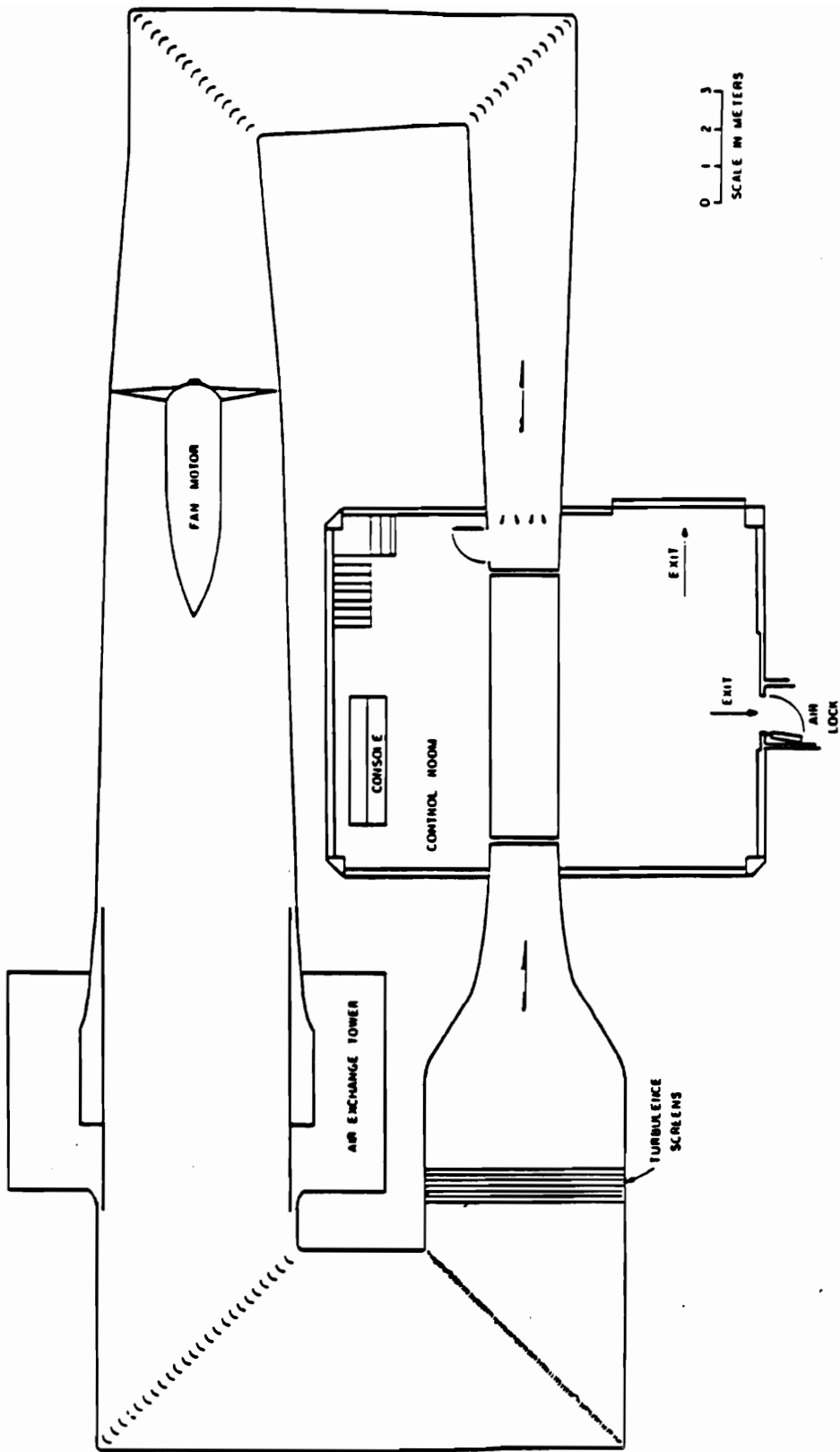


Figure 2.2. The VPI Stability Wind Tunnel.

flow is driven by an eight-blade propeller that can attain a maximum velocity of 67 m/sec in a 1.83 x 1.83 x 7.62 meter test section. The tunnel speed is regulated by a custom-designed Emerson Drive. A 600 hp dc motor is used to power the propeller. The fan motor assembly and motor-generator are mounted on an isolated foundation. However, a source of vibration at 15 Hz is found in the test section. The test section is enclosed in an air-tight control room to prevent any air from leaking into the tunnel. The pressure in the control room is kept at the same static pressure of the test section. A slight negative pressure gradient of approximately $\frac{\partial C_p}{\partial x} = 0.33\%$ per meter is present in the test section. The settling chamber is 3 meters long and has a contraction ratio of 9 to 1. The angle of the diffuser is 3°. The tunnel circuit has no heat-exchanger for temperature control. However, an air-exchange tower, open to the atmosphere, is placed immediately after the fan to stabilize the flow temperature. Streamlined turning vanes are placed at every corner of the wind tunnel to provide a uniform flow. The tunnel, equipped with seven anti-turbulence screens along with other flow smoothing features, provides a turbulence level from as low as 0.018% at a free-stream velocity of 9 m/sec up to 0.045% at a free-stream velocity of 30 m/sec. The average velocity variation across the test section is about 0.5%. Flow angularities in yaw and pitch are less than 2°. Further information on the VPI Stability Wind Tunnel can be found in the report by Choi and Simpson [1987].

2.4 Velocity Measurement Using LDV

Introduction

Since its introduction in 1964, the laser-Doppler velocimeter (LDV) has been recognized as a very reliable method in measuring velocity of complex flow fields including turbulent, separating, recirculating and vortical flows just to name a few. It can be used under hostile conditions as in chemically reacting flows, combustion, flames and flows with radiation. The instrument is capable of operating over wide velocity, density, temperature and composition ranges. However, at low density, measurements become more difficult due to problems in finding particles that follow the flow and scatter enough light. LDV provides means of non-intrusive measuring technique for flows that are sensitive to disturbance. The size of the measurement volume is small enough for essentially point measurements. Having the ability for rapid response, LDV is also suitable for measurements of high-frequency fluctuations. No calibration is required since the velocity is measured directly from light scattered by particles in the flow. However, a thorough knowledge of a wide range of disciplines is required to avoid serious measurement errors. This includes optics, electronics, light propagation and signal processing. In carefully controlled environments, the errors can be as low as 0.1%.

Two-Component LDV Fiber-optic Probe System

Figure 2.3 shows the system layout and optical components of the two-component LDV fiber-optic probe system. An INNOVA 70 two-Watt Argon-ion laser, capable of producing beams with twelve discrete wavelengths simultaneously from 351nm to

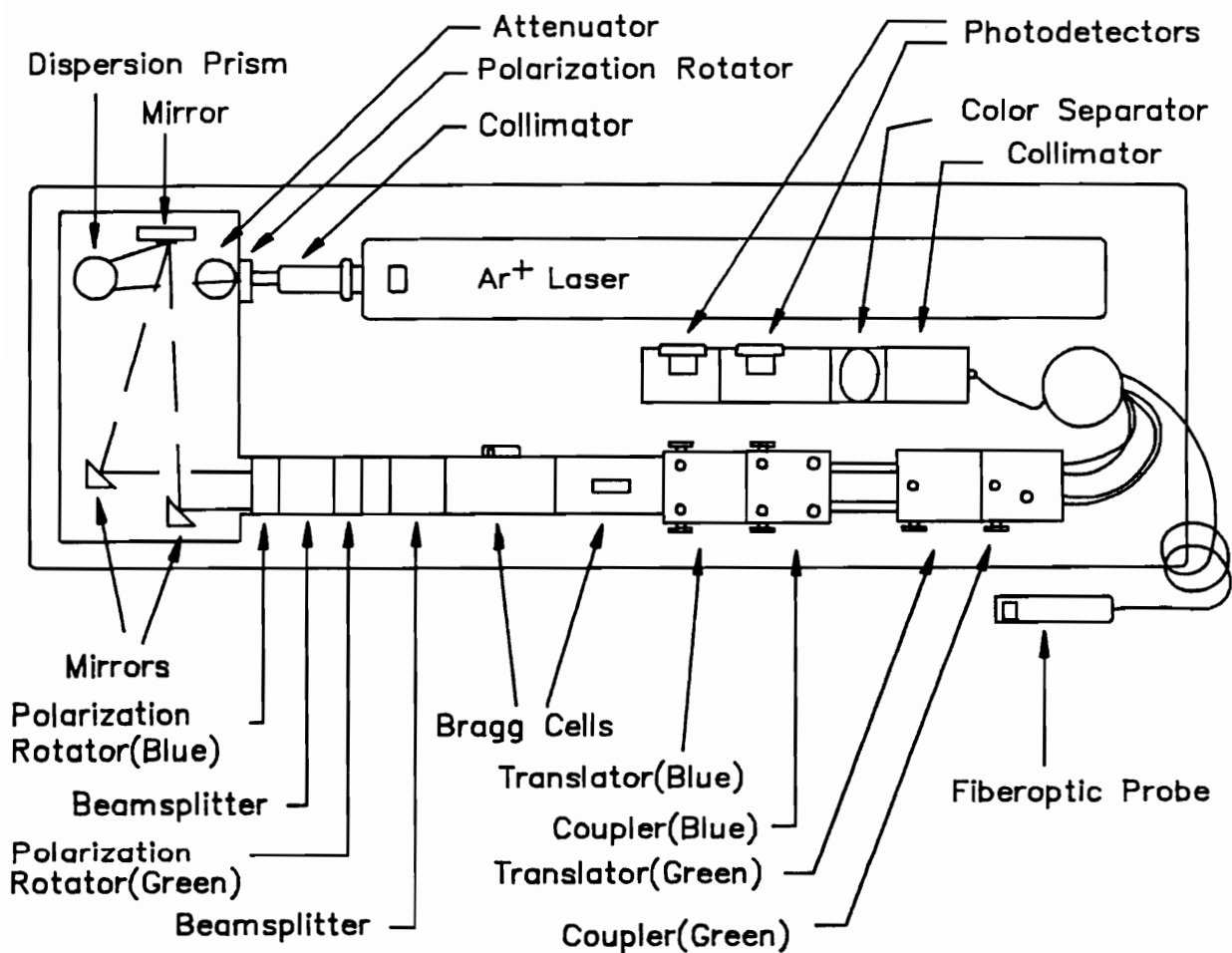


Figure 2.3. A layout of an LDV fiber-optic probe system.

528nm, is used. Two principal wavelengths of the Argon-ion laser are used - the green at 514nm and the blue at 488nm. The combined laser power of these two wavelengths is about 1.5 Watts. A collimator (TSI 9108) is located immediately at the exit of the laser. It ensures that the beam diameter remains constant along the optical bench. Without the collimator, the beam diverges and this results in non-uniform fringe spacing.

A multi-color polarization rotator (TSI 9101-1) is mounted next to the collimator. It is used to control the intensity of the laser beam during the alignment procedure to reduce any risk of exposure to high power laser. Following the polarization rotator is a layout of the color separator assembly; this includes an attenuator (TSI 9204A), a dispersion prism (TSI 9106) and three mirrors (TSI 9107). The dispersion prism can separate the color properly only if the light is horizontally polarized. The attenuator, contains a polarization-splitting cube which allows light of horizontal polarity to pass through and reflects light with vertical polarity. The dispersion prism is then separates the multi-line laser beams into ten visible color lines with various wavelengths. The two strongest color lines, the green color line at 514nm and the blue color line at 488nm, are reflected parallel to the optical bench by two mirrors. The blue beam then enters the 488nm polarization rotator (TSI 9102-12) which polarizes it vertically before being split into two equal power beams by a beamsplitter (TSI 9115). The green beam enters the 514nm polarization rotator (TSI 9102-11) which polarizes it horizontally. And again, the green beam is also being split into two beams by a beamsplitter (TSI 9115). One of each of the blue and green beams are shifted by their respective Bragg cells (TSI 9182-3A) to 5 MHz. This allows measurements of flow reversals.

All four beams are now ready to enter their corresponding translators (TSI 9259) and couplers (TSI 9262). The purpose of the translators is to make sure the beams are parallel to the optical bench before entering the couplers. The couplers direct all four beams into a fiber-optic cable (TSI 9297) consists of four separate transmitting lines and

one receiving line. The fiber optic cable transmits these four beams to a probe head of 25 mm in diameter and 100 mm in length. The probe head contains sending optics which set the beams to cross at a focal distance of 135 mm. The fringe spacings of the blue and green beams are $4.68\ \mu\text{m}$ and $5.01\ \mu\text{m}$, respectively. The diameter of the measuring volume is about $73.7\ \mu\text{m}$ with 1.42 mm in length. A set of receiving optics collects the scattered light and focuses it back to the receiving fiber. The diverged light from the receiving fiber is collimated by a receiving fiber collimator (TSI 9269) before entering a color separator (TSI 9145). The color separator then segregates the scattered blue and green light and directs them to their respective photodetectors (TSI 9160). Each photodetector contains a color filter (TSI 9158 and 9159 for the green and blue light, respectively) to further discard unwanted light. The photodetectors convert the scattered light into electrical signals which can be processed by two TSI IFA 550 signal analyzers. An IBM PC PS/2 Model 60, equipped with a DMA board, is used to receive data from the TSI IFA 550 through a 25-pin cable and an RS-232.

Theory Of Operation

An LDV measures the velocities of flowing fluid from Doppler frequency information contained in light scattered by particles injected into the flow. The Doppler frequency shift of the scattered light can be directly obtained using a scanning Fabry-Perot interferometer. However, the resolution of such method is about 2m/s which is inadequate except for very high speed flows. A more preferable technique for LDV measurements is the optical heterodyne (mixing) detection. By using a photodetector, the intensity of two light sources mixing on the photodetector surface is obtained. The intensity consists of two terms. A constant term represents the sum of the intensities of

each light source. The heterodyne term, oscillating at a certain frequency, is the Doppler shift of the scattered light.

Three methods can be used to accomplish the heterodyne technique as shown in Figure 2.4. For the reference beam system, scattered light from an illuminating beam is heterodyned with light from a reference beam usually obtained directly from the laser. In the case of dual scattered system, scattered light obtained from two directions of a single beam is heterodyned. Finally, for the dual-beam system, scattered light from two incident beams is heterodyned. The dual-beam system is used almost exclusively since it is the easiest system to align. In addition, the Doppler frequency is independent of the location of the collection optics when the light sources are plane, coaxial and uniform intensity waves.

When two light sources cross at a point in the dual system beam, they form an ellipsoidal measurement volume, containing light and dark fringe patterns. As a particle passes through these fringes, it scatters light which contains the Doppler frequency. With the relationship between incident and scattered light, known as the differential Doppler, the velocity of the particle can be derived. However, an alternate approach can be used to derive the velocity of the particle known as the "fringe model". The inverse of the Doppler frequency or equivalently the inverse of the fringe crossing frequency is the time for a particle to travel from one fringe to another. Since the distance between fringes can be obtained using theory of optical interference, the velocity of the particle can be readily computed. The fringe model is conceptually simple but can not be used to explain certain theoretical concepts of the Doppler signal characteristics such as signal-to-noise ratio (SNR) or visibility.

The differential Doppler approach is now described in the following paragraph. The relationship between the incident and scattered light from a single light beam is given by

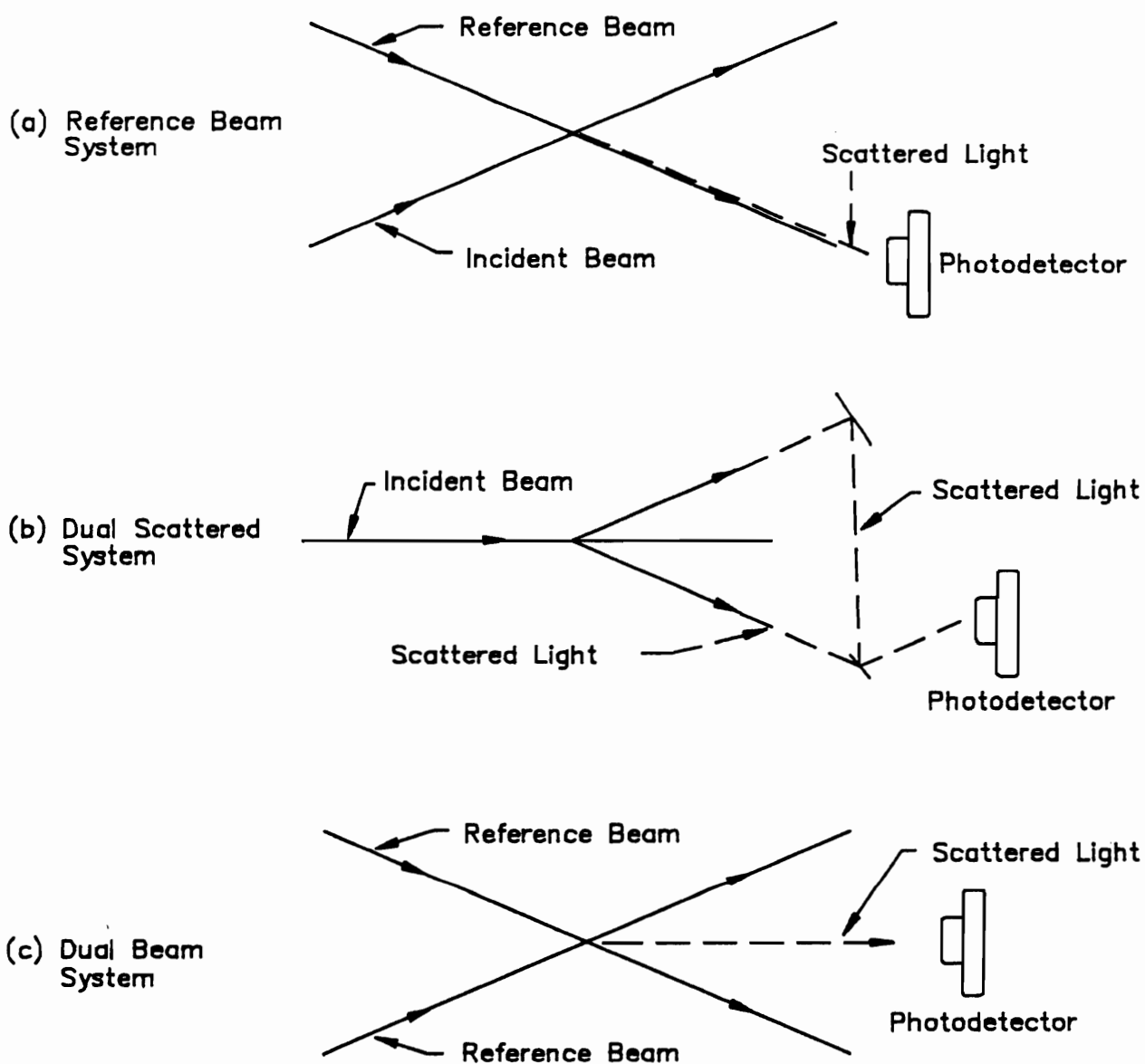


Figure 2.4. Heterodyne detection methods (a) reference beam system (b) dual scattered system (c) dual beam system.

$$f_s = f_i + \frac{\vec{u}}{\lambda} \cdot (\hat{s} - \hat{i}) \quad [2.1]$$

where f_s and f_i are the scattered and incident light frequencies, respectively, \vec{u} is the particle velocity, λ is the wavelength of the light, \hat{s} and \hat{i} are the unit vectors in the directions of the scattered and incident light, respectively. Equation [2.1] can be rewritten as

$$f_{s_1} = f_{i_1} + \frac{\vec{u}}{\lambda} \cdot (\hat{s}_1 - \hat{i}_1) \quad , \quad f_{s_2} = f_{i_2} + \frac{\vec{u}}{\lambda} \cdot (\hat{s}_2 - \hat{i}_2) \quad [2.2]$$

where the subscripts 1 and 2 denote light beam#1 and beam#2. For the dual-beam system, the Doppler frequency received by the photodetector is the difference of the Doppler shift of the scattered light beams,

$$f_D = f_{s_1} - f_{s_2} \quad [2.3]$$

By substituting equations [2.2] into equation [2.3] we obtain

$$f_D = (f_{i_1} - f_{i_2}) + \frac{\vec{u}}{\lambda} \cdot (\hat{s}_1 - \hat{i}_1 - \hat{s}_2 + \hat{i}_2) \quad [2.4]$$

Since this is the dual-beam setup, the unit vectors \hat{s}_1 and \hat{s}_2 are in the same direction. Equation [2.4] thus becomes

$$f_D = (f_{i_1} - f_{i_2}) + \frac{\vec{u}}{\lambda} \cdot (\hat{i}_2 - \hat{i}_1) \quad [2.5]$$

or

$$f_D = (f_{i_1} - f_{i_2}) + \frac{u_x}{\lambda} |\hat{i}_2 - \hat{i}_1| \quad [2.6]$$

where u_x is the velocity component perpendicular to the bisector of the two incident beams (Figure 2.5). If κ is defined as the half-angle between the two incident beams then,

$$|\hat{i}_2 - \hat{i}_1| = 2 \sin \kappa \quad [2.7]$$

By combining equations [2.6] and [2.7], we have

$$u_x = [f_D - (f_{i_1} - f_{i_2})] \frac{\lambda}{2 \sin \kappa} \quad [2.8]$$

The term $(f_{i_1} - f_{i_2})$ is obtained from shifting one of the incident beams by a certain frequency with respect to the other beam using the Bragg cell. This term can be appropriately set to zero if no Bragg cell is installed in the LDV system.

The principle of optical interference of two light sources is employed to describe the fringe model. There are conditions these light sources must meet if the interference pattern is to be observed. The light must remain coherent (constant phase difference) in time. A stable interference pattern can be established only if the frequencies of the light sources are equal and the planes of polarity are the same. A maximum contrast of constructive and destructive patterns is achieved only when the amplitudes are equal. These are reasons that laser light is chosen for LDV measurements. Consider two point light sources emitting waves of the same frequencies and wavelengths (Figure 2.6). The electric fields are given by

$$\vec{E}_1 = \sqrt{I_o} \hat{p}_1 \exp \left\{ j \left[\omega_o t - \frac{2\pi}{\lambda} (x \sin \kappa + y \cos \kappa) \right] \right\} \quad [2.9]$$

$$\vec{E}_2 = \sqrt{I_o} \hat{p}_2 \exp \left\{ j \left[\omega_o t - \frac{2\pi}{\lambda} (-x \sin \kappa + y \cos \kappa) \right] \right\} \quad [2.10]$$

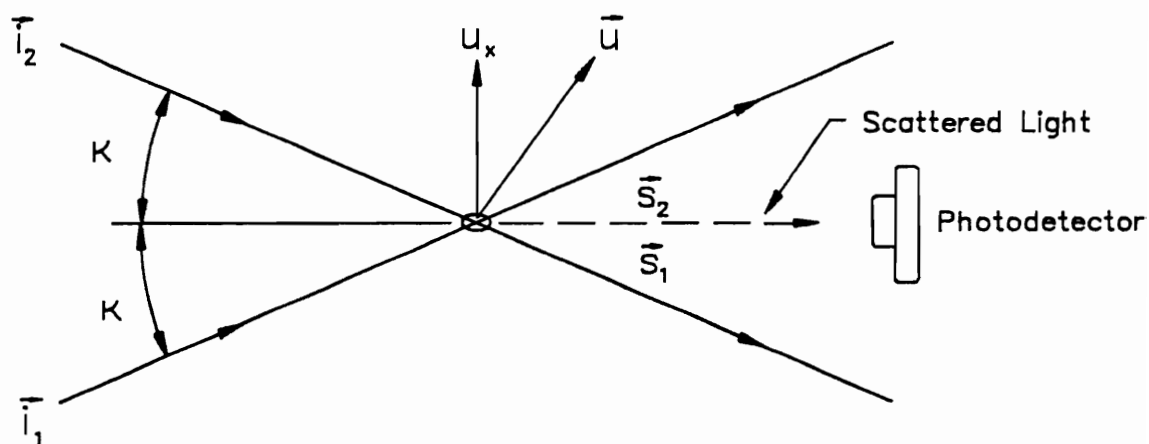


Figure 2.5. Definition of coordinates.

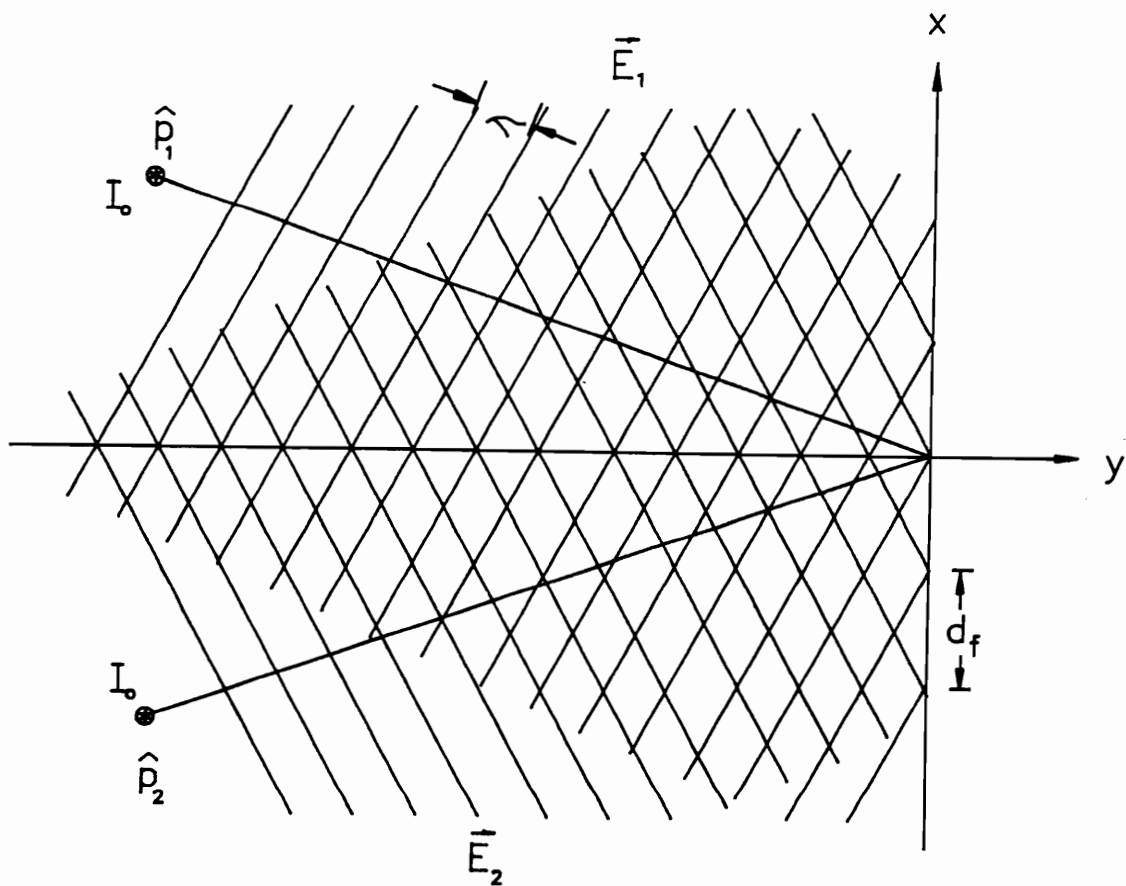


Figure 2.6. Interference pattern of two point light sources.

The resultant electric field at any point in space can be written as $\vec{E} = \vec{E}_1 + \vec{E}_2$. The principle of superposition is applicable here since the governing equation describing planar wave is linear. The total intensity is

$$\begin{aligned} I &= \langle \vec{E} \cdot \vec{E} \rangle = (\vec{E}_1 + \vec{E}_2) \cdot (\vec{E}_1^* + \vec{E}_2^*) \\ &= \vec{E}_1 \cdot \vec{E}_1^* + \vec{E}_2 \cdot \vec{E}_2^* + \vec{E}_1 \cdot \vec{E}_2^* + \vec{E}_2 \cdot \vec{E}_1^* \end{aligned} \quad [2.11]$$

Substituting equations [2.9] and [2.10] into equation [2.11], we obtain

$$\begin{aligned} I &= I_o + I_o + \hat{p}_1 \cdot \hat{p}_2 I_o \exp \left[j \frac{2\pi}{\lambda} (-2x \sin \kappa) \right] + \hat{p}_1 \cdot \hat{p}_2 I_o \exp \left[j \frac{2\pi}{\lambda} (2x \sin \kappa) \right] \\ &= 2I_o \left(1 + \hat{p}_1 \cdot \hat{p}_2 \cos \frac{4\pi x \sin \kappa}{\lambda} \right) \end{aligned} \quad [2.12]$$

The maximum intensity occurs when

$$\frac{4\pi x \sin \kappa}{\lambda} = 2\pi \quad [2.13]$$

Thus, the distance between a complete constructive or destructive fringe is

$$d_f = \frac{\lambda}{2 \sin \kappa} \quad [2.14]$$

It should be noted that two light sources having cross-polarized waves do not interfere since $\hat{p}_1 \cdot \hat{p}_2 = 0$. The velocity of a particle as it travels through the fringes can be written as

$$u_x = f_D d_f = f_D \left(\frac{\lambda}{2 \sin \kappa} \right) \quad [2.15]$$

where f_D is the frequency detected by the photodetector. If one of the light sources is shifted with respect to the other then the fringes will move at $(f_{i1} - f_{i2})$ frequency. Equation [2.15] becomes

$$u_x = [f_D - (f_{i1} - f_{i2})] \frac{\lambda}{2 \sin \kappa} \quad [2.16]$$

which is the same as equation [2.8].

Seeding Techniques

Seeding the flow poses, perhaps, the most difficult problem in setting up an LDV system. Since LDV measures the velocity of particles that move with the flow, proper selection of seeding material is vital for successful measurements. Chosen seeding material must consist of particles that follow the flow, scatter enough light to produce valid signals and be adequate in number. Uniform particle size (monodisperse) is preferable for LDV applications. A thorough study of seeding particulates for laser velocimetry applications can be found in Kamemoto [1989].

Four different instruments were used to generate particles in the VPI Stability Wind Tunnel. Two different fog generators, Martin and Theater Magic, were tested. Unfortunately, the particles were too small to give any valid signals even though an enormous amount of smoke was generated. In addition, the foggers were designed to produce smoke only over a short duration at a time, therefore, inappropriate for continuous use. The next three instruments used $1\mu m$ -polystyrene latex spheres mixed with 200 proof ethanol for seeding material. A TSI Six-jet Atomizer was the first to be tested using monodispersed particles. The atomizer did not generate enough particles for a wind tunnel of such dimensions. An eight-nebulizer cyclone was built in-house and had

proven to be the least effective method in seeding the flow. The most successful method, which was used for all LDV measurements, was the nozzle designed by Seegmiller [1985] of NASA Ames Research Center shown in Figure 2.7. This nozzle worked on the principle of shearing seeding material flowing out of circular openings with a high-jet air. The seeding material was also drawn out of a container through two small tubes by pressurizing the container. The concentration distribution of the particle could be regulated by varying the velocity of the high-jet air and the pressure of the container.

Signal Processing and Data Reduction

Two TSI IFA 550 Signal Processors are used to process output signals from the photodetectors. The IFA 550 can detect a signal with signal-to-noise ratio (SNR) as low as 1.7. A 33 percent change of the Doppler frequency between two consecutive measurements can still be validated by the IFA. It can be considered as both a counter and tracker with a maximum detectable frequency of 15MHz.

When a particle passes through the measurement volume, the light signal registering at the photodetector contains three components; the "pedestal" caused by particles crossing the focusing beams, the Doppler signals, oscillating at the fringe frequency, is superimposed on the pedestals, noise generated by electrons, room lights, scattered laser light reflected off the walls and optical components. The pedestal is removed from the signal by high-pass filtering at a frequency higher than the pedestal frequency. The noise can only be partially reduced by low-pass filtering at a frequency higher than the Doppler frequency. The IFA 550, then, measures the Doppler signal by performing the following steps:

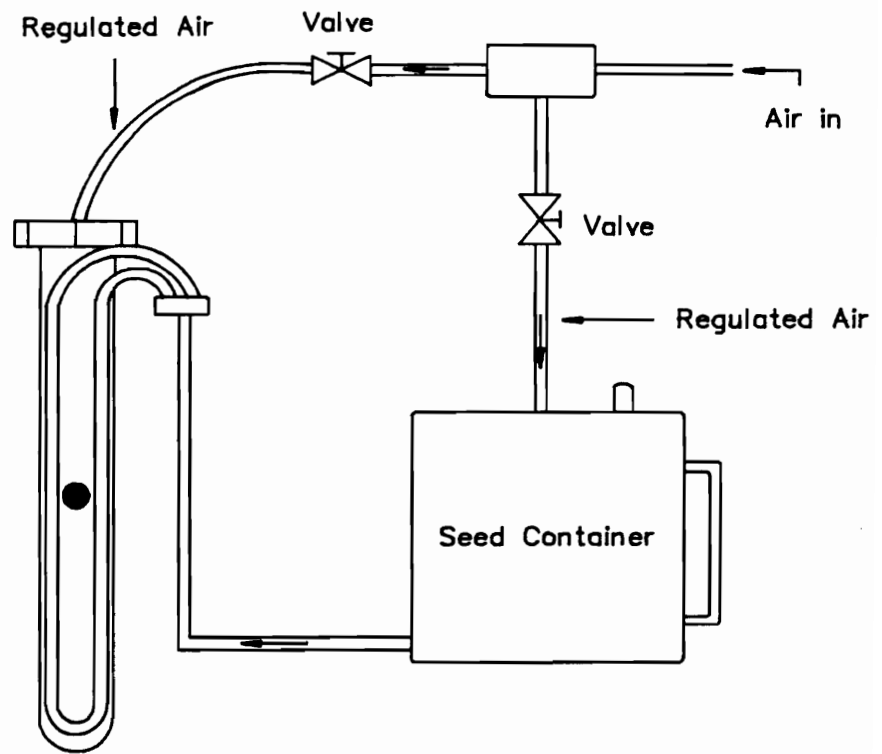


Figure 2.7. Seeding system configuration.

1) A build-in "search" function initially finds the Doppler signal with as little as ten valid fringe crossings. Half-period of Doppler frequency, T_1 , is calculated. A thorough description of the search function can be found in the TSI P/N 1990298 Manual.

2) A timer starts after three contiguous zero-crossings of the signal. This prevents the timer from starting on a pure noise.

3) If the time between one zero-crossing to the next, T , is less than $\frac{1}{3} T_1$ then it is assumed to be noise riding on the Doppler signal. The timer continues to run. Step (3) is repeated until one half-cycle of the Doppler signal is validated. If T is between $\frac{1}{3} T_1$ and $\frac{2}{3} T_1$ then the timer is stopped and step (2) is executed. If T is between $\frac{2}{3} T_1$ and $\frac{4}{3} T_1$, then it is a valid half-cycle of the Doppler signal. Step (3) is repeated until 16 contiguous half-cycles are validated.

4) When 16 contiguous half-cycles are validated, the timer is stopped. The valid Doppler period is one-eighth of the elapsed time, T . A new T_1 is established using the most recent validated Doppler signal and step (2) is repeated. If for some reasons the Doppler signal is lost, then step (1) is executed.

An IBM PC PS/2 Model 60 computer is used for data acquisition and reduction process. The computer communicates with the TSI IFA 550 through a DMA 6260/6265 Interface card and serial port. Data transferred from the DMA Interface card to the computer are in 1K strings. Chauvenet's criterion was used to reject questionable data points. The data acquisition and reduction programs are listed in Appendix. They are written in four different computer languages - Assembly, Basic, Fortran and Pascal.

Uncertainty Analysis

An experimental result R is a function of many independent measured quantities x_1, x_2, \dots, x_n or $R = R(x_1, x_2, \dots, x_n)$. If w_R is defined as the uncertainty in the result and

w_1, w_2, \dots, w_n are the uncertainties in the independent measured quantities; then the equation used to estimate the uncertainty in the result, given by Kline and McClintock [1953], is

$$w_R = \left[\left(\frac{\partial R}{\partial x_1} w_1 \right)^2 + \left(\frac{\partial R}{\partial x_2} w_2 \right)^2 + \dots + \left(\frac{\partial R}{\partial x_n} w_n \right)^2 \right]^{1/2} \quad [2.17]$$

For the fiber-optic LDV system, two velocity components normal to the fringes of the measuring volume in the polar coordinates were measured, V'_z and V'_θ , and were calculated using equation [2.16]. If ξ is denoted as the angle between the fringes of the measuring volume and the flow, then the equations for the velocity components of the flow can be expressed as

$$V_z = V'_z \sin \xi + V'_\theta \cos \xi \quad [2.18]$$

$$V_\theta = V'_z \cos \xi + V'_\theta \sin \xi$$

The uncertainties in the velocity components can be obtained with equation [2.17] if the uncertainties in f_D , f_s , ξ , λ and κ are known. The uncertainty in the wavelength of the laser light can be ignored since λ is precisely known. The half-angle between the beams, κ , was set by the manufacturer to within 0.01° . The angle, ξ , was measured to within 0.1° by a Schaevitz digital inclinometer. The uncertainties in the TSI IFA 550s and the DMA 6260/6265 interface card were found to be 0.56 KHz by sampling a 2 MHz sine-wave signal, typical of the measured Doppler frequency, produced by a function generator (HP 3311A). The uncertainty of the LV frequency shifter (TSI 9186A) was estimated with a frequency counter (HP 5381A). The largest value of uncertainty of the LV frequency shifter occurred at 5 MHz and was 0.20 KHz. From equation [2.17], the uncertainties in the velocity components were computed to be 0.058 m/sec.

2.5 Static Pressure Measurement

Introduction

Surface pressure distribution is mapped out by having series of holes at various points on the body of the model. The pressure coefficient, C_p , is usually presented rather than the absolute static pressure. The pressure coefficient is defined as

$$C_p = \frac{p_s - p_\infty}{\frac{1}{2} \rho U_\infty^2} \quad [2.19]$$

where p_s is the measured surface static pressure, p_∞ is the free-stream static pressure which can be obtained from a Pitot tube, ρ is the density of the measuring medium, and U_∞ is the free-stream velocity. The dynamic pressure, $\frac{1}{2} \rho U_\infty^2$, can also be measured directly from a Pitot tube. Perfect gas law and Sutherland's law may be used to calculate density and viscosity, respectively.

Instrumentation

Figure 2.8 shows a schematic diagram of the instrumentation used in the ESM Wind Tunnel. The SGM S5-48 ScaniValve, equipped with five 48-port pneumatic connectors, is capable of reading up to 240 pressure sources. A CTRL2/S2-S6 Solenoid Controller controls the scanning process of the ScaniValve from one port to another by taking commands from an IBM PC PS/2 computer through a DT2801 Board, a DT507 Multiplexer and a Relay Box. The pressure output from the ScaniValve is connected to one end of a 590 Integral Barocel Pressure Transducer. The other end is referenced to

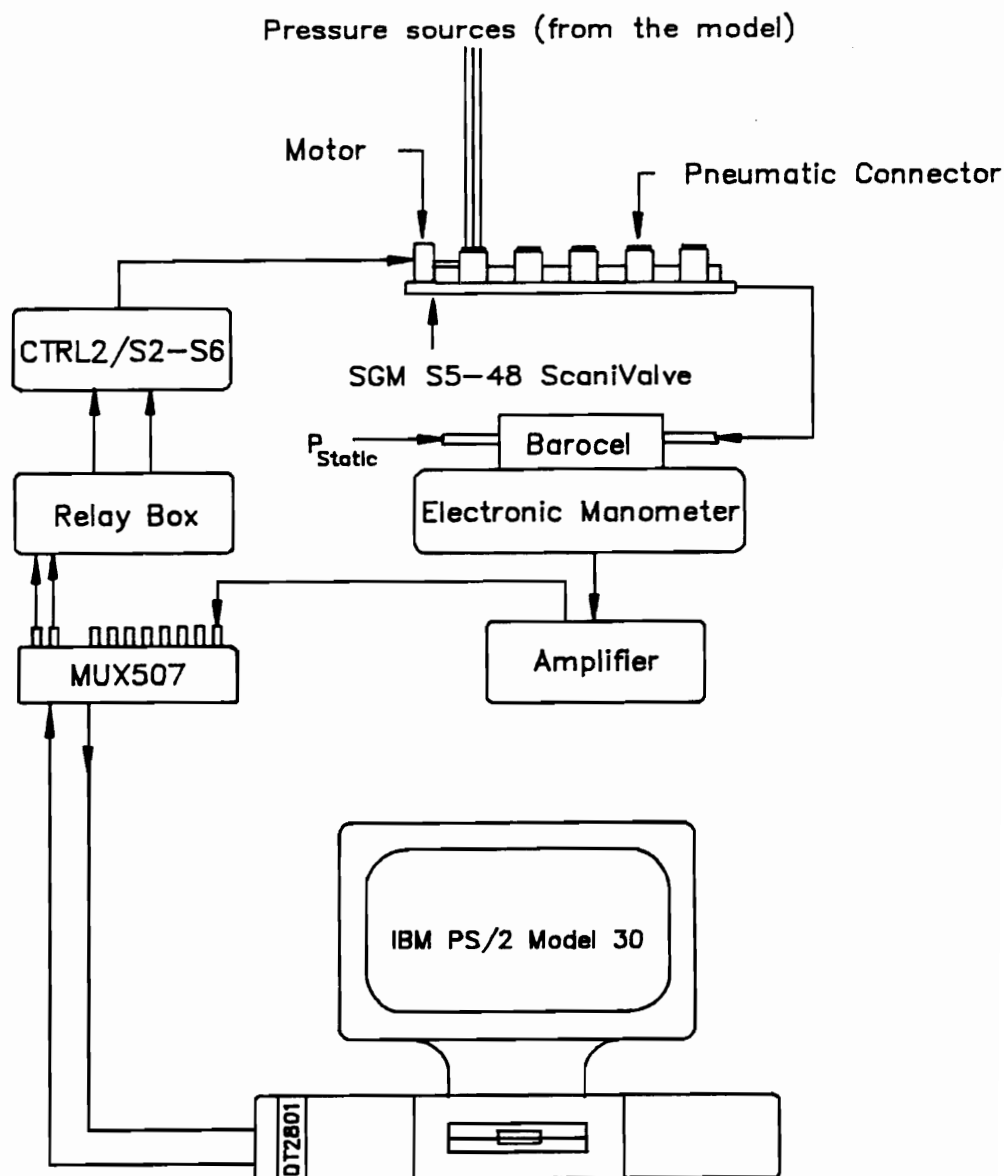


Figure 2.8. A schematic diagram of instrumentation for pressure measurements in the ESM Wind Tunnel.

the static pressure of the free-stream of the flow from a Pitot tube. The total pressure of the Pitot tube is also connected to the ScaniValve so that the wind tunnel air speed can be obtained. For each pressure measurement, 1000 samples are taken at a sampling frequency of 300 Hz. The settling time between each port of the ScaniValve is 3 seconds. The Barocel and a 1450 Electronic Manometer provide the capability for pressure measurement over a range of 0-133 kN/m² with an accuracy of $\pm 0.15\%$ of the reading plus 0.001% of the full scale. The Electronic Manometer converts pressure from each port of the ScaniValve to an electronic signal between -10 volts to $+10$ volts. A 2210 Signal Condition Amplifier was also used to increase the resolution of the output signal of the Electronic Manometer before sending it to the multiplexer. Since the ESM Wind Tunnel is located inside a building, the temperature of the test section and the control room remain at 72°. A thermometer is available to monitor the room temperature. The data acquisition program is written in Turbo Pascal and is listed in Appendix.

Figure 2.9 shows a schematic diagram of the instrumentation used in the VPI Stability Wind Tunnel. A ScaniValve Model D is used to read a maximum of 48 pressure sources. A Pressure Scanner Controller, equivalent to the CTRL2/S2-S6 Solenoid Controller, controls the ScaniValve scanning procedure by taking commands from an HP9836 desktop computer via a Relay Actuator HP 59306A. A Druck differential pressure transducer is used to convert the pressure source to an electrical signal with an accuracy of $\pm 0.1\%$ of the full scale over the range of 0-6.8 kN/m². For each pressure measurement, 50 samples are taken and the settling time between each port of the ScaniValve is 3 seconds. The transducer is referenced to the pressure of the wind tunnel control room. The reader is reminded here that the pressure in the control room is kept at the same static pressure of the test section. Free-stream temperature is monitored by an InstruLab 1563 Digital Thermometer. The temperature inside the test section can change as much as 30° between day-time and night-time measurement. Finally, the test

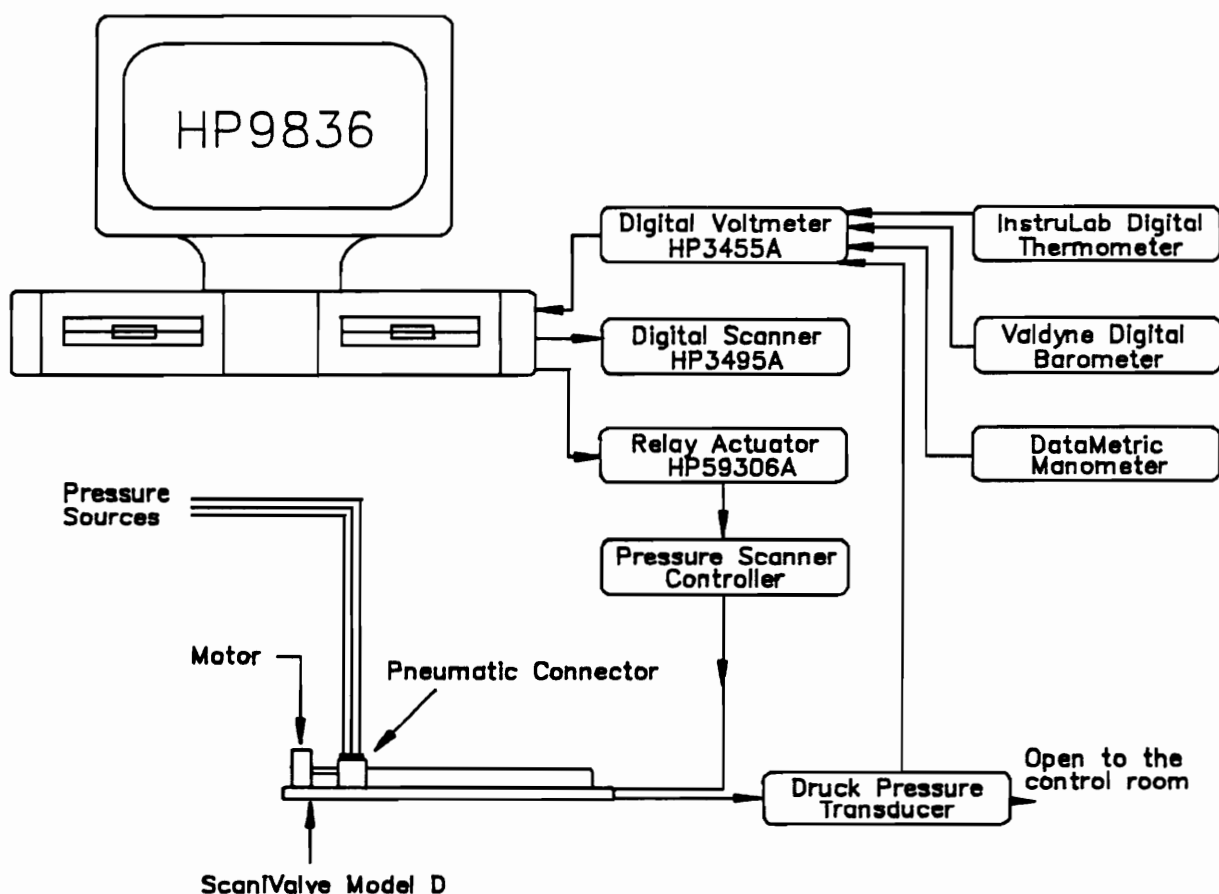


Figure 2.9. A schematic diagram of instrumentation for pressure measurements in the VPI Stability Tunnel.

section dynamic pressure is measured using a DataMetric 1173 Electronic Manometer. All of the digital inputs are read by an HP3495A Data Scanner and an HP3455A Digital Voltmeter. The data acquisition program is written in HP Basic, also listed in Appendix.

2.6 Velocity Measurement Using a Seven-Hole Probe

Introduction

Five-hole probes and triaxial hot-wire probes have been used commonly to map out velocity fields. Unfortunately, with these probes, it is not possible to obtain accurate measurements for local flow angles higher than 40° due to massive separation on the leeside of the probe. The seven-hole probe, capable of measuring flow conditions at angles up to 70° , has been introduced only recently. This section outlines two different calibration methods introduced by Gallington [1980] and Zilliac [1989].

The dimensions and geometry of a seven-hole probe shown in Figure 2.10a were obtained through private communication with Dr. G.S. Jones of NASA Langley. The chosen probe diameter is small to minimize the flow disturbance. However, it was our intention to design the probe diameter large enough to measure pressure fluctuation so that unsteady velocity can be obtained. The probe was constructed by fitting seven small tubes into a larger one. The space between the tubes was filled with steel guitar strings and epoxy to prevent tube displacement. The probe nose was machined to form a cone with a half-angle of 30° . No two probes can be machined exactly the same, therefore, the calibration process must be performed for every probe. During calibration, the probe was mounted on a traversing mechanism which constrained its tip to remain at the same point in the test section. A microstep CXT29-32 Compumotor stepping motor

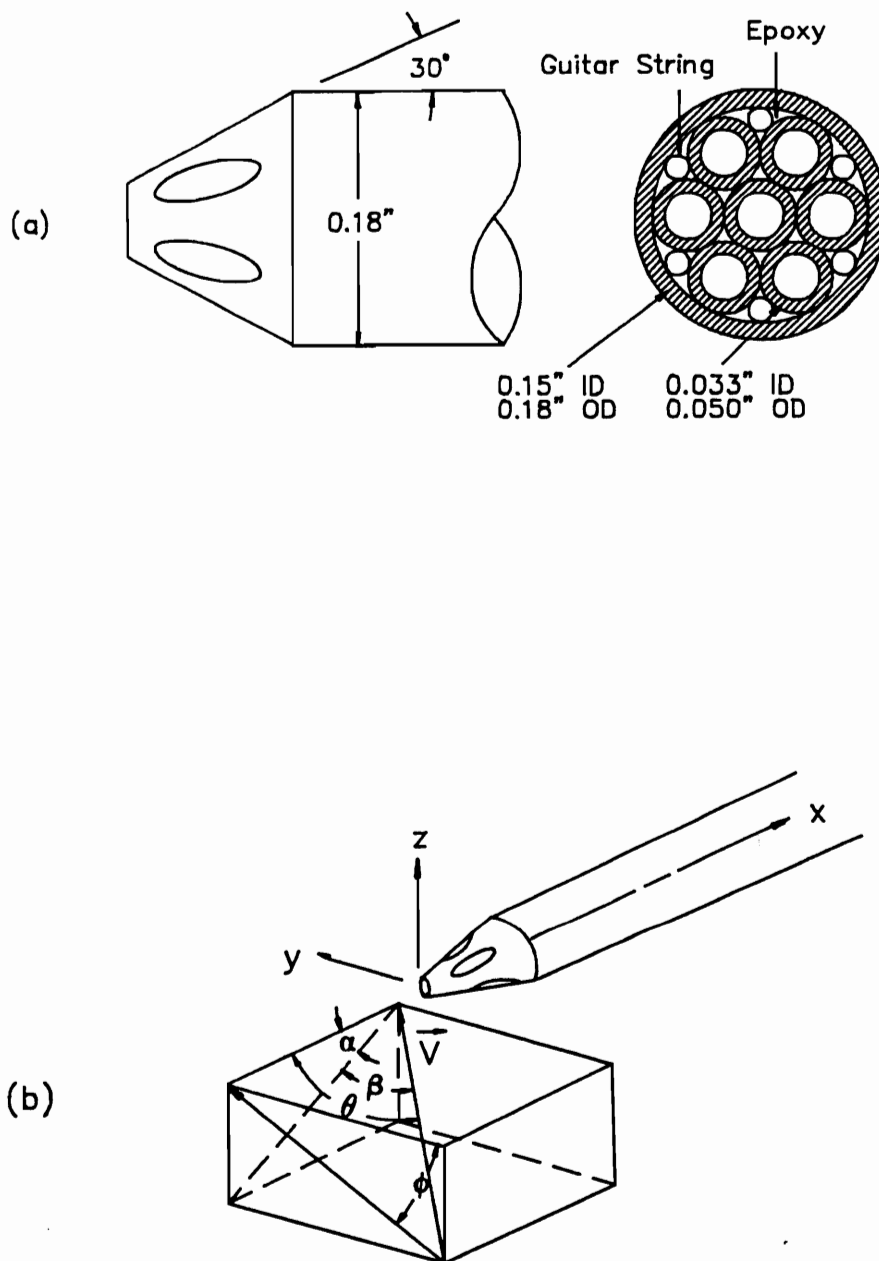


Figure 2.10. (a) Probe geometry and (b) flow angle definition.

was used to roll the probe in 1.8° increments. The instrumentation setup is the same as the setup for static pressure measurement in the ESM Wind Tunnel, therefore, will not be repeated here again.

Calibration Procedure Using The Gallington's Method

The Gallington's calibration method involves positioning the probe at known angles to the flow and then measuring the seven pressures. Based on combinations of differences between the seven measured pressures, dimensionless pressure coefficients are formed. Flow properties are then determined based on the dimensionless pressure coefficients and the known probe orientation as third-order polynomial functions. When the probe is placed in an unknown flow field, the position of the probe, the local static and total pressures are computed from their corresponding polynomial expressions. Since the local static and total pressures and the angles of the flow are known, the local velocity can also be found using the incompressible Bernoulli's equation.

The objective of the calibration is to establish third-order polynomial functions that represent the orientation of the probe with respect to the flow (usually defined by two angles), the local static and total pressures as functions of pre-defined (dimensionless) pressure coefficients calculated from the seven measured pressures. Ten constants are needed to completely describe each third-order polynomial function. Therefore, the probe is first placed in the flow field at ten known positions corresponding to ten known local static and total pressures. The seven measured pressures at each probe position are used to calculate the pressure coefficients. All the constants for the polynomial functions can be found with known probe positions, local static and total pressures and the pressure coefficients; thus, the polynomial functions themselves are established.

The flow over the seven-hole probe can typically be divided into two regimes; low-angle and high-angle flows. For low-angle flows, the pressure registers by hole#1 (Figure 2.11), p_1 , is always the highest among the seven measured pressures. The flow remains attached over the entire probe, therefore, a unique set of seven pressures exists at every probe's position with respect to the flow denote by p_1 through p_7 . Since p_1 is the highest pressure, it is referred to as the approximate total pressure. The approximate static pressure, \bar{p}_{2-7} , is defined by averaging the pressures surrounding the stagnation pressure hole. The equation is given by

$$\bar{p}_{2-7} = \frac{p_2 + p_3 + p_4 + p_5 + p_6 + p_7}{6} \quad [2.20]$$

A new variable, known as the total pressure coefficient, C_t , is introduced to correct for the difference between the true total pressure, p_t , and the approximate total pressure

$$C_t = \frac{p_1 - p_t}{p_1 - \bar{p}_{2-7}} \quad [2.21]$$

Similarly, the same analogy is used to derived the static pressure coefficient

$$C_s = \frac{p_1 - p_s}{p_1 - \bar{p}_{2-7}} \quad [2.22]$$

where p_s is the true static pressure. The orientation of the probe with respect to the flow is defined by two angles, the pitch angle α and the yaw angle β . The pitch angle is the angle between the probe's axis and the projection of the velocity vector onto the x-z plane. The yaw angle is the angle between the velocity vector and the projection of the velocity vector onto the y-z plane (see Figure 2.10b). The pitch pressure coefficient, $C_{p,\alpha}$, is derived from the linear relationship between the change of angle of attack and the seven pressures

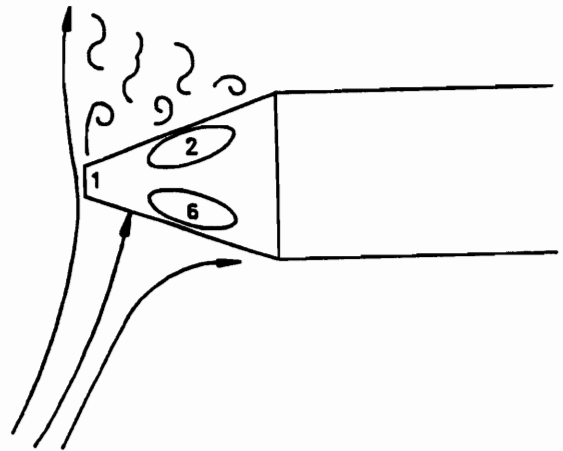
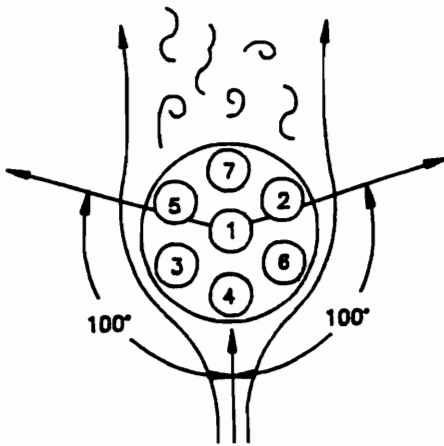


Figure 2.11. Flow over the probe at high angles of attack.

$$C_\alpha = \frac{\left(\frac{p_5 + p_7}{2} \right) - \left(\frac{p_4 + p_6}{2} \right)}{p_1 - \bar{p}_{2-7}} \quad [2.23]$$

Likewise, the yaw pressure coefficient is given by

$$C_\beta = \frac{p_2 - p_3}{p_1 - \bar{p}_{2-7}} \quad [2.24]$$

For high-angle flows, the pressure at hole#i, p_i , registers the highest pressure where i takes on a value from 2 to 7. Equation [2.20] through [2.24] must be modified since the flow may not remain attached over the entire probe. The holes lying on the leeside of the probe are insensitive to the change of the flow direction. Figure 2.11, taken from Everett et al. [1983], shows flow over the probe at high angles of attack where the separation points are at $\pm 100^\circ$ from the stagnation point for turbulent flow or $\pm 90^\circ$ for laminar flow. The approximate static pressure, \bar{p} , is redefined to include only holes within the attached region

$$\bar{p} = \frac{p_i^- - p_i^+}{2} \quad [2.25]$$

where p_i^- and p_i^+ are the pressures measured from the holes in the clockwise and counterclockwise direction, respectively, adjacent to hole#i. The approximate total pressure is again given to the highest registered pressure, p_i . The total and static pressure coefficients are

$$C_t = \frac{p_i - p_t}{p_i - \bar{p}} \quad , \quad C_s = \frac{p_i - p_s}{p_i - \bar{p}} \quad [2.26]$$

For high-angle flows, the position of the probe with respect to the flow is more conveniently defined in polar coordinates. The cone angle, θ , is the angle between the velocity vector and the probe's axis and the roll angle, ϕ , is the angle between the y-axis and the projection of the velocity vector onto the y-z plane. The cone and roll pressure coefficients are

$$C_\theta = \frac{p_i - p_1}{p_i - \bar{p}} \quad , \quad C_\phi = \frac{p_i^- - p_i^+}{p_i - \bar{p}} \quad [2.27]$$

For low-angle flows, the flow properties α , β , C_i and C_r can be expressed using a third-order polynomial expansion as functions of C_α and C_β . The general expression is given by

$$\begin{aligned} A = & K_1^A + \\ & K_2^A C_\alpha + K_3^A C_\beta + \\ & K_4^A C_\alpha^2 + K_5^A C_\alpha C_\beta + K_6^A C_\beta^2 + \\ & K_7^A C_\alpha^3 + K_8^A C_\alpha^2 C_\beta + K_9^A C_\alpha C_\beta^2 + K_{10}^A C_\beta^3 + \text{ignored higher order terms} \end{aligned} \quad [2.28]$$

where A represents α , β , C_i and C_r . The constants K_i^A for each flow property can be solved for with a set of ten data points obtained from the calibration. In the case of high-angle flows, equation [2.28] is modified by replacing C_α and C_β with C_θ and C_ϕ , respectively. The term A becomes θ , ϕ , C_θ or C_ϕ . Taking a sample of ten α 's and rewriting equation [2.28] in the matrix form

$$\begin{bmatrix} \alpha_1 \\ \alpha_2 \\ \alpha_3 \\ \vdots \\ \vdots \\ \alpha_{10} \end{bmatrix} = \begin{bmatrix} 1 & C_{\alpha_1} & C_{\beta_1} & \dots & C_{\beta_1}^3 \\ 1 & C_{\alpha_2} & C_{\beta_2} & \dots & C_{\beta_2}^3 \\ 1 & C_{\alpha_3} & C_{\beta_3} & \dots & C_{\beta_3}^3 \\ \vdots & \vdots & \vdots & \dots & \vdots \\ \vdots & \vdots & \vdots & \dots & \vdots \\ 1 & C_{\alpha_{10}} & C_{\beta_{10}} & \dots & C_{\beta_{10}}^3 \end{bmatrix} \begin{bmatrix} K_1^\alpha \\ K_2^\alpha \\ K_3^\alpha \\ \vdots \\ \vdots \\ K_{10}^\alpha \end{bmatrix} \quad [2.29]$$

or

$$[\alpha] = [C][K^\alpha] \quad [2.30]$$

The matrix $[\alpha]$ is set during the calibration. The matrix $[C]$ is obtained by solving equations [2.23] and [2.24] using ten sets of the seven measured pressures. The matrix $[K^\alpha]$ can be readily solved with a Gaussian-elimination scheme. The same procedure is repeated to find $[K^\beta]$, $[K^{C_t}]$ and $[K^{C_r}]$.

The probe is now ready to be used in an unknown flow field. For low-angle flows, with the seven measured pressures, C_α and C_β can be obtained using equations [2.23] and [2.24], respectively. To find α , β , C_t and C_r , substitute C_α and C_β into equation [2.28]. The local static and total pressures are obtained by solving equations [2.21] and [2.22]. The local velocity, U , is given by the incompressible Bernoulli's equation

$$U = \sqrt{\frac{2(p_t - p_s)}{\rho}} \quad [2.31]$$

where ρ is the density of air. The three velocity components, as functions of pitch and yaw angles, are

$$u = U \cos \alpha \cos \beta \quad , \quad v = U \sin \beta \quad , \quad w = U \sin \alpha \cos \beta \quad [2.32]$$

The above approach is repeated to obtain θ , ϕ , C_p and C_f for high-angle flows. And again, the three velocity components, as functions of cone and roll angles, are

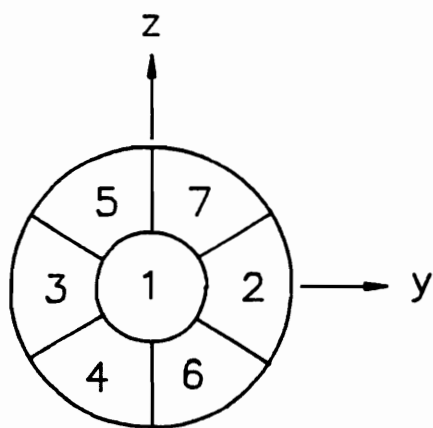
$$u = U \cos \theta \quad , \quad v = U \sin \theta \cos \phi \quad , \quad w = U \sin \theta \sin \phi \quad [2.33]$$

The previous calibration method cannot be used in the compressible flow regime. The reader is referred to Everett et al. [1983] on how to resolve the compressibility effect.

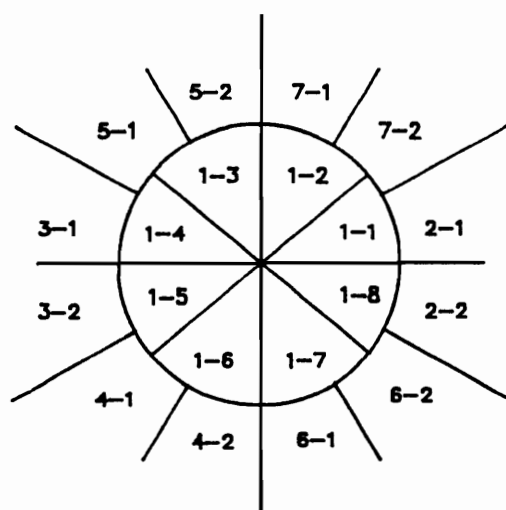
The calibration was conducted in the ESM Wind Tunnel at a Reynolds number of 3000 based on the probe's diameter. The probe's calibration domain is divided into seven major sectors as mentioned previously. Surface area of sector#i is enclosed within a region where p_i registers the highest pressure (i takes on a value between 1 and 7). The accuracy of this method can be further improved by dividing sector#1 into eight equal sub-sectors. Each of the other sector is divided into two equal sub-sectors as shown in Figure 2.12. The calibration is performed for each individual sub-sector. Consequently, twenty sets of third-order polynomial functions of flow properties are found. An extra set of fourth-order polynomial functions is also established for sector#1. This is a means for determining which set of the sub-sector polynomial expressions is to be used when the probe is placed in an unknown flow field and the flow lies in sector#1. For other sectors, it is obvious that by investigating the adjacent pressure holes the sub-sector can be determined. The flow angle accuracy by this method is found to be within 1° and the velocity magnitude to within 2%.

Calibration Procedure Using The Zilliac's Method

The second calibration method is based on a procedure proposed by Zilliac [1989]. Similar to the previous method, flow properties (α , β , C_p and C_f or θ , ϕ , C_θ and C_ϕ) can



(a)



(b)

Figure 2.12. Division of the calibration domain (a) seven main sectors (b) twenty sub-sectors.

be expressed as surface functions of discrete points defined by a pair of pressure coefficients (C_a and C_b or C_θ and C_ϕ). These surface functions are obtained during the calibration procedure. When the probe is placed in an unknown flow field, the flow properties can be obtained by interpolating the surface functions using the ISML DSURF routine (IMSL User's Manual, 1987), therefore, the velocity components can be found. The IMSL DSURF routine used the Akima [1978] method to compute a smooth bivariate interpolation to scattered data which is locally a quintic polynomial in two variables.

The probe calibration domain for this method is also divided into seven sectors having the same definitions as before. For sector#1 or low angle flows, three pressure coefficients are defined

$$C_a = \frac{p_2 - p_3}{p_1 - \bar{p}} \quad , \quad C_b = \frac{p_5 - p_6}{p_1 - \bar{p}} \quad , \quad C_c = \frac{p_7 - p_4}{p_1 - \bar{p}} \quad [2.34]$$

where \bar{p} has the same definition as \bar{p}_{2-} in equation [2.25]. The pitch and yaw pressure coefficients are given by

$$C_\alpha = \frac{1}{\sqrt{3}} (C_b + C_c) \quad , \quad C_\beta = \frac{1}{3} (2C_a + C_b - C_c) \quad [2.35]$$

The static and total pressure coefficients are

$$C_s = \frac{\bar{p} - p_s}{p_1 - \bar{p}} \quad , \quad C_t = \frac{p_1 - p_t}{p_1 - \bar{p}} \quad [2.36]$$

For high angle flows, the flow properties are defined by equations [2.25] and [2.27].

Comparison Between The Two Calibration Methods

The errors involved in seven-hole probe measurements depend on many factors which will be discussed in Chapter 4. One of the major contributions in reducing errors is the selection of a proper calibration method. As mentioned earlier, two unique methods are employed to calibrate the probe; each has its own advantages and disadvantages. The Gallington's method has flow-angle accuracy to within 2.5° and velocity magnitude to within 5%. An improved version of this calibration further increases the flow-angle accuracy to within 1.0° and velocity magnitude to within 2.5%. When the probe is placed in an unknown flow field, with this calibration method, the velocity vector field can be reduced and displayed immediately during the experiment. The advantage of being able to reduce data "on-line" is comparable to having a feedback system. This allows the researcher to concentrate on measuring specific flow regions of interest rather than guessing. Zilliac's method can determine flow angles to within 0.5° and velocity magnitude to within 1%. The increase in accuracy by this method is due largely to an unlimited number of calibration points used to fit the surface. A major disadvantage of this approach is the requirement of vast amount of computer time to interpolate data. This eliminates any chances of displaying velocity data during the experiment. Consequently, both methods are employed to alleviate the disadvantages. Data were displayed on the screen during the tunnel operation using the first method. Data were also stored and processed later, employing the second method.

2.7 Hot-Wire Anemometry

Two single-wire DISA type 55D01 Constant Temperature Anemometers are used in this experiment to detect vortex shedding and heaving. The frequency response of the anemometers are about 100 KHz. Their electrical output signals are processed by an HP3562A Dynamic Signal Analyzer. The output signals can be displayed on both time and frequency domain by the signal analyzer. The resulting spectrum is an average of thirty sample spectra. A phase difference between two signals is also provided for a two-channel input. The signal analyzer has a measurement range from 60 μHz to 100 KHz for both channels. The anemometers were tested by placing a pair of hotwires in the wake of a 2-D circular-cylinder spanning the entire height of the wind tunnel to observe vortex shedding. The reduced shedding frequencies are calculated for models with different diameters and at various wind tunnel velocities. The results are compared with the well known Strouhal number frequency of 0.2.

2.8 Flow Visualization And Digital Processing

Introduction

In the experimental field, flow visualization is clearly the first step in identifying the key features of the flow. However, such information is often lost, because it is not documented in quantitative form. Good documentation of flow visualizations is necessary, preferably in the form of digital data. Surface flow visualization is used in this re-

search effort to study the structure of the flow over the model in the neighborhood of separation, with emphasis on the separation bubble and the lines of separation.

Flow Visualization Techniques

Skin-friction lines are visualized at different angles of attack and Reynolds numbers by painting the surface of a model with a mixture of Oleic Acid, Titanium Dioxide and kerosene. The surface of the model is sanded and waxed to reduce surface roughness and allow the mixture to move freely about the model. When the model is placed in a flow, the mixture dries up to form traces of discrete skin-friction lines. The results are photographed at different views and later digitized and displayed in composite figures. Liquid crystal solution is also used to visualize skin-friction lines although not as successful. This solution can change color from blue to green with a minute temperature variation. Thus, by painting the surface of the model with liquid crystal solution, regions of different magnitude of skin-friction can be detected.

Setup Of The Instrumentation

A DATATAB Graphic Digitizer is used to convert the flow visualizations to numerical data. The operational system consists of four major units: a graphic table (DATATAB), a controller (AC 90C), a sixteen-digit keypad and an output device (IBM PC). The graphic table has an imbedded-electronic grid that can be read by the controller via a keypad. The controller communicates with the IBM PC through a serial port. The data are transmitted to the computer in the form of two five-digit numbers. When the keypad is placed on the graphic table surface, the X-Y positions of the cross-

hair on the keypad with respect to the table are displayed. As the keypad moves about the surface of the table, the X-Y positions may be recorded with a resolution and repeatability of 0.001". The digitization program was written in Turbo Pascal.

Chapter 3: Low-Reynolds Number Measurements

3.1 Introduction

The flow over a hemisphere-cylinder has been the subject of only a few experimental and computational investigations. All previous efforts were carried out in the transonic or the low supersonic regimes and were limited to angles of attack $\alpha = 0^\circ$ to 27.5° . Data at low Reynolds numbers and low Mach numbers are currently not available. The main contribution of this chapter is a careful documentation of the development of the symmetric and asymmetric leeward vortices, the horn vortices and the separation bubble on the a hemisphere-cylinder body at low Reynolds numbers, namely $Re = 10^4$ based on the diameter of the model. Flow visualization, static pressure measurements and seven-hole probe velocity measurements were chosen to provide a complete picture of the flow.

Skin-friction patterns obtained at high Mach number are discussed here to compare with the present experimental results (conducted at low Mach numbers and low Reynolds numbers). Hsieh [1975, 1976, 1977] employed surface oil-flow, shadowgraphs,

surface pressure measurements and laser-Doppler velocimetry measurements to study flow patterns of the hemisphere-cylinder at incidences from 0° to 19° in Mach number range from 0.6 to 1.5; the corresponding Reynolds number range was from 3.4×10^5 to 8.6×10^5 , respectively, based on the diameter of the circular afterbody. His model had the dimensions of 1 inch diameter and 10 inches in length.

Hsieh observed that at $\alpha = 0^\circ$, the existence of nose separation or separation bubble (Figure 3.1a) depended on the free-stream Mach number. At Mach number $M_\infty = 0.6$, the flow was well attached everywhere on the model. Between $M_\infty = 0.7$ and 0.85, the separation bubble appeared and was most pronounced at $M_\infty = 0.85$. The flow formed a closed-type separation with limiting streamlines as shown in Figure 3.1a. All of the drawings in Figure 3.1 are taken directly from Hsieh's [1976] paper. The separation region vanished for $M_\infty \geq 0.9$. In order to define the conditions under which nose separation occurs, Hsieh defined a critical minimal pressure coefficient, $C_{P_{min,c}}$. This coefficient must be determined empirically for different nose configurations. If the nose separation were to be expected, the minimum pressure coefficient, $C_{P_{min}}$, calculated from inviscid theory, must be less $C_{P_{min,c}}$. Hsieh plotted $C_{P_{min}}$ versus Mach number and found that $C_{P_{min}}$ dropped below -1.2 in the range of $0.6 < M_\infty < 0.9$. He concluded that for $M_\infty \leq 0.6$ or $M_\infty \geq 0.9$, $C_{P_{min}}$ was not low enough to initiate separation in the nose region of the model. He found that for a hemisphere-cylinder, $C_{P_{min,c}}$ has an approximate value of -1.2 .

At an incidence slightly higher than $\alpha = 0^\circ$, strong cross-flow caused the boundary layers to separate and roll up far downstream to form a pair of leeward vortices as shown in Figure 3.1e. The separation bubble gradually disappears on the windside while growing on the leeside. Hsieh concluded that the size of the separation bubble depends on both Mach number and angle of attack; although he did not elaborate on this relationship and did not discuss the dependence on Reynolds number. The nose separation

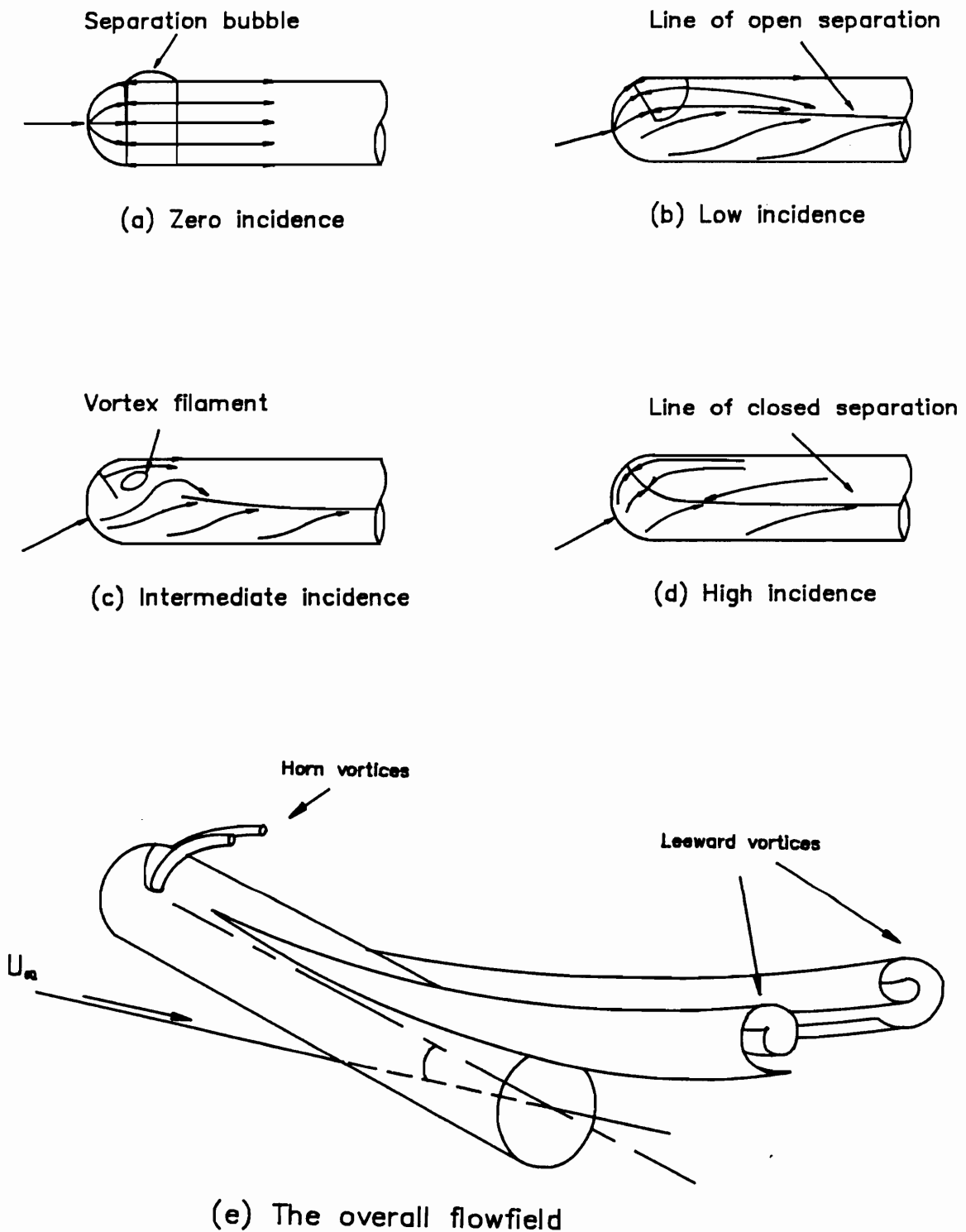


Figure 3.1. Skin-friction patterns over a hemisphere-cylinder at various incidences.

ration and the leeward vortices usually co-existed. However, for $M_\infty \geq 0.9$, the nose separation did not occur until an angle of attack $\alpha \geq 15^\circ$. The flow exhibited an open-type separation. The interaction between the separation bubble and the leeward vortices was negligible since they were far apart. At moderate angles of attack, the bubble grew bigger as the leeward vortices moved forward. The interaction between the separation bubble and the leeward vortices became stronger, resulting in a pair of counterclockwise concentrated vortices (or horn vortices) formed near the nose of the model as shown in Figure 3.1c. Hsieh and Wang [1976] described a unique tornado-like feature displayed by these vortices whose axes were found to be normal to the surface. At even higher incidences, although there were no data, Hsieh speculated that the separation bubble and the leeward vortices merge together to form a closed-type separation as shown in Figure 3.1d; the concentrated vortices disappear. A three-dimensional sketch of the flow field over a hemisphere-cylinder at moderate angle of attack is given in Figure 3.1e. As all earlier authors recognized, there exist three types of separation lines on axisymmetric model as shown in Figure 3.2a - the nose separation line, the primary and secondary separation lines. In the crossflow plane we display and denote the primary and secondary separation points by S_1 and S_2 , respectively, while V_1 , V_2 and V_3 represent possible existence of vortices.

Figure 3.2b displays the topological structure reported by Tobak and Peak [1979] for flow over a hemisphere-cylinder at an angle of attack. Various nodes and saddle points in the pattern of skin-friction lines occur at isolated points near the hemispherical nose. Tobak and Peak postulated that the line of primary separation originates from a saddle point of attachment (S_1) and a nodal point (N_3) on the windside of the model as shown in Figure 3.2b. The vortex filament emerging from the focus (N_1) nearest to the plane of symmetry acts as the core of the horn-type dividing surface which extends the line of secondary separation into the flow.

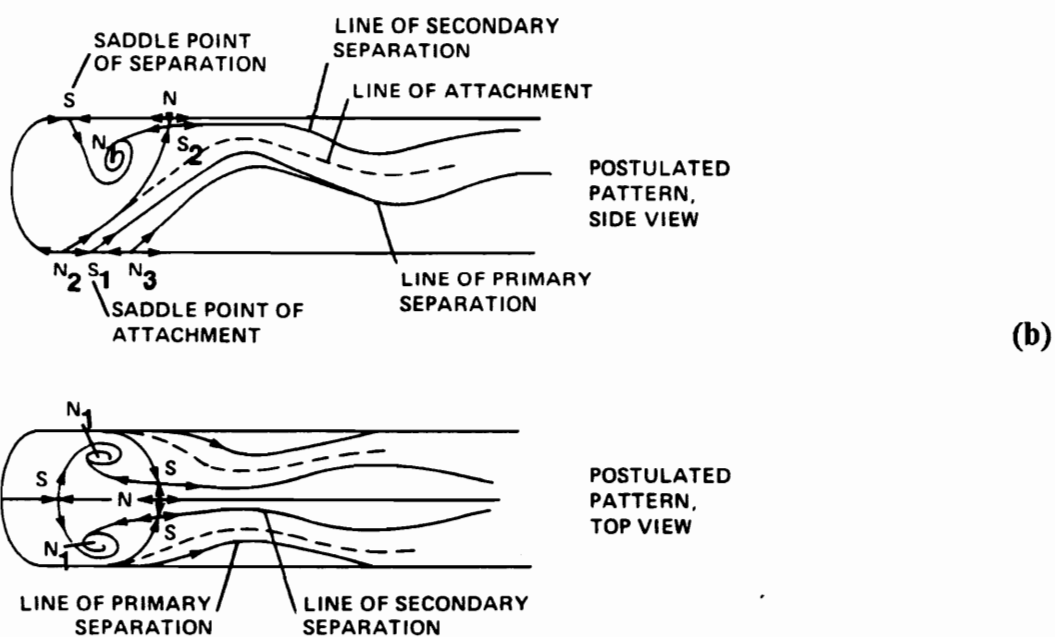
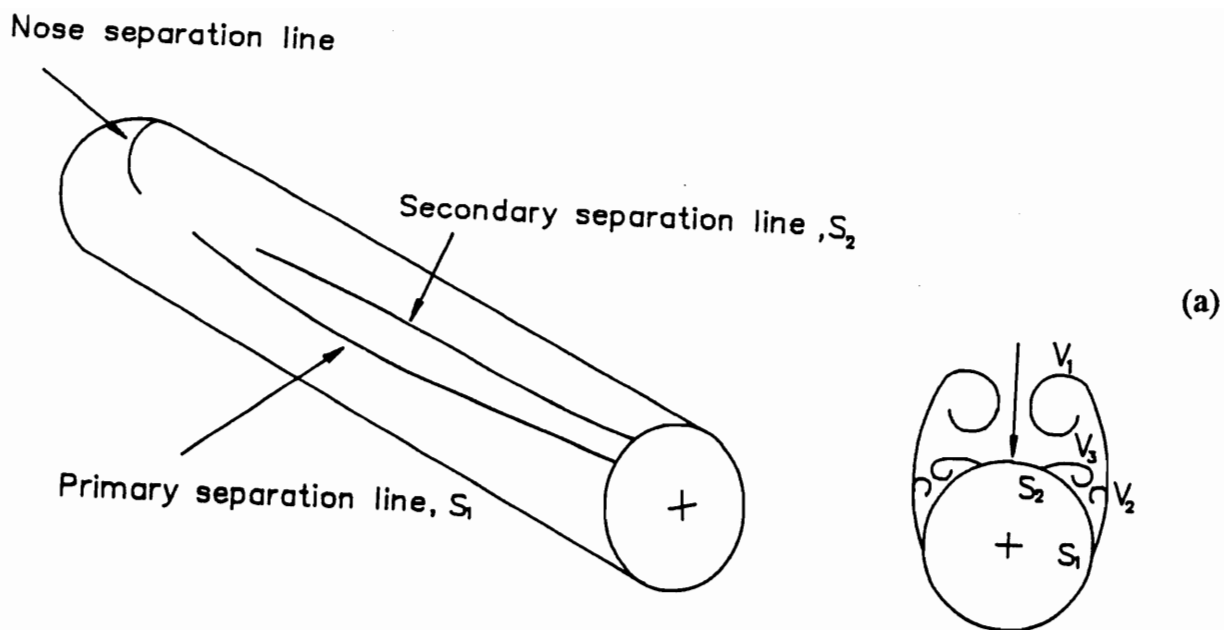


Figure 3.2. (a) Lines of separation and (b) topological structure for flow over a hemisphere-cylinder at a moderate incidence.

Natural or forced vortex asymmetry patterns over a hemisphere-cylinder model have not been documented experimentally in literature. Ying et al. [1987] showed vortex asymmetry numerically for a hemisphere-cylinder model at 19° angle of attack and $M_\infty = 1.2$ using the algorithm described in their [1986] paper with the exception of a finer grid. Although Ying et al. did not offer an explanation of their results, the present author firmly believes there must be some sort of computational error since no other computational or experimental evidence are available to support this contention. Extensive efforts, both numerical and experimental, were focused on the sharp-nosed and blunt-nosed ogive-cylinder models at low Reynolds numbers. As mentioned in Chapter 1, vortex asymmetry pattern over sharp-nosed axisymmetric body is sensitive to many parameters - irregularities at the nose, surface roughness, total body length, slenderness of the nose, angle of attack, free-stream turbulence and Reynolds number. Moskovitz et al. [1989] investigated the effects of geometric perturbations on the asymmetric flow past an ogive/cone-cylinder. The perturbations included variations in model tip sharpness and discrete surface disturbances (cylindrical beads of various dimensions). Techniques used to investigate the flow were flow visualizations and static pressure measurements. At angles of attack $\alpha > 30^\circ$, Moskovitz et al. concluded that the flow was usually asymmetric under normal conditions but the level of asymmetry depended on the amount of disturbances near the tip. The principal drivers of flowfield asymmetry were machined imperfections near the nose region. The blunt-nosed models were less prone to asymmetry because they can be machined more accurately. Moskovitz et al. reported that discrete surface disturbances triggered the highest degree of asymmetry when located at a circumferential position near $\phi = 140^\circ$. The effectiveness of the disturbance decreased with decrease in size and increase in distance from the model tip. The reader should be reminded that vortex asymmetry did not exist at $\alpha \leq 30^\circ$ for

axisymmetric bodies regardless of the nose configuration. Other researchers, listed in Chapter 1, found similar results on the cause of vortex asymmetry.

An effective method in controlling vortical flow over an ogive-cylinder model is by using forebody strakes as shown in Figure 3.3a. Chapman et al. [1975], Hall et al. [1990] and Ng and Malcolm [1991] showed that a fixed pair of strakes attached symmetrically to the nose tip of the body can force asymmetric vortices to be symmetric at zero sideslip. Although the asymmetry was not completely eliminated. Malcolm et al. [1989] used strakes with several different lengths mounting near the nose of the model. They found that short strakes were as effective in controlling vortex asymmetry as longer strakes. Stahl [1989] observed that a large single strake mounted along the leeward meridian of the entire model could also hinder vortex asymmetry. The strake acted as a splitter plate which forced the flow to be symmetric. Ng [1990] also showed similar results with a strake extended only over a small portion of the nose tip. Roos and Kegelmann [1991] investigated asymmetric flow at angles of attack up to 60° over three generic forebodies - ogive, elliptical and chined bodies (Figure 3.3b). At angles of attack greater than 30° , large side forces developed for both the ogive and elliptical bodies. Moreover, the ogive bodies were extremely sensitive to roll angle even at low angles of attack. A small bump mounted at the nose of the ogive and elliptical bodies stabilized asymmetric flowfield characteristic. The chined body did not produce a side force at any incidence; therefore, the flow was always symmetrical. For the purpose of completeness, it should be mentioned that Ericsson [1989] showed that asymmetric vortices generated by a slender-nosed forebody such as an ogive-cylinder can cause wing rock on a wing-body configuration. He clearly demonstrated that the wing rock motion was not the results of interaction between the wing and the vortex generation by the nose. The wing-rock motion is more severe when generated by forebody asymmetric vortices than leading-edge vortices by a slender delta wing.

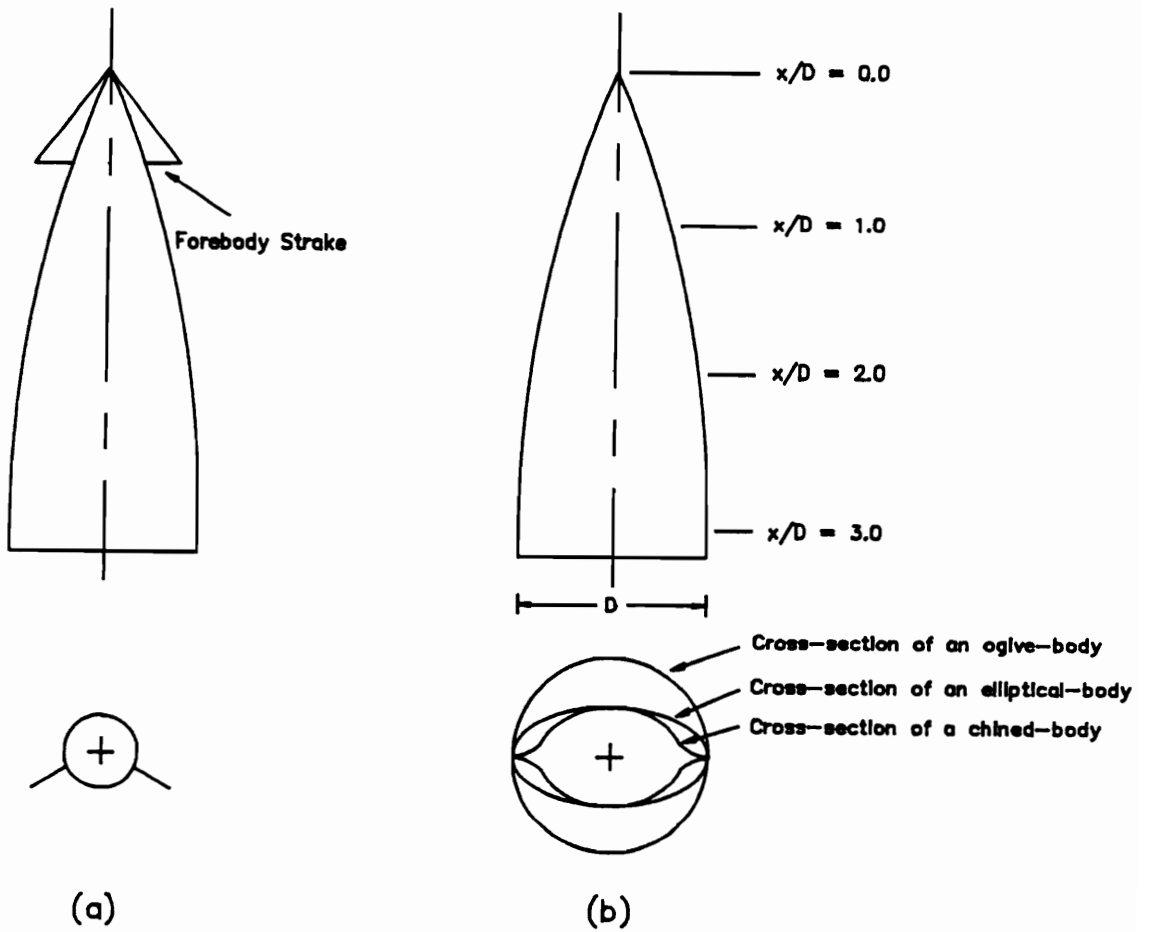


Figure 3.3. Models with (a) forebody strakes and (b) three different configurations - ogive, elliptical and chined bodies.

3.2 Experimental Setup

Two different hemisphere-cylinder models, provided by the Fluids Dynamic Branch of NASA-Langley, were tested in this experiment. The first model, used for both flow visualization and velocity measurements, was machined out of aluminum. It consisted of a 1.65 inch diameter cylindrical afterbody and 13.5 inches in total length. The model could be shortened to a length of 8.3 inches by removing the end-piece. The surface was carefully sanded and coated with household furniture wax to reduce surface roughness. After each flow visualization run, the model was thoroughly washed with ethanol to remove stains from the flow visualization mixture. The model had to be re-waxed and repainted when necessary before the next run. For a number of tests, two beads were used as disturbance sources. The beads were attached to the model surface with Krazy Glue. The geometry of the first bead was spherical with a $3/16$ inch base-diameter and $3/32$ inch height (Figure 3.4a). The second bead was a circular cylinder with a $1/32$ inch diameter and $1/24$ inch in length.

The second model, used for static pressure measurements, was also machined out of aluminum. The overall length of the model was 5.8 inches and 1.16 inches in diameter. It was equipped with 32 pressure orifices, each $1/32$ inch in diameter, along the x-direction at a constant ϕ . Figure 3.4a displays the definition of coordinates. The x-axis is measured along the periphery of the hemispherical cap in a meridional plane and along a generator of the cylindrical afterbody starting from $\phi = 90^\circ$. The y- and z-axes are normal to the free-stream velocity when the model is at zero degree incidence. The origin of the axes is located at the tip of the model and remains fixed to the body. The orifices were spaced closer to each other near the nose than the afterbody to facilitate reliable measurements of the axial pressure gradient across the separation bubble.

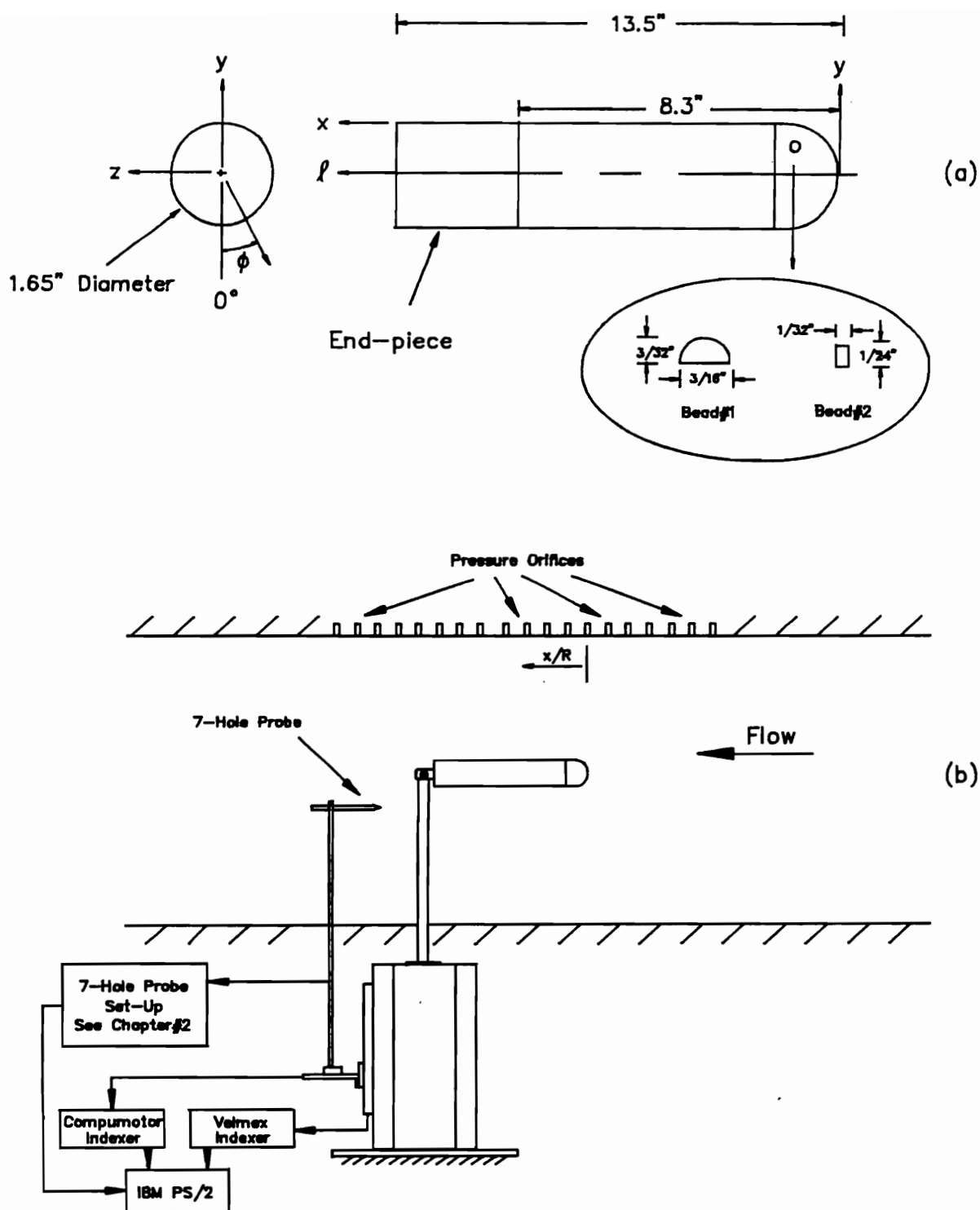


Figure 3.4. (a) Definition of coordinates and (b) seven-hole probe experimental setup.

During the experiment, at each angle of attack, the model was manually rotated about its axis of symmetry to measure pressure at various cross-sectional stations. This yielded surface-pressure distributions containing 608 data points per incidence.

The velocity measurement setup is shown in Figure 3.4b. A seven-hole probe was positioned parallel to the oncoming flow. The plane of measurement of the seven-hole probe was, therefore, normal to the free-stream velocity and 3 inches away from the trailing-edge of the model when at zero degree angle of attack. Velocity fields were mapped out in a 40-by-30 square grid consisting of a total of 1200 points per plane. Each plane of data took approximately sixteen continuous wind tunnel hours to complete. Free-stream velocity was measured at every data point and then used to normalize all three velocity components. The mesh sizes, Δy and Δz , were equal to 0.1 inch apart.

The displacement of the seven-hole probe in the y- and z-direction was controlled by a Velmex UniSlide Traversing Table and a MicroSlide Traversing Table, respectively. The Velmex UniSlide Traversing Table was equipped with a stepping motor and a 8300 Series Velmex Indexer. The stepping motor could give a maximum torque of 30 oz-in with a resolution of 0.008 inch. The MicroSlide Traversing Table was equipped with a Compumotor Stepping Motor CXT 29-35 and a CX Indexer/Driver. The stepping motor produced a maximum torque of 7 oz-in with a resolution of 0.01 inch. Each indexer was capable of storing and executing complex motion programs from its own non-volatile memory (EPROM). A program, written in Turbo Pascal and Inline Assembly Code, was downloaded to each indexer via an RS-232 interface from an IBM PS/2 computer to control the stepping motors.

3.3 Experimental Conditions

Skin-friction line visualizations were carried out in the ESM Wind Tunnel at a free-stream velocity of 31.8 ft/sec. The corresponding Reynolds number was 2.7×10^4 based on the diameter of the circular afterbody. Photographs taken included three different views, $\phi = 90^\circ$ (side view), 120° (oblique view) and 180° (leeward view). The angle of attack varied from $\alpha = 0^\circ$ to 45° in 5° increments. The model could be dismounted from the mounting sting. It was thus easy to remove and place on a flat surface to be photographed after each run. The flow visualization mixture was very sluggish, in spite of repeated attempts with various combinations of mixture. As a result, there were no flow streaks and these photographs were not digitized. Only flow visualization photographs at high Reynolds numbers were digitized and included later in Chapter 4.

Static pressure coefficients on the surface of a hemisphere-cylinder were obtained in the ESM Wind Tunnel at four angles of attack $\alpha = 0^\circ, 10^\circ, 20^\circ$ and 30° . Data were taken along the x-axis from $\phi = 0^\circ$ to 180° in 10° increments. A test case was performed in the VPI Stability Wind Tunnel at $\alpha = 20^\circ$ to examine deviations between results obtained under two different turbulence levels. The ESM Wind Tunnel wall pressure distributions were also measured, with the model placed at various incidences, to investigate the effect of the tunnel walls on the model. All measurements were conducted at free-stream velocities of 25.9 ft/sec and 45.2 ft/sec corresponding to Reynolds numbers of $Re = 1.5 \times 10^4$ and 2.7×10^4 , respectively. Pressure data presented in this chapter represent only half of the model's surface. It was not necessary to obtain data for the whole surface of the model since the flow was symmetric. No smoothing schemes were applied to the raw data.

Velocity fields of the wake of a hemisphere-cylinder were obtained in the ESM Wind Tunnel at angles of attack $\alpha = 20^\circ$ and 30° and a Reynolds number of 2.7×10^4 to confirm that the leeward vortices are symmetric. Discrete surface disturbances were then positioned on the model at various locations near the nose to force vortex asymmetry. At the same Reynolds number and angle of attack $\alpha = 30^\circ$, velocity measurements were obtained with two different sizes of beads. The first bead (bead#1, see Figure 3.4a) was placed in front of the separation bubble at $x/R = 0.5$ and $\phi = 30^\circ, 70^\circ, 90^\circ, 120^\circ$ and 150° . The same bead was placed at $\phi = 120^\circ$ and $x/R = 1.8$ (on the separation bubble) and $x/R = 2.5$ (behind the separation bubble). A second smaller bead (bead#2) was mounted at $x/R = 0.5$ and $\phi = 120^\circ$. All measurements were taken in a plane normal to the free-stream velocity, behind the model, using a seven-hole probe. Calculated vorticity fields were smoothed using the International Mathematics Subroutine Library (IMSL) routine DCSSMH. The IMSL routine DCSSMH computed a smooth cubic spline approximation to the data. The vorticity fields were then plotted to determine the effectiveness of the bead size and location.

3.4 Results and Discussion

Flow Visualization

At zero angle of attack, the separation bubble forms two complete rings around the model - a separation ring at about $x/R = 1.5$ and a reattachment ring at $x/R = 2.4$. The fluid inside the bubble is trapped in the bubble and the fluid outside originates far upstream. This type of flow is known as closed or bubble separation. Figures 3.5a and 3.5b display both leeward and side views, respectively, to demonstrate that the bubble

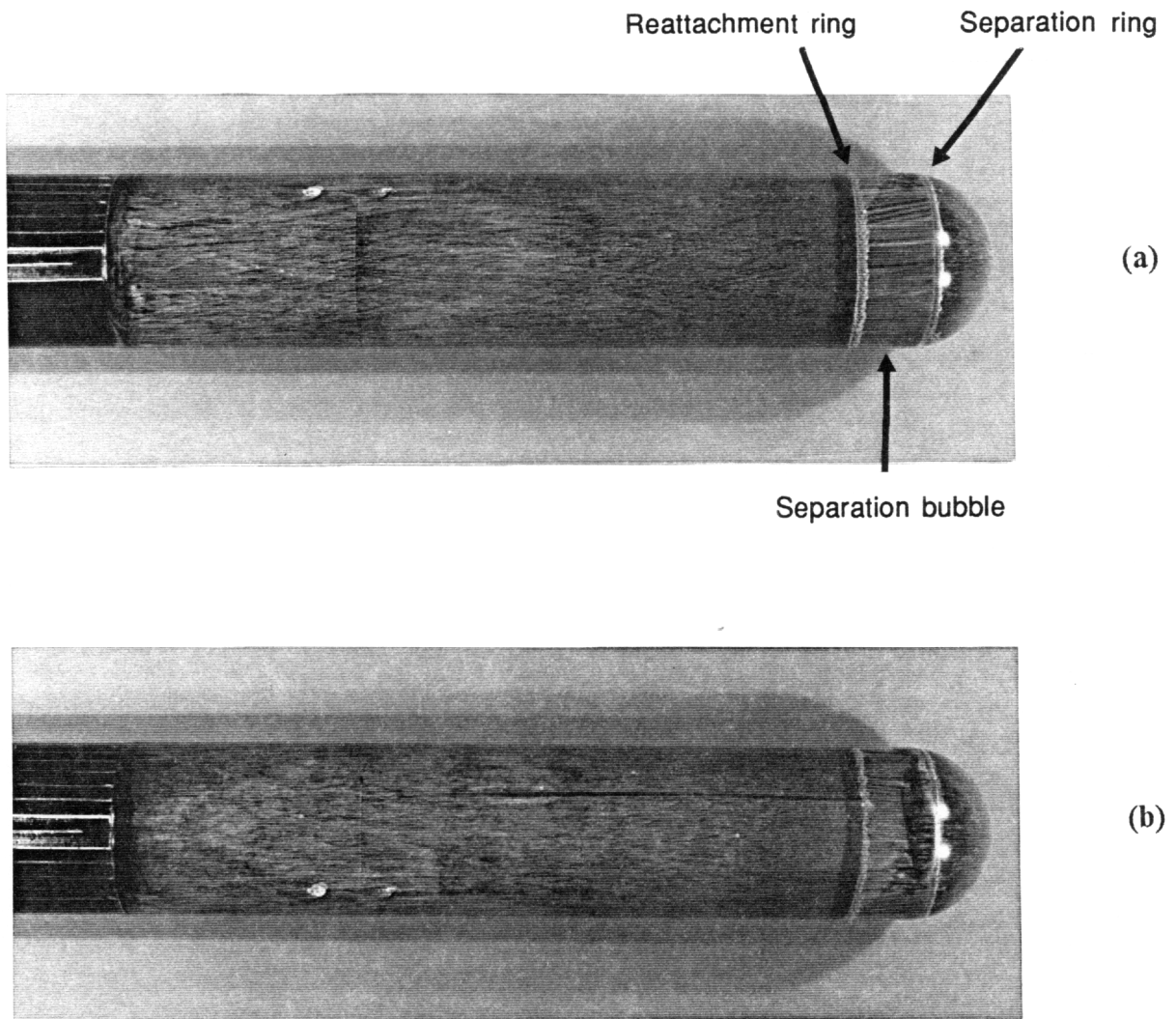


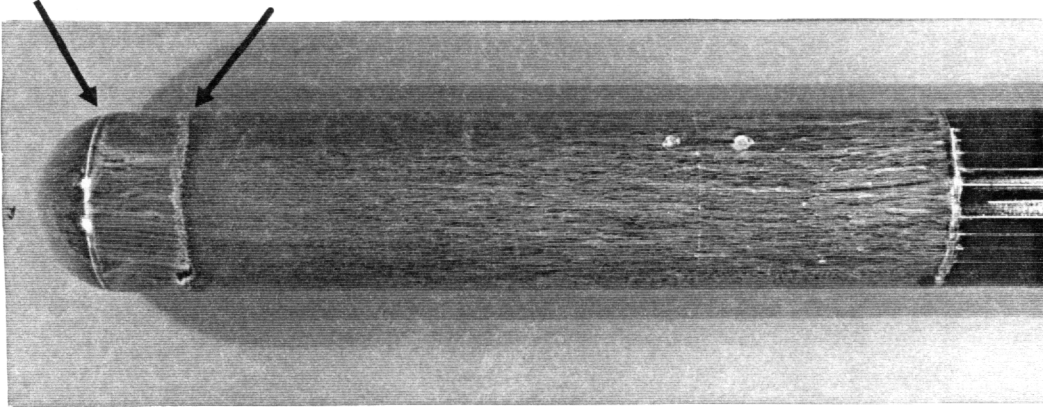
Figure 3.5. Surface flow visualizations at $\alpha = 0^\circ$ and $Re = 27000$ (a) $\phi = 180^\circ$ (b) $\phi = 90^\circ$.

is perfectly axisymmetric. The flow visualization mixture (titanium dioxide) accumulation along the rings of separation and reattachment can be seen in these figures. Very slow-moving fluid exists inside the bubble; consequently, the original paintbrush marks within this region do not change after the model was placed in the flow. The results show that Hsieh's assumption of the existence of the separation bubble at $\alpha = 0^\circ$ is not valid.

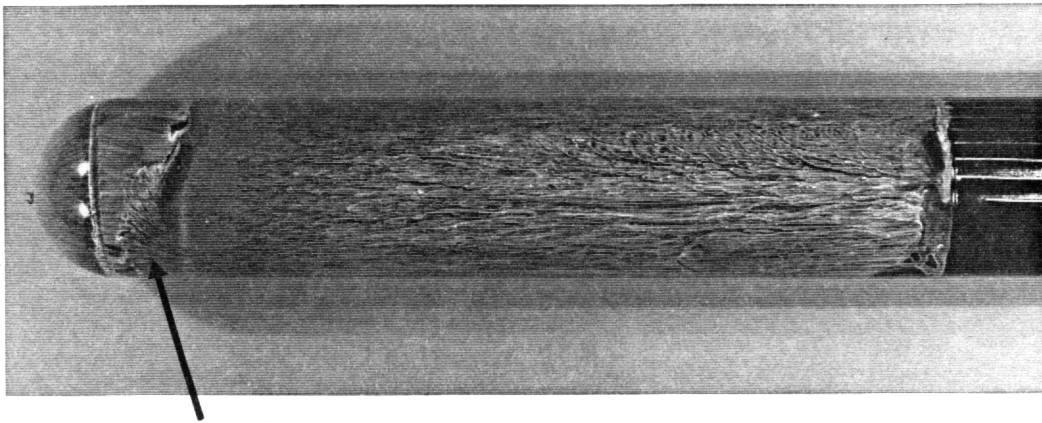
At 5° incidence, the separation bubble is no longer axisymmetric (Figure 3.6). Part of the reattachment ring on the windside moves forward, resulting in a gradual decrease in the width of the bubble from the largest at $\phi = 180^\circ$ to the smallest at $\phi = 0^\circ$. An interesting detail occurs on the flank of the model where the reattachment ring smears over an area from $\phi = 10^\circ$ to 100° at $x/R = 1.6$ (see Figure 3.6b). This phenomenon is observed only during transition from closed to open separation. Leeward vortices have not yet appeared due to strong axial velocity and will be confirmed later with static pressure data. However, lines of primary and secondary separation have already begun to take shape on the cylindrical portion of the body. The existence of horn vortices is also not detected at this angle of attack. Similar to the zero degree incidence case, the flow exhibits closed separation.

Figures 3.7a, 3.7b and 3.7c show three different views $\phi = 180^\circ$, 120° and 90° , respectively, of the hemisphere-cylinder at 10° incidence. The largest part of the separation bubble is once again on the leeside from $\phi = 120^\circ$ to 240° . In contrast to the previous angle of attack, the bubble reaches a minimum at $\phi = \pm 80^\circ$ and grows larger as ϕ approaches 0° . Two horn vortices appear in the vicinity of $\phi = \pm 150^\circ$ and $x/R = 2.1$ and rotate in the counterclockwise direction. The skin-friction patterns indicate a closed-type separation. The results contradict Hsieh's assumption who stated that the horn vortices occur only when the flow is of an open-type separation. A pair of secondary separation lines is clearly evident over the full length of the afterbody at $\phi \simeq \pm$

Separation ring Reattachment ring



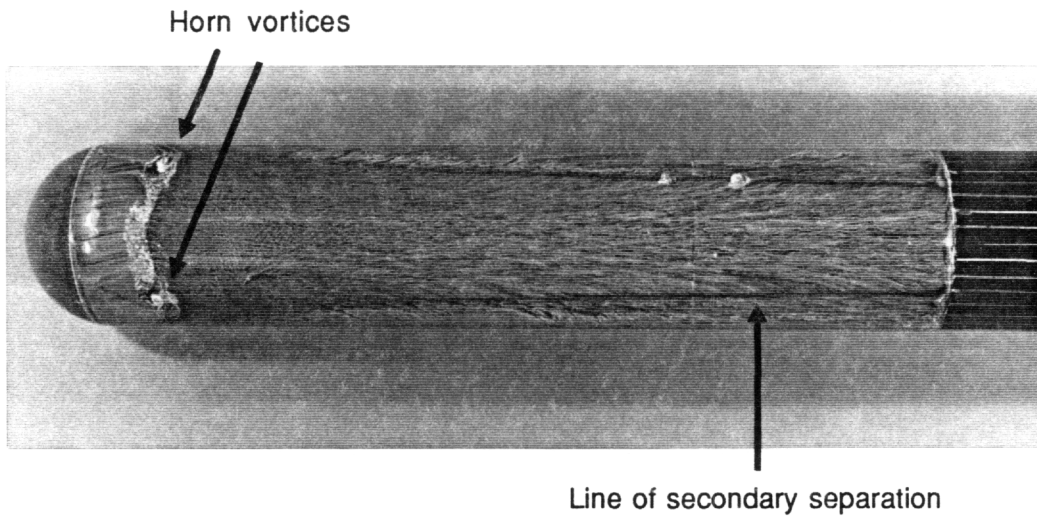
(a)



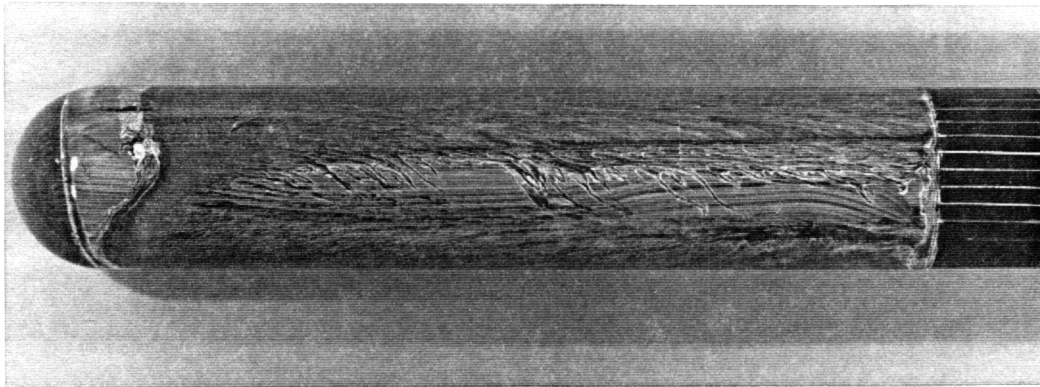
(b)

Smearing of reattachment ring

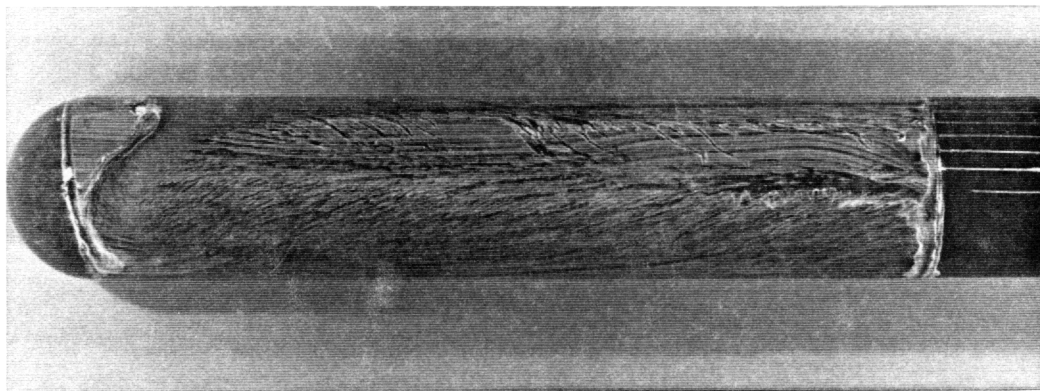
Figure 3.6. Surface flow visualizations at $\alpha = 5^\circ$ and $Re = 27000$ (a) $\phi = 180^\circ$ (b) $\phi = 90^\circ$.



(a)



(b)



(c)

Figure 3.7. Surface flow visualizations at $\alpha = 10^\circ$ and $Re = 27000$ (a) $\phi = 180^\circ$ (b) $\phi = 120^\circ$ (c) $\phi = 90^\circ$.

150°. Absence of the primary separation lines suggests that the leeward vortices have not quite fully developed. Pressure data present in the next section reveal similar findings.

At 15° angle of attack, the separation bubble is confined to the suction side of the model. The flow becomes open separation because the fluid originated upstream can enter from both sides of the separation lines along the afterbody (Figure 3.8). Since the axes of the horn vortices are perpendicular to the surface of the model, their swirling motions cause flow visualization mixture to accumulate at around $\phi = \pm 130^\circ$ and $x/R = 2.3$. Two primary separation lines stretch along the afterbody from $x/R = 3.0$ ($\phi = \pm 100^\circ$) to the trailing-edge of the model ($\phi = \pm 80^\circ$). A pair of secondary separation lines is also visible from $x/R = 3.6$ ($\phi = \pm 130^\circ$) to the trailing-edge ($\phi = \pm 150^\circ$). Along the cylindrical afterbody, from our observation of the flow visualization photographs, it appears that the boundary-layers separate along the lines of primary separation. The flow reattaches at $\phi = 180^\circ$ and separates again along the lines of secondary of separation. Vortex sheets emanating from the primary and secondary separation lines merge into a single sheet and rollup to form two axial vortices (Figure 3.2a). There is very little fluid motion in the area between the lines of primary and secondary separation; thus, no distinct flow streaks form. The distances between the separation bubble and the axial vortices are still further apart (see Figure 3.8c). Their interaction is expected to be minimal.

At $\alpha = 20^\circ$, the separation bubble becomes smaller both axially and circumferentially and stretches over only the top half of the hemispherical cap. The horn vortices create large patterns of swirling imprints near the nose of the model (Figure 3.9). An obvious difference from the previous angles of attack is the heavy amount of titanium dioxide mixture collected around the regions of the horn vortices. The swirling motions of the pair horn vortices, having the opposite direction of rotations, cause the paintbrush

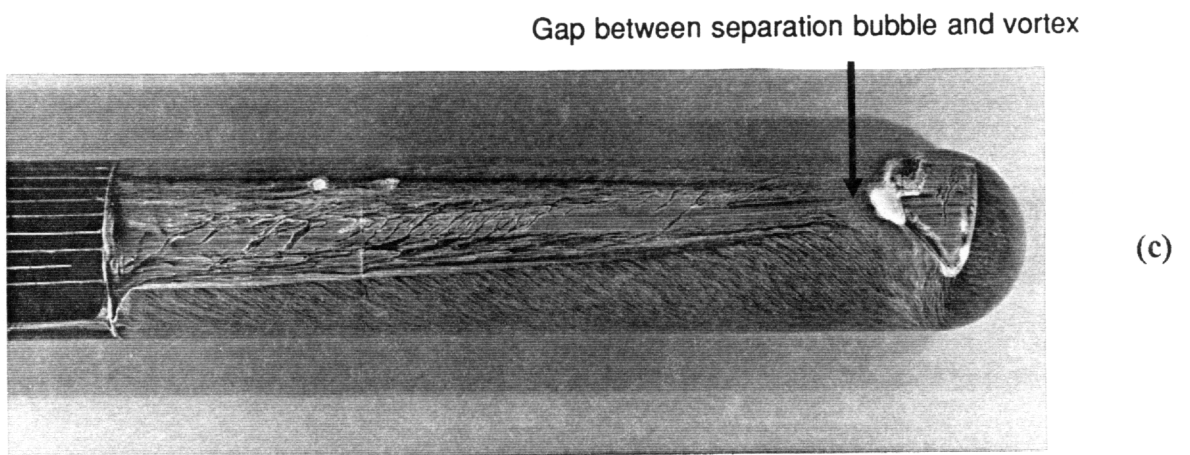
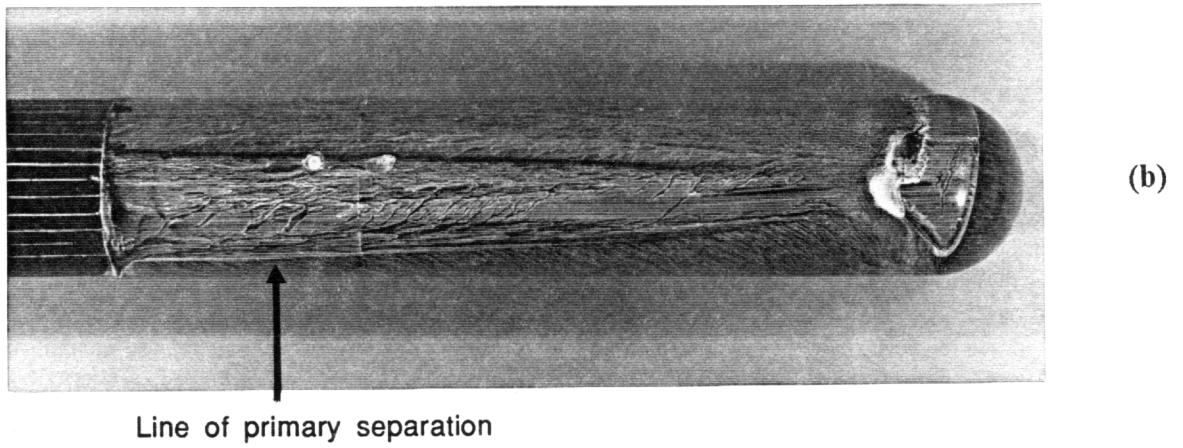
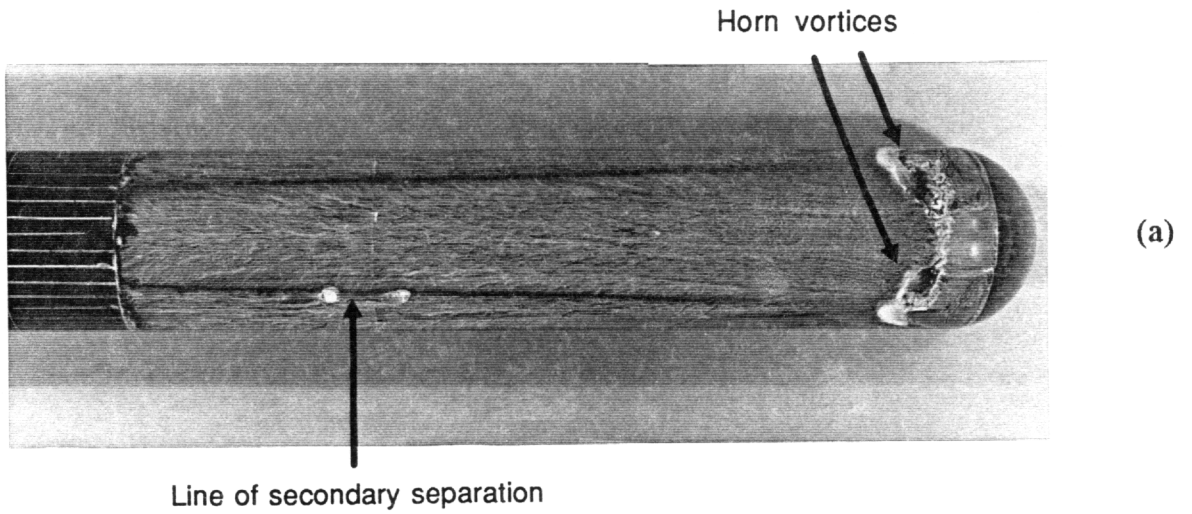
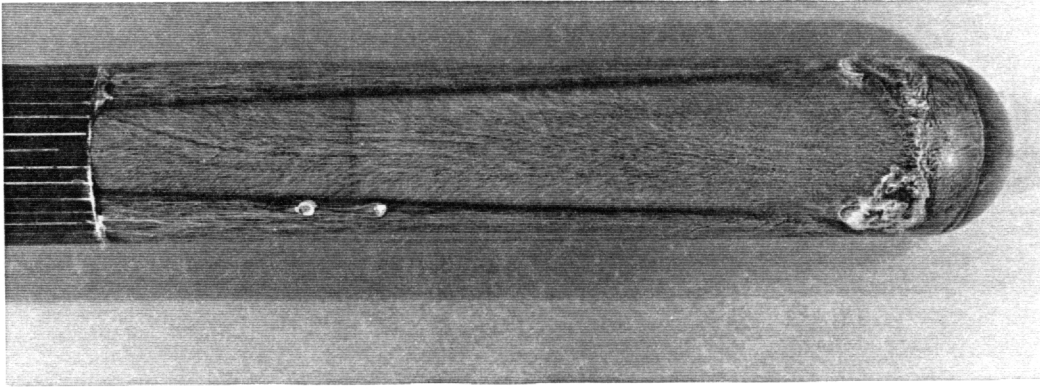
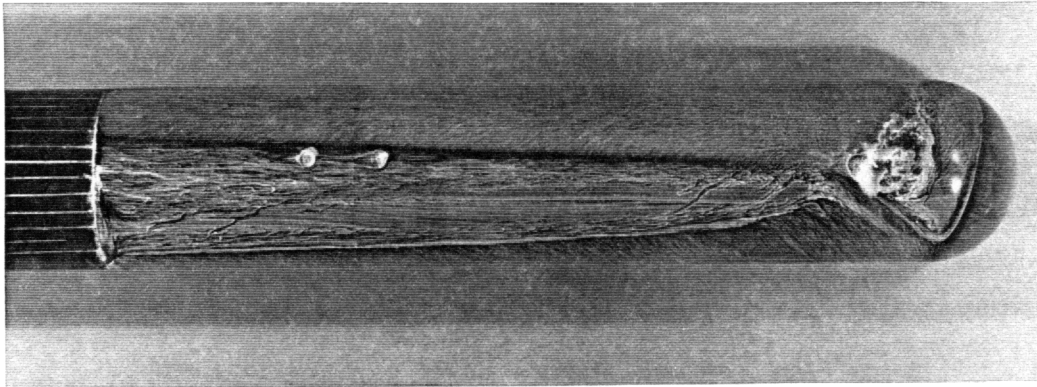


Figure 3.8. Surface flow visualizations at $\alpha = 15^\circ$ and $Re = 27000$ (a) $\phi = 180^\circ$ (b) $\phi = 120^\circ$ (c) $\phi = 90^\circ$.

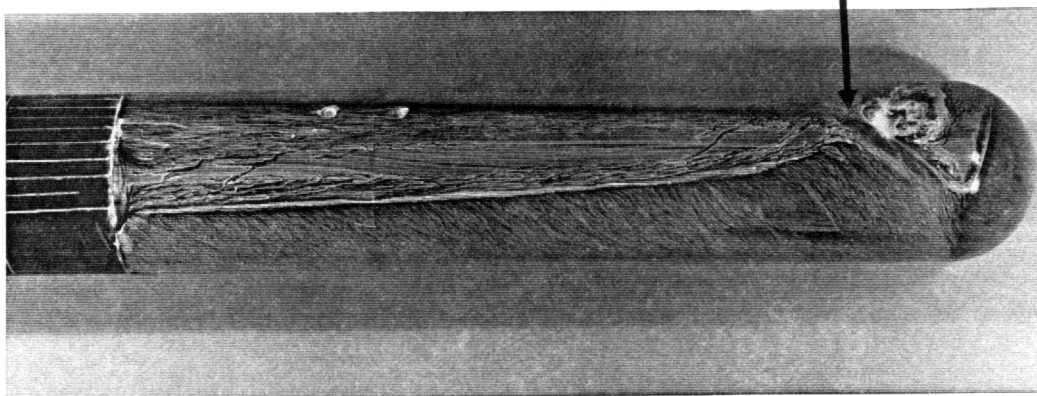


(a)



(b)

Gap between separation bubble and vortex is decreasing



(c)

Figure 3.9. Surface flow visualizations at $\alpha = 20^\circ$ and $Re = 27000$ (a) $\phi = 180^\circ$ (b) $\phi = 120^\circ$ (c) $\phi = 90^\circ$.

marks within part of the separation bubble disappear. Narrow gaps separate the horn vortices and the leeward vortices from each other; hence, the flow retains its open separation character. Lines of primary and secondary separation remain at the same positions as the 15° incidence case. The origins of the leeward vortices can be easily identified at $x/R = 3.70$. From the leeward view, $\phi = 180^\circ$, skin-friction patterns do not display any features of vortex asymmetry.

At 25° angle of attack, the separation bubble and the leeward vortices merge together to become a single separation region (Figure 3.10). The lines of primary and secondary separation connect with the separation and reattachment lines of the separation bubble, respectively. The horn vortices are reduced considerably in size but can still be clearly detected on the suction side of the hemispherical cap. It can be concluded that the horn vortices reach their maximum size and strength at angles of attack just before the flow exhibits closed separation. These results are in contradiction to Hsieh's assumption that the horn vortices vanish when the separation bubble and the leeward vortices merge together to form closed separation. There seems to be a lot more titanium dioxide mixture accumulated along lines of primary and secondary separation than previous photographs. At $\alpha = 30^\circ$, the photographs show some weak swirling motions near the nose (Figure 3.11). A kink appears on the primary separation line where the separation bubble and the leeward vortices merge. The horn vortices completely disappear at angles of attack $\alpha = 35^\circ$, 40° and 45° as shown in Figures 3.12, 3.13 and 3.14, respectively. The leeward vortices produce a pattern known as "necklace vortex" or sometimes called "horse-shoe vortex" (Yates and Chapman, 1991). There is no flow asymmetry detected even at angles of attack up to $\alpha = 45^\circ$.

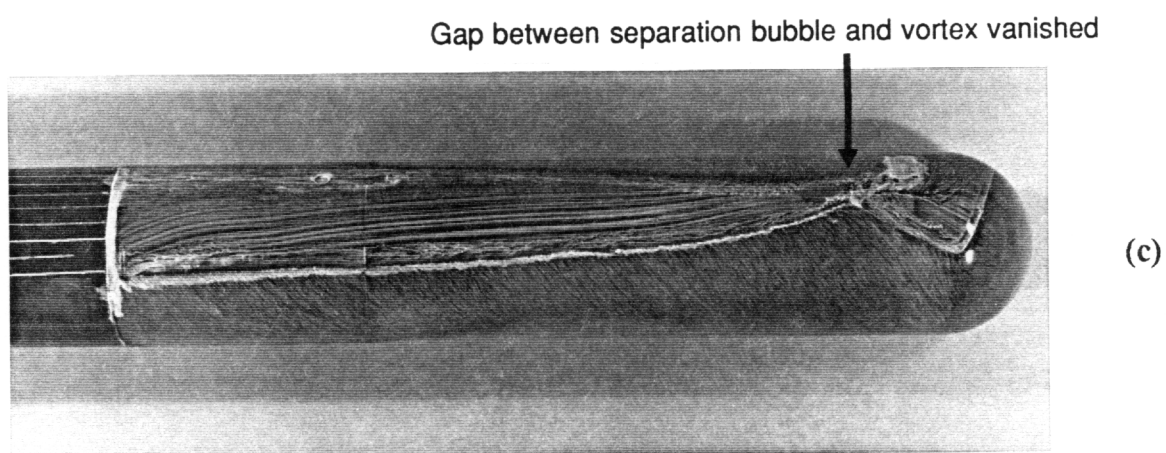
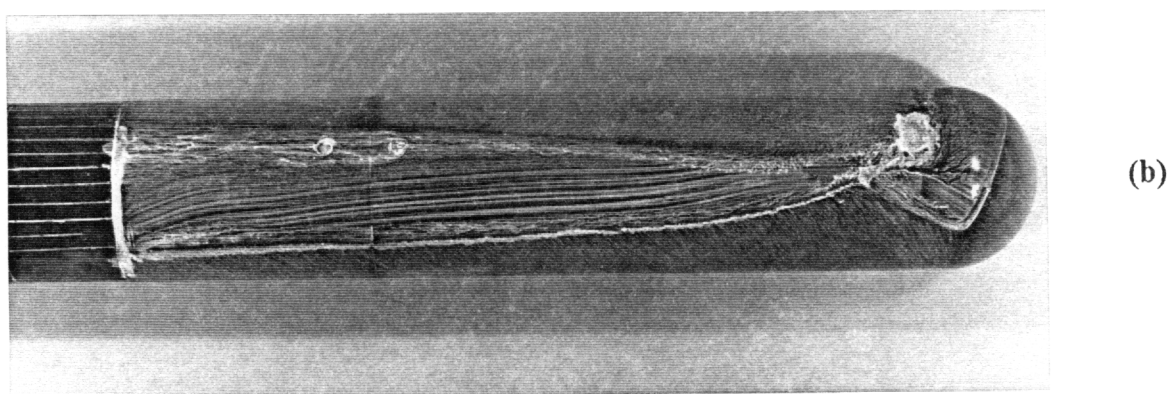
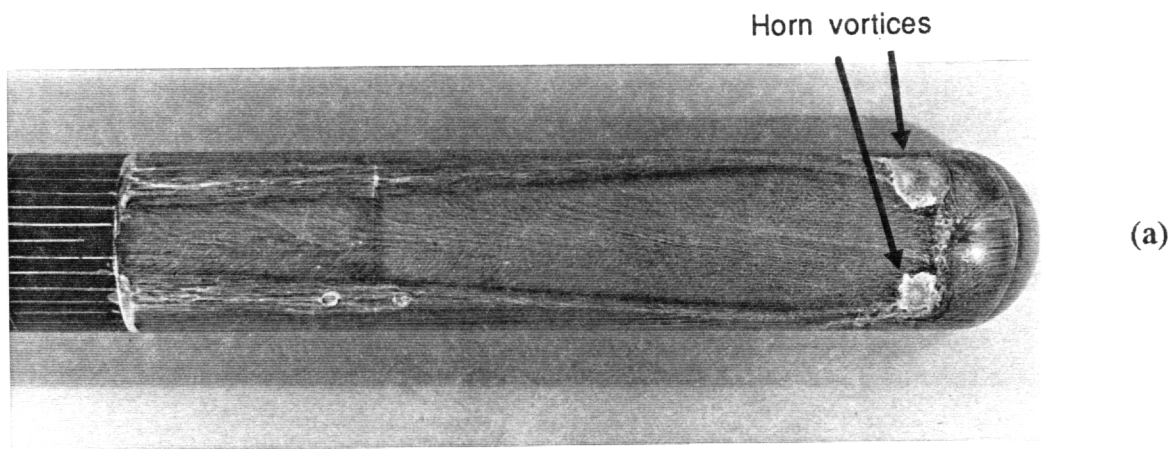
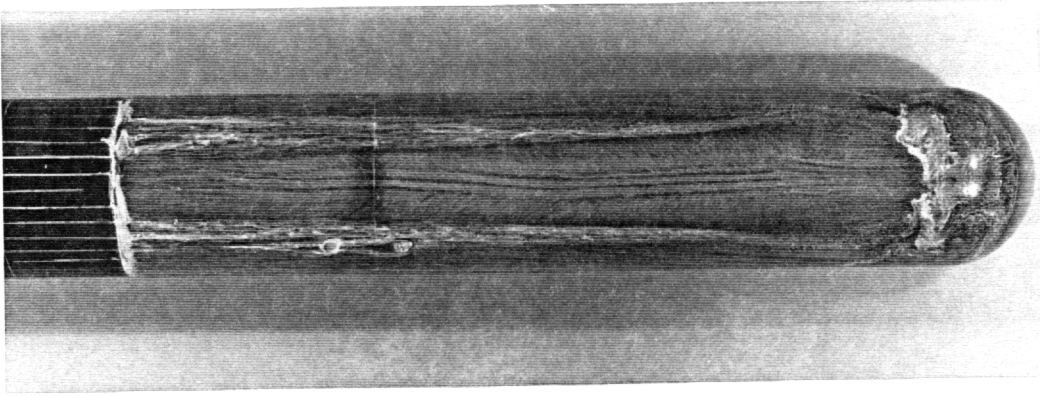
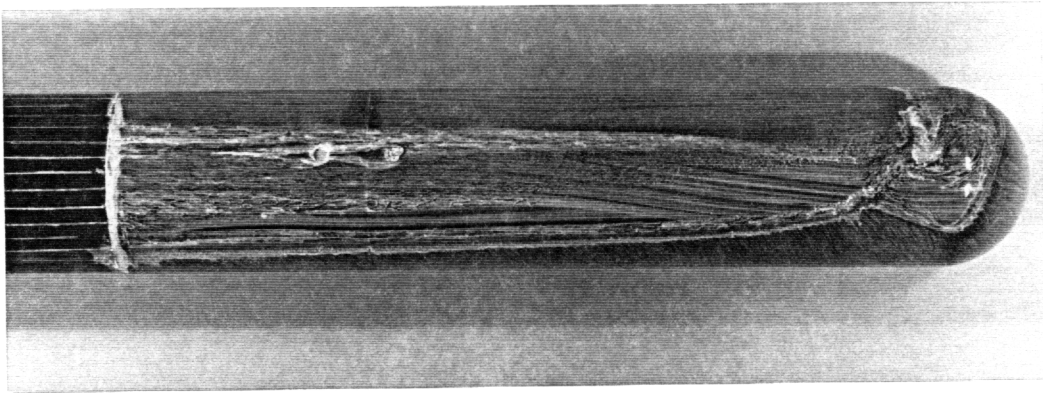


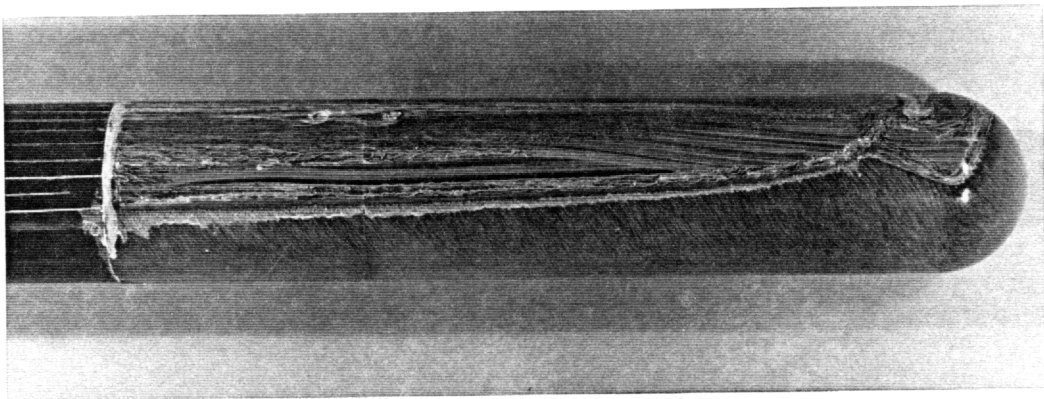
Figure 3.10. Surface flow visualizations at $\alpha = 25^\circ$ and $Re = 27000$ (a) $\phi = 180^\circ$ (b) $\phi = 120^\circ$ (c) $\phi = 90^\circ$.



(a)

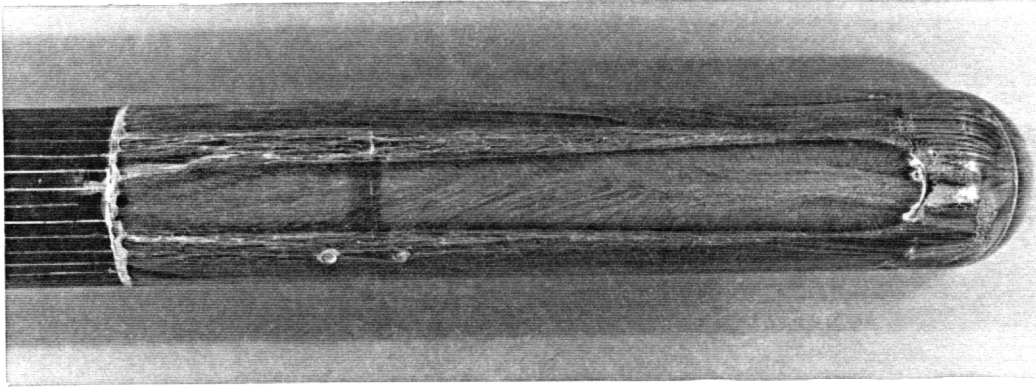


(b)

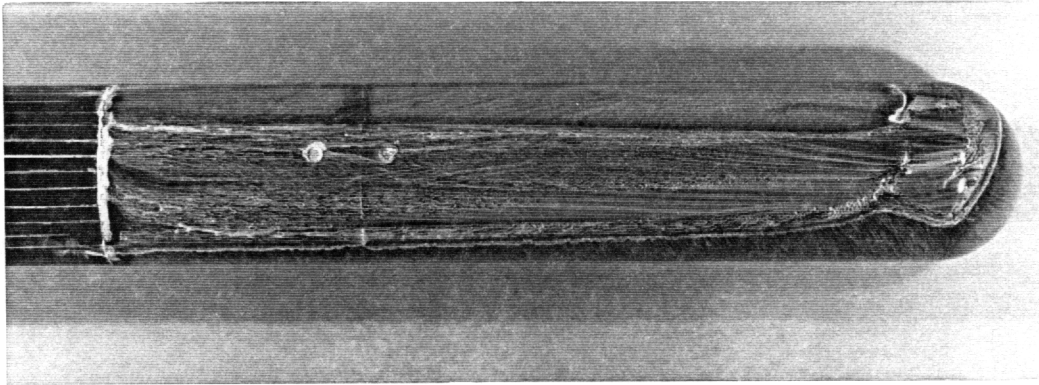


(c)

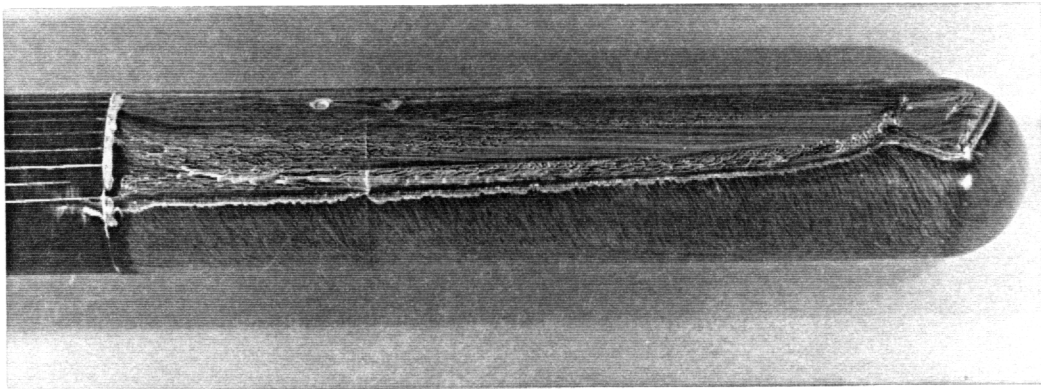
Figure 3.11. Surface flow visualizations at $\alpha = 30^\circ$ and $Re = 27000$ (a) $\phi = 180^\circ$
(b) $\phi = 120^\circ$ (c) $\phi = 90^\circ$.



(a)

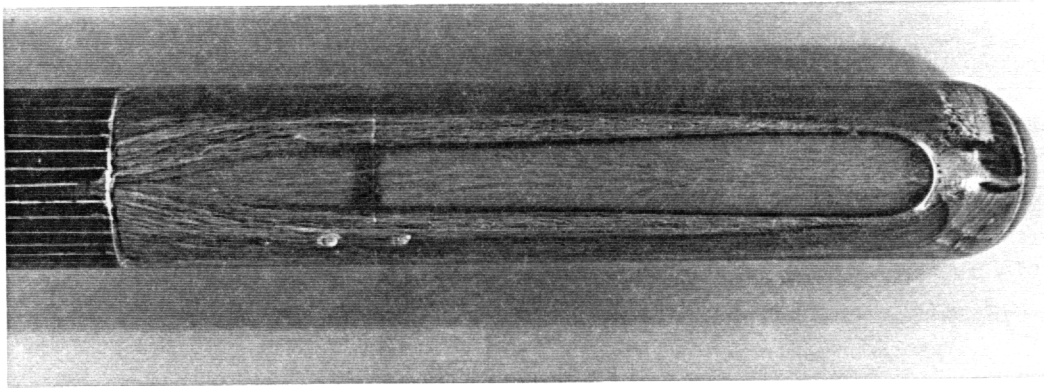


(b)

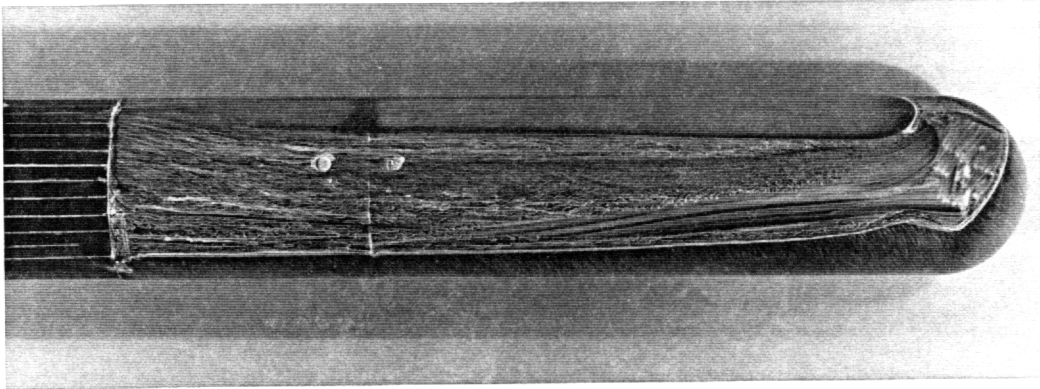


(c)

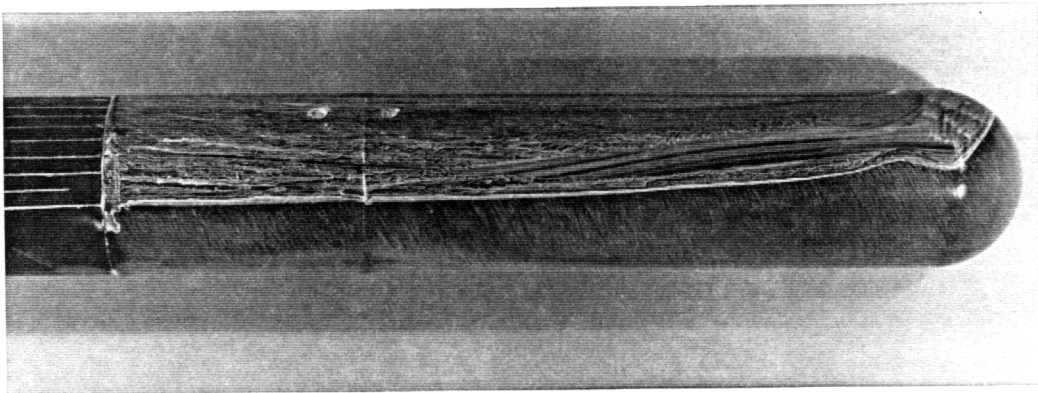
Figure 3.12. Surface flow visualizations at $\alpha = 35^\circ$ and $Re = 27000$ (a) $\phi = 180^\circ$ (b) $\phi = 120^\circ$ (c) $\phi = 90^\circ$.



(a)

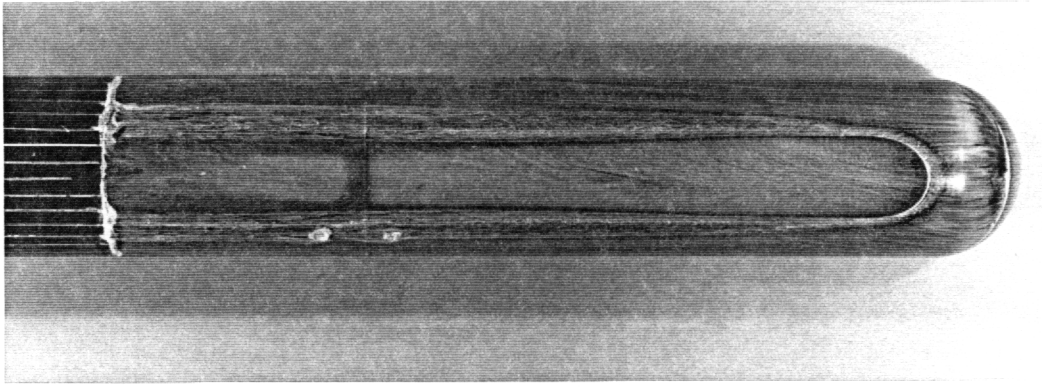


(b)

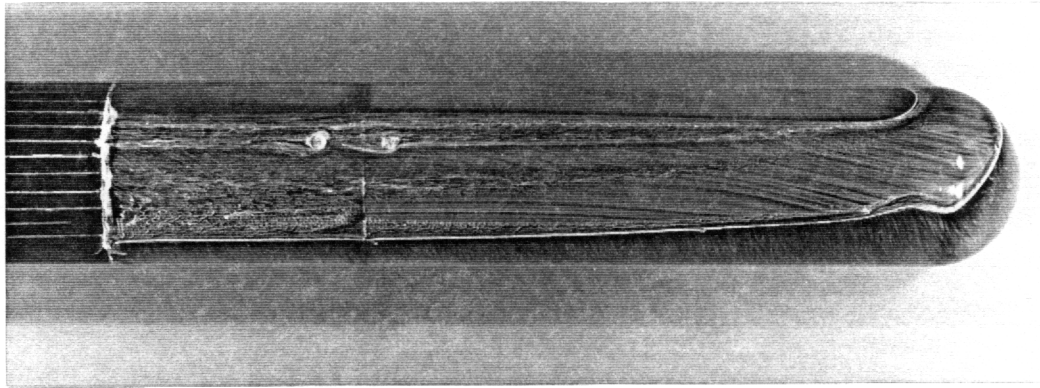


(c)

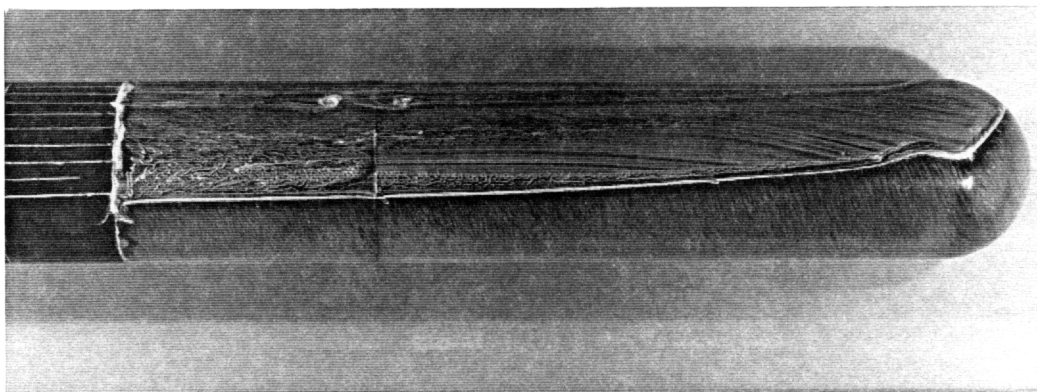
Figure 3.13. Surface flow visualizations at $\alpha = 40^\circ$ and $Re = 27000$ (a) $\phi = 180^\circ$ (b) $\phi = 120^\circ$ (c) $\phi = 90^\circ$.



(a)



(b)



(c)

Figure 3.14. Surface flow visualizations at $\alpha = 45^\circ$ and $Re = 27000$ (a) $\phi = 180^\circ$ (b) $\phi = 120^\circ$ (c) $\phi = 90^\circ$.

Pressure Measurements

Static pressure distributions on the test-section wall of the ESM Wind Tunnel were collected under various conditions. The purpose was to study the effect of the wind tunnel walls on the model. A row of eighteen 1/16 inch diameter orifices, positioned at 1 inch apart, were mounted on the top wall of the test section in a plane normal to the leeward meridian of the model (Figure 3.4b). The experiment was carried out at a Reynolds number of 2.7×10^4 (again based on the diameter of the cylindrical afterbody of the model) for four different cases - no model in the test section, the model placed in the test section at 10° , 20° and 30° angles of attack. The interferences between the walls and the model are found to be minimal as shown in Figure 3.15. Even for the worst case, when the model was at $\alpha = 30^\circ$, the largest deviation of the wall pressure coefficients between the test section with and without the model is 0.014. The x-distance in this figure was measured along the wind tunnel wall parallel to the free-stream velocity and the point $x = 0$ was at the position of the origin of the model in its zero angle of attack position.

Using the same model, pressure data were obtained in the ESM Wind Tunnel and the VPI Stability Wind Tunnel at a Reynolds number of 2.7×10^4 . Figure 3.16 shows pressure coefficients measured along the x-axis at $\phi = 180^\circ$ and $\alpha = 20^\circ$. The flow quality of the wind tunnels such as level of free-stream turbulence and blockage seem to have a significant effect on the value of the local pressure coefficients but not the overall behavior of the flow. The flow still retains its characteristics since the curves in Figure 3.16 display the same shapes and differ only in magnitude. The ESM Wind Tunnel has a free-stream turbulence level of 0.5% compared to 0.018% of the VPI Stability Wind Tunnel. The blockage ratios of model frontal area to tunnel cross sectional area are

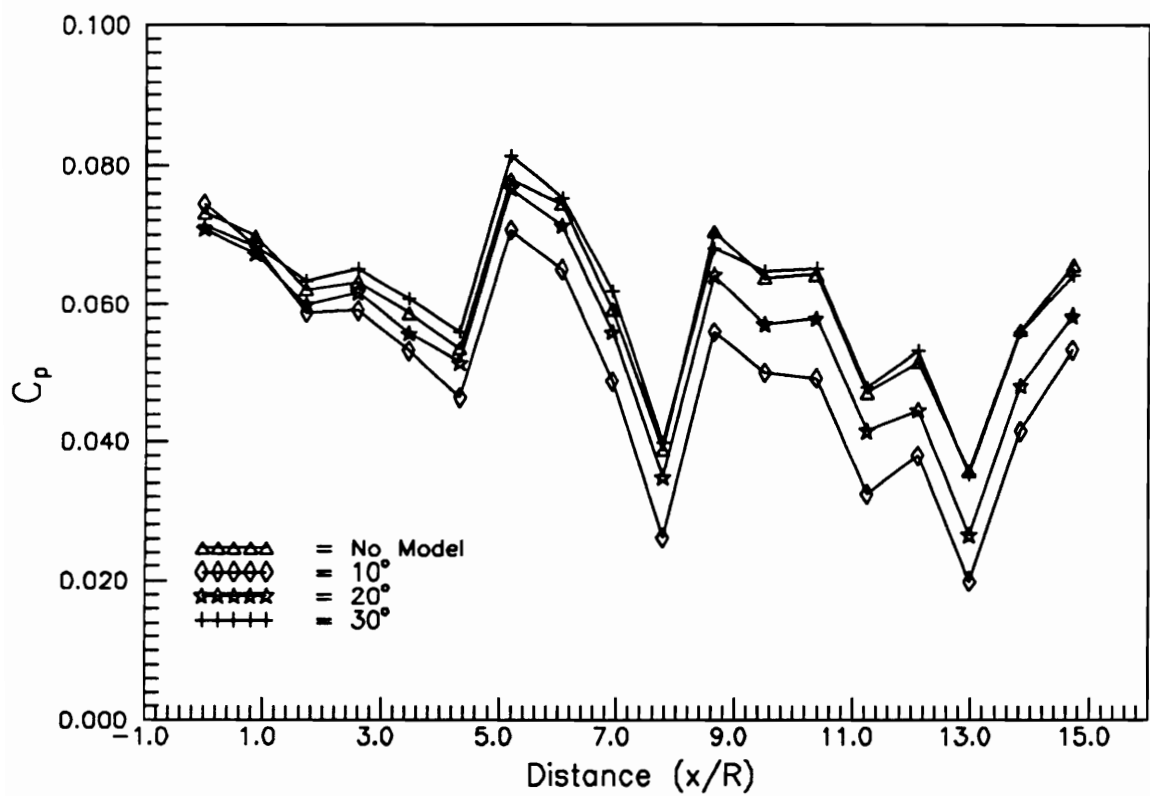


Figure 3.15. Pressure distributions on the ESM Wind Tunnel wall when the hemisphere-cylinder model is placed at various angles of attack.

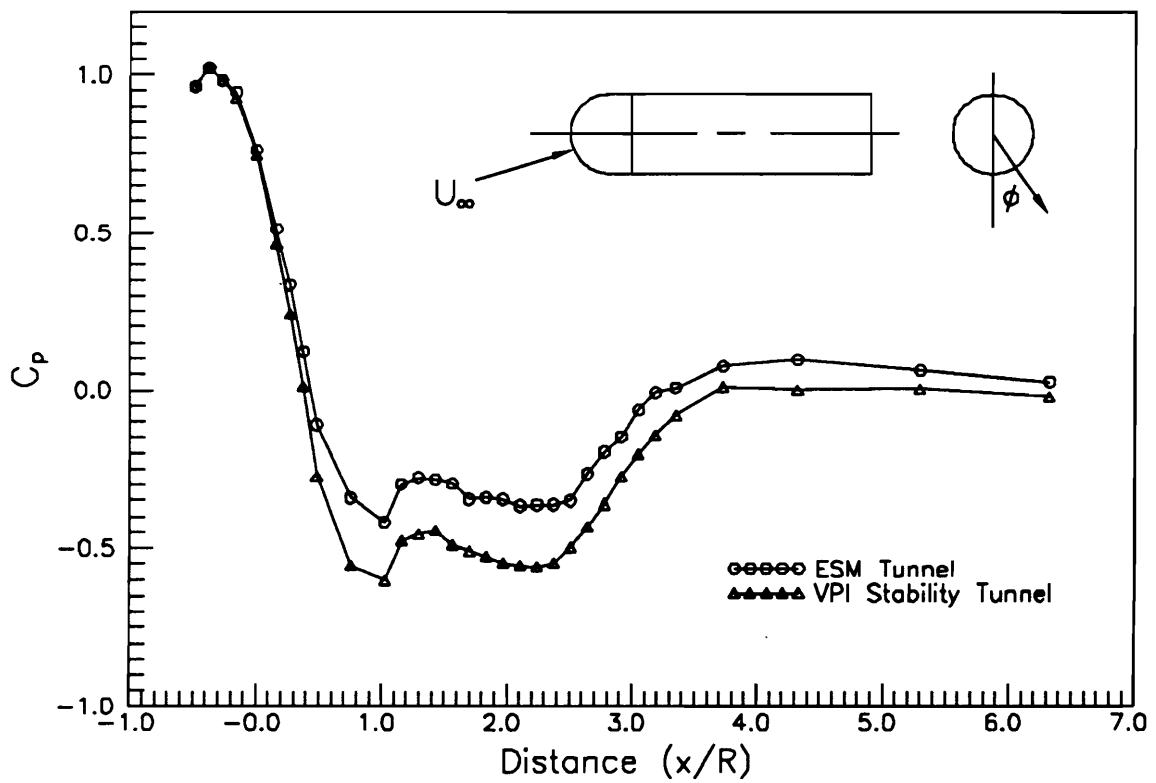


Figure 3.16. Axial pressure distributions on a hemisphere-cylinder at $\phi = 180^\circ$ and $\alpha = 20^\circ$ in two different wind tunnels.

0.008 and 0.0006 for the ESM Wind Tunnel and the VPI Stability Tunnel, respectively. Although not included here, data at other positions demonstrate similar findings.

At zero degree angle of attack, all pressure data were taken at $\phi = 180^\circ$ along the x-axis. Pressure coefficients at $\phi = 0^\circ, 90^\circ$ and 270° were used for aligning the model with the tunnel. Figure 3.17 displays axial pressure distributions at $\alpha = 0^\circ$ for two different Reynolds numbers - $Re = 1.5 \times 10^4$ and 2.7×10^4 . The flow stagnates at $x/R = 0$ where the highest pressure coefficients, $C_p = 1.0$, are registered. Pressure coefficient progressively decreases to a minimal value of -0.38 for Reynolds number of 1.5×10^4 and drops slightly lower, -0.41 , for $Re = 2.7 \times 10^4$ at $x/R = 1.3$. The flow then tries to recover, instead, separates approximately at $x/R = 1.5$. Within the separated region (or the separation bubble), pressure coefficients stay nearly constant at about -0.2 . For $Re = 1.5 \times 10^4$, the flow reattaches at $x/R = 3.0$ as indicated by a sudden jump in pressure coefficients. After the point of reattachment, the pressure coefficients level off to zero along the afterbody of the model. At a higher Reynolds number, $Re = 2.7 \times 10^4$, the point of reattachment is at about $x/R = 2.4$, implying that the separation bubble decreases in size with increasing in Reynolds number. Pressure coefficients along the circular part of the body also remain at zero. Hsieh's theory, which stated that the nose separation is not expected for $M_\infty \leq 0.6$, does not hold at these Reynolds numbers.

Figure 3.18 displays axial surface pressure distributions at $\alpha = 10^\circ$ and a Reynolds number of 1.5×10^4 . Although data were measured from $\phi = 0^\circ$ to 180° in 10° increments, for the purpose of clarity, only results at every 20° were plotted. Nevertheless, the curves were still undistinguishable; strategically chosen constant was then added to each curve to separate them from each other. At $\phi = 180^\circ$, similar to the zero degree angle of attack case, the curve displays a flat region of constant pressure coefficients in the range of $1.3 \leq x/R \leq 2.5$, indicating the presence of a separation bubble. The flat region disappears for $\phi < 100^\circ$ although the bubble still exists as shown in flow visual-

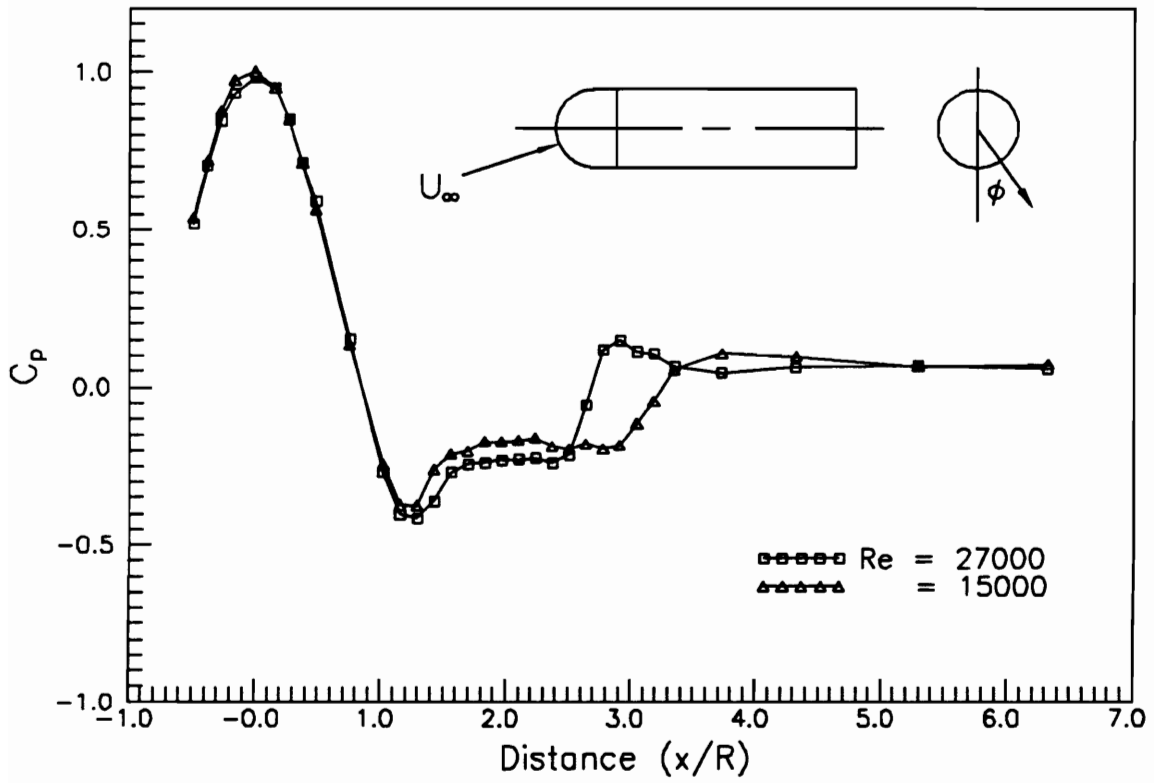


Figure 3.17. Axial pressure distributions on a hemisphere-cylinder at $\alpha = 0^\circ$ and two different Reynolds numbers.

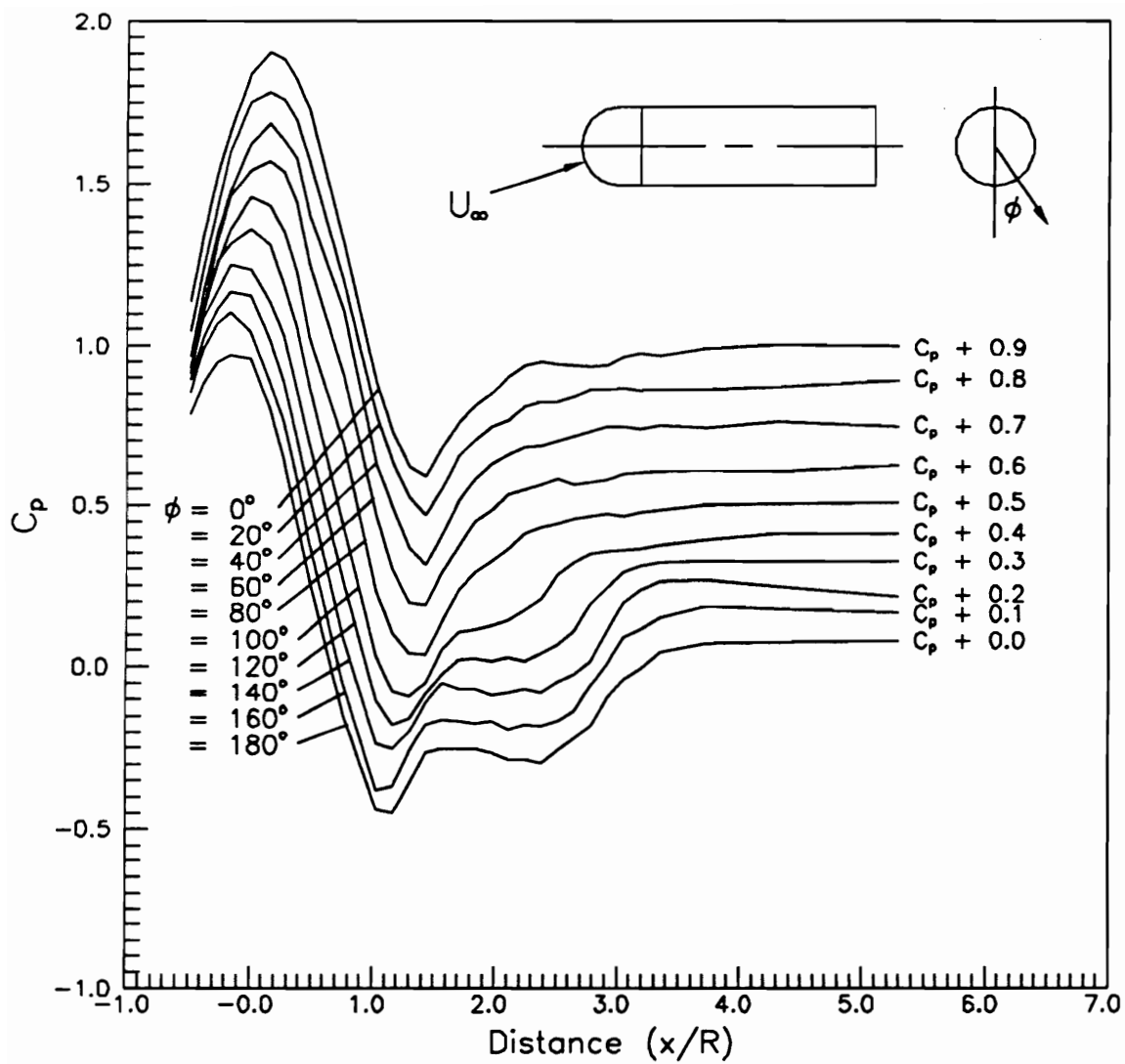


Figure 3.18. Axial pressure distributions on a hemisphere-cylinder at $\alpha = 10^\circ$ and $Re = 15000$ with added constants.

ization photographs (Figure 3.7). The separation bubble in the area between $0^\circ \leq \phi \leq 100^\circ$ is too small to cause a discontinuity in pressure distributions; therefore, no flat regions appear in the pressure plots. The equivalent pressure coefficient contours are displayed in Figure 3.19. In this figure, the distance ℓ is measured along the model's axis of revolution and $\ell = 0$ is at the tip of the model. Large pressure gradients are shown in nose region ahead of the separation bubble. Along the afterbody of the model, pressure coefficients remain somewhat uniform.

Pressure coefficients were also plotted circumferentially at various cross-sections in 10° increments (Figure 3.20). Circumferential pressure coefficients in this plot are normalized with the free-stream velocity component perpendicular to the model's axis of revolution. The core of a vortex is a low-pressure region, and when it is next to a solid surface it induces low pressures on the surface. A "dip" on the surface pressure curve is usually associated with the presence of a vortex core immediately above it. Leeward vortex formation is not detected from curves shown in Figure 3.20. These curves display similar characteristic to the potential flow over a two-dimensional circular cylinder placed normal to the flow even at a location far downstream of the afterbody.

Figures 3.21 and 3.22 display axial pressure distributions and pressure coefficient contours at a Reynolds number of 2.7×10^4 and $\alpha = 10^\circ$, respectively. By examining the pressure curves, the separation bubble seems to decrease in size at higher Reynolds number which is also consistent with the zero degree incidence case. Pressure coefficient contours show a large region of low pressure in the vicinity of the separation bubble, $x/R = 1.0$ to 2.0 . Circumferential pressure coefficients were plotted as shown in Figure 3.23; similar to the flow at lower Reynolds number, leeward vortices are not observed.

Axial pressure distributions at 20° incidence and a Reynolds number of 1.5×10^4 are shown in Figure 3.24. The separation bubble again is isolated to the top of the hemispherical cap and appears as a region of somewhat constant pressure coefficients.

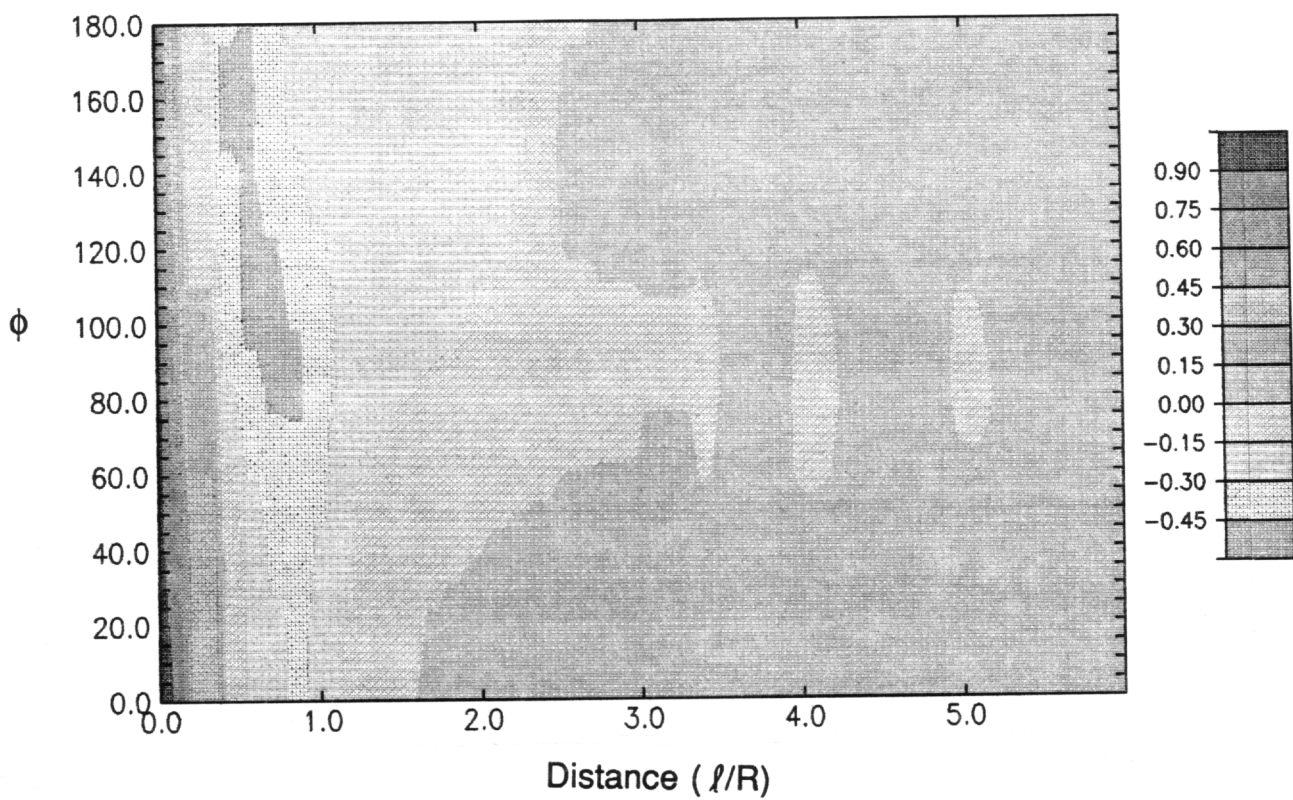


Figure 3.19. Pressure coefficient contours on a hemisphere-cylinder at $\alpha = 10^\circ$ and $Re = 15000$.

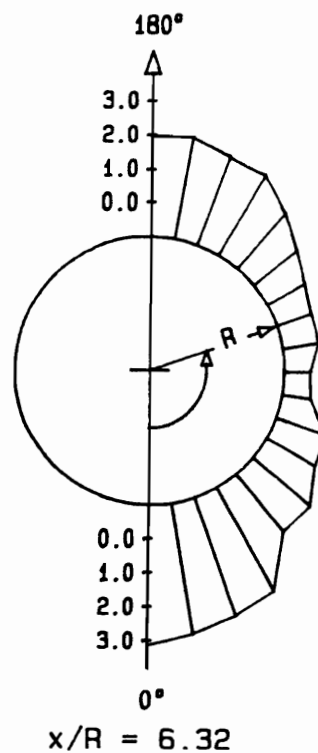
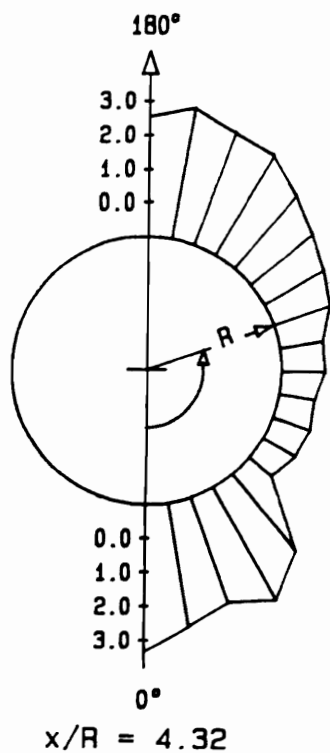


Figure 3.20. Circumferential pressure distributions on a hemisphere-cylinder at $\alpha = 10^\circ$ and $Re = 15000$.

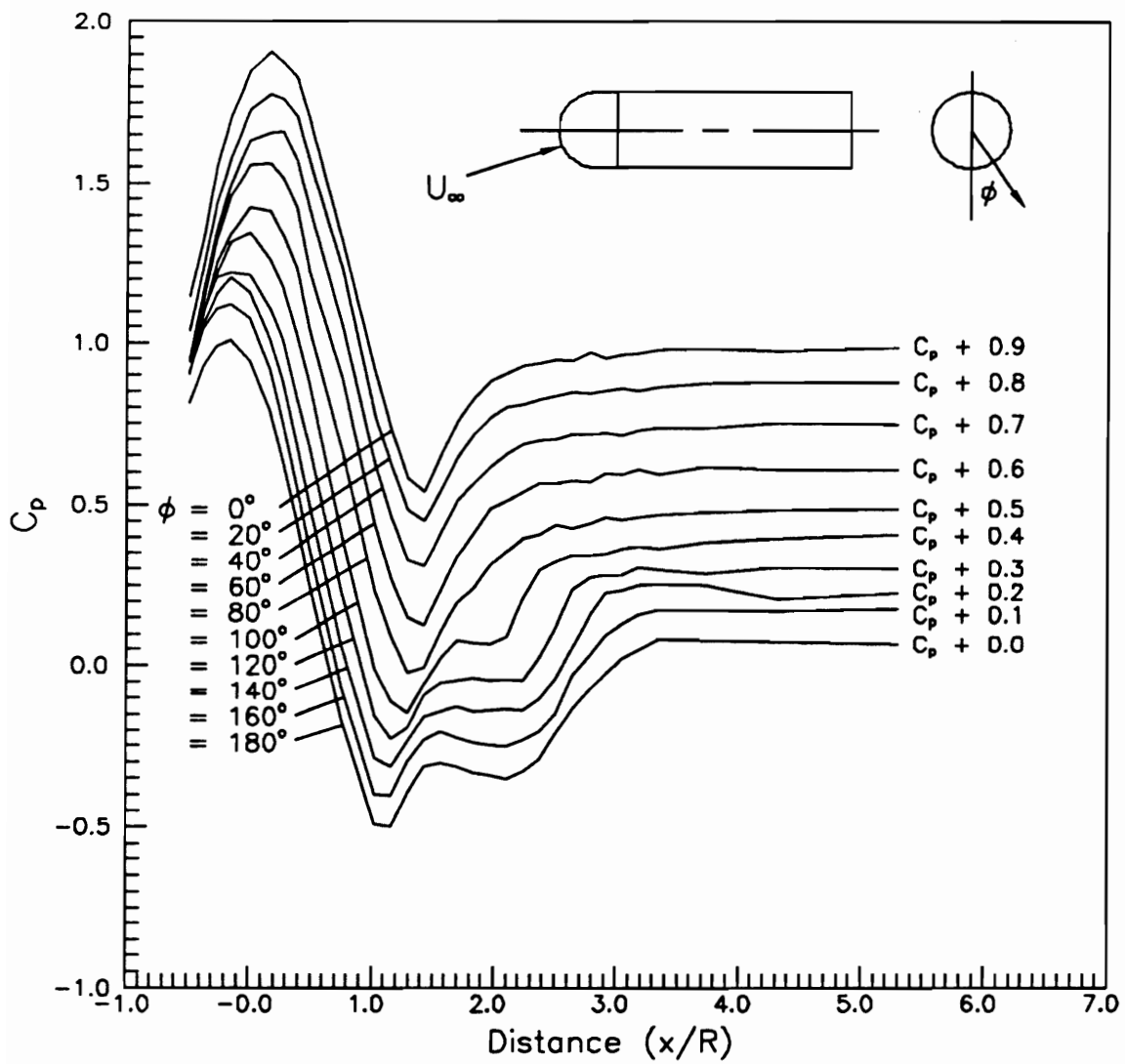


Figure 3.21. Axial pressure distributions on a hemisphere-cylinder at $\alpha = 10^\circ$ and $Re = 27000$ with added constants.

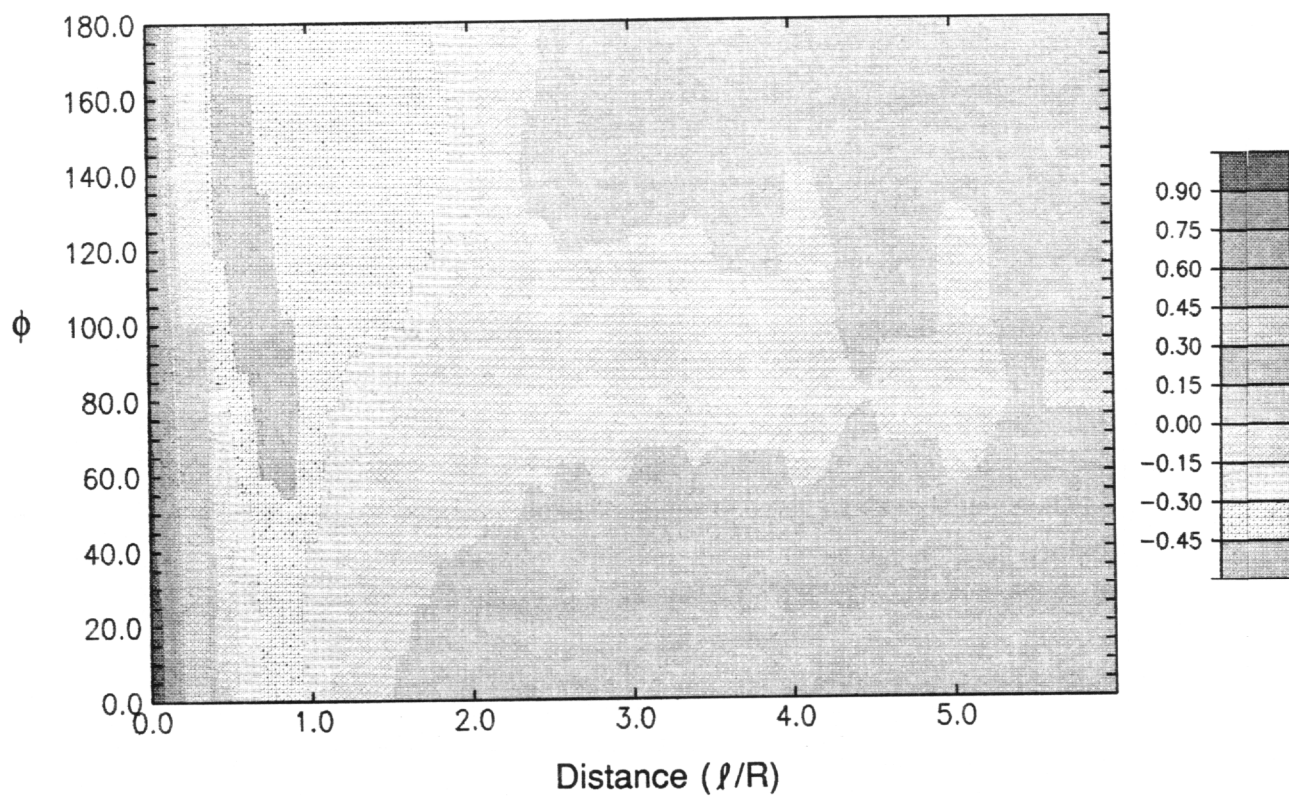


Figure 3.22. Pressure coefficient contours on a hemisphere-cylinder at $\alpha = 10^\circ$ and $Re = 27000$.

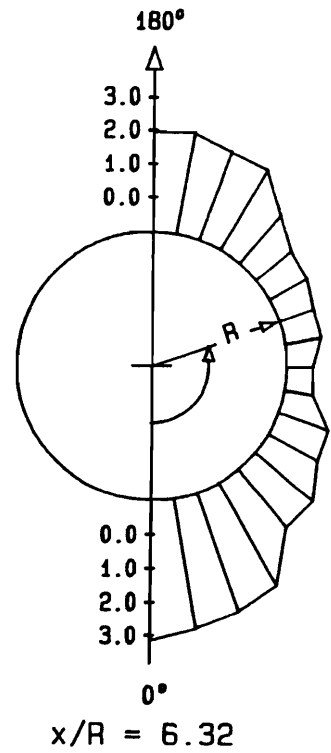
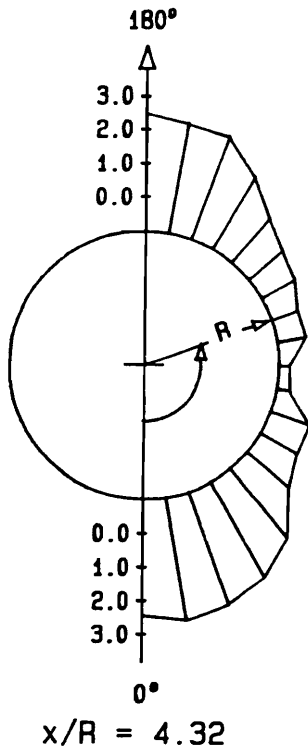


Figure 3.23. Circumferential pressure distributions on a hemisphere-cylinder at $\alpha = 10^\circ$ and $Re = 27000$.

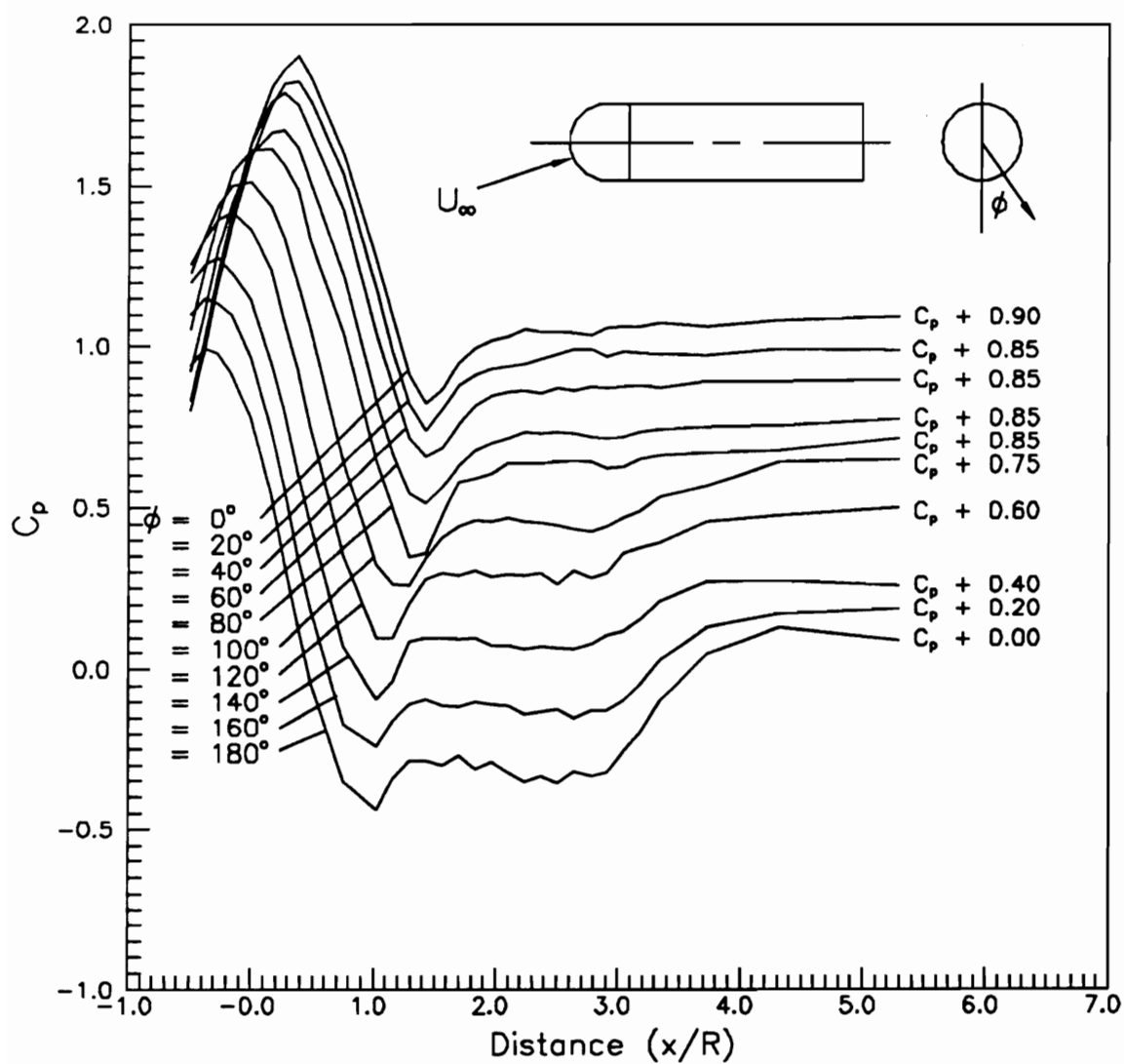


Figure 3.24. Axial pressure distributions on a hemisphere-cylinder at $\alpha = 20^\circ$ and $Re = 15000$ with added constants.

It has increased in length when compared with the 10° incidence case for the same Reynolds number. The pressure plots reveal a peculiar behavior; the curves become jagged within the separation bubble, especially at $\phi = 180^\circ$. During the experiment, the sampling time was doubled, from three seconds per data point to six seconds, to eliminate flow unsteadiness from the measurements. However, the same characteristic persists. Pressure coefficient contours are shown in Figure 3.25. Plots of circumferential pressure distribution are displayed in Figure 3.26. The leeward vortex is observed at approximately $x/R = 3.72$ and $\phi = 150^\circ$ and continues downstream along the same ϕ . This is a symmetrical vortex pattern as detected from the flow visualization photographs. The vortex induces a strong swirling motion on the surface of the model resulting in a dip on the pressure curves.

Figure 3.27 represents axial pressure distribution plots of a hemisphere-cylinder at $\alpha = 20^\circ$ and $Re = 2.7 \times 10^4$. The jagged characteristic, displayed by the pressure curves at lower Reynolds number has vanished. Unlike the previous cases, pressure coefficients within the separation bubble do not remain constant. As the curves cross the separation bubble, the pressure coefficient progressively drops to a minimum before leaving the separated region. Since the separation bubble locates between two horn vortices with the opposite rotational directions, the strong swirling motions of horn vortices induce a velocity component within the separation bubble. Thus the paintbrush marks within part of the separated region disappear as observed in the previous discussion of flow visualization. Figure 3.28 shows a large region of low pressure coefficients on the leeside of the model from $\ell/R = 0.3$ to 1.8 (or $x/R = 0.8$ to 2.5). On the windside of the model, steep pressure gradients are observed. The axes of the leeward vortices for this case originate at $x/R = 3.72$ and $\phi = 130^\circ$ (Figures 3.9 and 3.29). For larger x/R , the vortex axes gradually move toward $\phi = 140^\circ$. For both of these Reynolds numbers, the dips displayed by the circumferential pressure curves have the same depth.

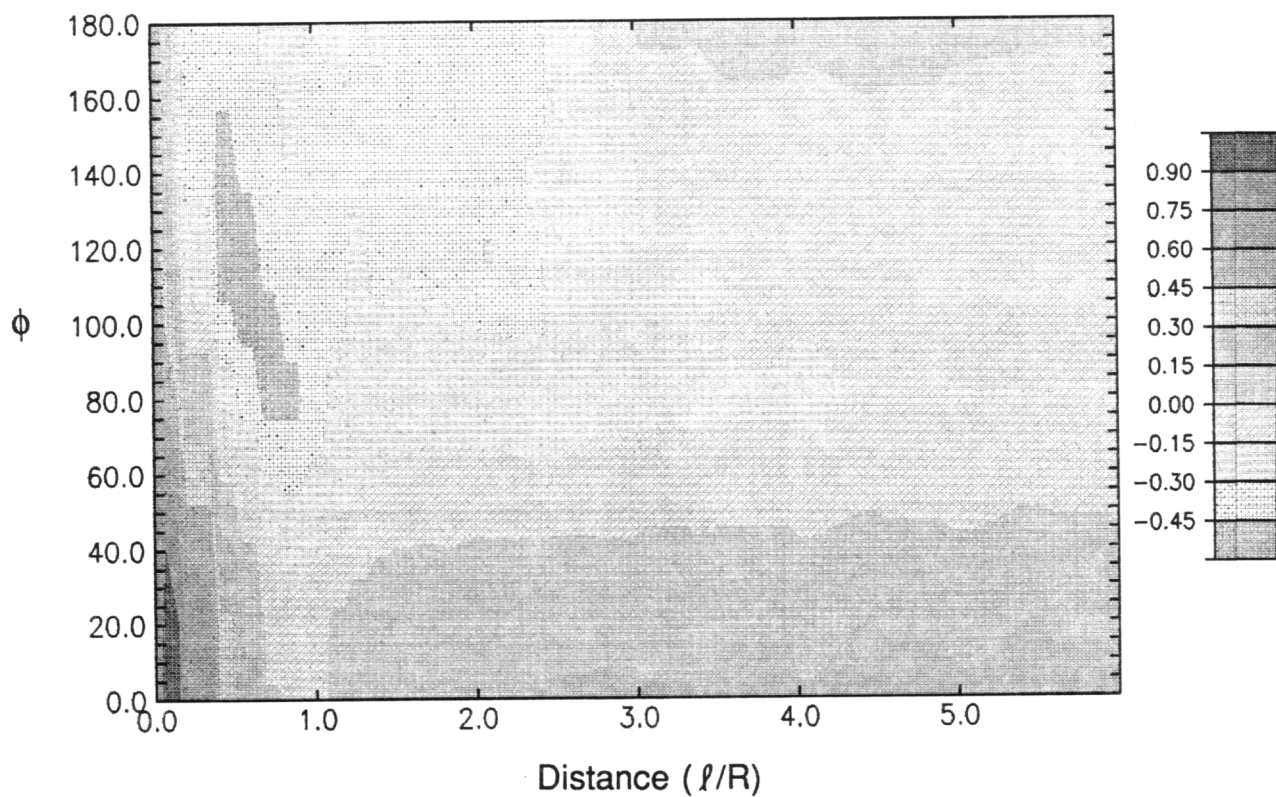


Figure 3.25. Pressure coefficient contours on a hemisphere-cylinder at $\alpha = 20^\circ$ and $Re = 15000$.

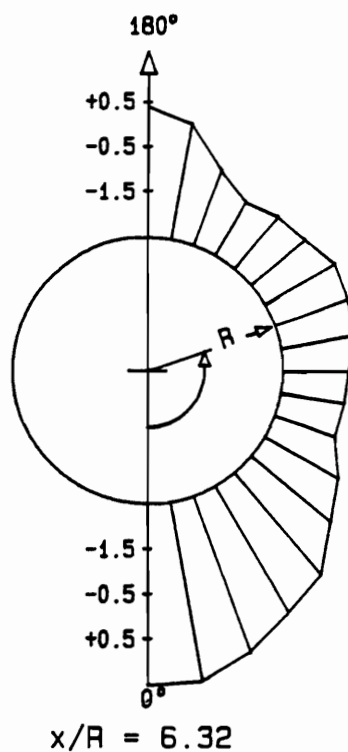
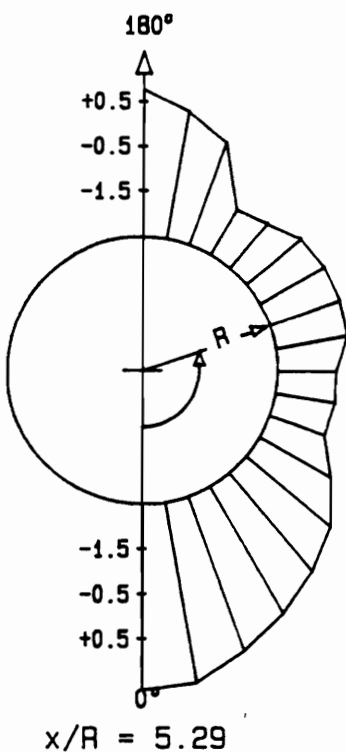
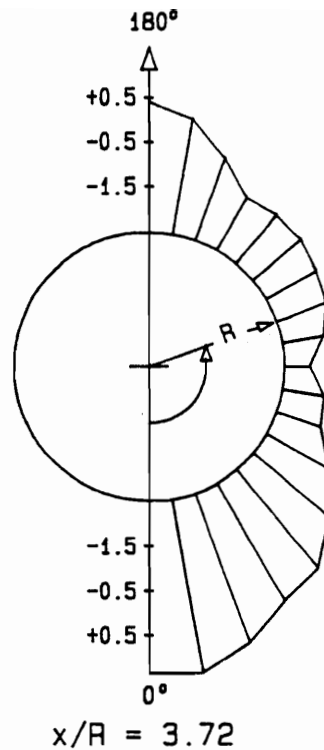
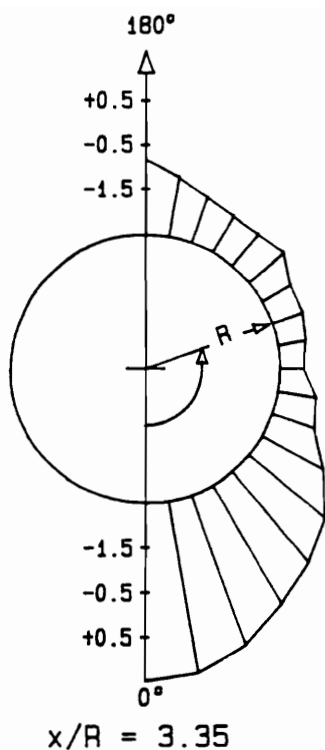


Figure 3.26. Circumferential pressure distributions on a hemisphere-cylinder at $\alpha = 20^\circ$ and $Re = 15000$.

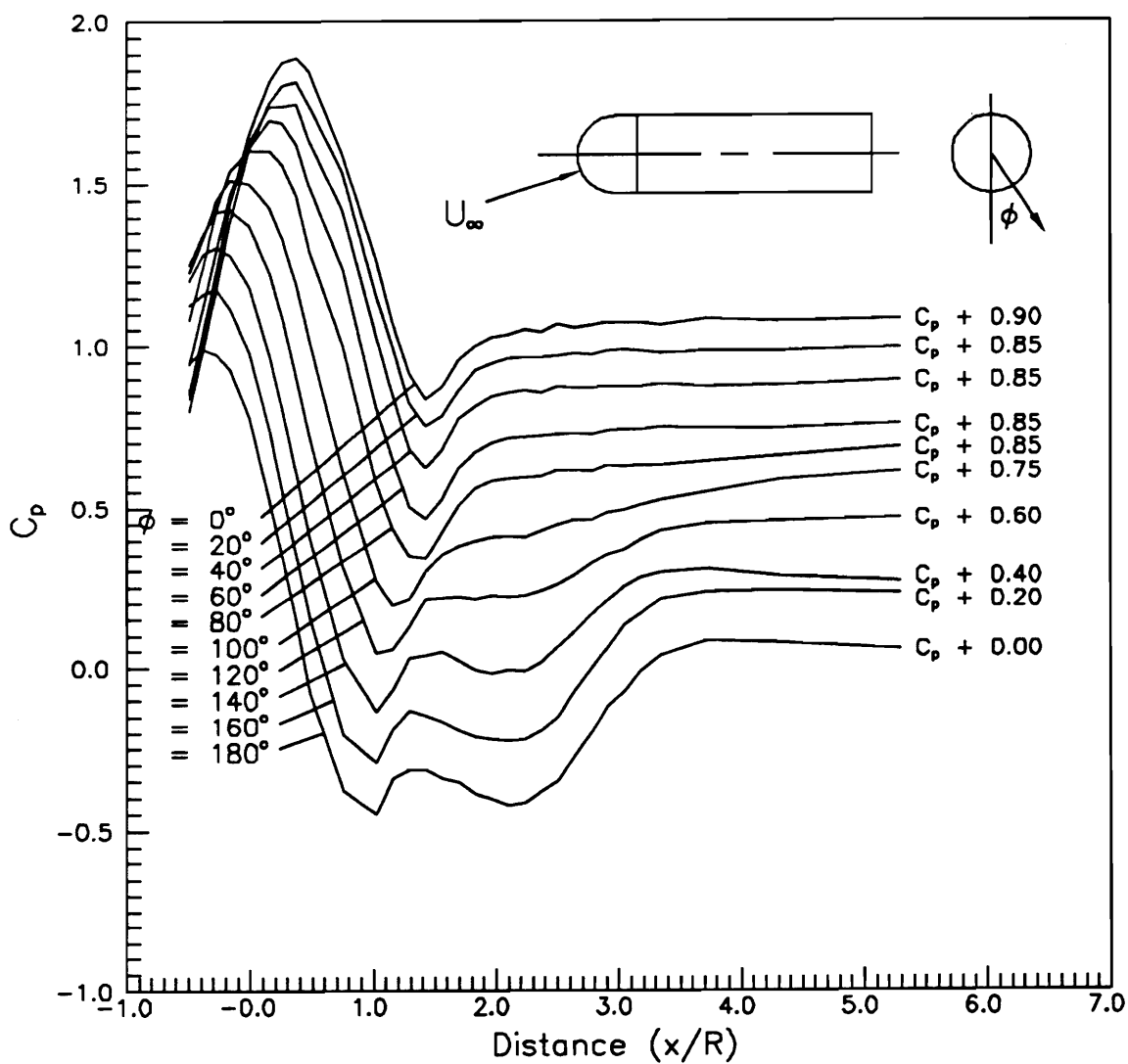


Figure 3.27. Axial pressure distributions on a hemisphere-cylinder at $\alpha = 20^\circ$ and $Re = 27000$ with added constants.

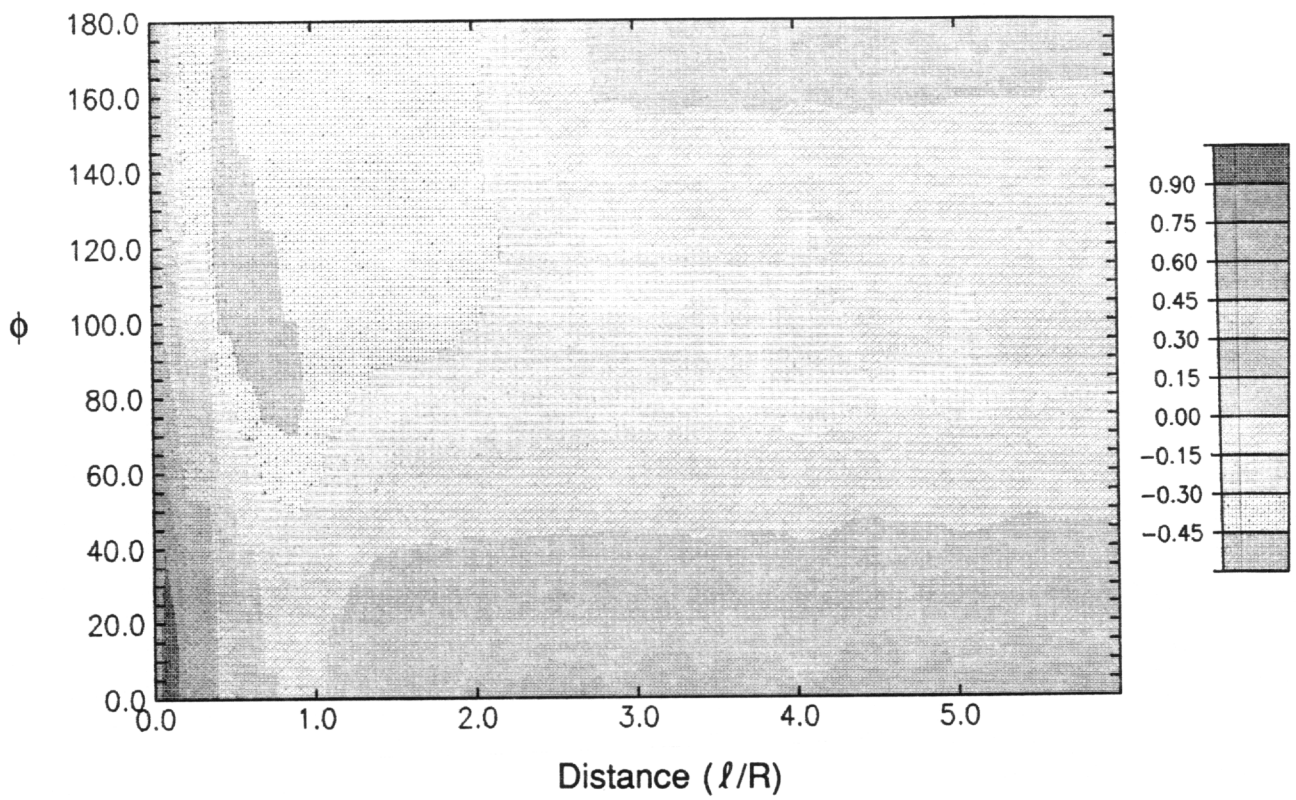
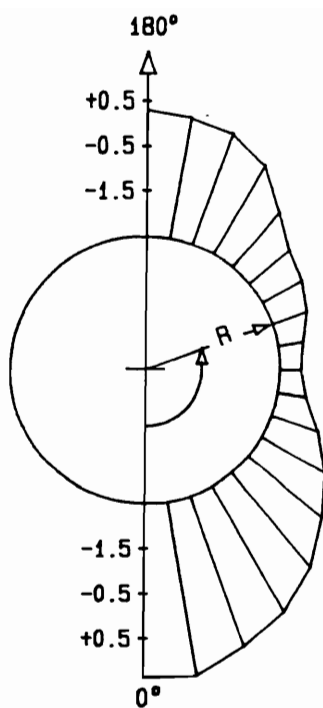
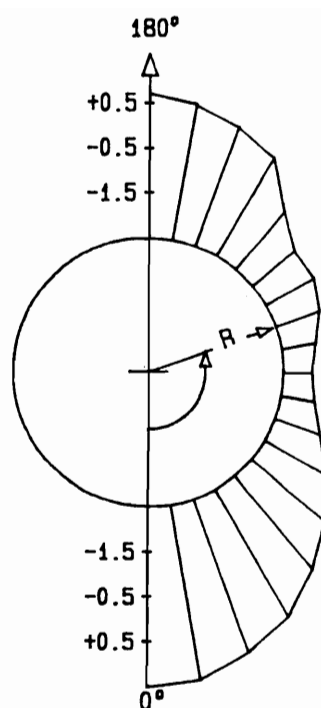


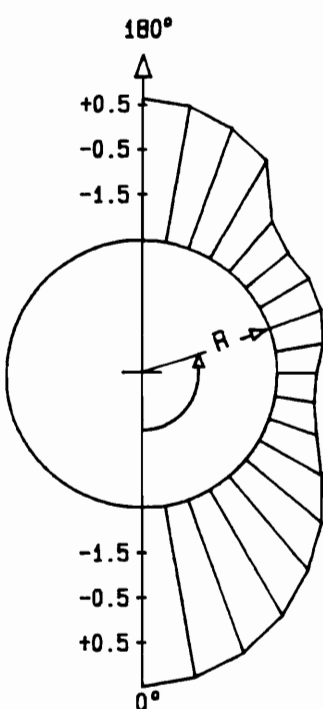
Figure 3.28. Pressure coefficient contours on a hemisphere-cylinder at $\alpha = 20^\circ$ and $Re = 27000$.



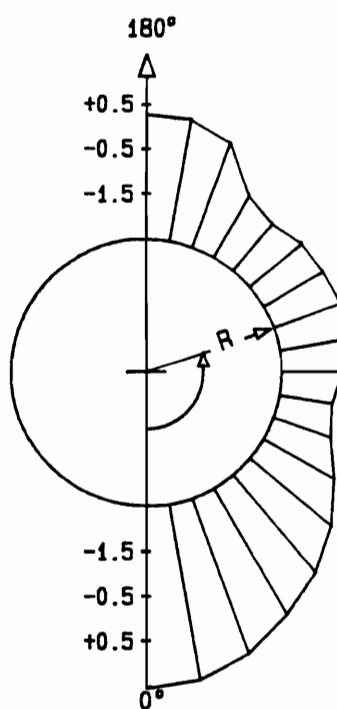
$x/R = 3.35$



$x/R = 3.72$



$x/R = 4.32$



$x/R = 6.32$

Figure 3.29. Circumferential pressure distributions on a hemisphere-cylinder at $\alpha = 20^\circ$ and $Re = 27000$.

At $\alpha = 30^\circ$ and $Re = 1.5 \times 10^4$, pressure plot is displayed in Figure 3.30. At this incidence, the separation bubble and the leeward vortices have already merged into one large region of separation (Figure 3.11). The pressure curve at $\phi = 180^\circ$ is the only line crossing the separated region that displays a section of constant pressure coefficients. Pressure curves between $100^\circ \leq \phi \leq 160^\circ$ reside entirely inside the separated region; consequently, pressure coefficients remain constant along the afterbody of the model. The pressure coefficient contours are displayed in Figure 3.31. Although the leeward vortices originate at $x/R = 1.2$, the swirling motion does not begin until $x/R = 2.64$ and $\phi = 160^\circ$. The location of the vortex core stays unchanged along the afterbody of the model at $\phi = 160^\circ$ (Figure 3.32). Very deep dips in the circumferential pressure curves demonstrate the existence of strong leeward vortices. The dips are most pronounced between $x/R = 3.05$ to 5.29 and then gradually become shallower toward $x/R = 6.32$. This suggests that the leeward vortices are either lifting off from the surface of the model or might lose vorticity due to some sort of vortex breakdown as they approach the trailing-edge. At a higher Reynolds number, $Re = 2.7 \times 10^4$, similar characteristics are displayed as shown in Figures 3.33, 3.34 and 3.35. The dips in the circumferential pressure curves locate at $\phi = 150^\circ$ along the afterbody of the model. This demonstrates that the leeward vortices move away from each other at higher Reynolds number.

Experiments at $\alpha > 40^\circ$ and $Re = 2.7 \times 10^4$ were carried out unsuccessfully. The model vibrated vigorously regardless of repeated attempts to hinder its motion. In a much bigger VPI Stability Wind Tunnel, where the mounting sting can rigidly hold models weighing up to 1500 pounds, a similar phenomenon was detected with the same model (weighing at about two pounds) and under the same flow conditions. Vortex shedding was believed to be the cause and will be discussed in Chapter 5.

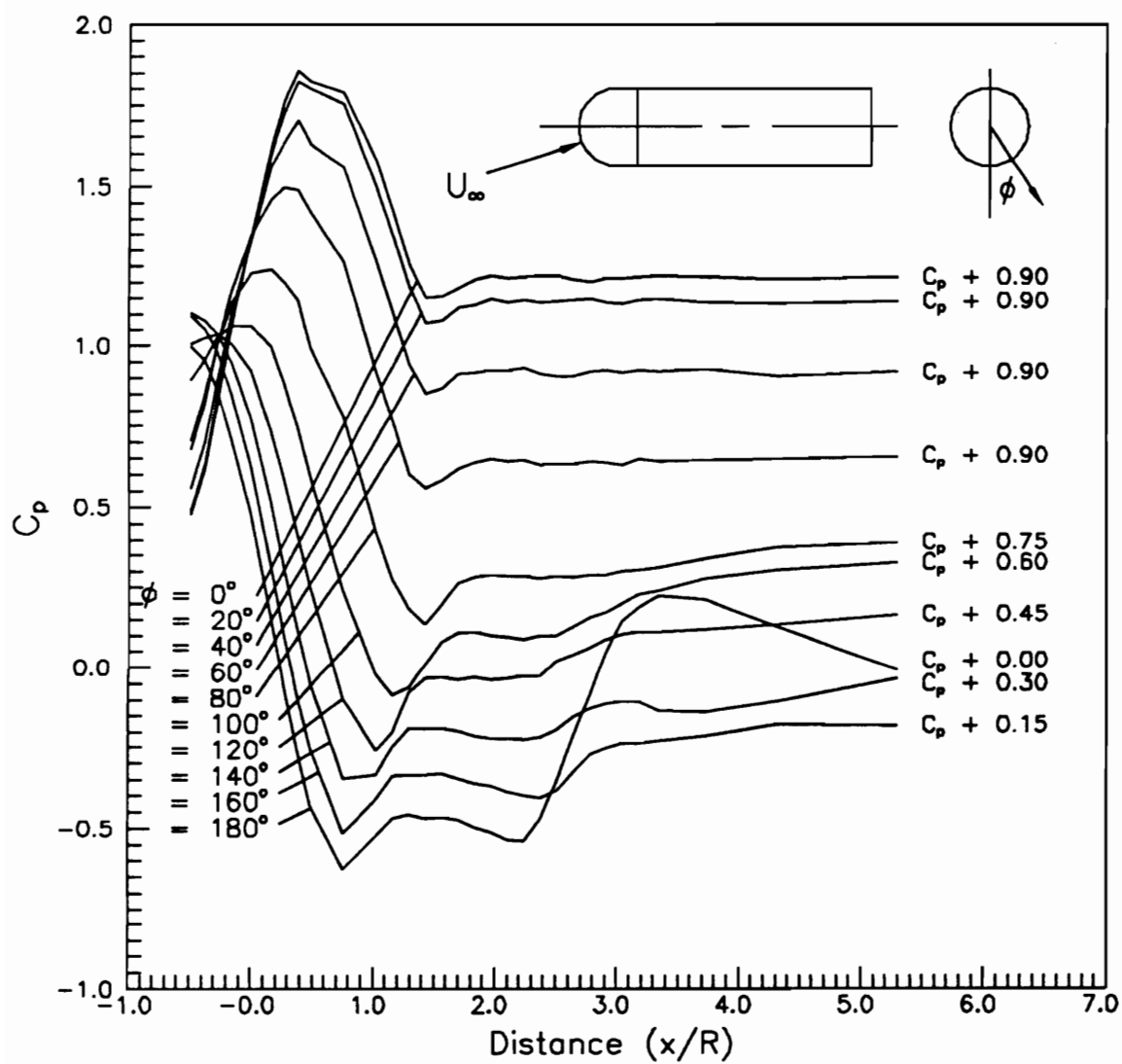


Figure 3.30. Axial pressure distributions on a hemisphere-cylinder at $\alpha = 30^\circ$ and $Re = 15000$ with added constants.

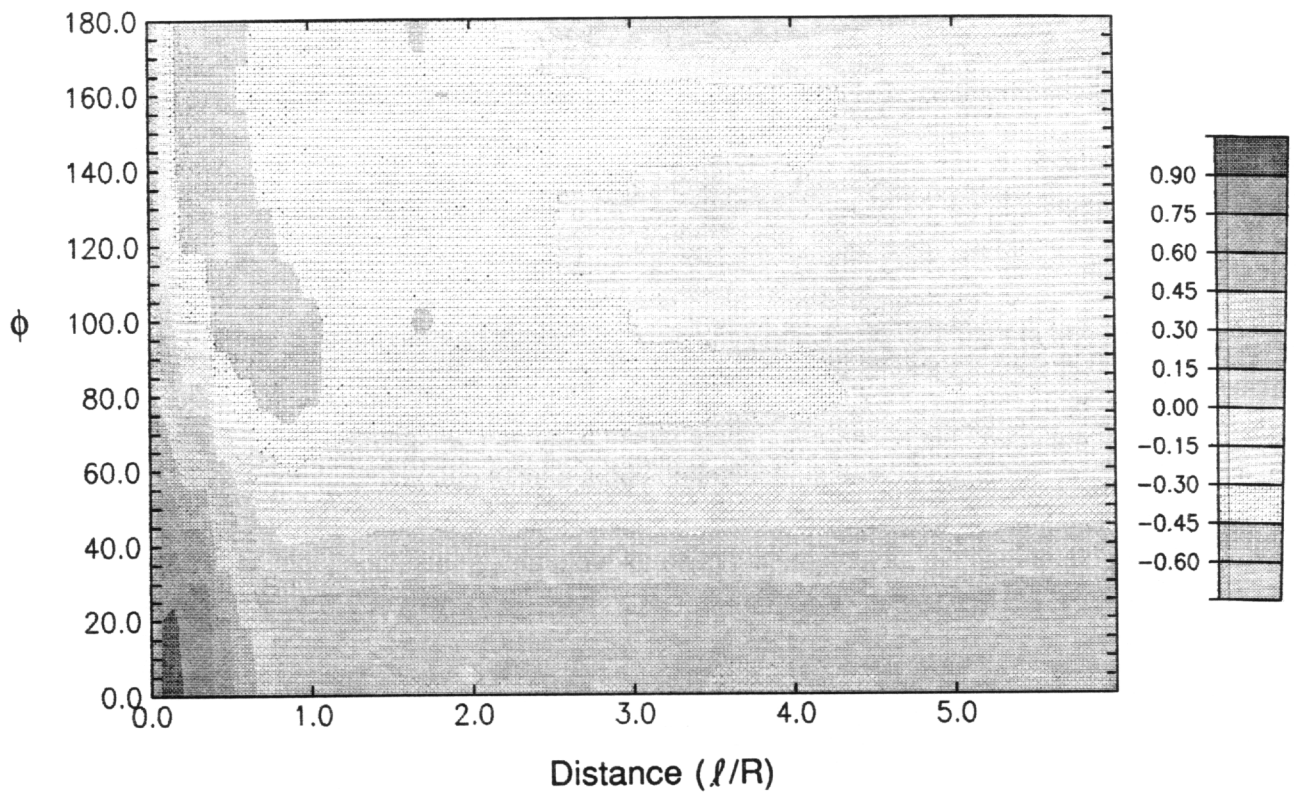


Figure 3.31. Pressure coefficient contours on a hemisphere-cylinder at $\alpha = 30^\circ$ and $Re = 15000$.

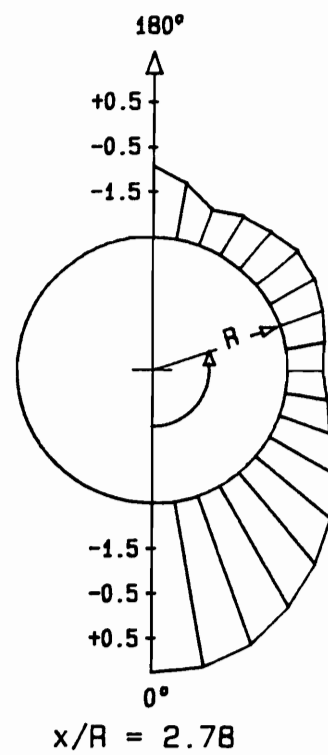
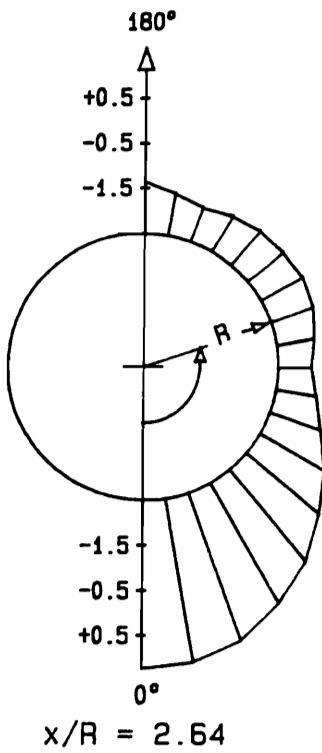
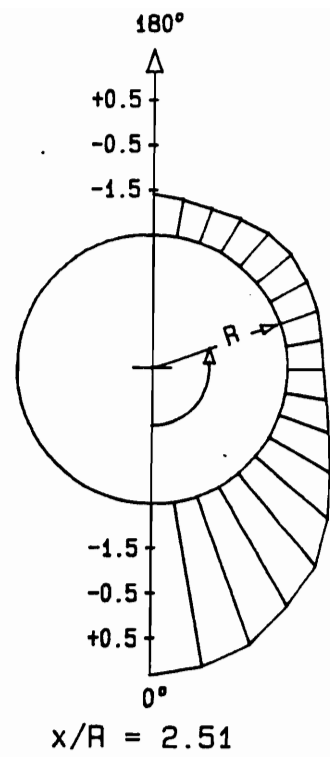
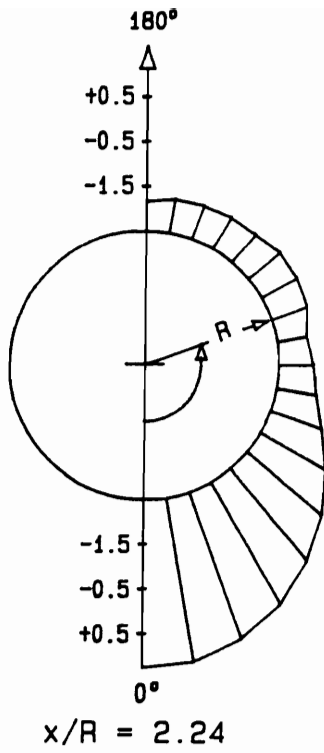


Figure 3.32. Circumferential pressure distributions on a hemisphere-cylinder at $\alpha = 30^\circ$ and $Re = 15000$.

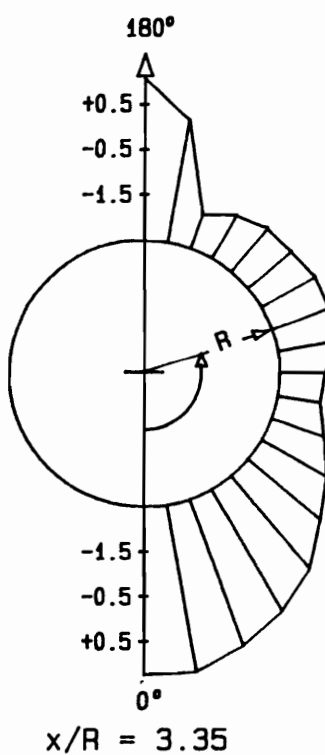
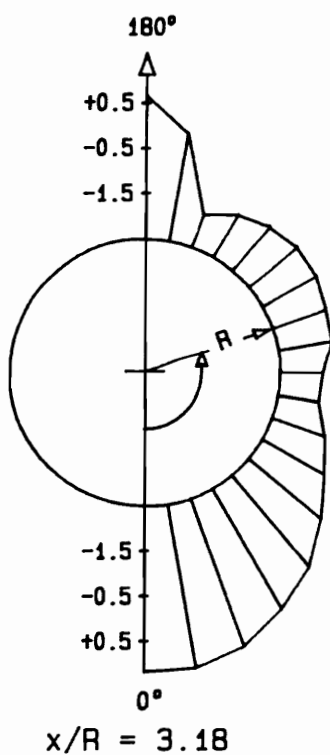
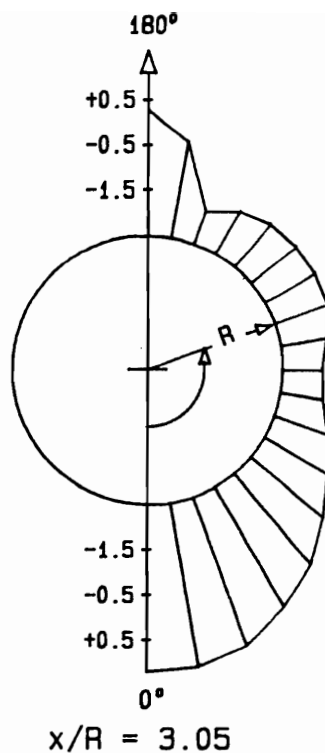
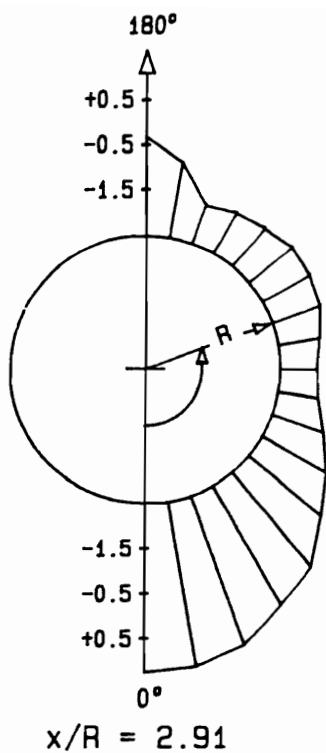


Figure 3.32. Continued

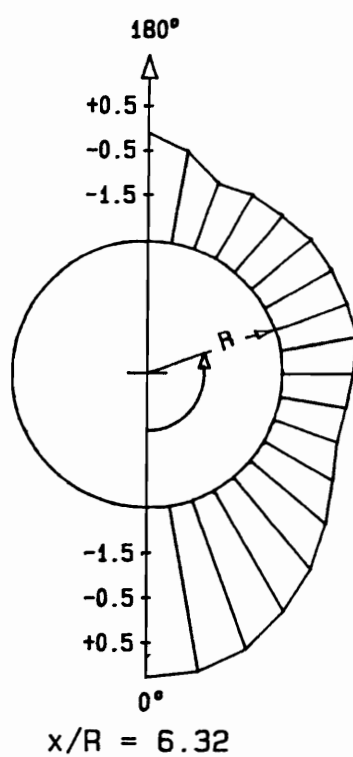
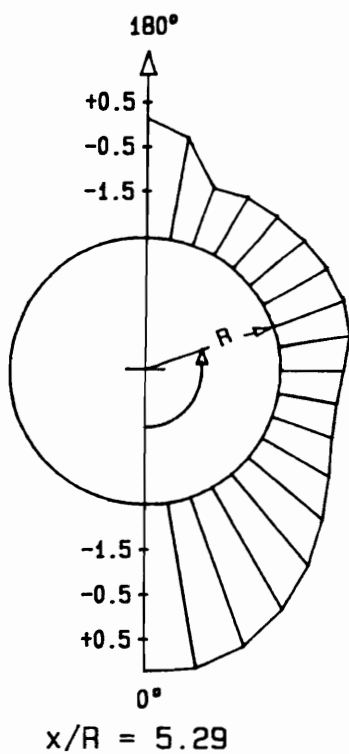
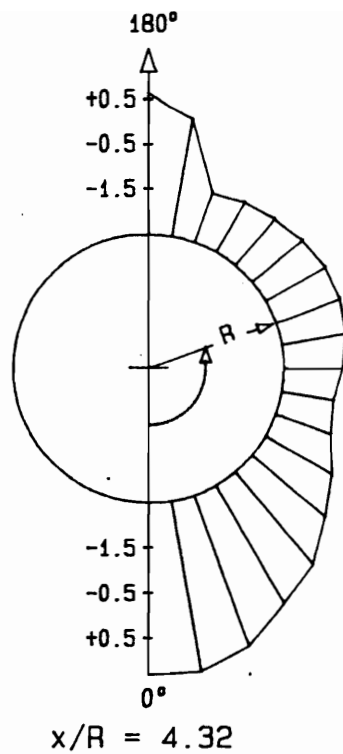
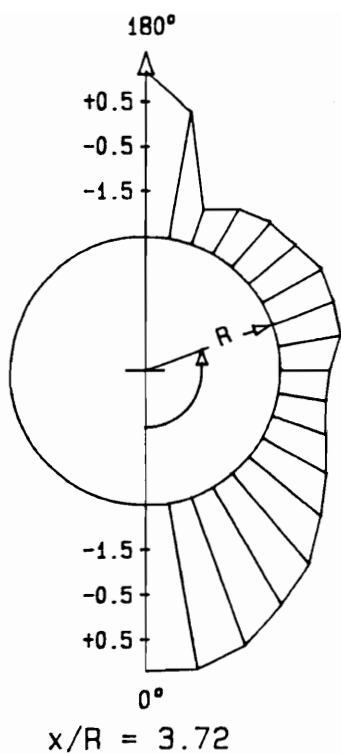


Figure 3.32. Continued

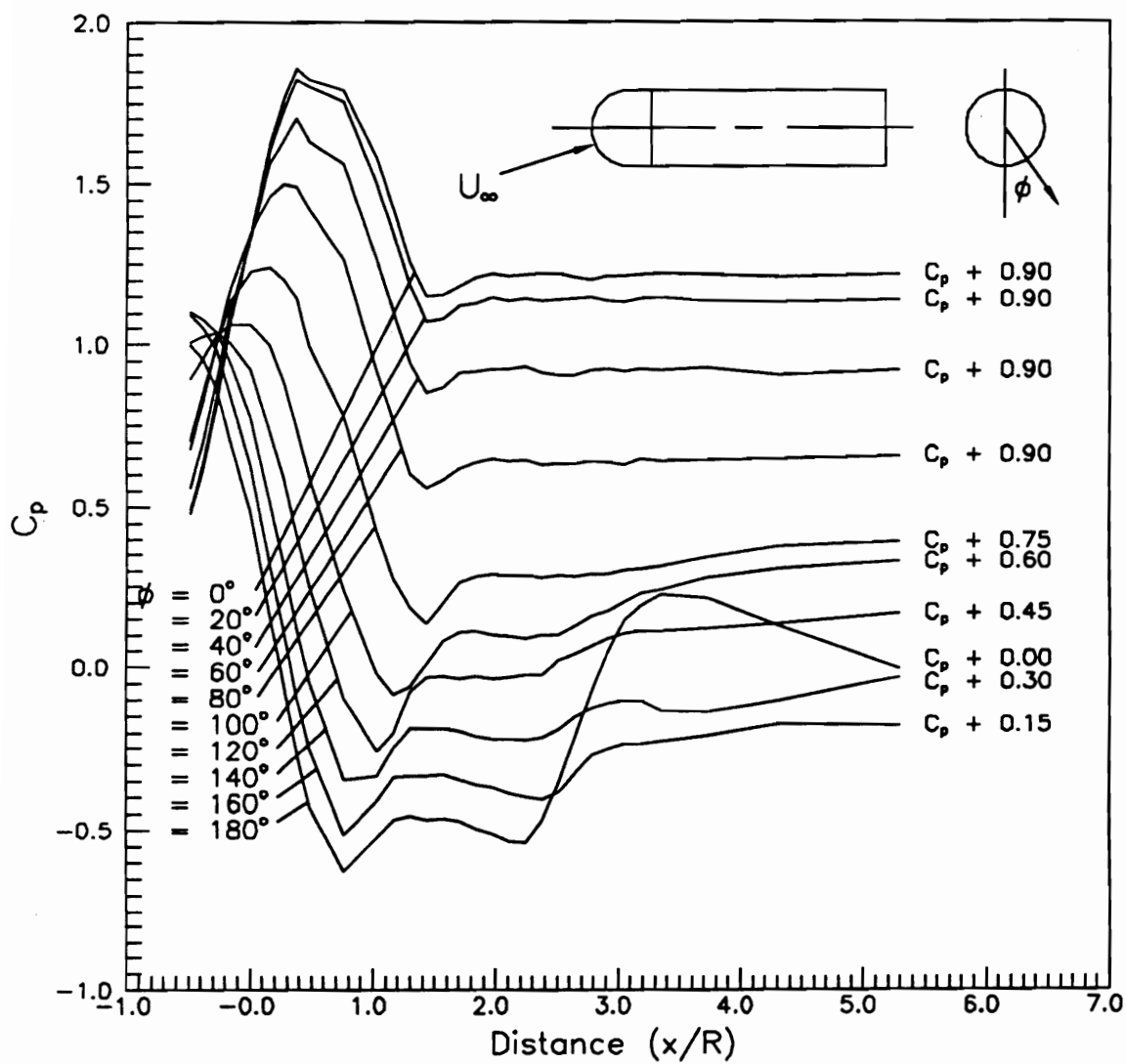


Figure 3.33. Axial pressure distributions on a hemisphere-cylinder at $\alpha = 30^\circ$ and $Re = 27000$ with added constants.

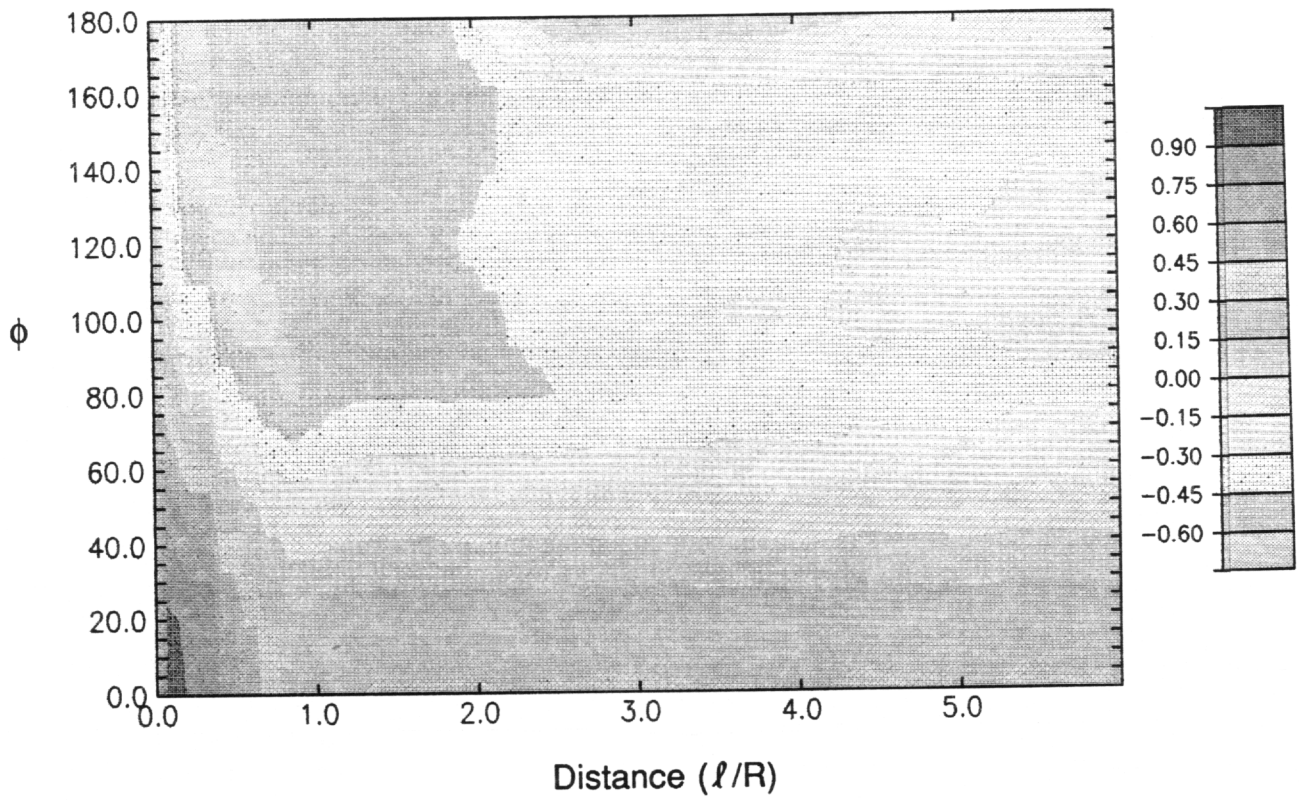


Figure 3.34. Pressure coefficient contours on a hemisphere-cylinder at $\alpha = 30^\circ$ and $Re = 27000$.

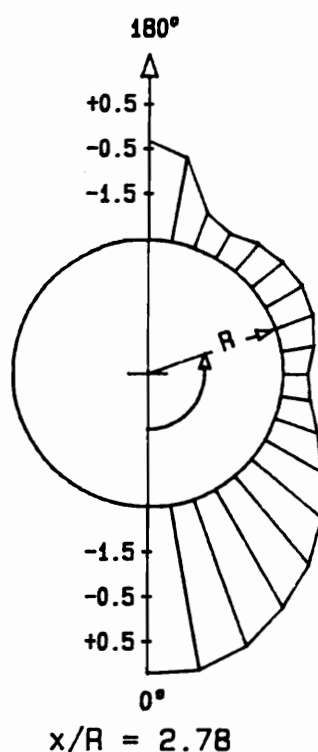
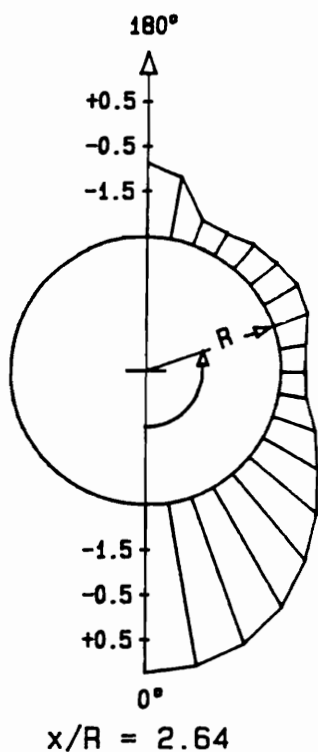
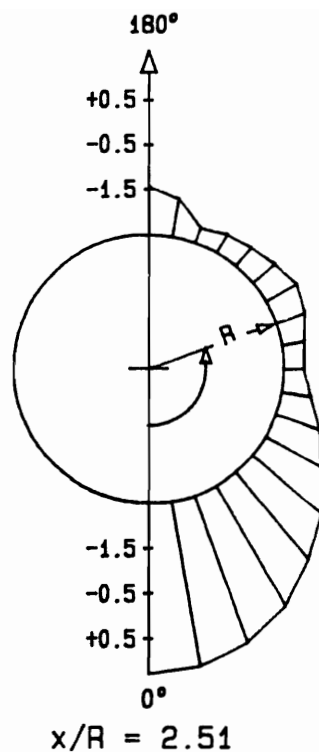
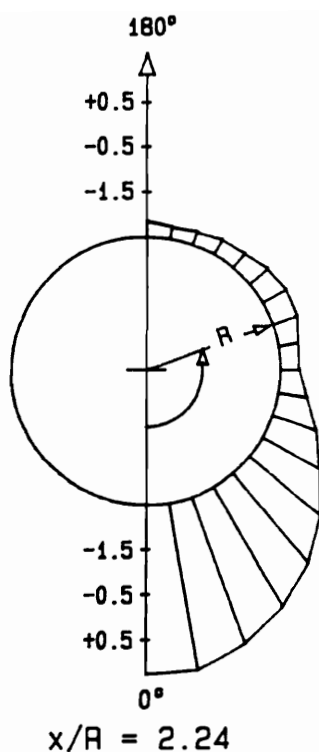


Figure 3.35. Circumferential pressure distributions on a hemisphere-cylinder at $\alpha = 30^\circ$ and $Re = 27000$.

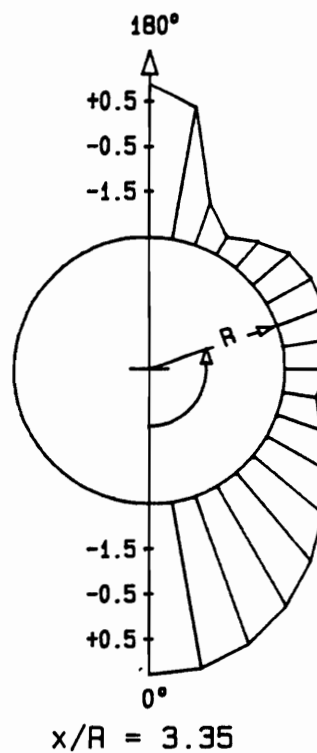
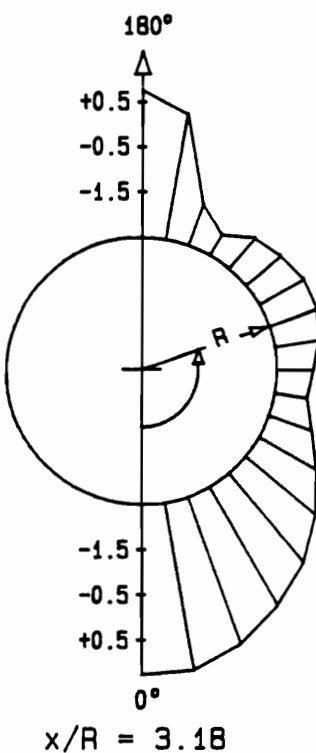
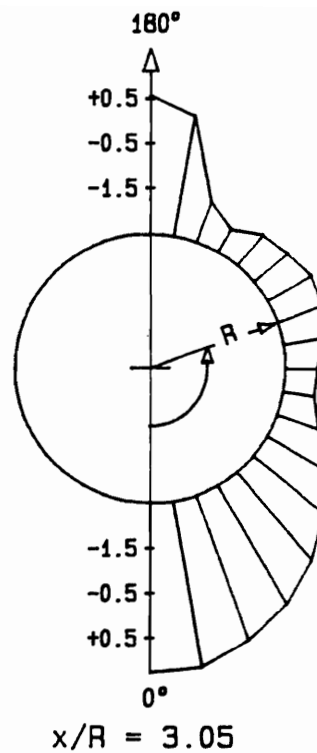
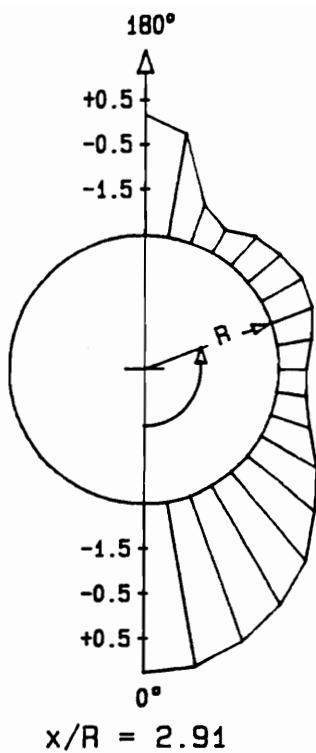


Figure 3.35. Continued

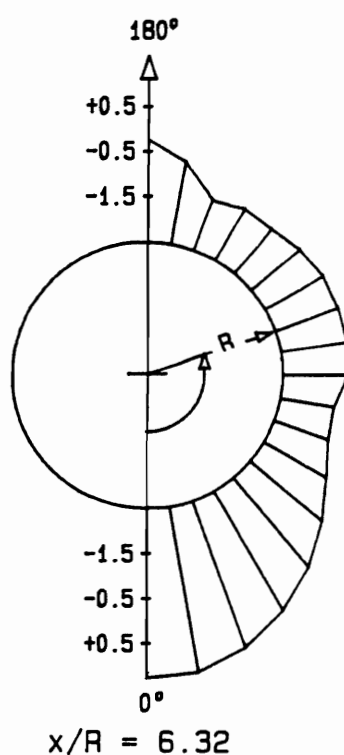
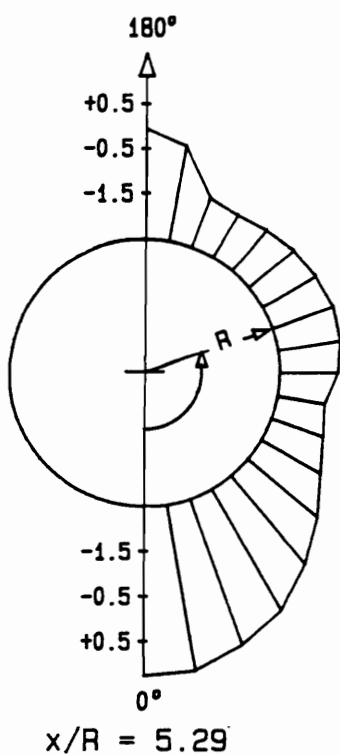
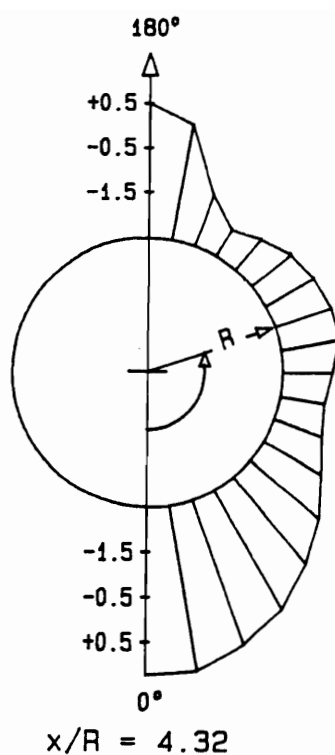
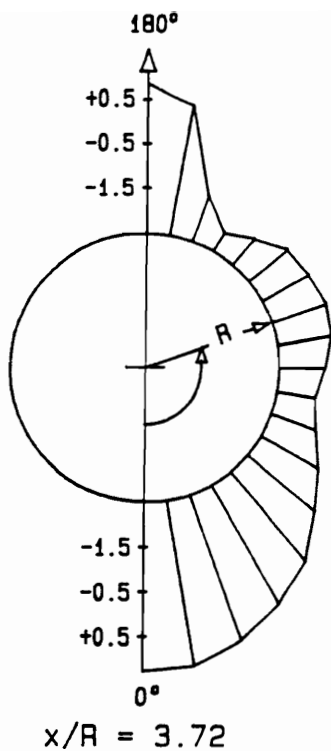


Figure 3.35. Continued

Velocity Measurements

Wake velocity measurements of the hemisphere-cylinder displayed in this section were taken in a plane perpendicular to the free-stream velocity (y-z plane) at a Reynolds number of 2.7×10^4 and $x/R = 20.5$. The velocity field of the hemisphere-cylinder at $\alpha = 20^\circ$ is displayed in Figure 3.36. A pair of symmetrical leeward vortices can be seen in this figure. The cores of these vortices are closer to the surface of the model than for the 30° incidence case (Figure 3.37). At $\alpha = 30^\circ$, the flowfield is still symmetric. The symmetric pattern of the leeward vortices displayed by both velocity measurements and flow visualization results justified taking pressures only on half of the model.

Axial velocity component is also available for all the data presented in this section. A typical example of axial velocity contours is displayed in Figure 3.38. A region of velocity defect appearing in the measuring domain is probably due to the model's blockage. A surprising fact is that there is no increase of axial velocity in the core of the leeward vortices. In contrast to our findings, the axial velocity component in the core of the vortices of a delta wing can reach as high as three times the free-stream velocity (Rediniotis et al., 1991).

Measurements shown in the rest of this section were conducted at a Reynolds number of 2.7×10^4 and $\alpha = 30^\circ$ to investigate the effects of bead size and location on vortex field asymmetries. Two different sizes of beads (bead#1 and bead#2) as shown in Figure 3.4 were employed at various positions. Presented in Figure 3.39 are the wake velocity vectors when bead#1 was mounted on the hemisphere-cylinder at $x/R = 0.5$ and $\phi = 30^\circ$. This is in front of the separation bubble that develops on the nose of the model. The flowfield exhibits a very low degree of vortex asymmetry. The effect of the bead on the overall flow behavior seems to be minimal. Non-dimensional axial vorticity was calculated using the following equation

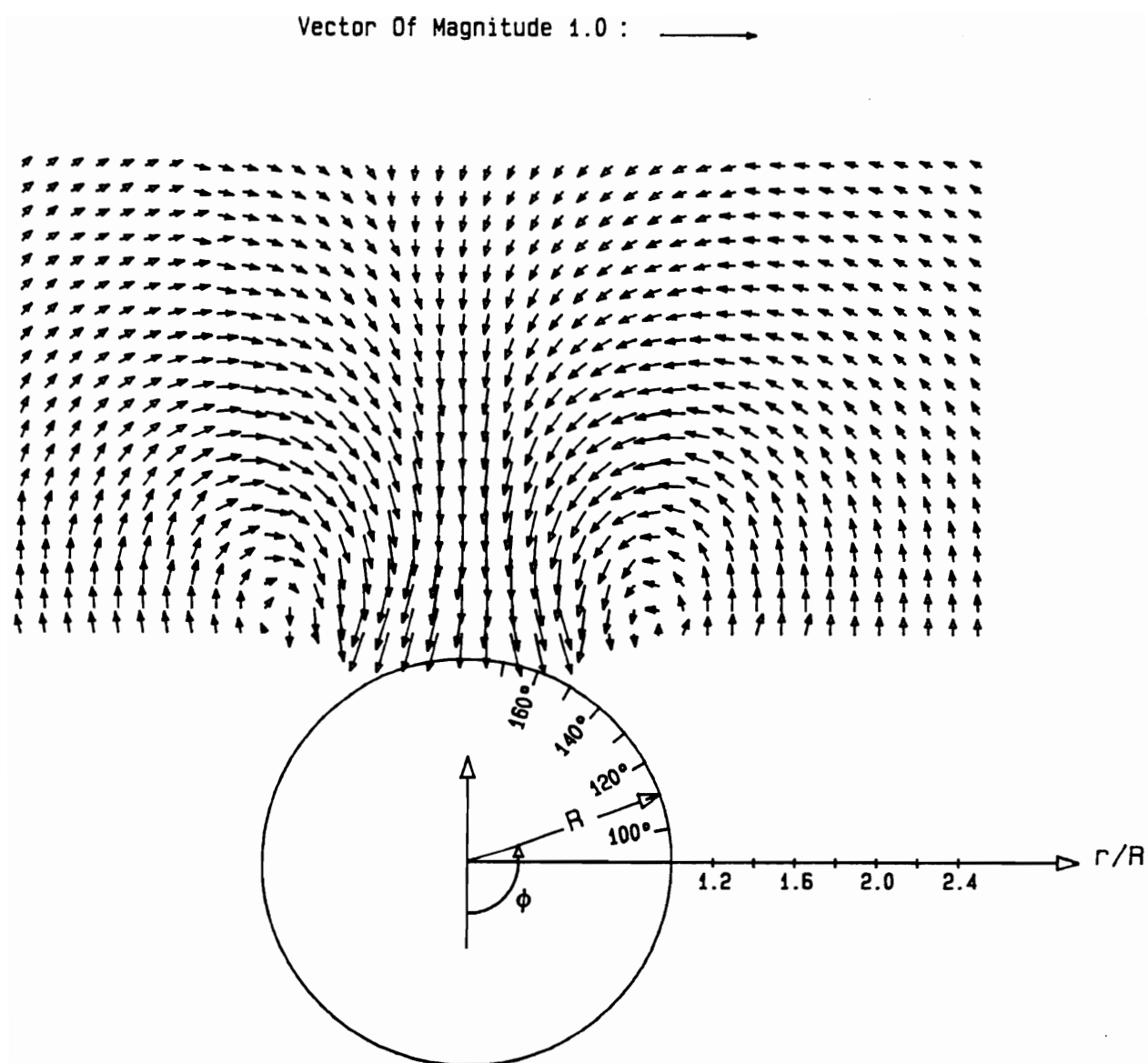


Figure 3.36. Velocity field at $\alpha = 20^\circ$ and $Re = 27000$ with no bead.

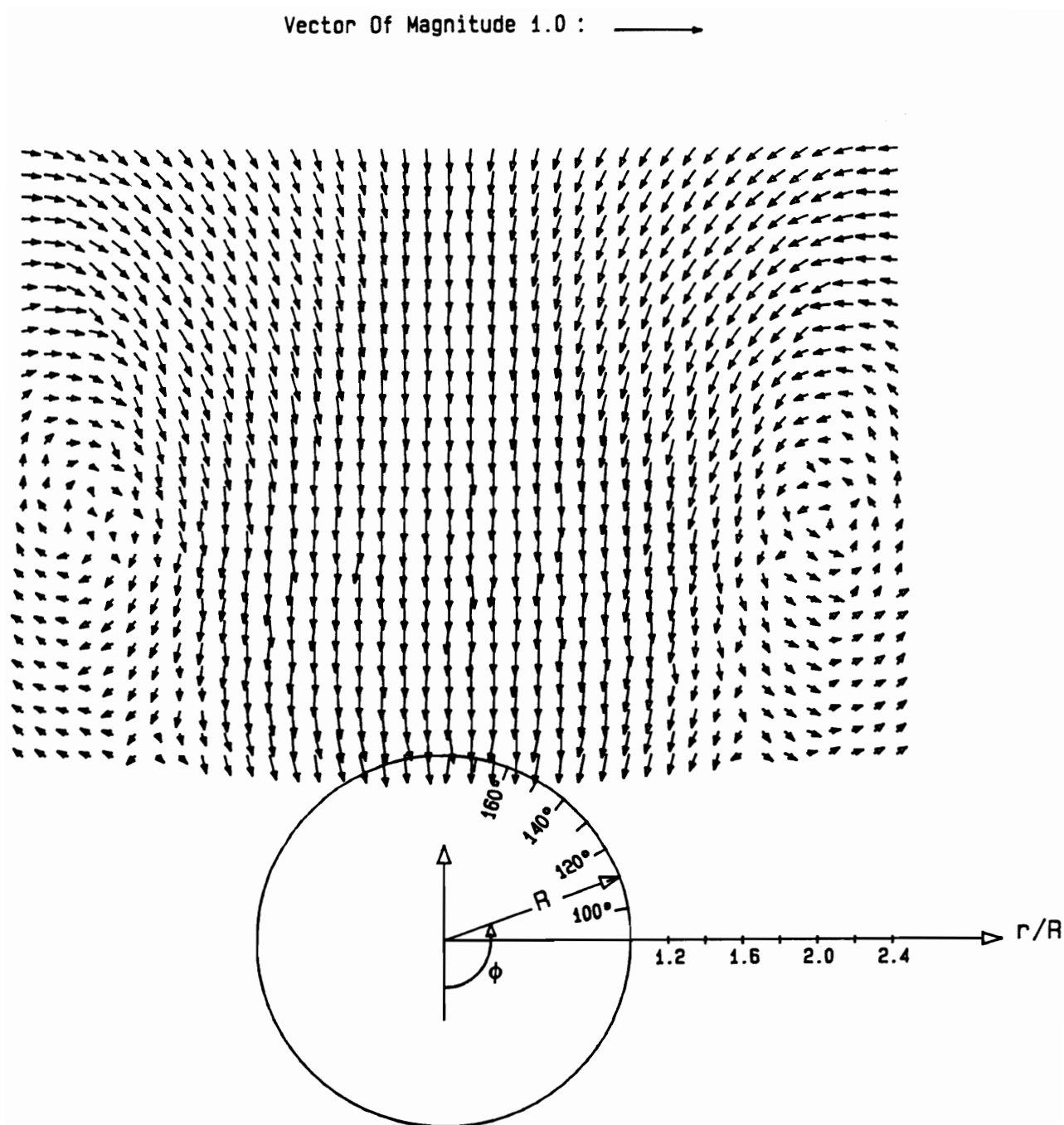


Figure 3.37. Velocity field at $\alpha = 30^\circ$ and $Re = 27000$ with no bead.

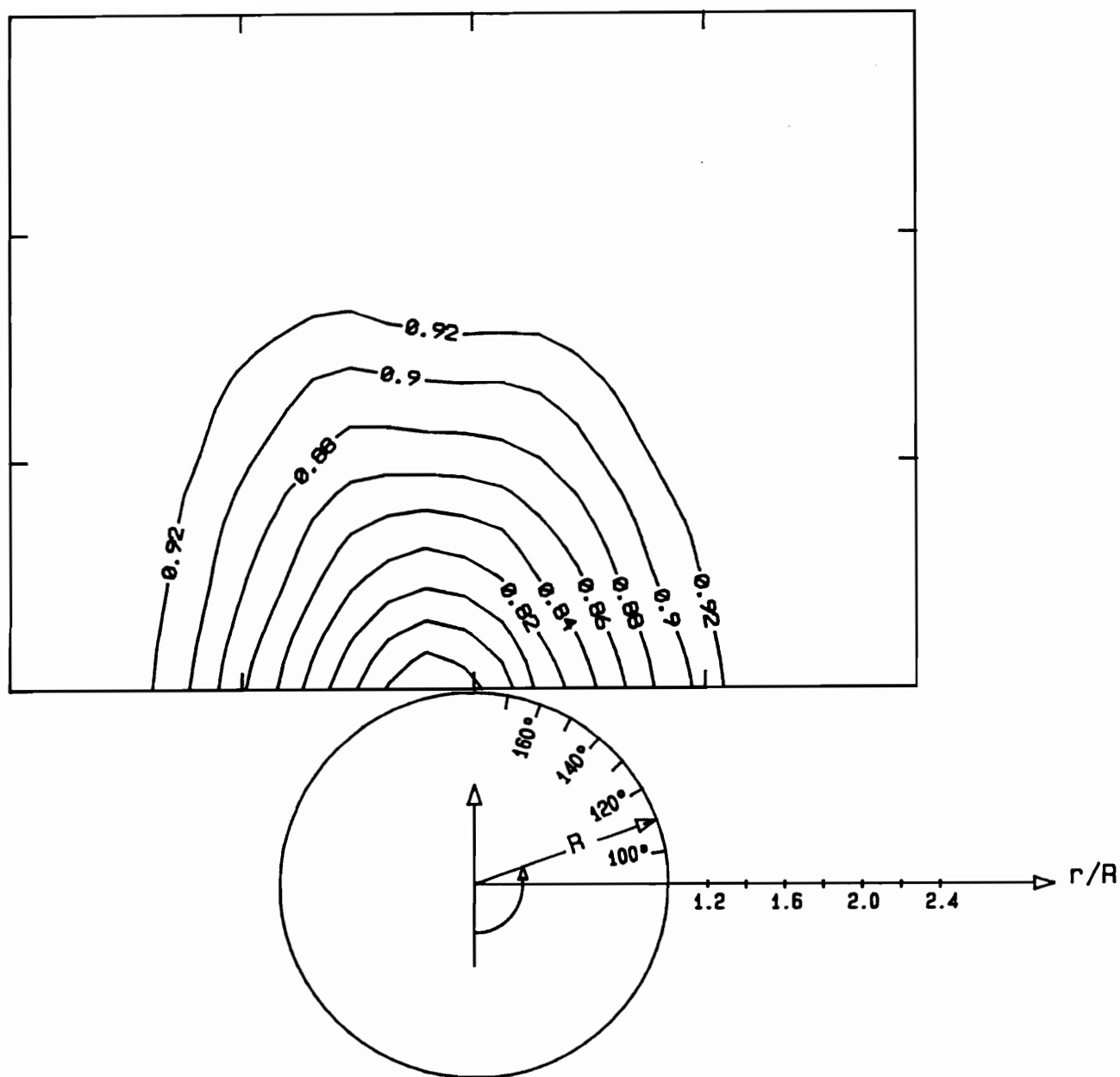


Figure 3.38. Axial velocity component contours at $\alpha = 30^\circ$ and $Re = 27000$ with no bead.

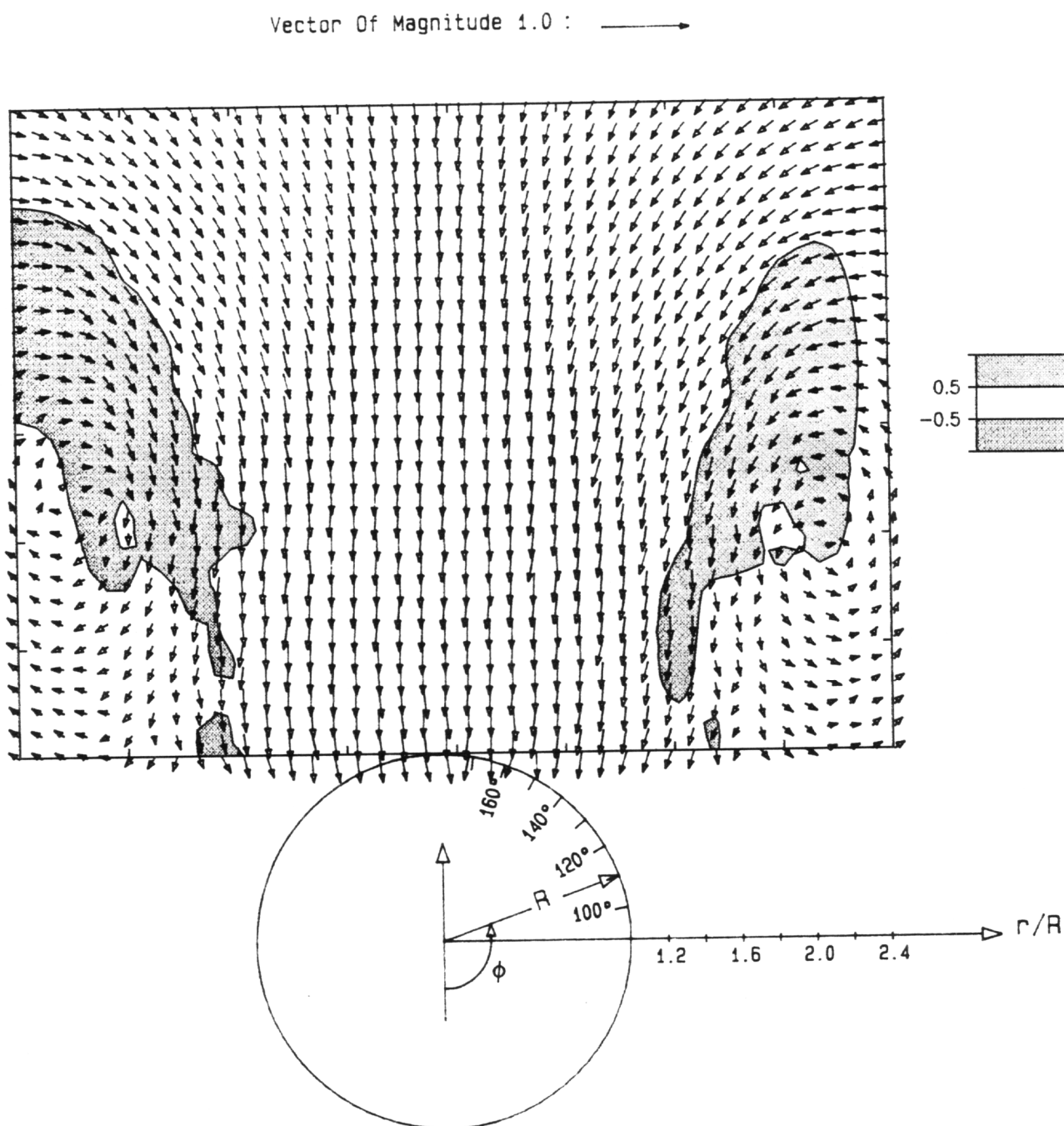


Figure 3.39. Velocity field and vorticity contours at $\alpha = 30^\circ$ and $Re = 27000$ with bead#1 at $\phi = 30^\circ$ and $x/R = 0.5$.

$$\Omega = \frac{D}{U_{\infty}} \left(\frac{\partial v}{\partial z} - \frac{\partial w}{\partial y} \right) \quad [3.1]$$

where D is the diameter of the cylindrical afterbody and U_{∞} is the free-stream velocity. The reader is referred to Figure 3.4a for the definition of coordinates. Vorticity contours of the flowfield displayed in Figure 3.39 do not show an asymmetric pattern.

When bead#1 was mounted at $x/R = 0.5$ and $\phi = 70^\circ$, the flow pattern becomes highly asymmetric. The right leeward vortex (the side with the bead) dominates the wake and spreads itself over a much larger region than the left leeward vortex (Figure 3.40). As expected, the locations of the vortices have changed. The dominant vortex moves toward the surface of the model while the other moves further away. Vorticity contours of the flowfield provide further insight into the asymmetric behavior. The ratio of the maximum vorticity between the right and left vortex is 3.2 to 1.0.

Figure 3.41 presents velocity field and vorticity contours obtained with bead#1 mounted at $x/R = 0.5$ and $\phi = 90^\circ$. The asymmetric pattern is even more pronounced than in the previous case. Both vortices gain considerable amount of strength and size. At the core of the right vortex, vorticity increases from 3.0 to 6.0; similarly, the left vortex also has an increase in strength from -1.0 to -3.0 . Velocity field and vorticity contours, when bead#1 was placed at $x/R = 0.5$ and $\phi = 120^\circ$, are shown in Figure 3.42. The flowfield pattern displays the highest degree of asymmetry. Both leeward vortices reach their maximum strength, however, with a slight decrease in size. The distance between the vortices is the largest recorded in these experiments. Only half of the left vortex is contained within the measuring domain. The axial velocity component for this case once again shows no evidence of the violent vortical motion (Figure 3.43). When bead#1 was positioned at $x/R = 0.5$ and $\phi = 150^\circ$, the degree of asymmetry decreases as shown in Figure 3.44.

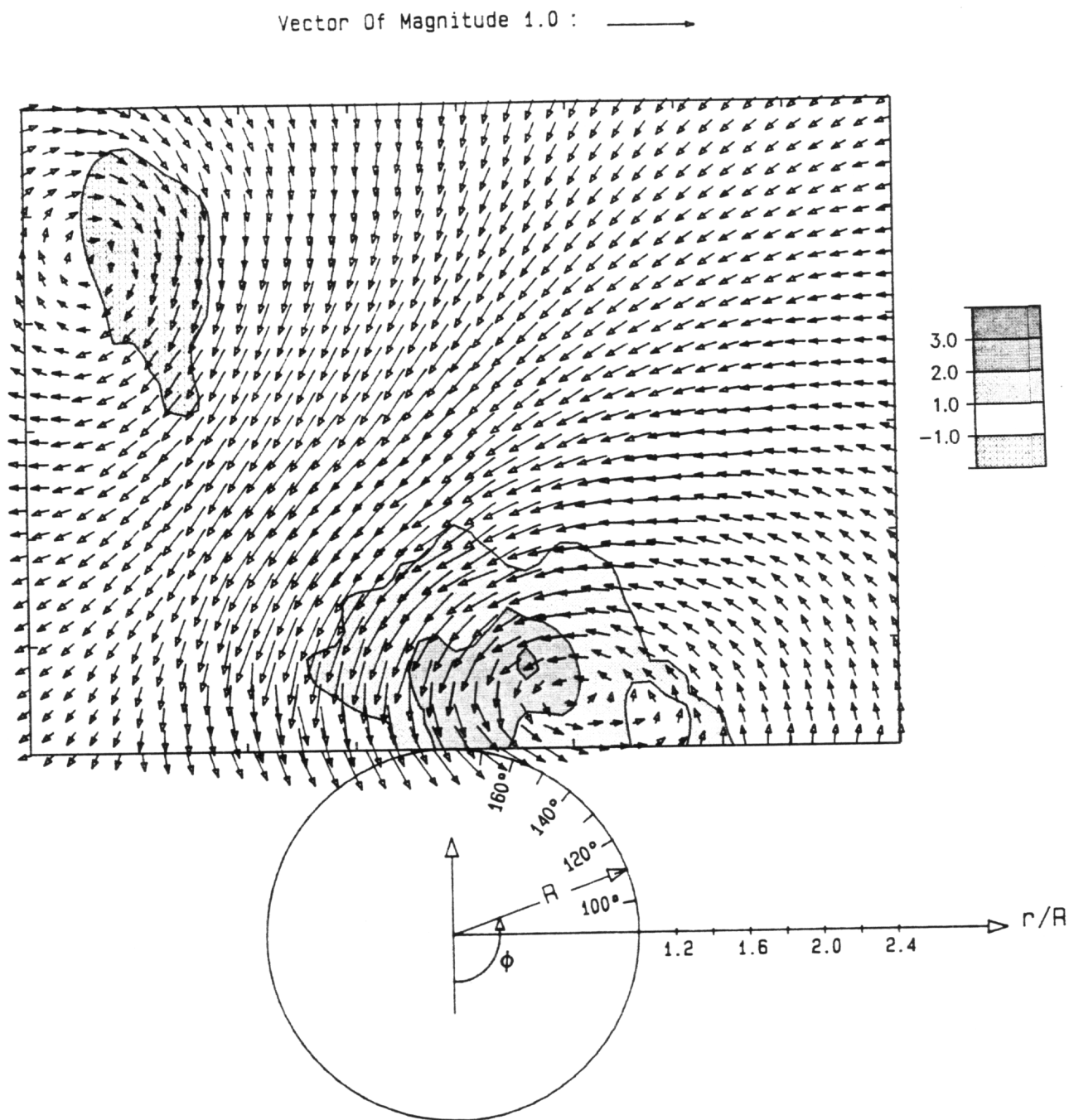


Figure 3.40. Velocity field and vorticity contours at $\alpha = 30^\circ$ and $Re = 27000$ with bead#1 at $\phi = 70^\circ$ and $x/R = 0.5$.

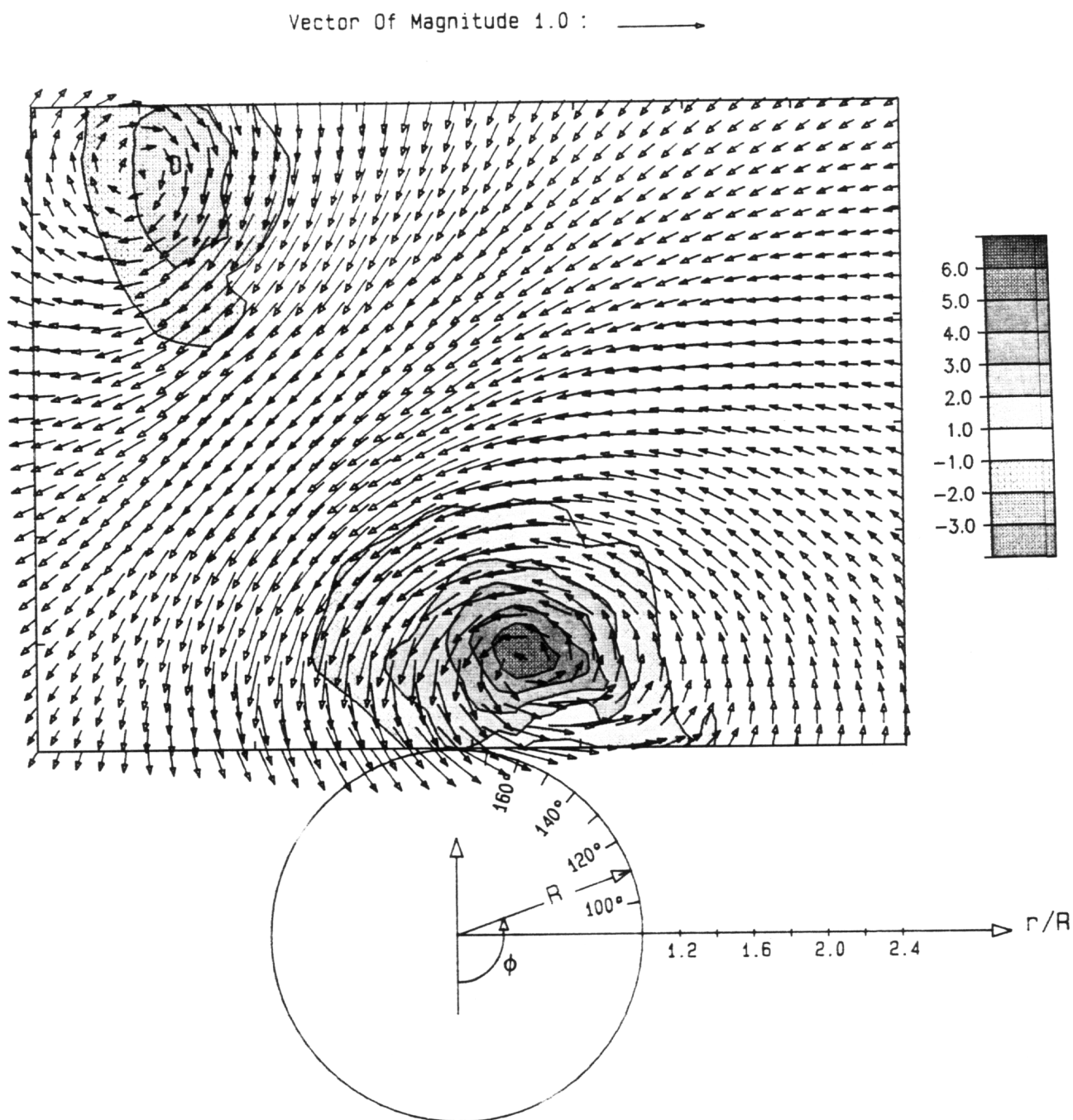


Figure 3.41. Velocity field and vorticity contours at $\alpha = 30^\circ$ and $Re = 27000$ with bead#1 at $\phi = 90^\circ$ and $x/R = 0.5$.

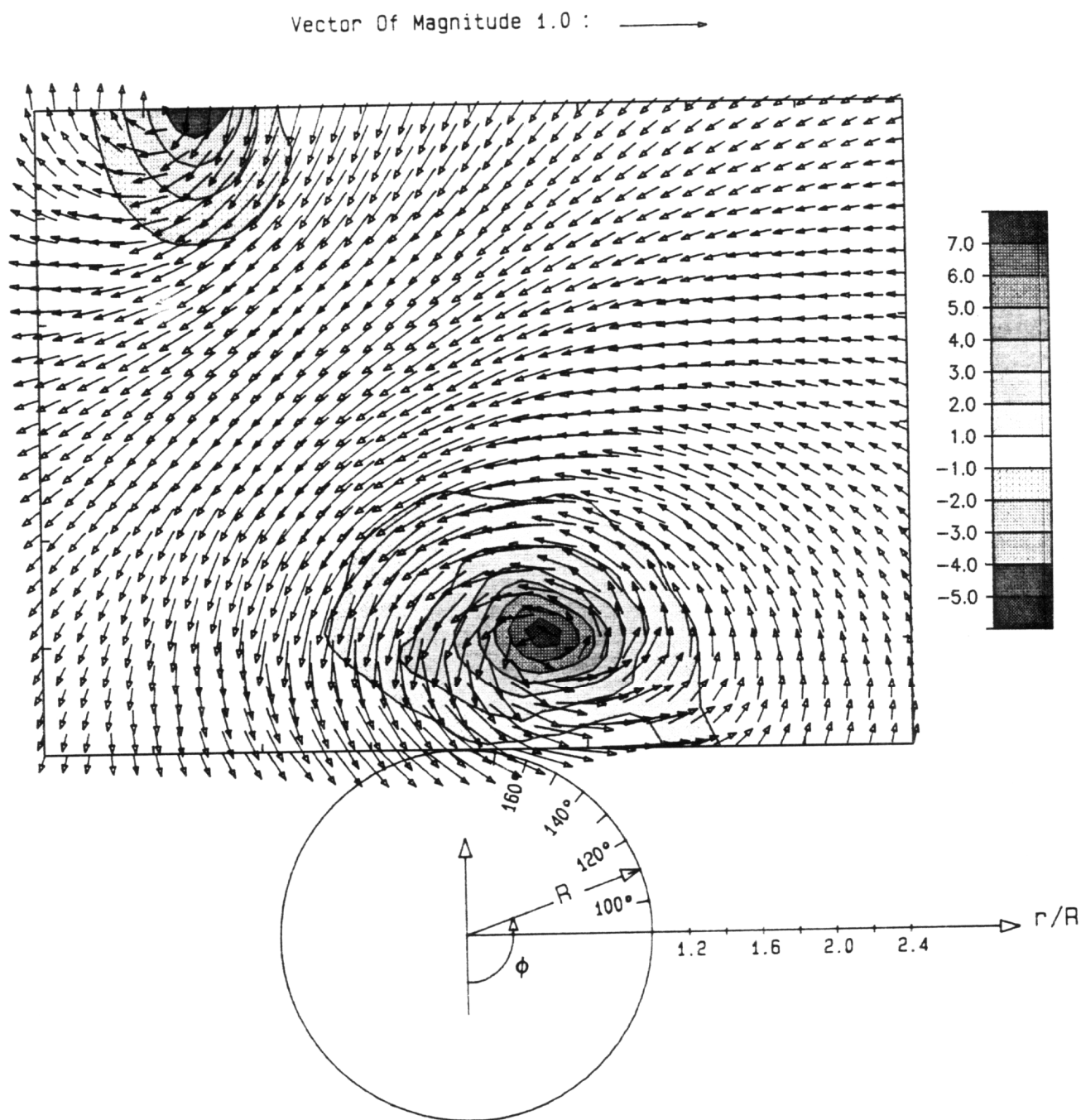


Figure 3.42. Velocity field and vorticity contours at $\alpha = 30^\circ$ and $Re = 27000$ with bead#1 at $\phi = 120^\circ$ and $x/R = 0.5$.

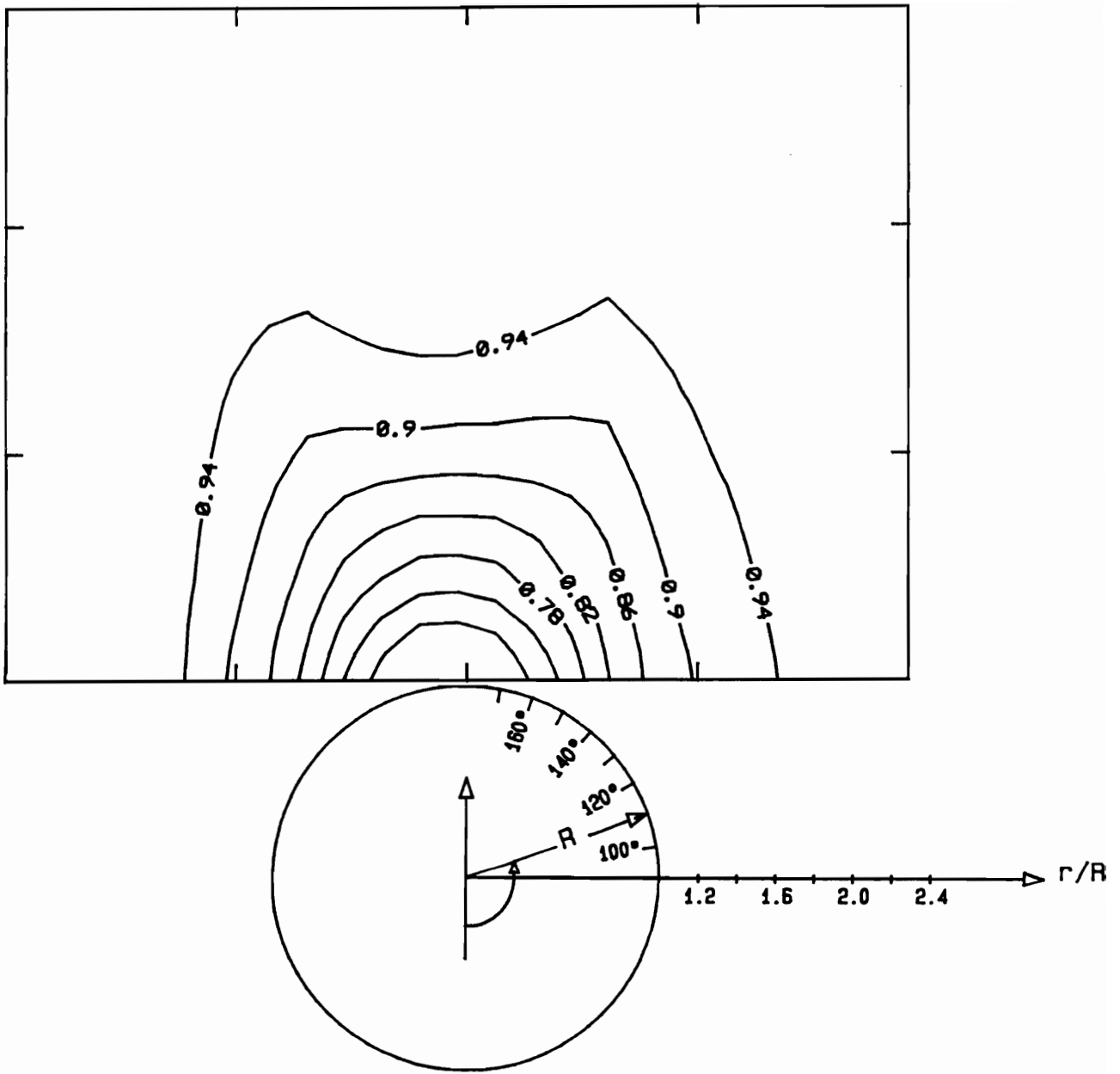


Figure 3.43. Axial velocity component contours at $\alpha = 30^\circ$ and $Re = 27000$ with bead#1 at $\phi = 120^\circ$ and $x/R = 0.5$.

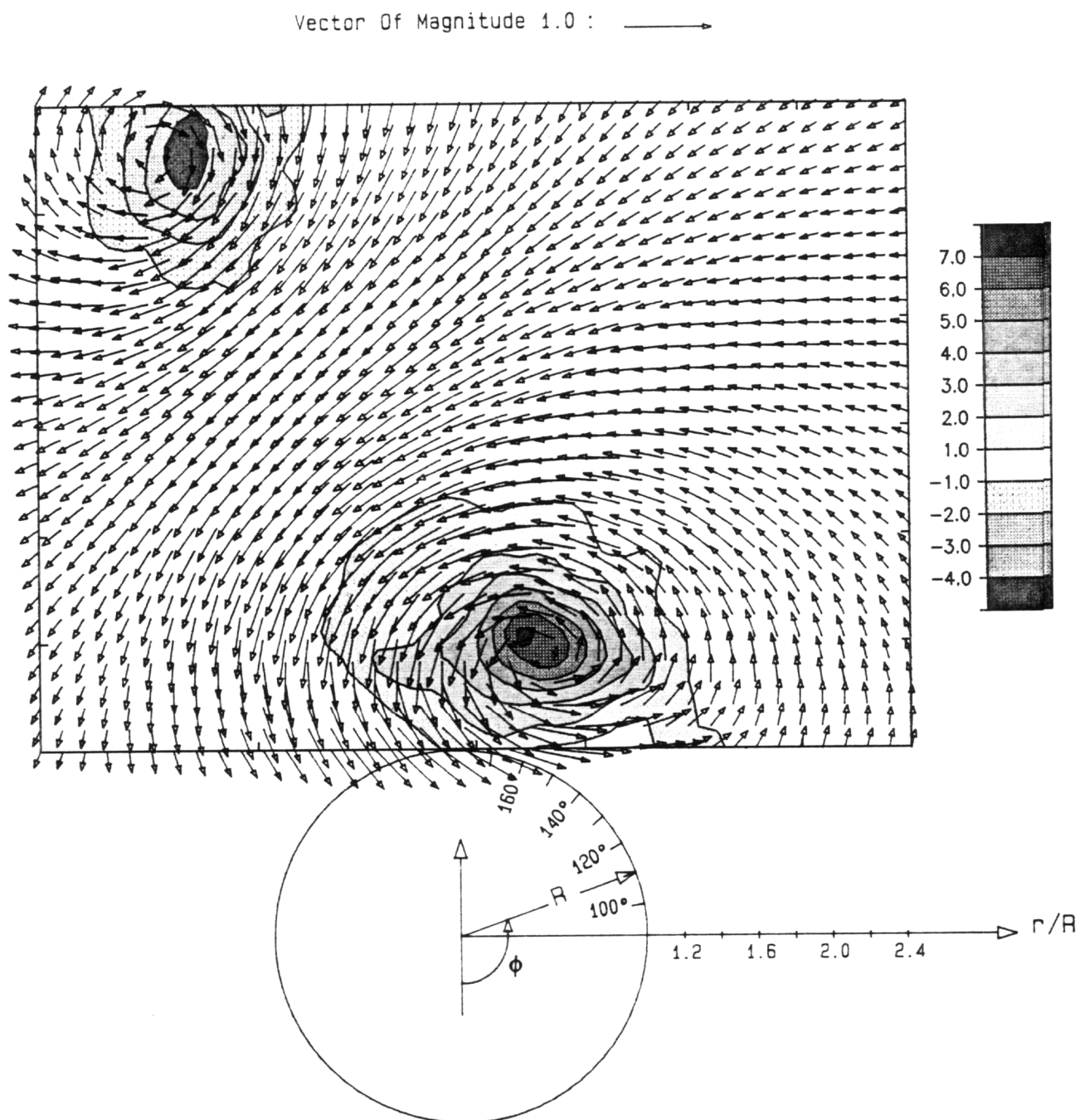


Figure 3.44. Velocity field and vorticity contours at $\alpha = 30^\circ$ and $Re = 27000$ with bead#1 at $\phi = 150^\circ$ and $x/R = 0.5$.

Bead#1 was moved to a location inside the separation bubble at $x/R = 1.8$ and $\phi = 120^\circ$. For this case, Figure 3.45 displays a lesser degree of asymmetry than the flowfield pattern when bead#1 was placed in front of the separation bubble and at the same azimuthal location, ϕ . Bead#1 was then mounted behind the separation bubble at $x/R = 2.5$ and $\phi = 120^\circ$. The flowfield assumes an almost symmetric orientation as shown in Figure 3.46. The asymmetric pattern switched side when bead#1 was placed at $x/R = 0.5$ and $\phi = 280^\circ$ (Figure 3.47). Velocity fields were measured with a smaller bead (bead#2) positioned at $x/R = 0.5$ and $\phi = 120^\circ$. Figure 3.48 again displays a lesser degree of asymmetric pattern than when a larger bead was placed at the same position.

Mechanisms that cause the flow over a slender body of revolution to become asymmetric are presently not well understood. It has been suggested that vortex asymmetry might be a result of an instability of the flow above the body or an asymmetric transition of the boundary-layer flow (Degani, 1991). Ericsson [1991] concluded that hydrodynamic instability can not be the cause of vortex asymmetry. The following discussion is an attempt by the author to explain the phenomenon of vortex asymmetry over bodies of revolution with different nose configurations. For a sharp-nosed axisymmetric body such as an ogive or a cone-cylinder at low angles of attack, vortex sheets roll up along the lines of primary and secondary separation to form leeward vortices. Although the separation lines originate at the apex of the model, the leeward vortices begin to appear downstream away from the nose (Figure 3.49a). Thus, each vortex forms independently of the other. They do not interact until much further downstream along the surface of the model. In addition, since the vortices do not form at the nose, there exists a gap between them. This allows the flow over the nose of the model to enter the space between the vortices causing a blockage and further preventing their interaction. The result is a symmetrical flow pattern. As the angle of attack in-

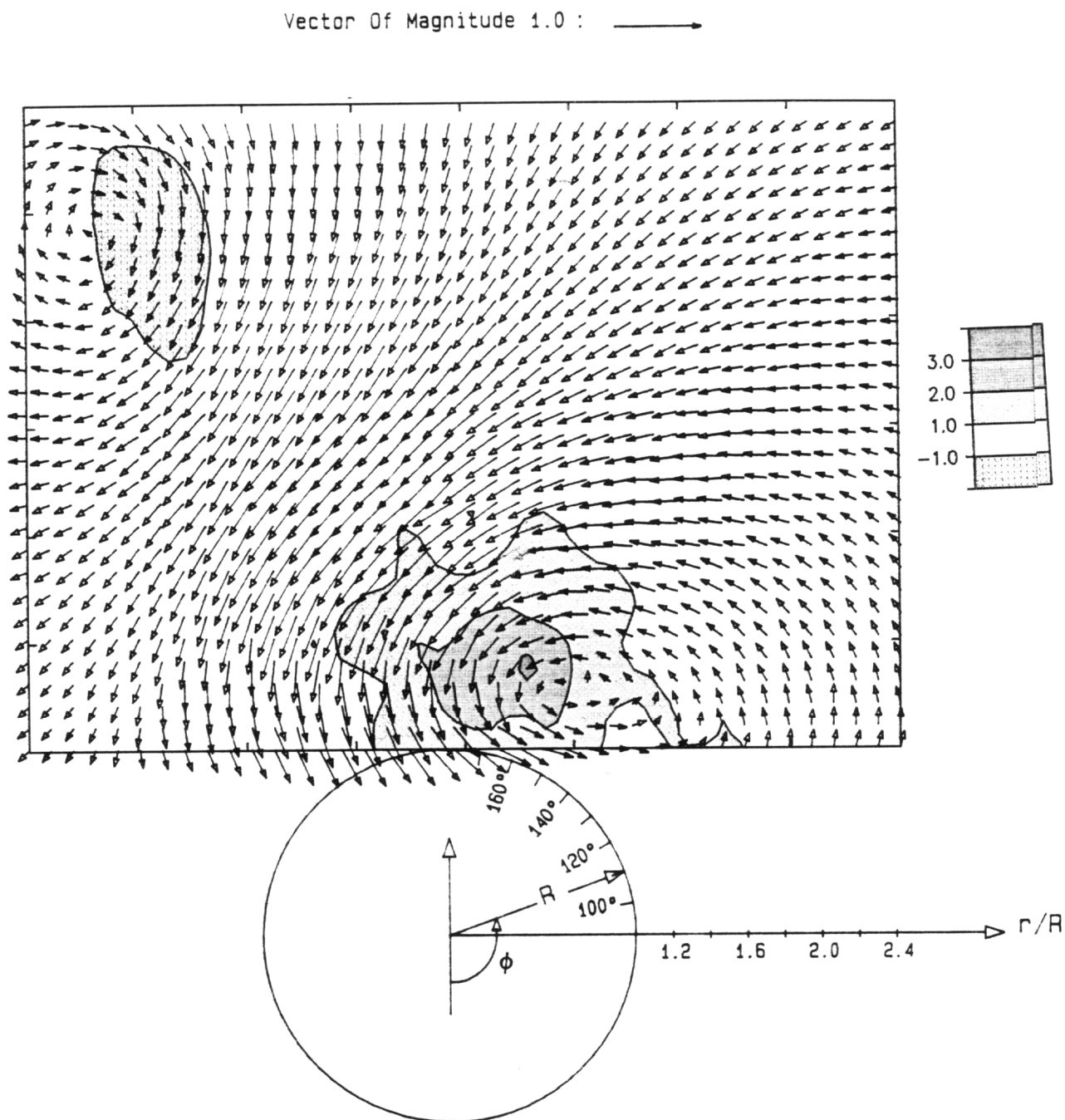


Figure 3.45. Velocity field and vorticity contours at $\alpha = 30^\circ$ and $Re = 27000$ with bead#1 at $\phi = 120^\circ$ and $x/R = 1.8$.

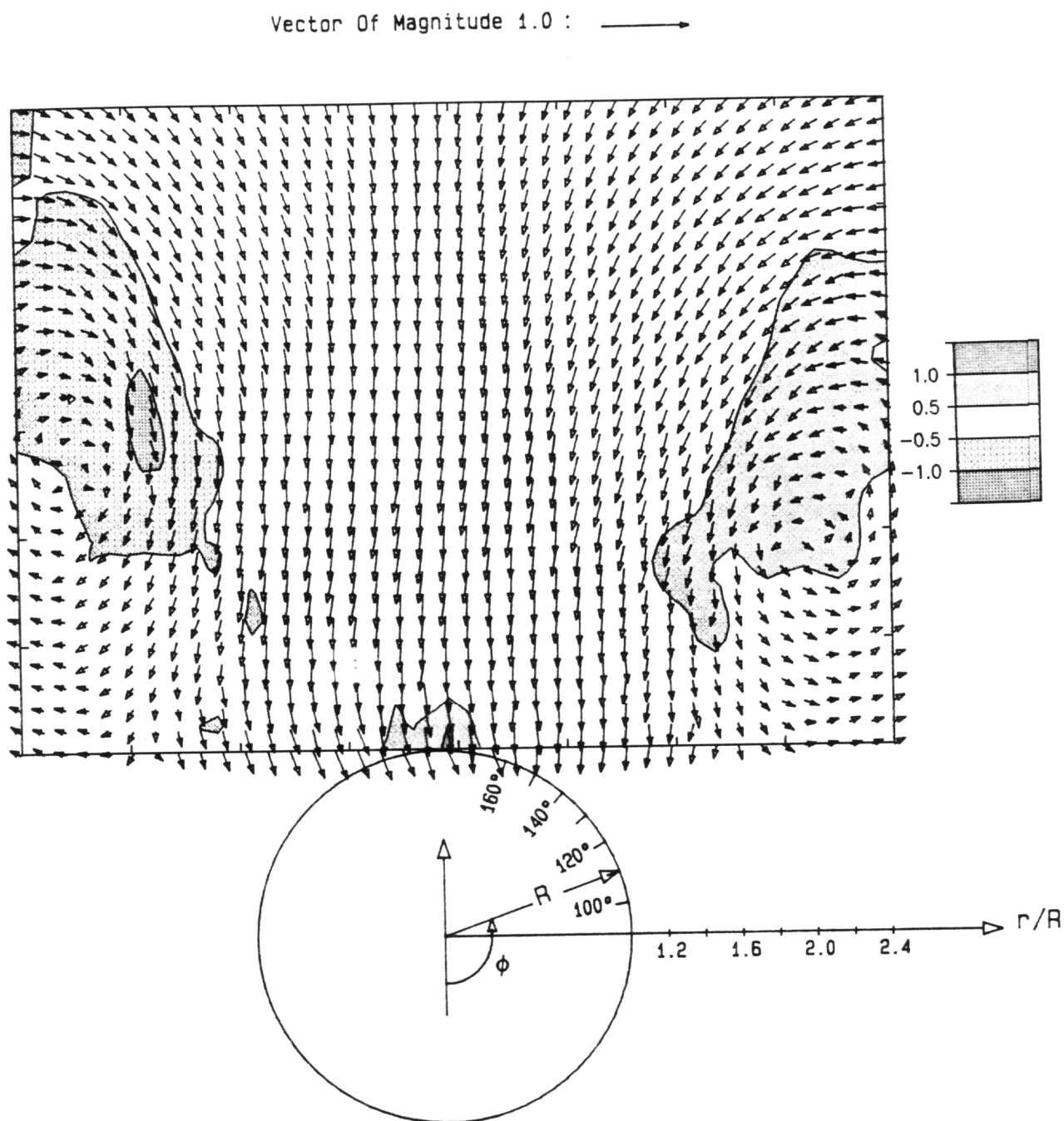


Figure 3.46. Velocity field and vorticity contours at $\alpha = 30^\circ$ and $Re = 27000$ with bead#1 at $\phi = 120^\circ$ and $x/R = 2.5$.

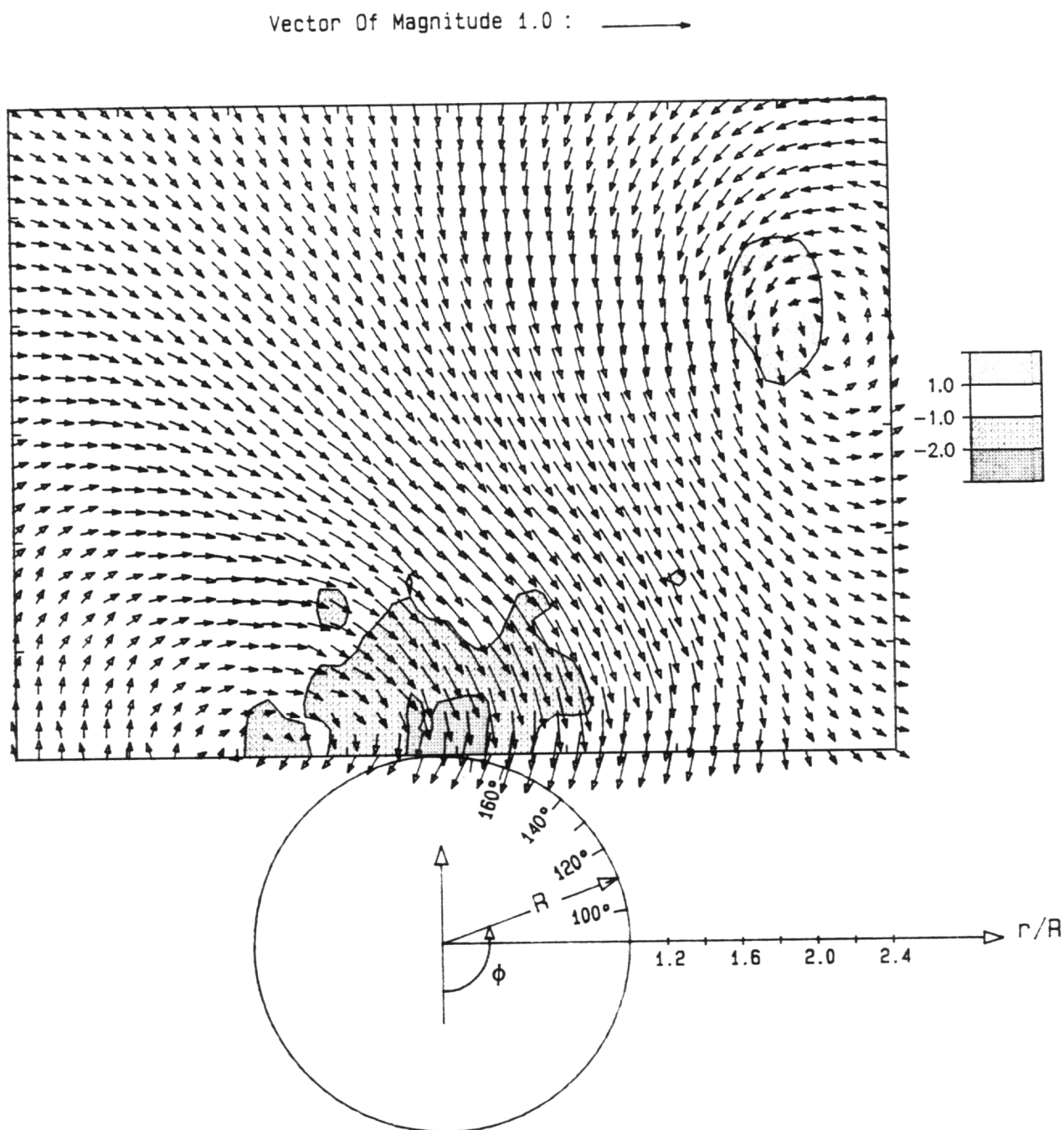


Figure 3.47. Velocity field and vorticity contours at $\alpha = 30^\circ$ and $Re = 27000$ with bead#1 at $\phi = 280^\circ$ and $x/R = 0.5$.

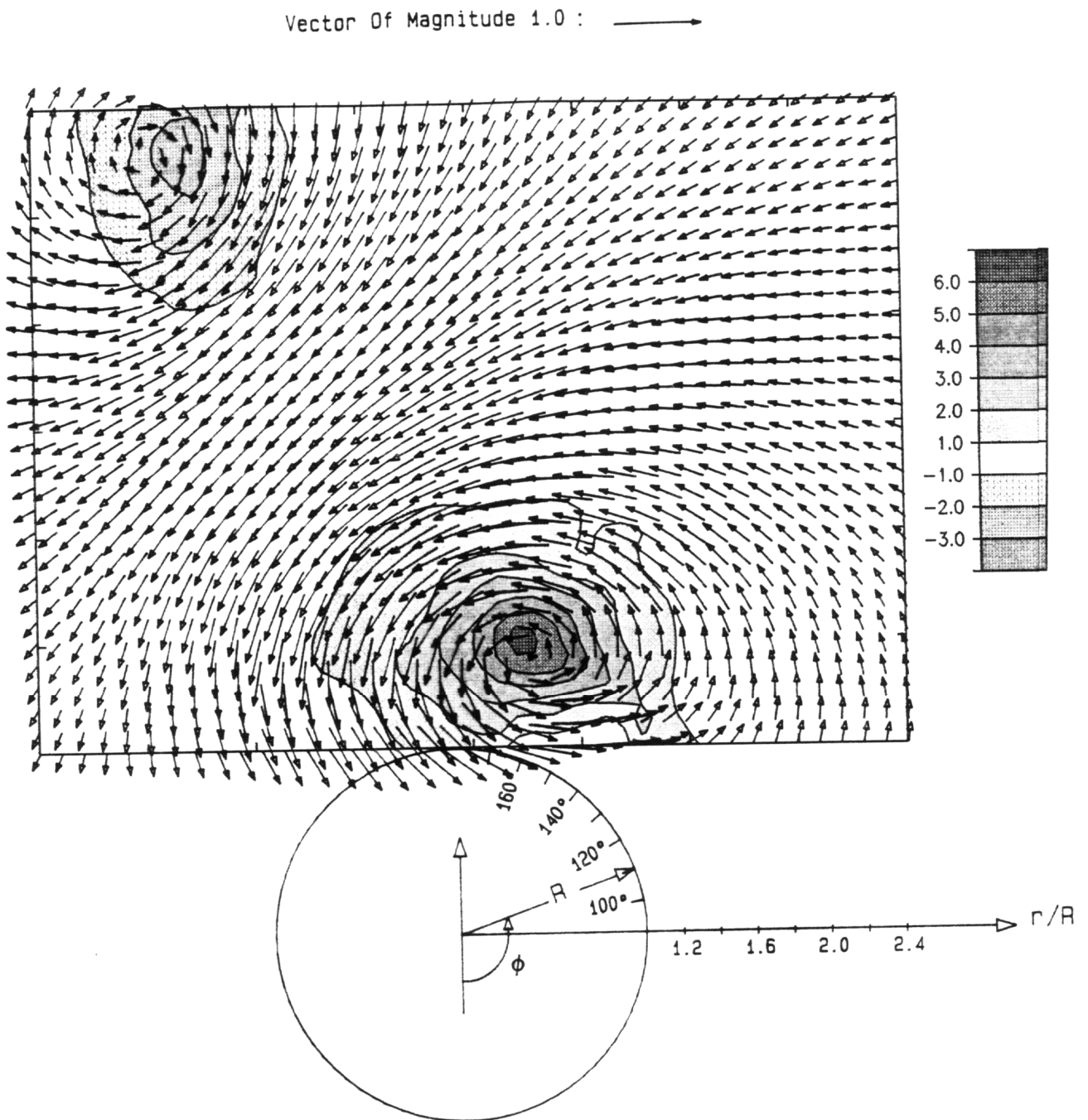
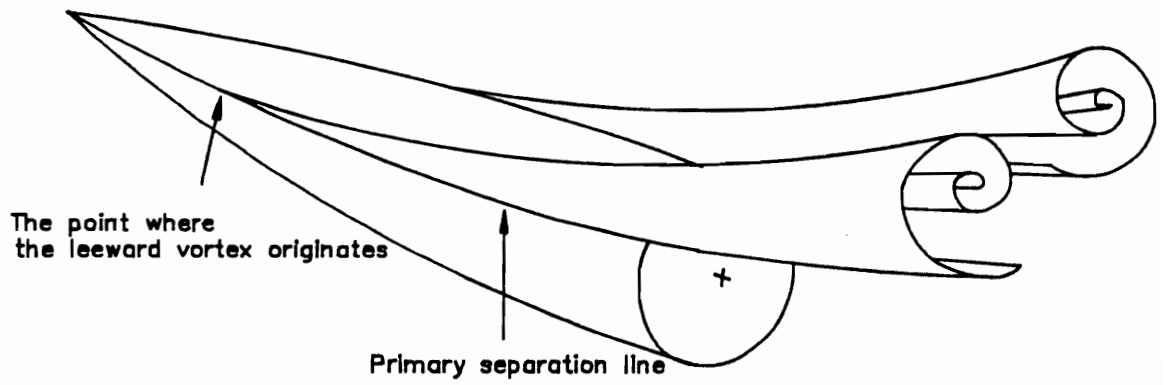
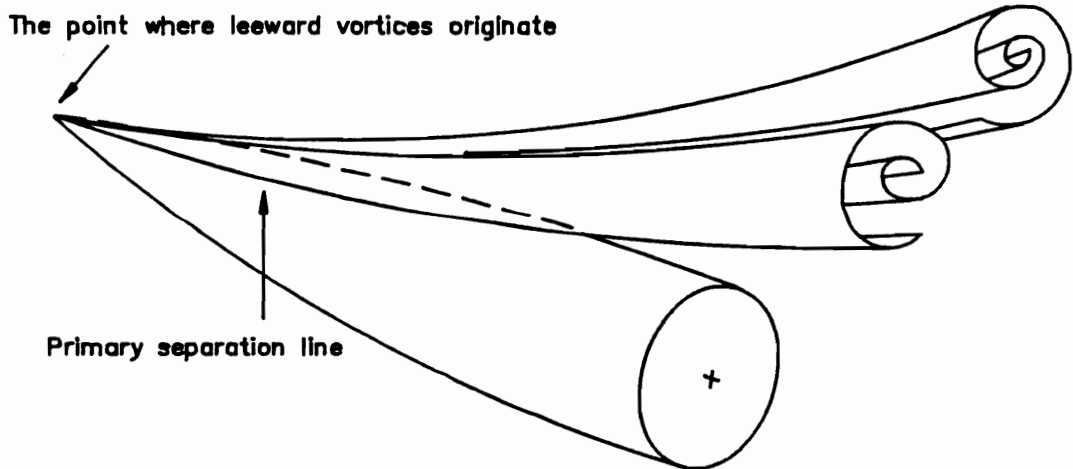


Figure 3.48. Velocity field and vorticity contours at $\alpha = 30^\circ$ and $Re = 27000$ with bead#2 at $\phi = 120^\circ$ and $x/R = 0.5$.



(a) Low incidence



(b) High incidence

Figure 3.49. Flow patterns over a sharp-nosed ogive cylinder at (a) low incidence (b) moderate incidence.

creases, the axial vortices progressively form closer to the nose and the gap between the vortices becomes smaller depending on the nose fineness ratio. Eventually, at some moderate angle of attack, the vortices will appear at the apex inhibiting the flow from entering the space between them (Figure 3.49b). The level of interaction between leeward vortices increases dramatically. Moreover, the formation of the vortices depends on each other since they originate at the same point. Any disturbance can cause one vortex to separate sooner than the other, thus triggering an asymmetric flow pattern. The cross-section of the vortex is very small near the nose; therefore, microscopic particles or machined imperfections can have devastating effects on the symmetry of the flow pattern.

Models with sharp edges, such as the chined body studied by Roos and Kegelman, always produce a pair of symmetrical axial vortices. With these types of configurations, the flow is forced to separate along the sharp edges regardless of the level of interaction between the vortices. The symmetric flow pattern is dictated by the symmetrical shape of the body. A single strake mounted along the leeward meridian of a pointed-nosed model hinders flow asymmetry because it prevents the interaction between the vortices; similar to the flow entering from the tip of the model. It is rather crucial to prohibit the vortices to interact at the point of formation, i.e. at the apex. Therefore, a short strake is as effective in preserving vortex symmetry as a long strake. A fixed pair of strakes attached symmetrically to the nose tip of the model can force vortex symmetry by displacing the origin of the leeward vortices further away from the nose.

For a blunt-nosed configuration such as a hemisphere-cylinder, our experimental results indicate that the flow does not exhibit any natural asymmetry behavior. The vortex pattern remains symmetrical up to an angle of attack when vortex shedding begins (see Chapter 5). The following reasons are given as an explanation of why the flow pattern over the leeside of the hemisphere-cylinder is always symmetric. At moderate

angles of attack, strong crossflow causes the boundary-layer to separate. This eventually gives birth to a pair longitudinal vortices (leeward vortices). Similar to the sharp-nosed body of revolution at low angles of attack, each vortex originates independently and does not communicate with the other (Figure 3.2e). In addition, the fluid over the hemispherical cap of the model also enters a large gap between the vortices. Thus, the leeward vortices do not interact and a symmetric flow pattern is always observed.

Many researchers have shown that small discrete disturbances mounted near the nose of a pointed-nosed body of revolution can cause the flow to assume an asymmetric orientation. Similar results had also been shown for a hemisphere-cylinder model. At an angle of attack, the flow over a hemisphere-cylinder stagnates near the nose of the model. As the fluid accelerates over the top of the hemispherical cap, it separates to form a bubble. The flow proceeds downstream by going over the bubble. When a discrete disturbance is placed anywhere in front of the separation bubble, the flow in the wake of the disturbance becomes turbulent. Thus, a small region of the flow behind the disturbance remains attached or part of the separation bubble vanishes as shown in Figure 3.50. This allows the fluid to enter the leeside of the model without an obstacle (the separation bubble) and causing the lines of separation on the side of the bead to separate sooner. The result is an imbalance in vortex formation and the flow becomes asymmetric. The separation bubble is not affected if the disturbance is mounted on the windside or behind the bubble, thus the flow assumes a symmetrical orientation. Discrete disturbance is most effective when placed in front of the bubble and in the vicinity of the core of the vortex, i.e. $\phi = 120^\circ$. The level of asymmetry is proportional to the size of the disturbance since large disturbances generate more turbulence than smaller ones and, therefore, washing away a bigger part of the separation bubble.

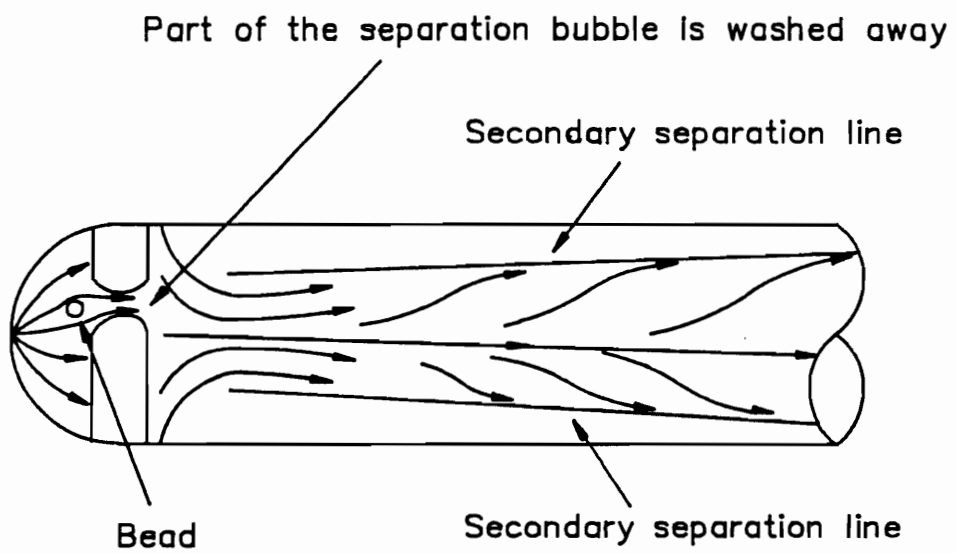


Figure 3.50. Skin-friction patterns over a hemisphere-cylinder with a bead mounted near the nose (leeward view).

Chapter 4: High-Reynolds Number Measurements

4.1 Introduction

Traditionally, both experimental and theoretical methods have been used to help understand the characteristics of fluid flows. With the advent of the digital computer, numerical methods have become available and have opened new horizons in fluid mechanics. In fact, in many areas, numerical analysts have pushed the frontiers ahead, overtaking the experimentalists. As a result, experimental data are often not available for code validation. It should be recognized that experimental methods continue to be important, especially when the flows involved are very complex, such as three-dimensional separation or turbulent flow.

Many practical engineering flows are at high Reynolds numbers. However, to fully understand the behavior of the flow over a certain model, research effort must be carried out for a wide range of Reynolds numbers. In this chapter, flow over a hemisphere-cylinder at high Reynolds numbers and low Mach numbers is documented experimentally. The main focus of this chapter is the vortical structure which develops in the

wake of the model and the separation bubble at $\alpha = 0^\circ, 10^\circ, 20^\circ$ and 30° for Reynolds numbers from 2.9×10^5 to 1.06×10^6 . To provide a complete picture of the flow, several experimental devices were employed. The velocity fields were obtained by a seven-hole probe and a fiber-optic LDV probe. Careful comparisons were made of the results obtained with these two instruments. Surface skin-friction lines and their respective digitized photographs and static pressure data were also provided.

As mentioned in Chapter 3, investigators working with the hemisphere-cylinder were more interested in the flows at the transonic or the low supersonic regimes. Meade and Schiff [1987] offered detailed experimental surface pressure coefficient measurements for a hemisphere-cylinder-flare at a Reynolds number of 3.0×10^6 per foot, a Mach number of 1.2 and angles of attack from 0° to 27.5° . At each incidence, the model was rolled in 3° increments about its own axis of symmetry yielding a total of 50,520 data points. At $\alpha = 19^\circ$, a finer roll increment was used, resulting in 101,040 data points. This represents the most comprehensive surface pressure distribution ever obtained per incidence. The pressure data at each angle of attack were smoothed and checked against oil-flow visualizations. These confirmed the topology rules of three-dimensional separation postulated by Tobak [1987]. Tobak related each of the singular points observed in the surface oil-flow to a local extremum in the surface pressure distribution.

A short discussion on the experimental work done by Hsieh [1975, 1976, 1977] including surface oil-flow visualizations and surface pressure measurements in the Mach numbers range from 0.6 to 1.5 can be found in Chapter 3. Hsieh [1977] confirmed the existence of the separation bubble on the nose of a hemisphere-cylinder using LDV data. However, he showed that LDV measurements inside the separation bubble were not reliable. Seeding particles did not follow the flow inside the bubble and a large number of the particles penetrated through the separated region due to inertia.

Hsieh [1975] conducted a computational study on the hemisphere-cylinder at zero incidence and Mach number from $M_\infty = 0.7$ to 2.0 using inviscid theory. The pressure distribution results showed satisfactory agreement with experimental data for Mach number between 1.05 to 2.0. However, there were large discrepancies for $0.7 \leq M_\infty \leq 1.0$. The errors were attributed to the existence of the nose separation in this Mach number range. Hsieh [1981] used the three-dimensional unsteady Navier-Stokes equations with "thin-layer" approximation to solve flow over the same model at 19° angle of attack. Most features of the three-dimensional separation and in particular the formation of the concentrated vortices were captured. Ying et al. [1986, 1987] employed an algorithm featuring two implicit factors and partial flux splitting to solve the thin-layer Navier-Stokes equations in the conservative form. The computed results showed good qualitative and quantitative agreement with experimental data at angles of attack ranging from 0° to 19° in the transonic and low supersonic regimes ($0.9 \leq M_\infty \leq 1.2$).

4.2 Experimental Setup

Experiments were conducted in the 6' x 6' VPI Stability Wind Tunnel. A hemisphere-cylinder was machined out of aluminum in three separate pieces; two cylindrical afterbody sections and a hemispherical nose (Figure 4.1a). The latter was given by the Fluids Dynamic Branch of NASA-Langley. The model was hollow to provide space for instrumentation. Two 0.9-inch slots were cut along the afterbody portion to allow the laser beams to be shined from the inside of the model. The slots were fitted with windows of different material including plexiglass and glass. However, it was discovered that high quality acrylic was best suited for the reduction of flare. The model was equipped for measuring static pressure, dynamic pressure and velocity. It was also

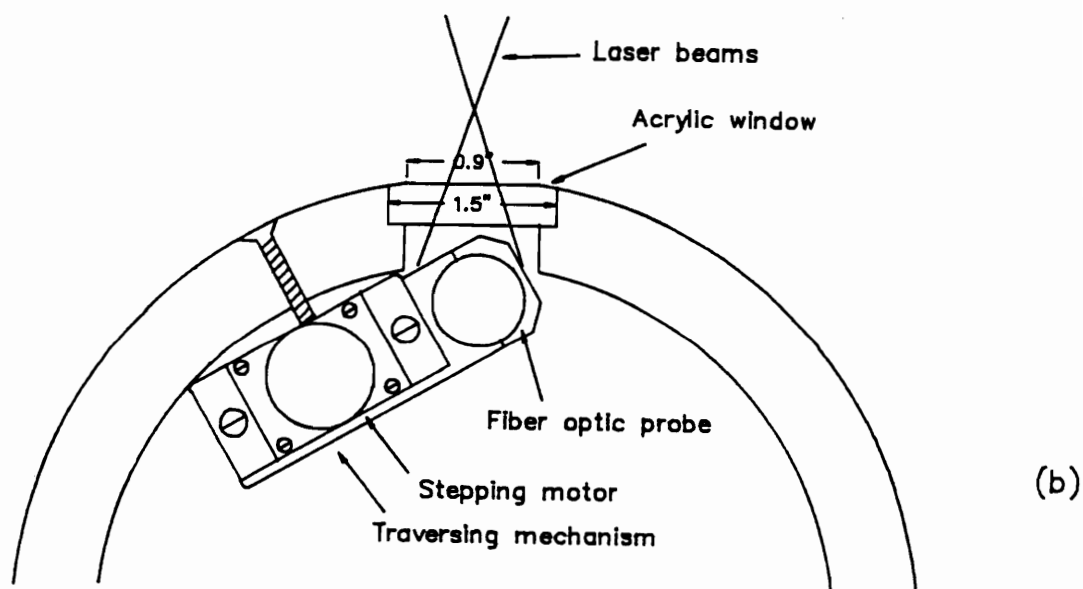
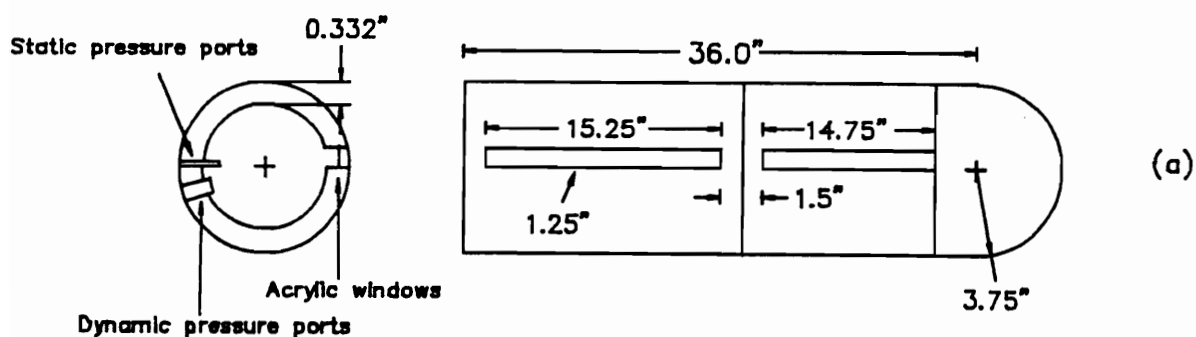


Figure 4.1. (a) The hemisphere-cylinder model showing windows for LDV measurements (b) cross-section of the traversing mechanism shown inside the model.

possible to visualize the surface flow. In this research effort, only dynamic pressure measurements were not conducted.

Static pressure was measured by standard pressure taps connected to a pressure scanner. The model had 94 pressure orifices, each 1/16 inches in diameter, along the x-direction at a constant ϕ . The system of coordinates employed in this chapter is the same as Figure 3.4a. Similar to the smaller model described in Chapter 3, the orifices were spaced finer near the nose than the afterbody cylinder to capture reliable measurements across the separation bubble. The model was manually rolled from $\phi = 0^\circ$ to 180° in 20° increments about its axis of symmetry to measure pressure at various cross-sectional stations.

For axisymmetric configurations, laser-Doppler velocimeters with beams directed through wind tunnel windows are inconvenient. For such configurations, difficulties are encountered in accessing all the regions of interest. More importantly, it is hard to position the measuring volume accurately with respect to the model. These problems can be solved by directing the beams from inside the model. This can be accomplished today with a fiber-optic LDV probe, in which the sending and receiving optics are packaged by TSI Inc. in a small cylinder of 1-inch diameter and 5 inches in length. The probe was mounted inside the model on a linear traversing table. The beams were directed through the windows, perpendicular to the surface of the model as shown in Figure 4.1b. Rotation of the entire model facilitated positioning along a parallel circle of a polar coordinate system. To traverse the measuring volume in the x-direction, the table could be placed at different locations inside the model. Finally, to traverse in the direction normal to the model, a traversing system was constructed as shown schematically in Figure 4.2. Mirrors were used to turn the beams normal to the model wall. A CXT 29-35 Compumotor stepping motor was employed in two optional configurations. In one option, the LDV probe was displaced while the mirror was kept fixed, thus facilitating

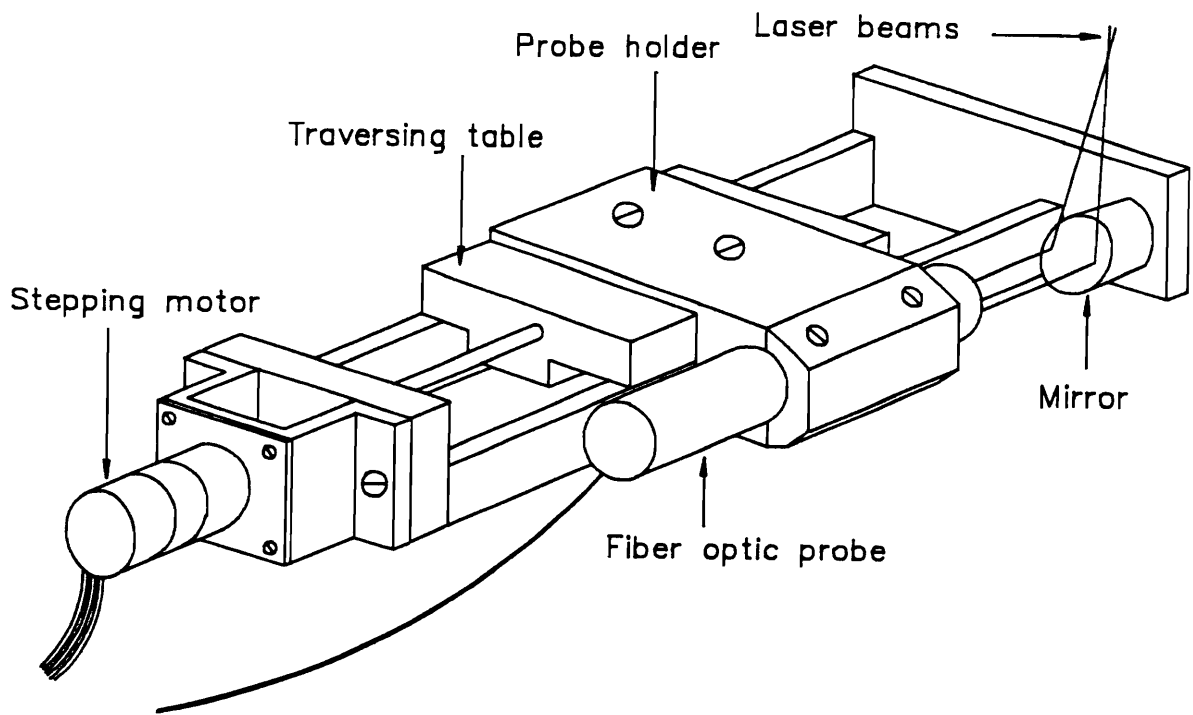


Figure 4.2. The traversing mechanism.

displacement of the measuring volume in a direction normal to the axis of the model. In the second option, probe and mirror were displaced together. This allowed the measuring volume to be traversed along a direction parallel to the axis of the model.

The setup for the seven-hole probe velocity measurements is shown in Figure 4.3. A traversing table was mounted on a sting support behind the model. Unlike the LDV setup, rotation of the entire traversing mechanism instead of the model facilitated positioning along a parallel circle of a polar coordinate system. To traverse along the x-direction, the traversing mechanism could be placed at different locations along the mounting sting. A stepping motor was employed to displace the seven-hole probe in the direction normal to the model.

4.3 Experimental Conditions

Skin-friction line visualizations were conducted in the VPI Stability Tunnel at two different free-stream velocities, $U_\infty = 74$ ft/sec and 108 ft/sec, and angles of attack $\alpha = 0^\circ$, 20° and 30° . The corresponding Reynolds numbers were 2.9×10^5 and 4.2×10^5 , respectively. Photographs were taken at $\phi = 90^\circ$ (side view) and 180° (leeward view), since the wind tunnel can only be accessed from these two directions. Side views of the flow visualization photographs were digitized for $\alpha = 20^\circ$ and 30° . When photographs were taken at $\phi = 180^\circ$, the camera had to be moved around to avoid scratches on the top plexiglass-window of the wind tunnel. Thus, the "true" leeward view is not shown. For this reason, the leeward view of the flow visualization photographs were not digitized.

Static pressure coefficients on the surface of the hemisphere-cylinder were obtained at $\alpha = 0^\circ$, 10° , 20° and 30° for $Re = 2.9 \times 10^5$ and 4.2×10^5 along the x-axis from $\phi =$

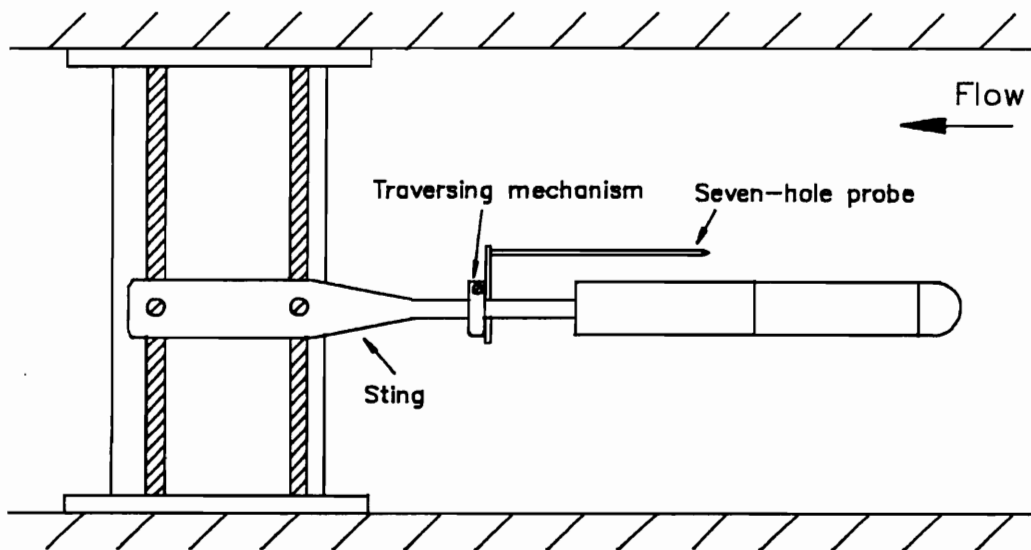


Figure 4.3. The seven-hole probe experimental setup.

0° to 180° in 20° increments. For $\alpha = 0^\circ, 10^\circ$ and 20° , pressure data were also taken along the x-axis at $\phi = 180^\circ$ and at five different Reynolds numbers. For the same reasons stated in Chapter 3, pressure data presented in this chapter represent only half of the model's surface. The tunnel wall pressure distributions were also measured, with the model placed at various incidences, to investigate the effect of the wind tunnel walls on the model.

The velocity field over the hemisphere-cylinder model was documented via seven-hole and LDV measurements at six different cross-sectional stations, $x/R = 5.8, 6.1, 8.1, 8.4, 9.7$ and 10.0 , and two angles of attack, $\alpha = 20^\circ$ and 30° . The experiments were carried out at a free-stream velocity of 37 ft/sec and the corresponding Reynolds number was 1.5×10^5 . The fiber-optic LDV system allows the simultaneous measurement of only two velocity components; whereas, three velocity components can be obtained with the seven-hole probe.

4.4 Results and Discussion

Flow Visualization and Digitization

At zero degree angle of attack and $Re = 2.9 \times 10^5$, a laminar separation bubble is developed near the juncture of the hemisphere and the cylinder, similar to the flow pattern at low Reynolds numbers (Chapter 3). This bubble is closed and forms two rings around the body - a separation ring at $x/R = 1.55$ and a reattachment ring at $x/R = 1.70$. The length of the separation bubble in the axial direction is much smaller here than at low Reynolds number flows. Figure 4.4 displays surface flow visualization at $\alpha = 0^\circ$ using titanium dioxide mixture. The separation bubble was also detected by

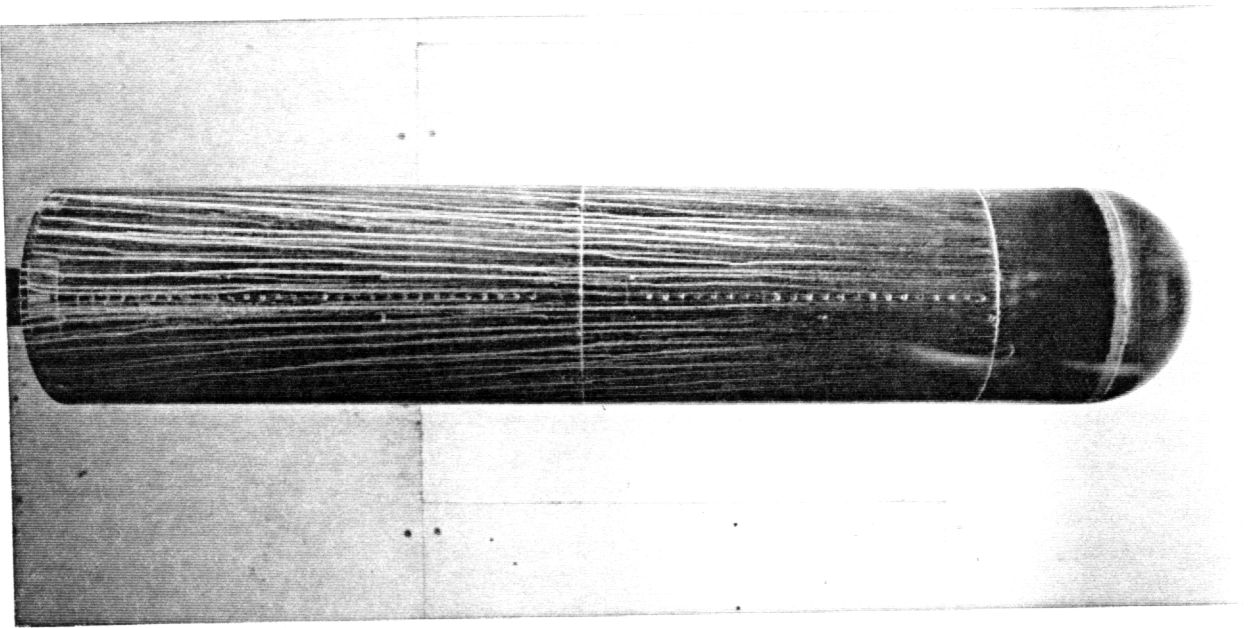
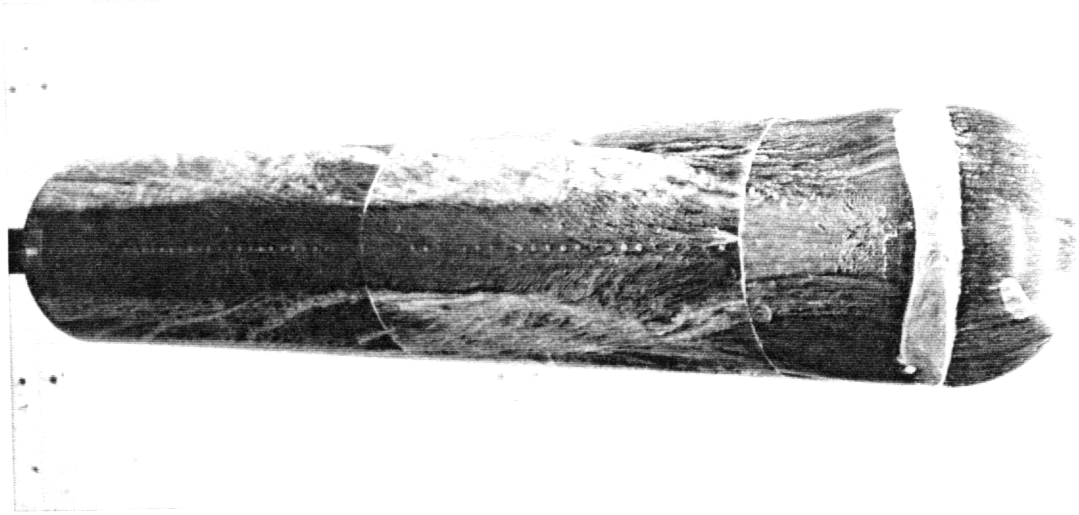


Figure 4.4. Surface flow visualization at $\alpha = 0^\circ$ and $Re = 2.9 \times 10^5$.

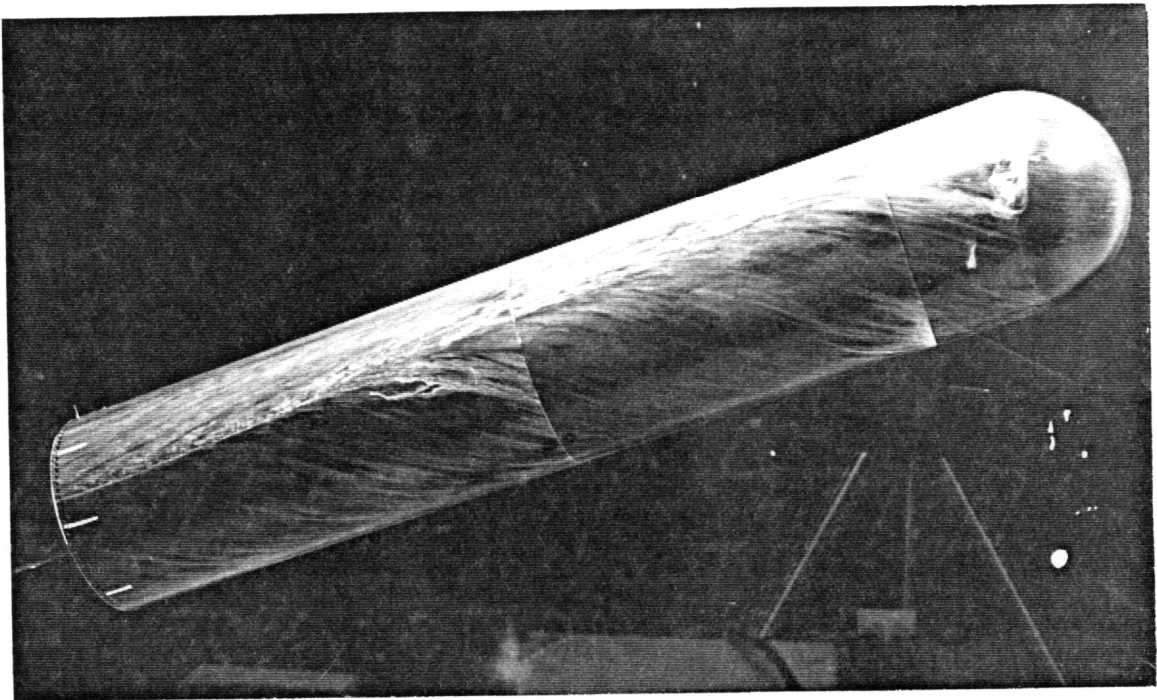
liquid-crystal tests, designed for skin-friction measurements. Although not shown here due to poor quality of the photographs, liquid-crystal solution visualizations indicate a region of very low skin-friction magnitude across the separation bubble.

Figures 4.5a and 4.5b show two different views $\phi = 180^\circ$ and 90° , respectively, of the hemisphere-cylinder at 20° incidence and $Re = 2.9 \times 10^5$. The separation bubble disappears on the windside and is confined to the leeside of the model at $x/R = 1.5$ and from $\phi = -90^\circ$ to 90° . The length of the bubble remains nearly constant in the circumferential direction. The existence of the horn vortices cannot be confirmed with certainty based on these flow visualization photographs. However, during the experiment, there seemed to be a heavy amount of titanium dioxide mixture swirling around the region of $\phi = 90^\circ$ and $x/R = 1.5$. While photographs were taken during the experiment, the wind tunnel had to be kept on to prevent flow visualization mixture accumulation near the nose from running. Thus, it appears that two very weak horn vortices do exist at this Reynolds number. The reader is reminded here that at the same angle of attack, $\alpha = 20^\circ$, and low Reynolds number, the horn vortices seem to reach their maximum size and strength.

Further downstream, the flow develops an open separation region. This can be best detected by digital skin-friction lines displayed in Figure 4.6. In this figure, the distance ℓ is measured along the model's axis of revolution and $\ell = 0$ is at the tip of the model. A primary separation line appears, from $\phi = 130^\circ$, $\ell/R = 3$ to $\phi = 100^\circ$, $\ell/R = 10$, as an envelop of skin-friction lines. The secondary separation line stretches along the cylindrical afterbody from $\phi = 165^\circ$, $\ell/R = 5$ to $\phi = 150^\circ$, $\ell/R = 10$. Two free shear-layers emanate along primary and secondary separation lines to form two vortex sheets. These shear-layers interact with each other and roll into a large scale vortex to fill up the wake. The same phenomenon also occurs on the other half of the model. The skin-friction lines do not exhibit any features of vortex asymmetry.

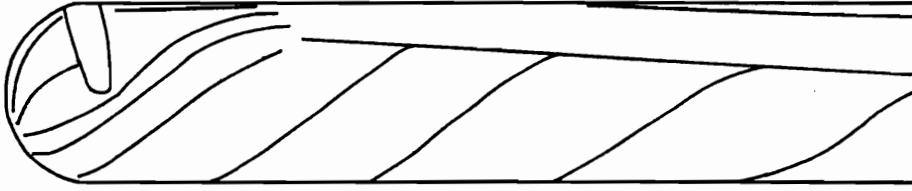


(a)

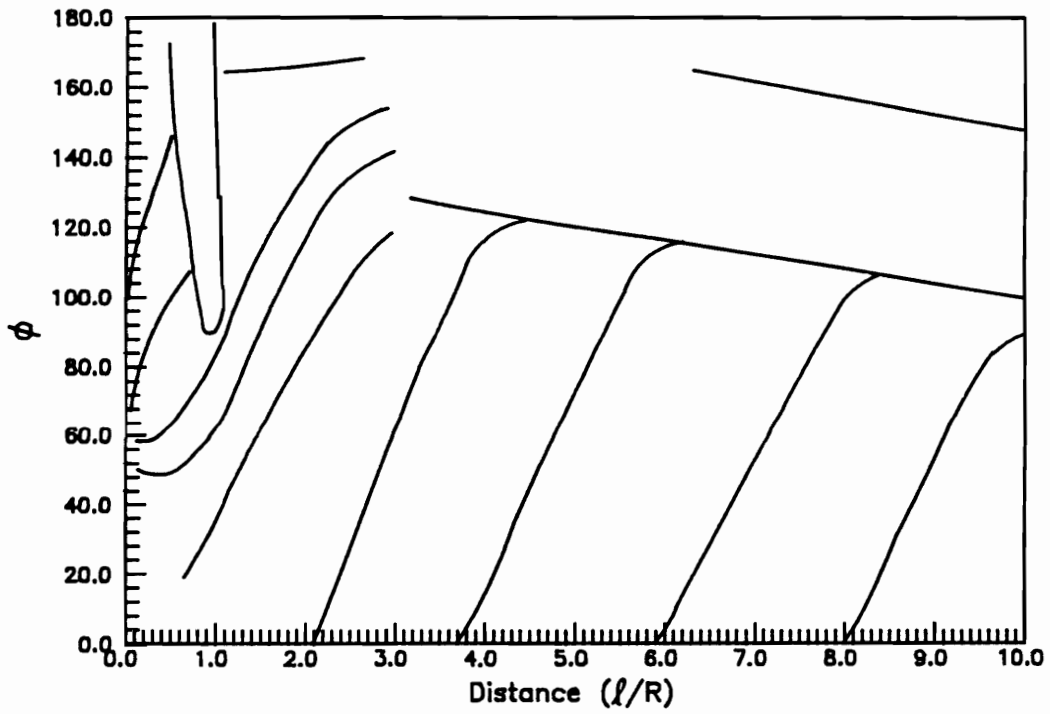


(b)

Figure 4.5. Surface flow visualization at $\alpha = 20^\circ$ and $Re = 2.9 \times 10^5$ (a) $\phi = 180^\circ$
(b) $\phi = 90^\circ$.



(a)

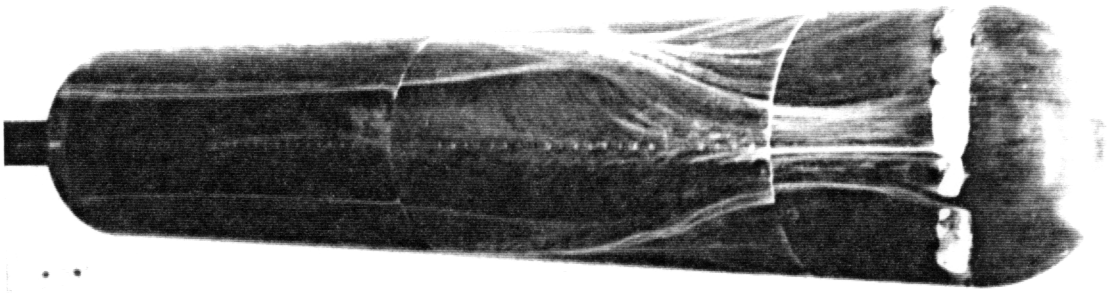


(b)

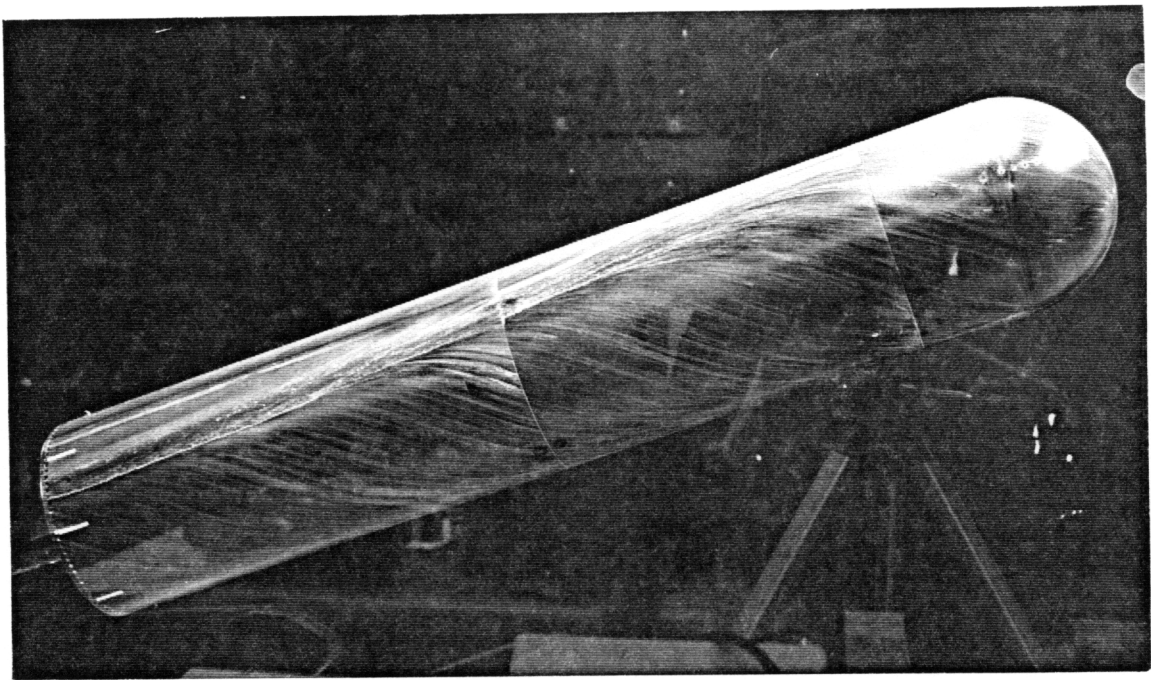
Figure 4.6. Side view of digitized skin-friction lines for $\alpha = 20^\circ$ and $Re = 2.9 \times 10^5$
(a) actual view (b) unwrapped view.

Figure 4.7 displays the flow visualization photographs of a hemisphere-cylinder at $\alpha = 20^\circ$ and $Re = 4.2 \times 10^5$. The skin-friction line patterns again indicate an open-type separation. The separation bubble becomes smaller both circumferentially and axially. Horn vortices are not detected in these pictures. The primary separation line remains nearly at the same location as the previous case ($Re = 2.9 \times 10^5$ and $\alpha = 20^\circ$). However, due to strong leeward vortices, the secondary separation line separates much sooner, from $\phi = 155^\circ$, $\ell/R = 5$ to $\phi = 140^\circ$, $\ell/R = 10$, decreasing the gap between the primary and secondary separation lines. Figure 4.8 represents the corresponding digitized skin-friction lines.

Surface flow visualizations and digital data of skin-friction lines for $\alpha = 30^\circ$ and $Re = 2.9 \times 10^5$ are displayed in Figures 4.9 and 4.10, respectively. At $\alpha = 30^\circ$ and for low Reynolds number flows, the leeward vortices and the separation bubble merge together to form a single separated region known as horseshoe vortex as discussed in Chapter 3 (see also Yates and Chapman, 1991). The flow displays a closed-type separation. The opposite is observed here for high Reynolds number flows. There is a large space between the leeward vortices and the separation bubble and the flow patterns indicate open separation. The horn vortices completely vanish. Along the cylindrical afterbody, the separation is appeared to be laminar but further downstream it changes over to turbulent. This can be deduced by the location of the primary separation line. From $\ell/R = 2.3$ to 4.5, separation occurs along $\phi = 95^\circ$ and from $\ell/R = 6.0$ to the trailing-edge of the model, separation occurs around $\phi = 105^\circ$. The flow indicates a symmetrical pattern. Figures 4.11 and 4.12 represent skin-friction patterns and the corresponding digital data, respectively, at $\alpha = 30^\circ$ and $Re = 4.2 \times 10^5$.

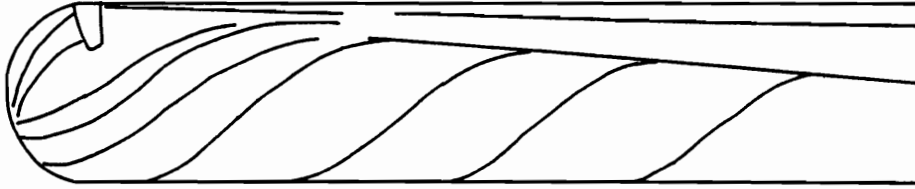


(a)

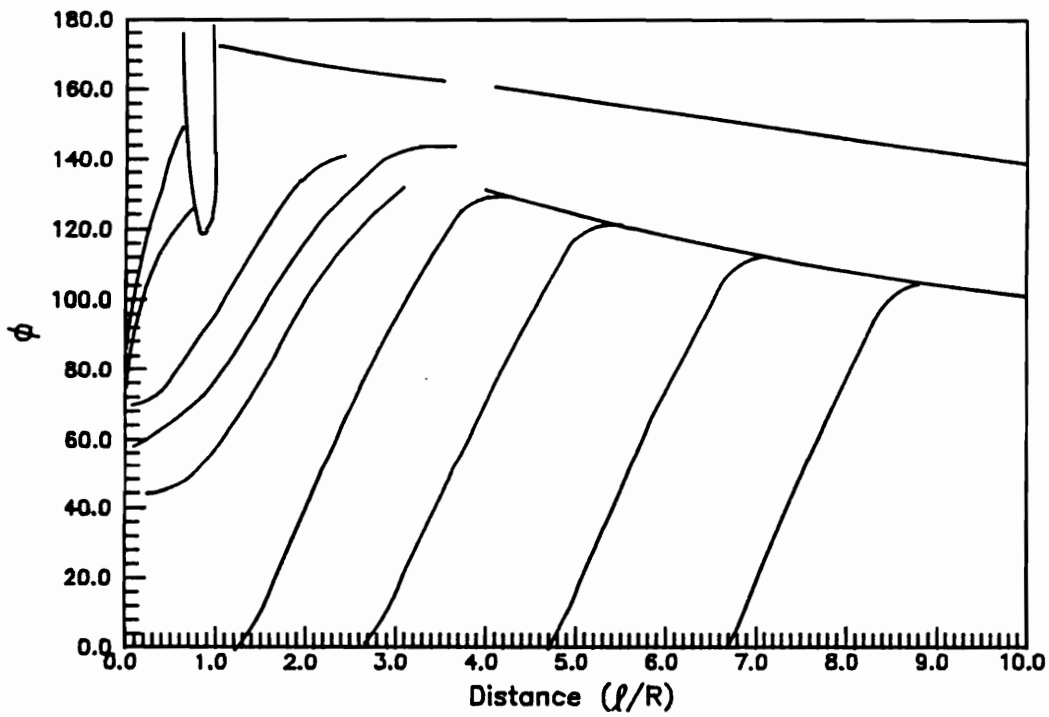


(b)

Figure 4.7. Surface flow visualization at $\alpha = 20^\circ$ and $Re = 4.2 \times 10^5$ (a) $\phi = 180^\circ$
(b) $\phi = 90^\circ$.

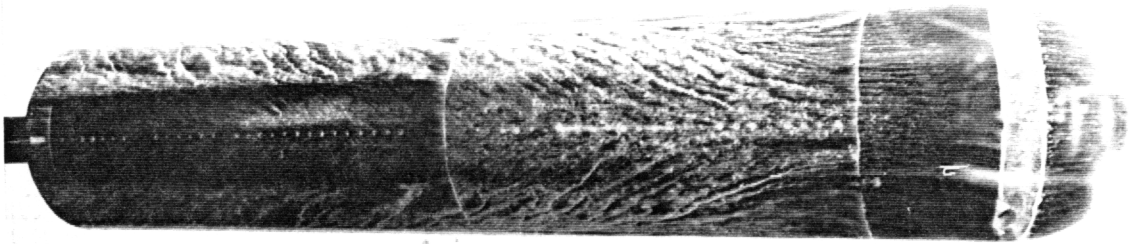


(a)

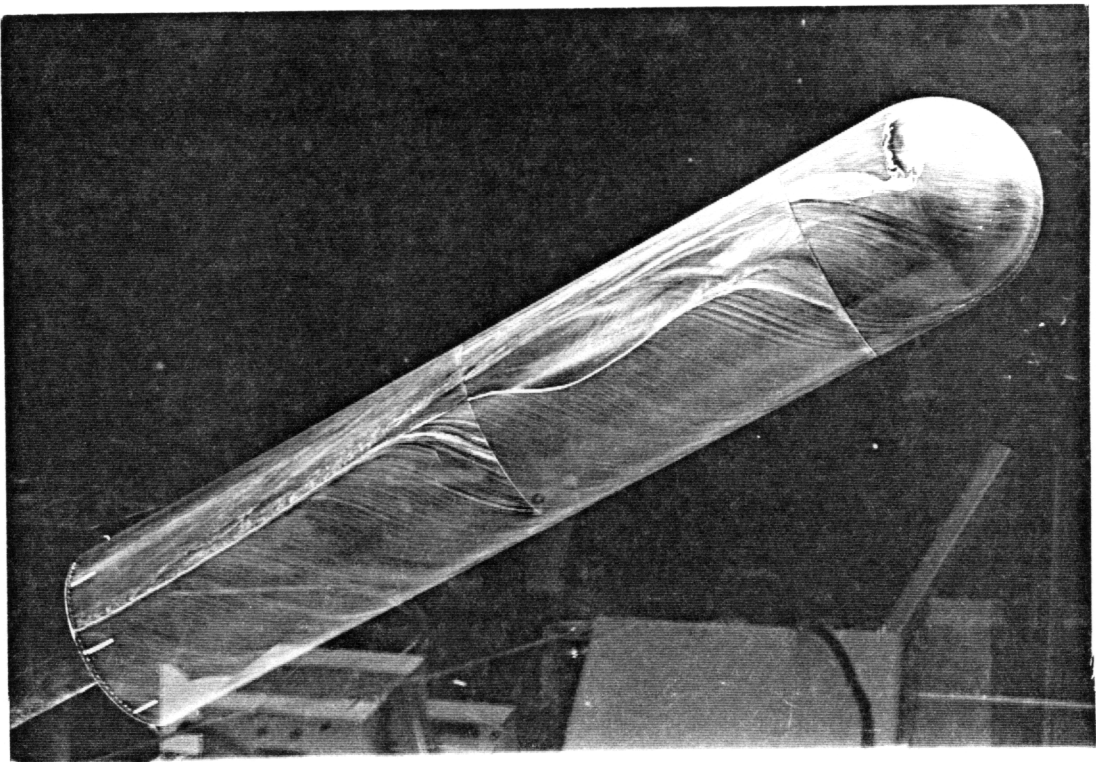


(b)

Figure 4.8. Side view of digitized skin-friction lines for $\alpha = 20^\circ$ and $Re = 4.2 \times 10^5$
(a) actual view (b) unwrapped view.



(a)

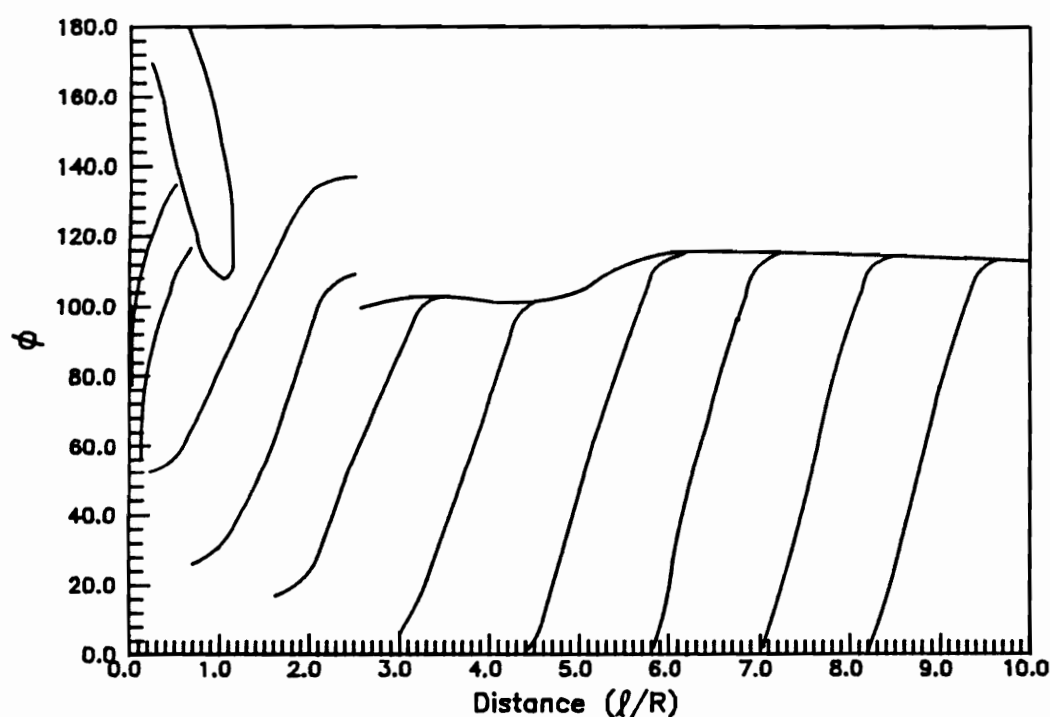


(b)

Figure 4.9. Surface flow visualization at $\alpha = 30^\circ$ and $Re = 2.9 \times 10^5$ (a) $\phi = 180^\circ$
(b) $\phi = 90^\circ$.

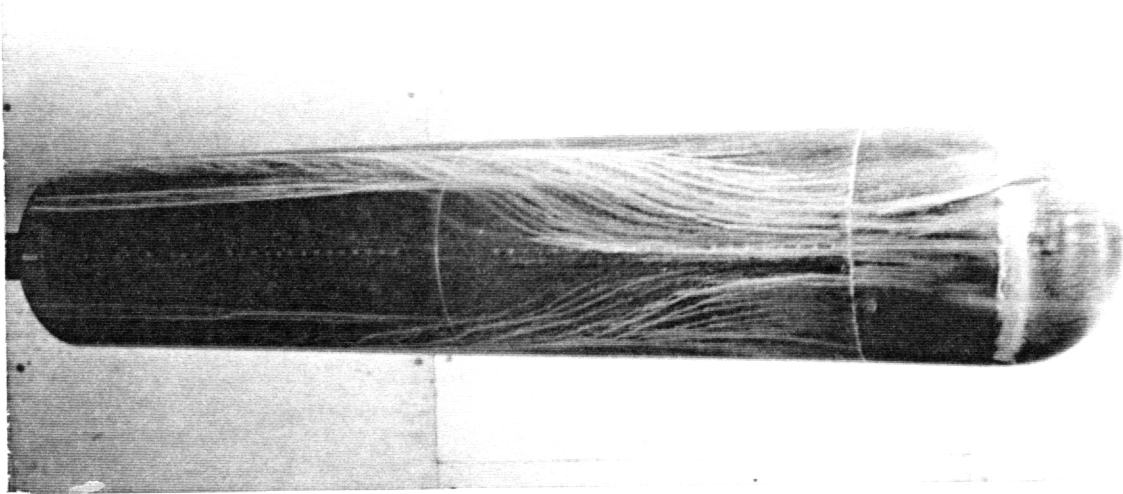


(a)

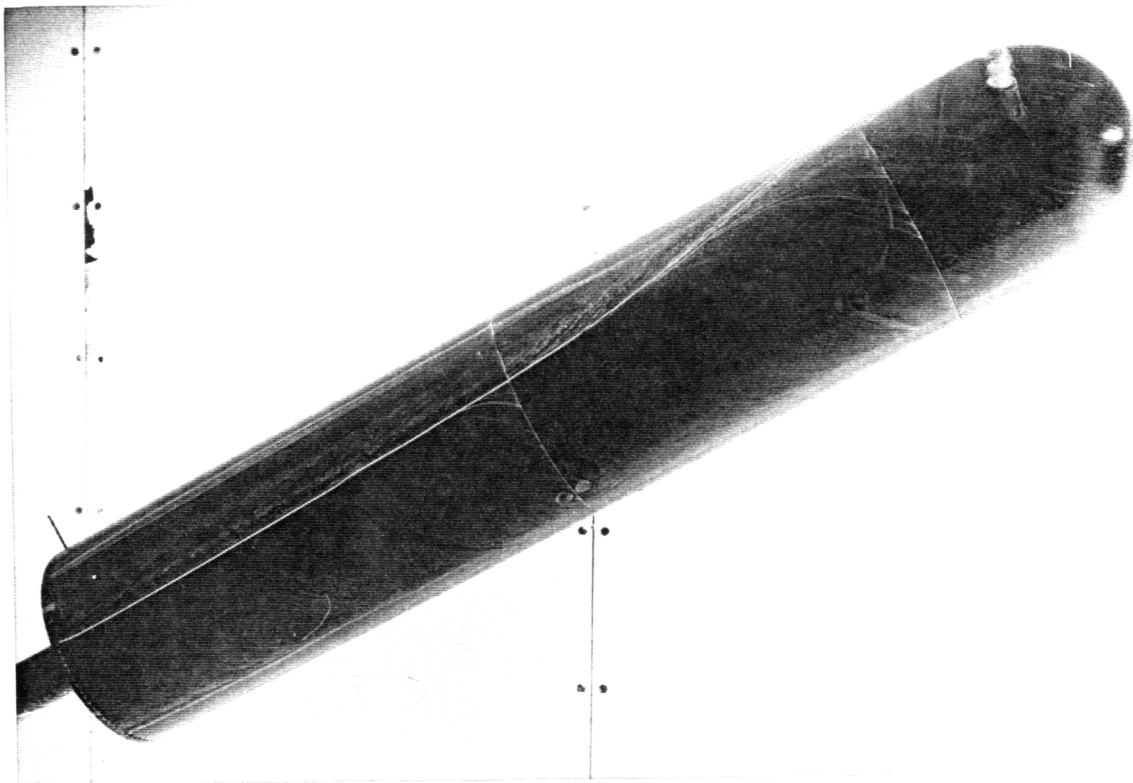


(b)

Figure 4.10. Side view of digitized skin-friction lines for $\alpha = 30^\circ$ and $Re = 2.9 \times 10^5$ (a) actual view (b) unwrapped view.

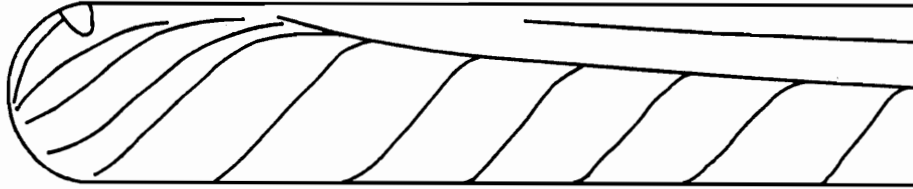


(a)

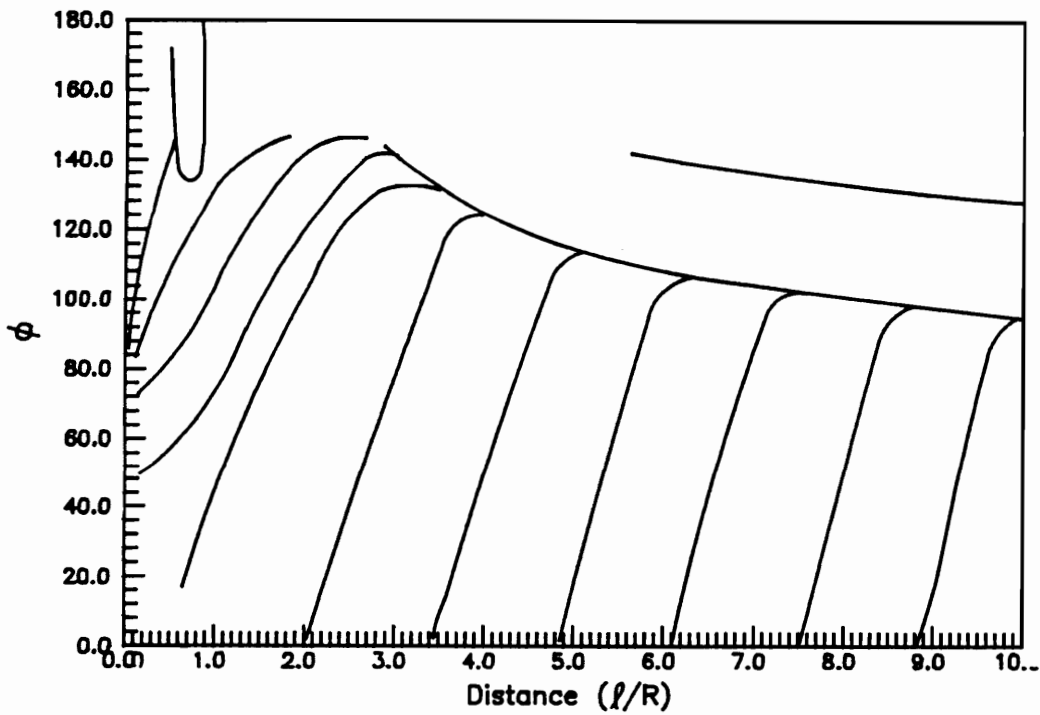


(b)

Figure 4.11. Surface flow visualization at $\alpha = 30^\circ$ and $Re = 4.2 \times 10^5$ (a) $\phi = 180^\circ$
(b) $\phi = 90^\circ$.



(a)



(b)

Figure 4.12. Side view of digitized skin-friction lines for $\alpha = 30^\circ$ and $Re = 4.2 \times 10^5$ (a) actual view (b) unwrapped view.

Pressure Measurements

Static pressure distributions on the test-section wall of the 6' x 6' VPI Stability Wind Tunnel were obtained with the hemisphere-cylinder model at $\alpha = -20^\circ, -10^\circ, 10^\circ$ and 20° . Twenty four 1/16-inch diameter orifices were drilled along the bottom wall of the test-section at a spacing of one inch. The experiments were conducted at a Reynolds number of 2.9×10^5 . Figure 4.13 shows very small deviations in the wall pressure distribution curves between the wind tunnel with the model at various angles of attack and without the model. Thus, it can be safely assumed that any blockage effect introduced by the presence of the body in the wind tunnel is negligible.

Figure 4.14 presents pressure data over the forward portion of the hemisphere-cylinder at zero degree incidence and $Re = 2.9 \times 10^5$. The axial pressure distributions were obtained along two meridional planes, $\phi = 0^\circ$ and 90° . The x-distance in this figure is measured from the point $x=0, \phi = 0^\circ$ along the periphery of the model. The data at $\phi = 0^\circ$ and 90° collapse, confirming the fact that the flow is symmetric and that the free-stream contains no deviations from uniform flow. A separation bubble is displayed in the form of some flattening of pressure distribution in the region from $x/R = 1.5$ to 1.7.

A rather significant contribution of our findings is the influence of the Reynolds number. This is most clearly demonstrated in the axial pressure distributions displayed in Figure 4.15. It is apparent that for low Reynolds numbers the pressure does not drop as much ($C_p = -0.4$) and that the separation bubble is much wider in the x-direction. This was also confirmed by flow visualization photographs in the previous discussion. For higher Reynolds number, with a much smaller separation bubble, the pressure over the attached region drops to a lower value ($C_p = -0.75$), approaching close to the ideal distribution (not shown here).

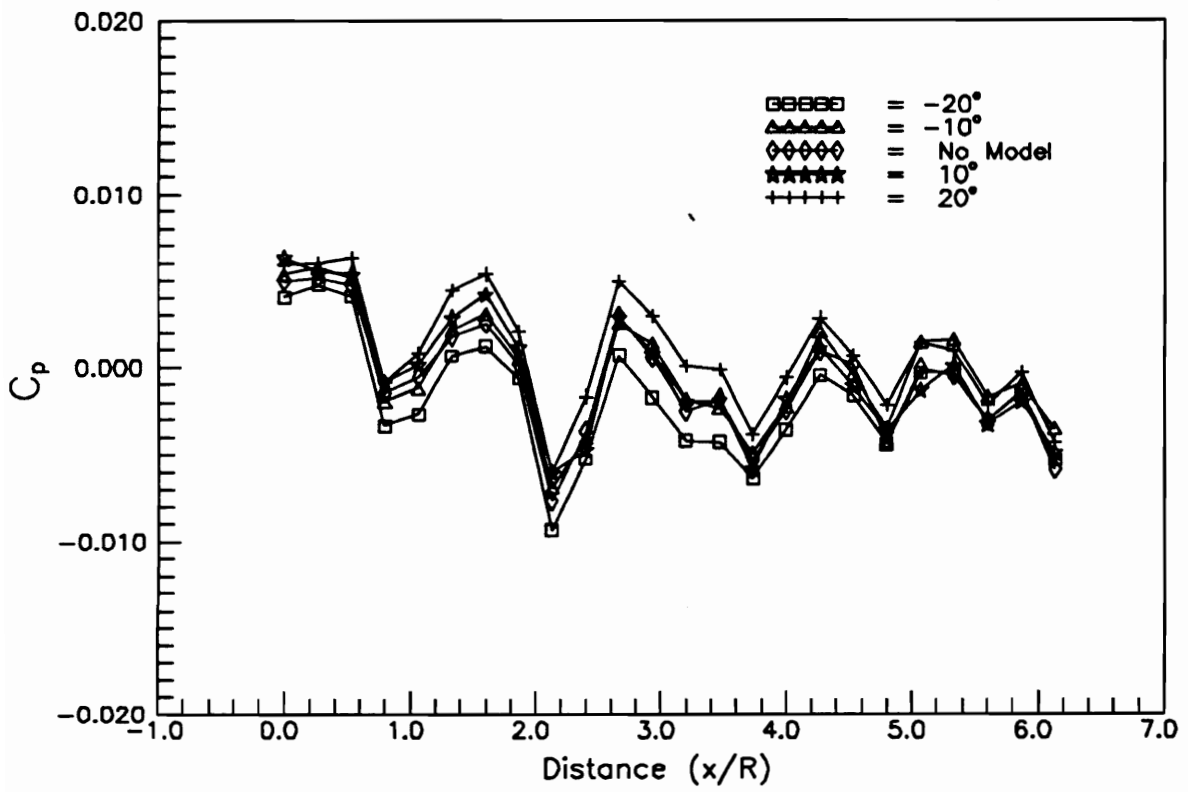


Figure 4.13. Pressure distributions on the VPI Stability Wind Tunnel wall when the hemisphere-cylinder model is placed at various angles of attack.

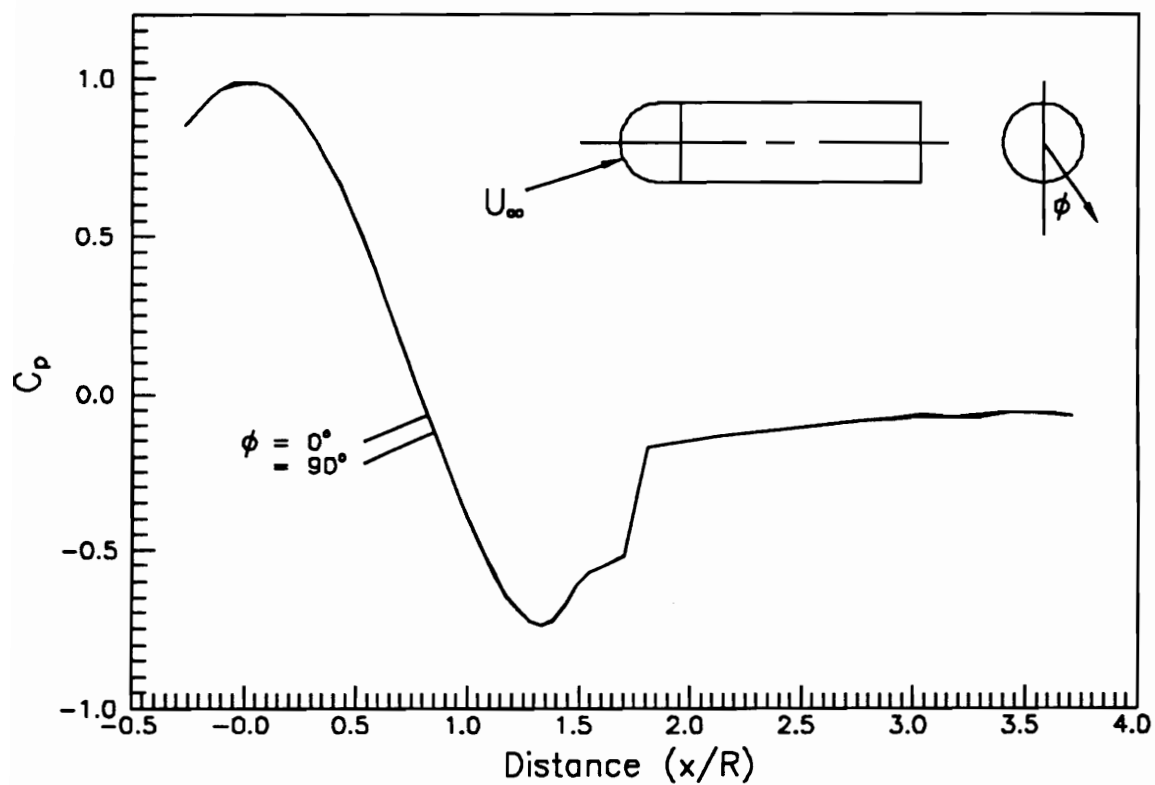


Figure 4.14. Axial pressure distributions on a hemisphere-cylinder at $\alpha = 0^\circ$ and $Re = 2.9 \times 10^5$.

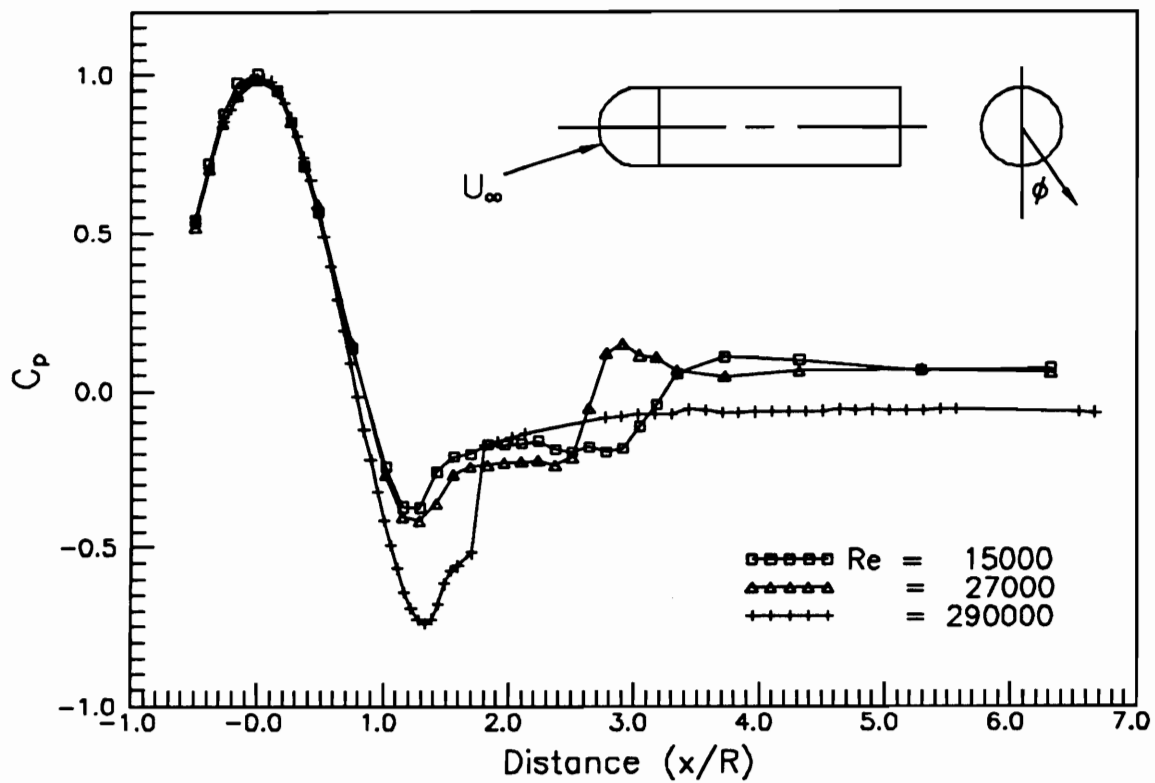


Figure 4.15. Axial pressure distributions on a hemisphere-cylinder at $\alpha = 0^\circ$ and three different Reynolds numbers.

Axial pressure data obtained for $\alpha = 0^\circ$ and at different Reynolds numbers are displayed in Figure 4.16. Since the curves in this figure are similar, a constant was added to each curve to separate them. The results are presented in Figure 4.17. The flat region displayed by the pressure curve progressively disappears with increasing Reynolds number (Mach number). In fact, at $Re = 1.10 \times 10^6$ ($M_\infty = 0.26$), the flat region can no longer be detected. Apparently, the separation bubble vanishes. Hsieh [1981] stated that the nose separation is not expected for $M_\infty \leq 0.6$. This had already been proven to be invalid in Chapter 3. However, with the additional pressure data at high Reynolds numbers presented here, it can be concluded that the separation bubble does not exist in the Mach number range $0.26 \leq M_\infty \leq 0.6$.

The pressure distributions plotted along the axial direction are presented in Figure 4.18 for Reynolds number equal to 2.9×10^5 and $\alpha = 10^\circ$. All the pressure data display flat regions of constant pressure coefficients, indicating the existence of a separation bubble at $1.4 \leq x \leq 1.6$. Pressure coefficient contours are shown in Figure 4.19. Steep pressure gradients are isolated in a small the region in front of the separation bubble, from $x/R = 0.0$ to 0.6 . For x/R greater than 1.0 , the pressure coefficients remain virtually uniform. Pressure distribution along the cylindrical part of the model is easier to interpret if this quantity is plotted along the circumferential direction. The pressure coefficients are scaled by the factor $(\sin \alpha)^{-2}$ which corresponds to a free-stream velocity equal to the component normal to axis of the model. For an infinite yawed cylinder in ideal flow, the quantity $\frac{C_p}{\sin^2 \alpha}$ should be equal to unity at the front and rear stagnation points, $\phi = 0^\circ$ and 180° . Pressure coefficients plotted circumferentially at various cross-sections in 20° increments are displayed in Figure 4.20. The corresponding Reynolds number is 2.9×10^5 . The behavior of these curves is reminiscent of the potential flow over a two-dimensional circular cylinder whereby, as mentioned above, the front and rear stagnation points have the same value of pressure coefficients. The curves

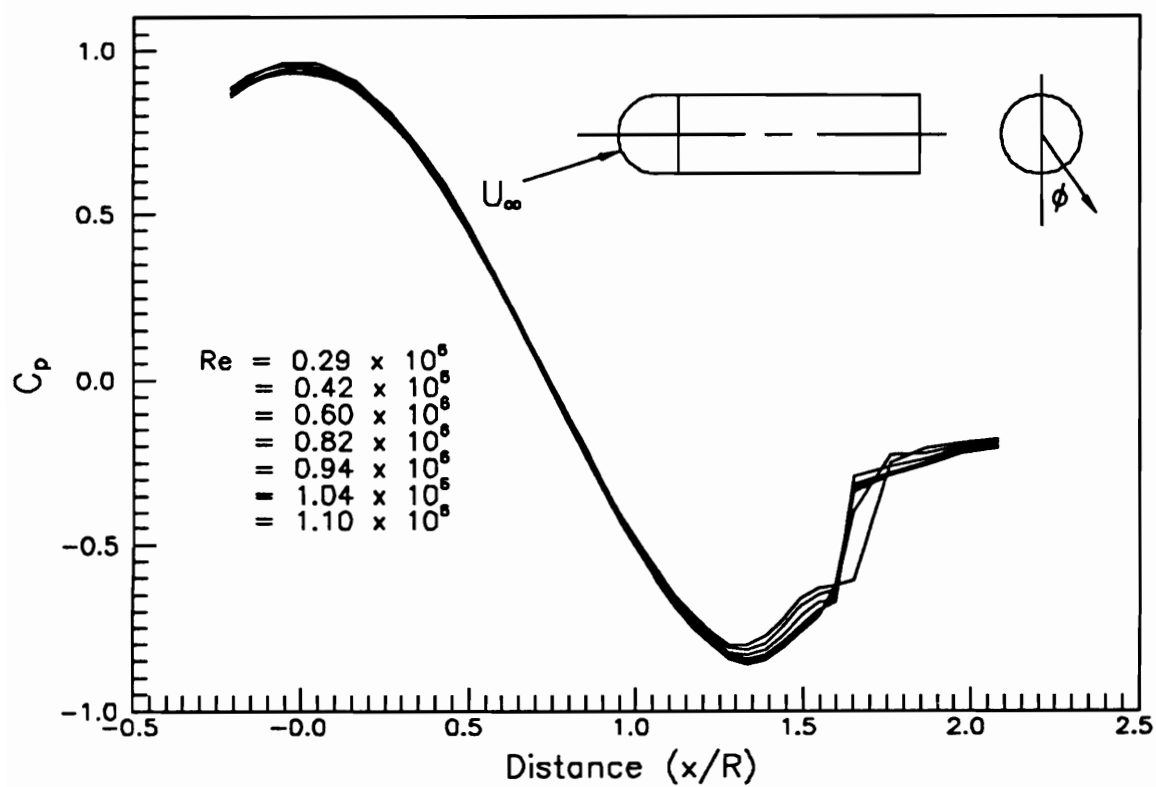


Figure 4.16. Axial pressure distributions on a hemisphere-cylinder at $\alpha = 0^\circ$ and various Reynolds numbers.

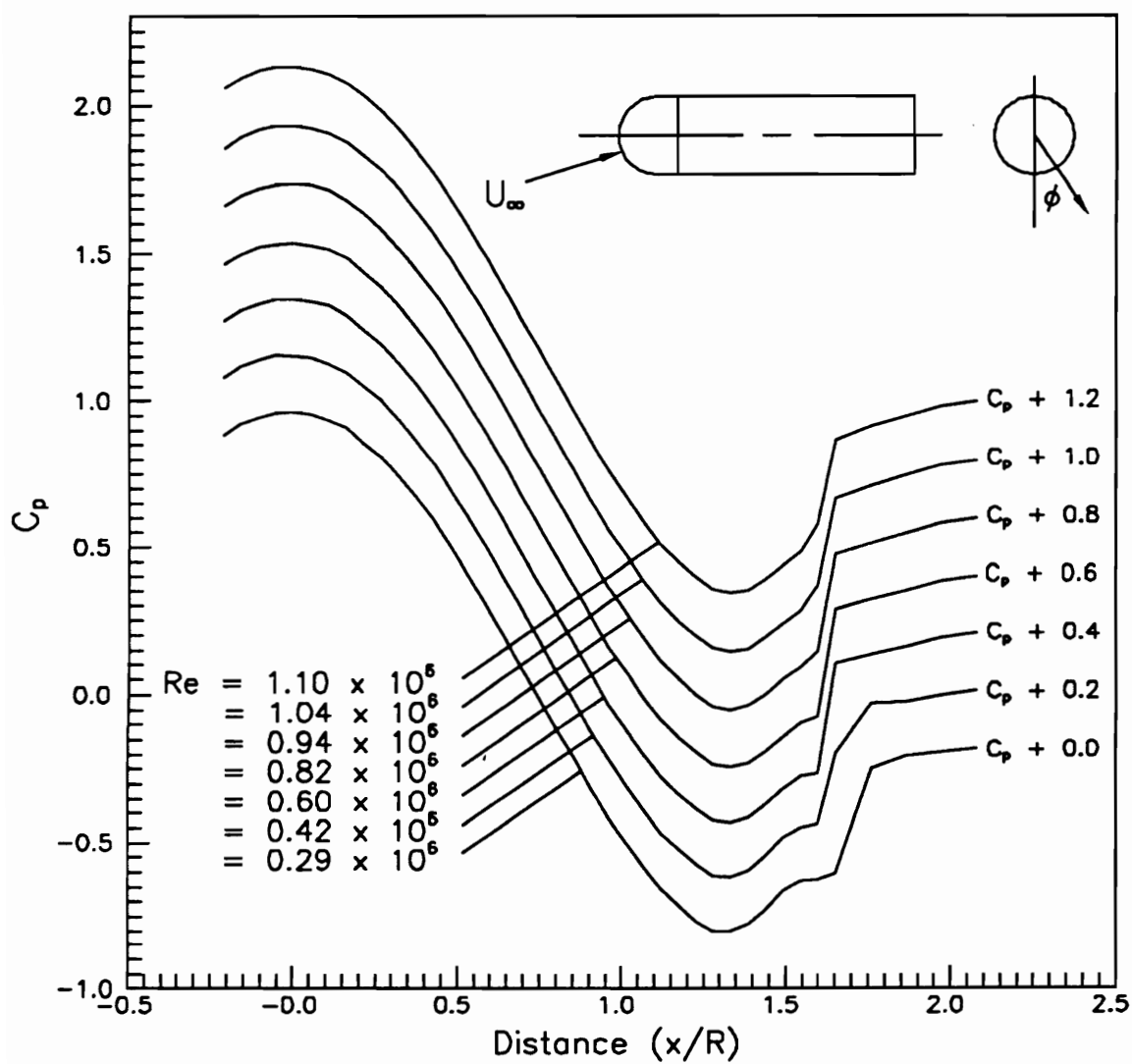


Figure 4.17. Axial pressure distributions on a hemisphere-cylinder at $\alpha = 0^\circ$ and various Reynolds numbers with added constants.

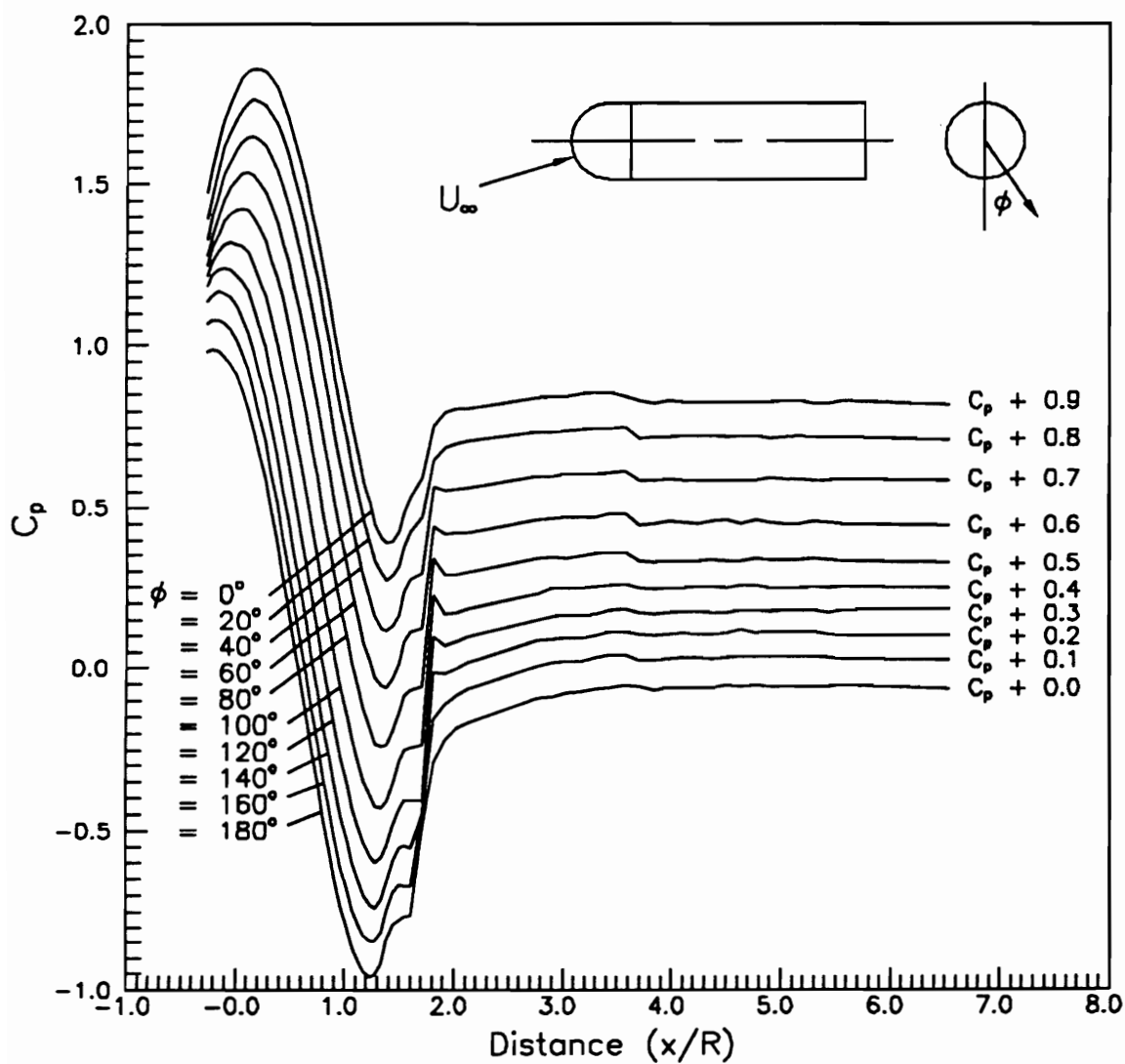


Figure 4.18. Axial pressure distributions on a hemisphere-cylinder at $\alpha = 10^\circ$ and $Re = 2.9 \times 10^5$ with added constants.

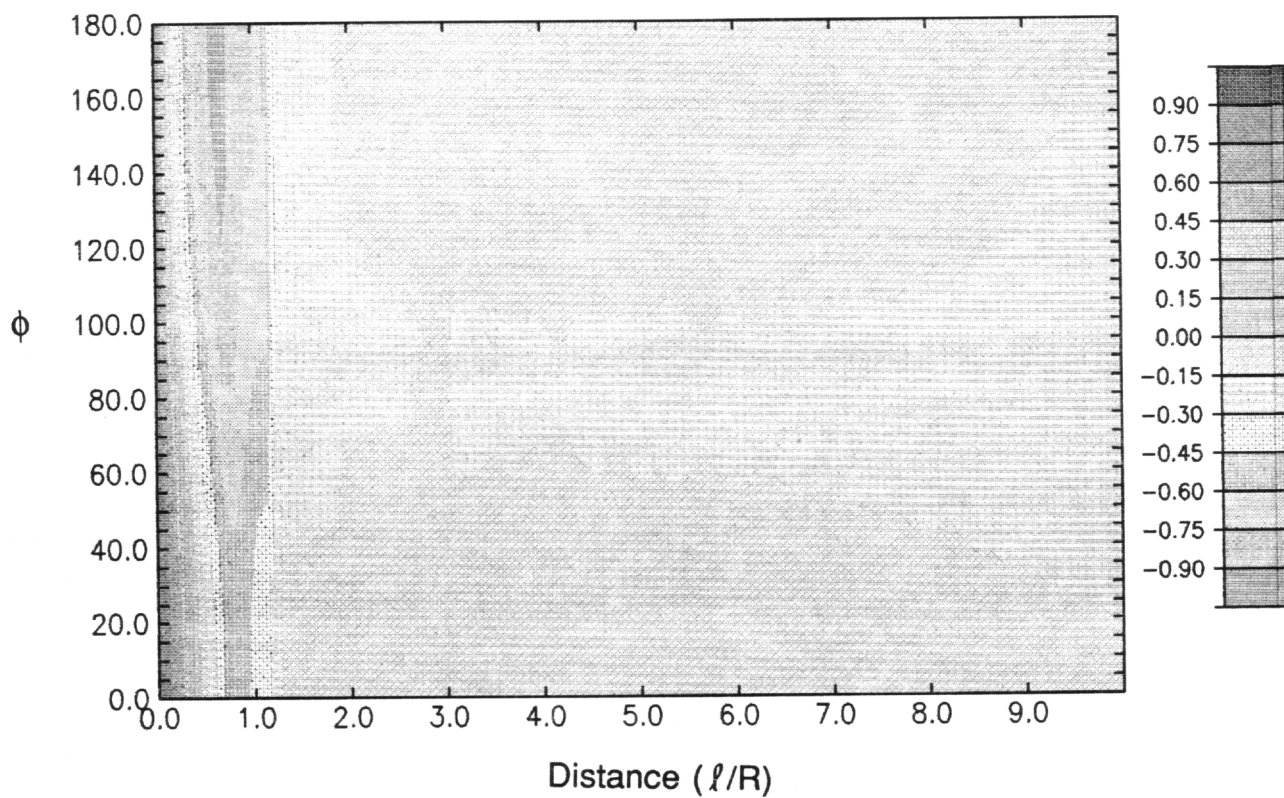


Figure 4.19. Pressure coefficient contours on a hemisphere-cylinder at $\alpha = 10^\circ$ and $Re = 2.9 \times 10^5$.

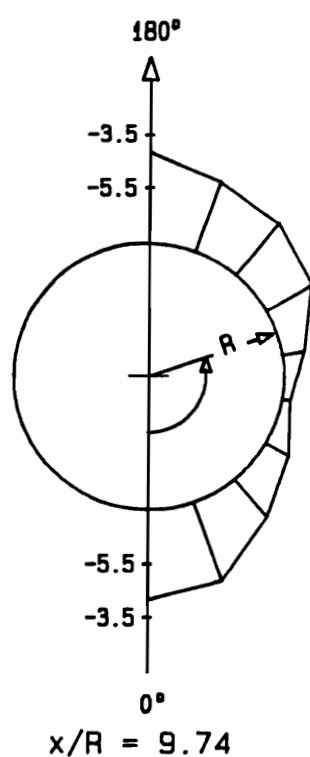
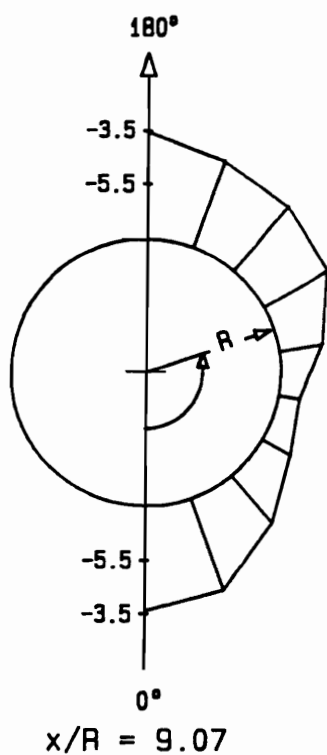
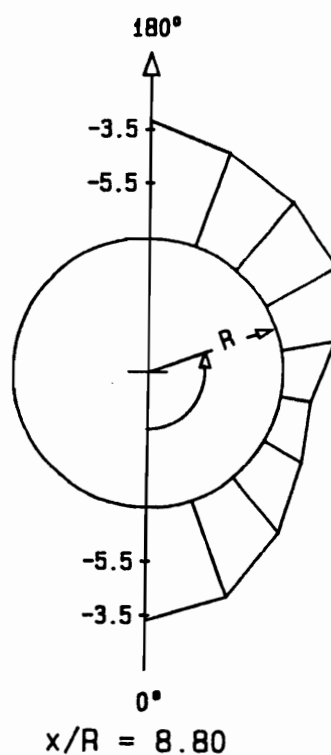
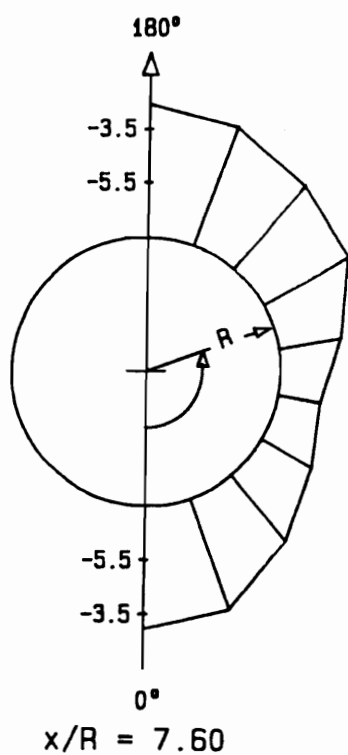


Figure 4.20. Circumferential pressure distributions on a hemisphere-cylinder at $\alpha = 10^\circ$ and $Re = 2.9 \times 10^5$.

in Figure 4.20 start from values near -3.5 at $\phi = 0^\circ$, continuously decrease towards $\phi = 90^\circ$ and then again increases to -3.5 at $\phi = 180^\circ$. There are no "dips" displayed by the pressure curves, indicating that leeward vortices had not yet developed.

Figures 4.21 and 4.22 depict axial pressure distributions and pressure coefficient contours, respectively, at a Reynolds number of 4.2×10^5 and $\alpha = 10^\circ$. Like other cases mentioned above and in Chapter 3, the curves show characteristics of a separation bubble as regions of constant pressure coefficients, in the range $1.5 \leq x/R \leq 1.7$. Circumferential pressure coefficients were plotted as shown in Figure 4.23. There is a slight "dip" on the pressure curve at $x/R = 9.74$ and $\phi = 160^\circ$ indicating the existence of a weak leeward vortex.

At 10° incidence, axial pressure coefficients were obtained along a meridional plane, $\phi = 180^\circ$, for seven different Reynolds numbers (Figures 4.24 and 4.25). Similar to the zero degree incidence case, the separation bubble decreases in size with increasing Reynolds number and almost vanishes at $Re = 1.10 \times 10^6$.

At $\alpha = 20^\circ$ and $Re = 2.9 \times 10^5$, axial pressure plots are displayed in Figure 4.26. A peculiar behavior is revealed by these plots; pressure coefficient within the separation bubble, along $\phi = 180^\circ$ and 160° , drops to a minimum instead of remaining constant. However, the flat regions appear along $100^\circ \leq \phi \leq 140^\circ$ indicating that the separation bubble is confined to the top of the model's nose. Figure 4.27 displays a composite of the digitized skin-friction patterns superimposed on the pressure coefficient contours. The separation bubble locates in an area of minimum pressure coefficients. Figure 4.28 displays the corresponding circumferential pressure distributions. The curves exhibit a behavior similar to two-dimensional potential flow over a circular cylinder in the region $3.97 \leq x/R \leq 5.04$. For $x/R \geq 6.54$, swirling motion by the leeward vortices caused the appearance of dips in the pressure curves along $\phi = 160^\circ$.

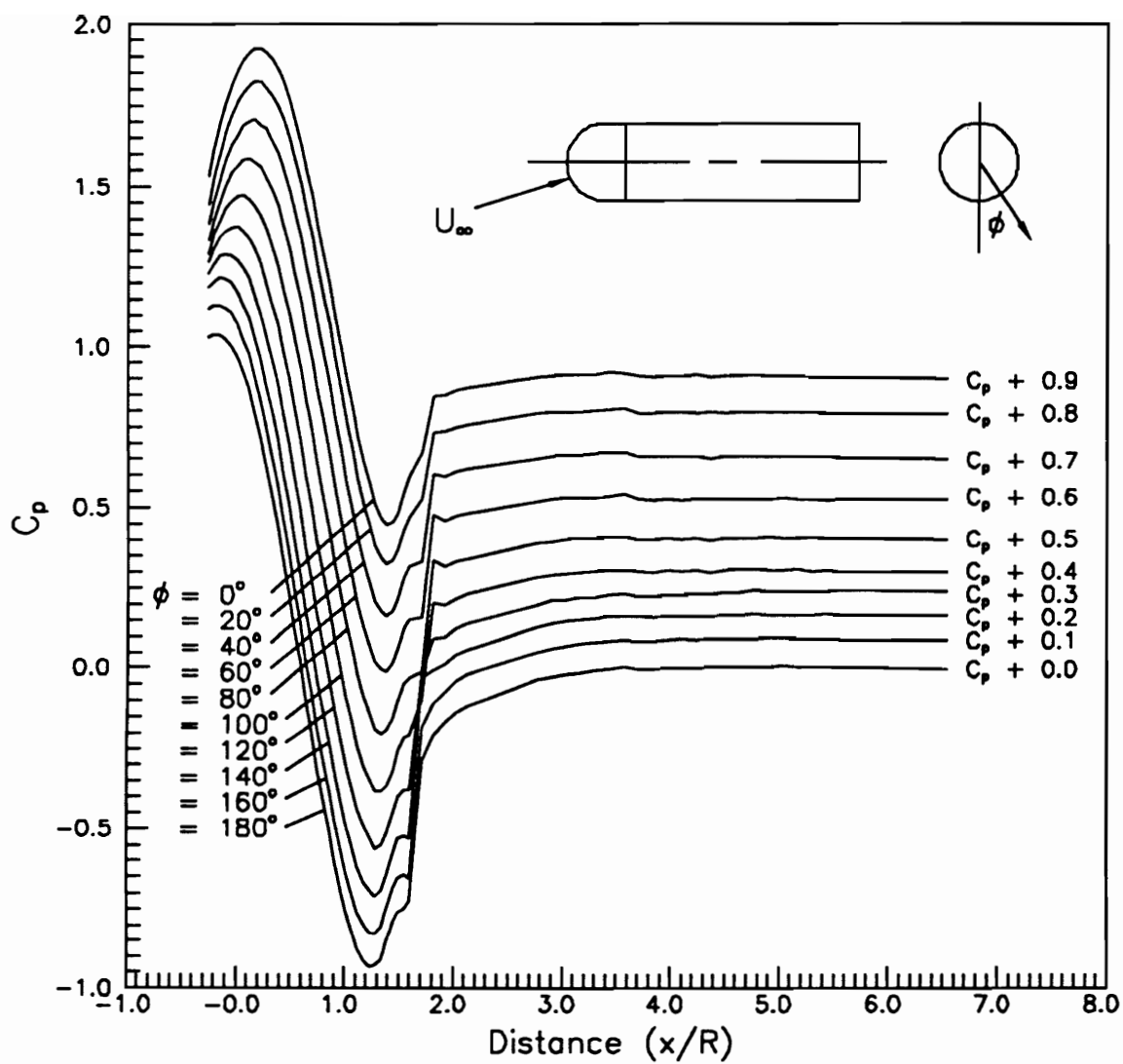


Figure 4.21. Axial pressure distributions on a hemisphere-cylinder at $\alpha = 10^\circ$ and $Re = 4.2 \times 10^5$ with added constants.

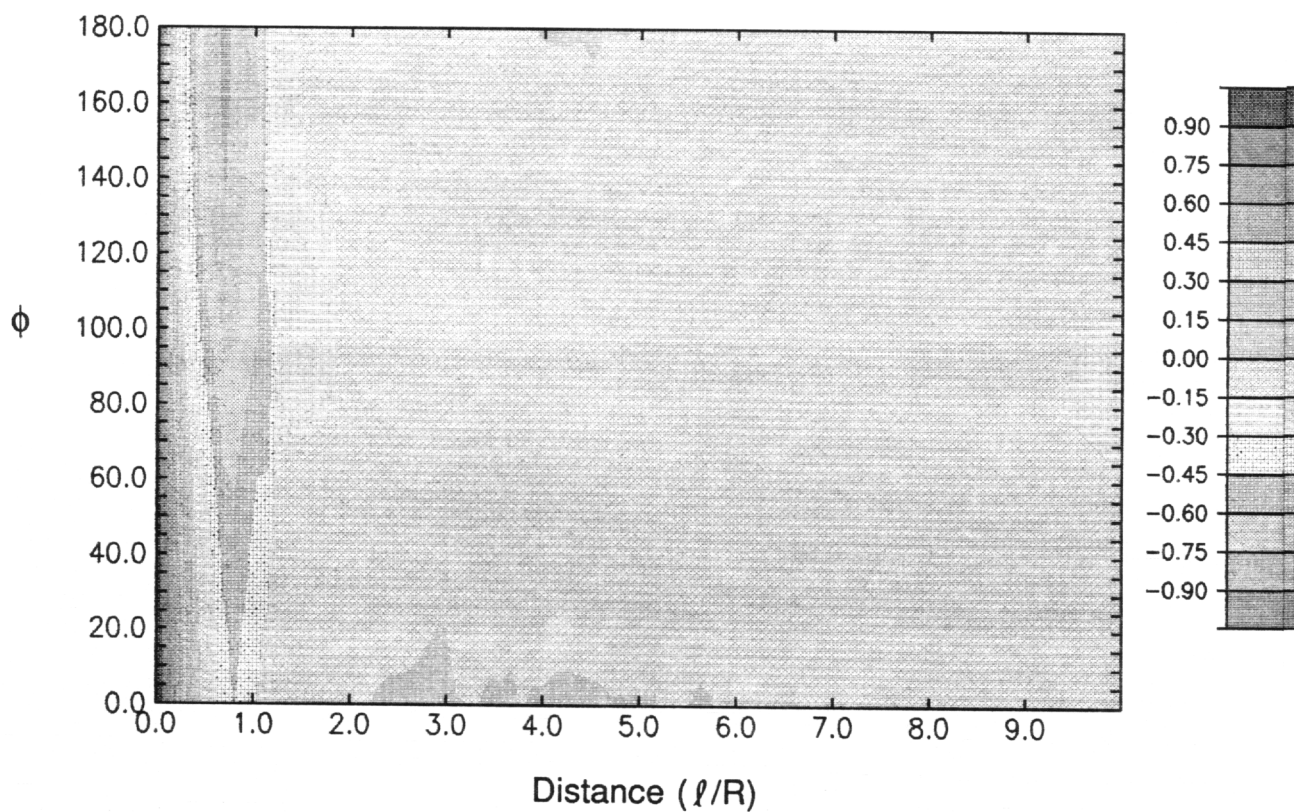


Figure 4.22. Pressure coefficient contours on a hemisphere-cylinder at $\alpha = 10^\circ$ and $Re = 4.2 \times 10^5$.

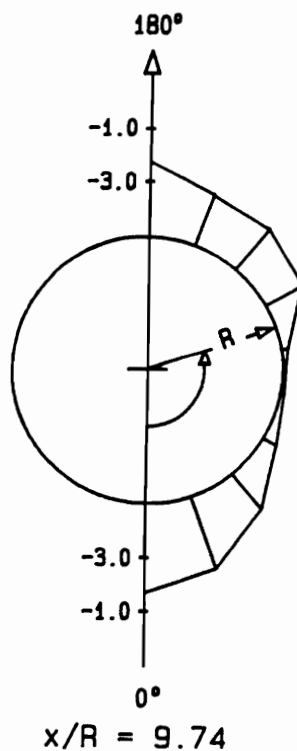
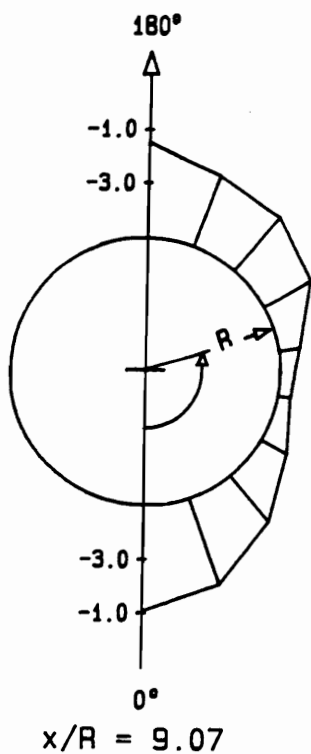
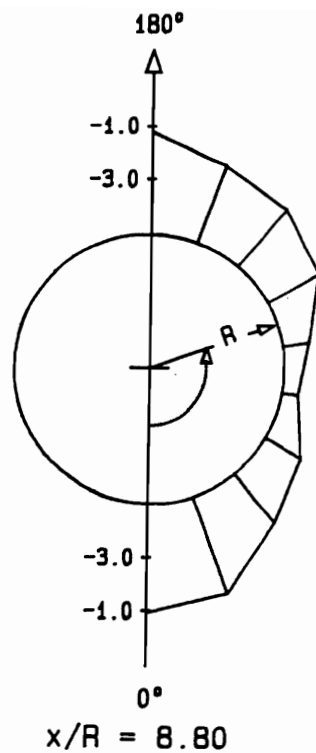
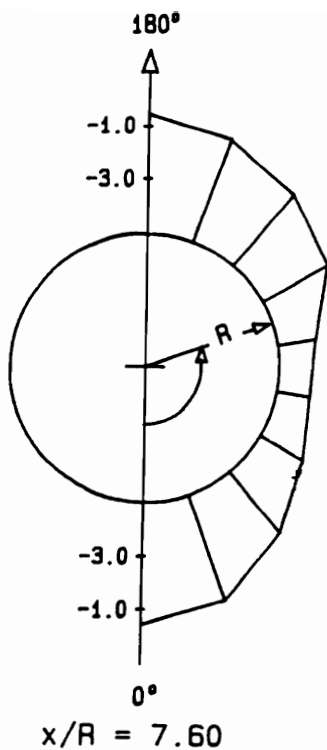


Figure 4.23. Circumferential pressure distributions on a hemisphere-cylinder at $\alpha = 10^\circ$ and $Re = 4.2 \times 10^5$.

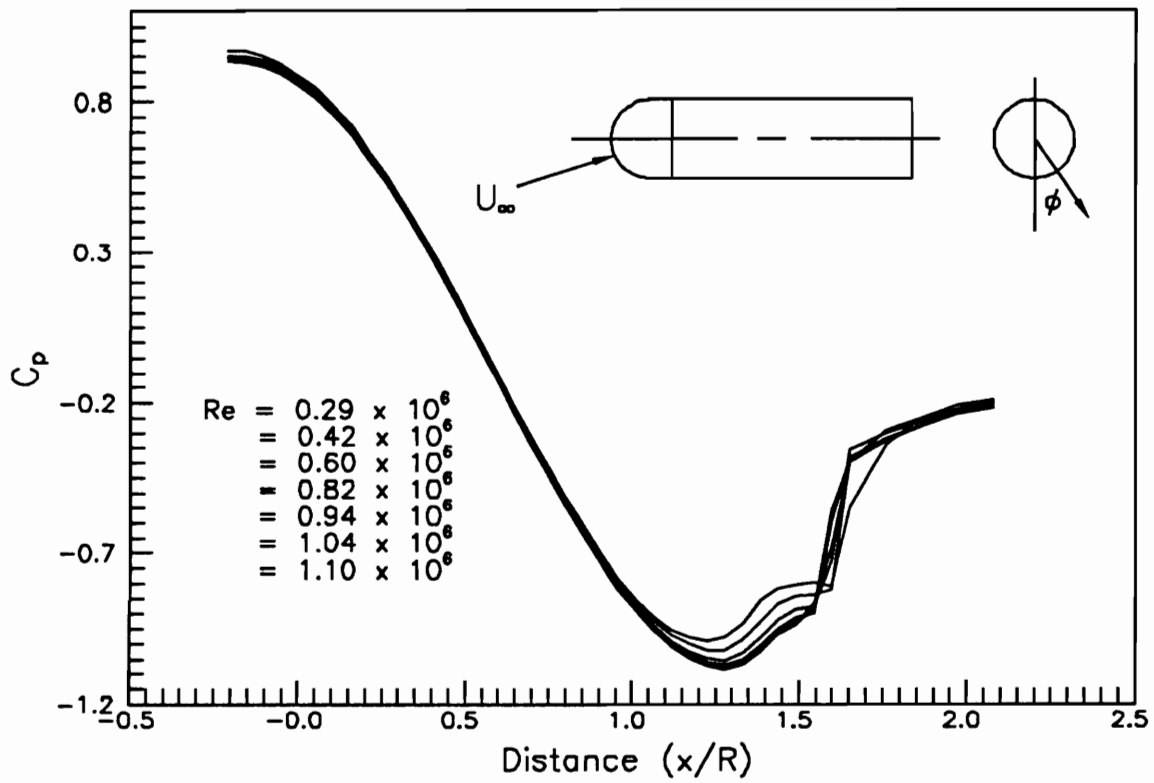


Figure 4.24. Axial pressure distributions on a hemisphere-cylinder at $\alpha = 10^\circ$ and various Reynolds numbers.

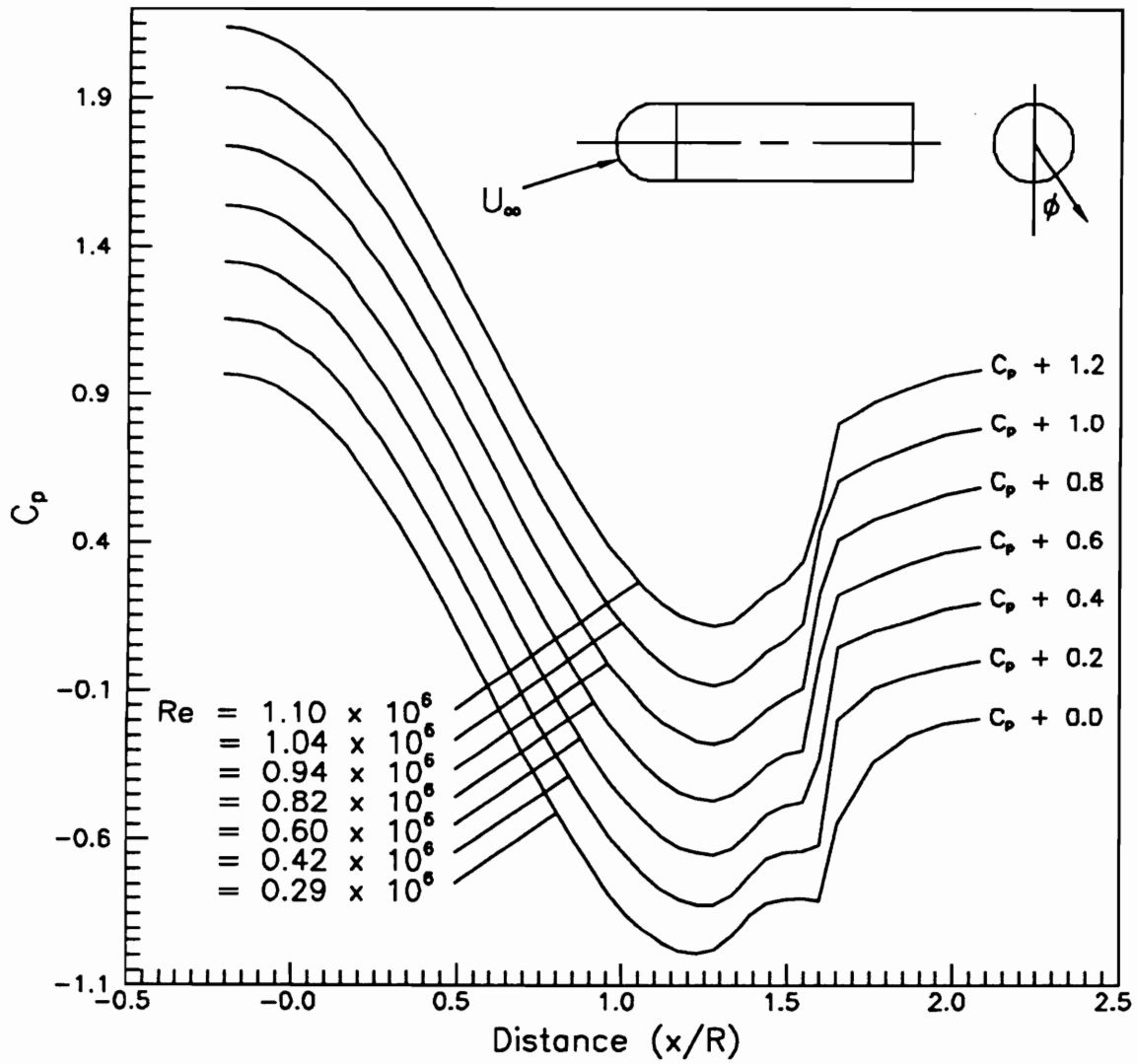


Figure 4.25. Axial pressure distributions on a hemisphere-cylinder at $\alpha = 10^\circ$ and various Reynolds numbers with added constants.

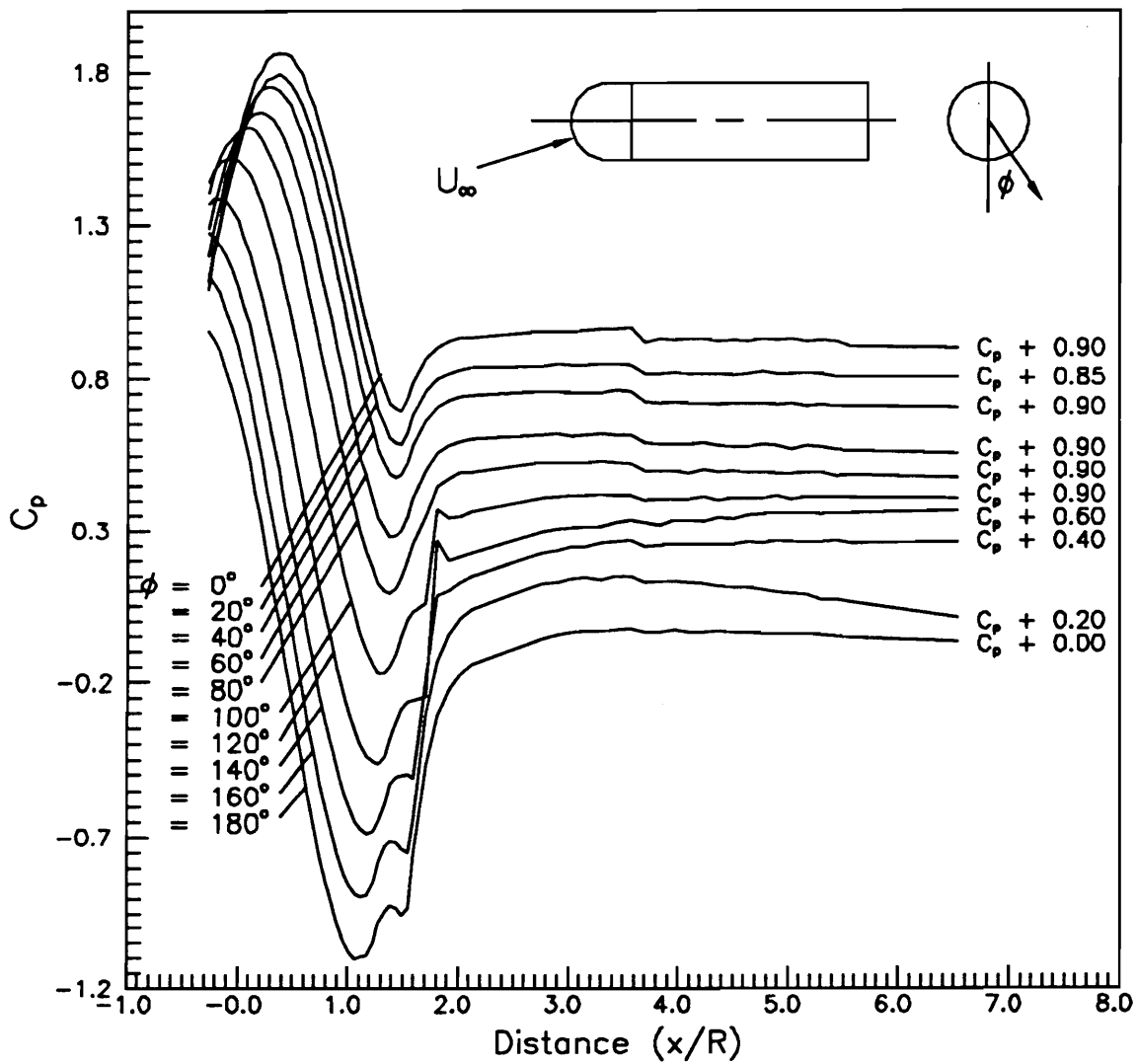


Figure 4.26. Axial pressure distributions on a hemisphere-cylinder at $\alpha = 20^\circ$ and $Re = 2.9 \times 10^5$ with added constants.

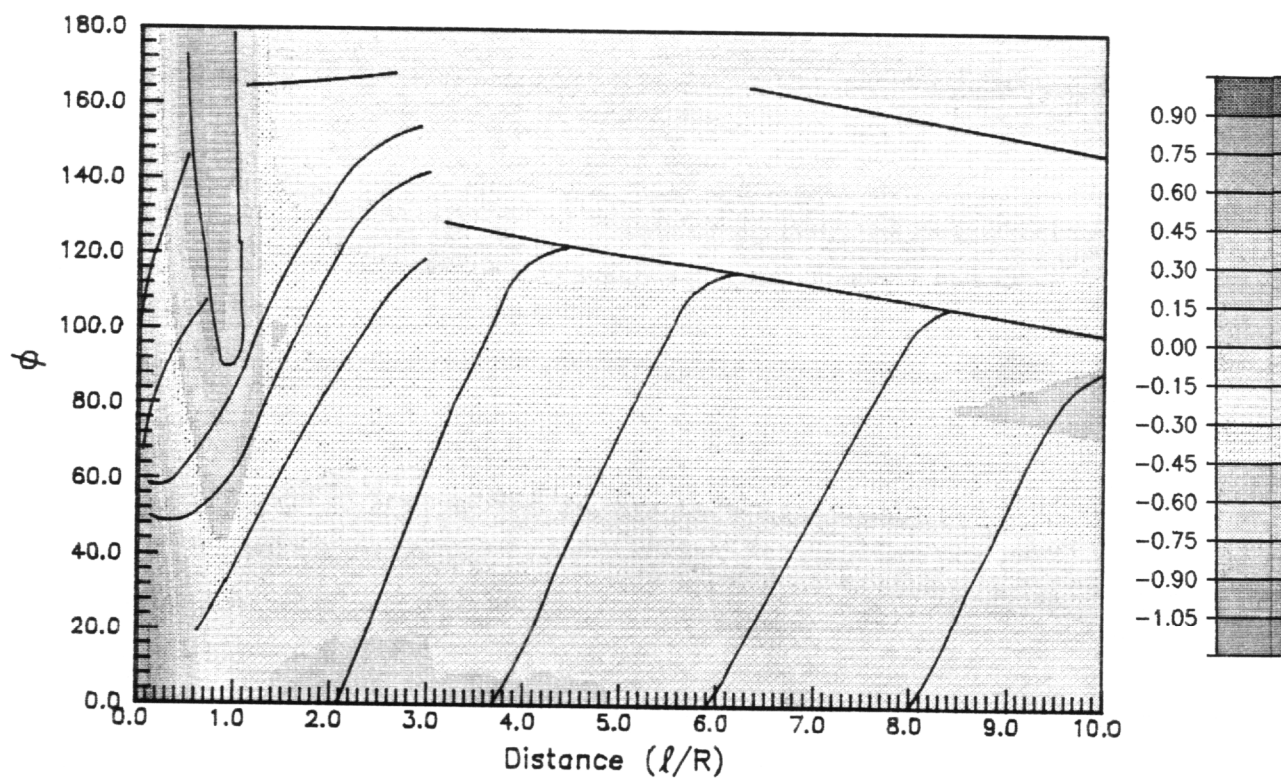


Figure 4.27. Pressure coefficient contours and digitized skin-friction patterns on a hemisphere-cylinder at $\alpha = 20^\circ$ and $Re = 2.9 \times 10^5$.

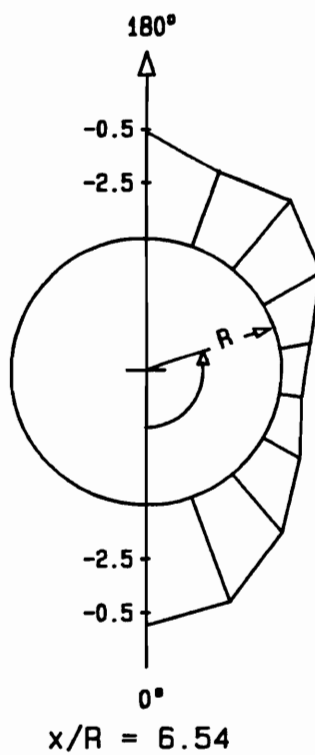
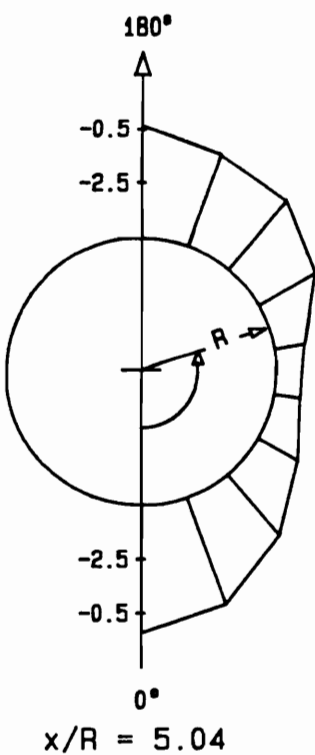
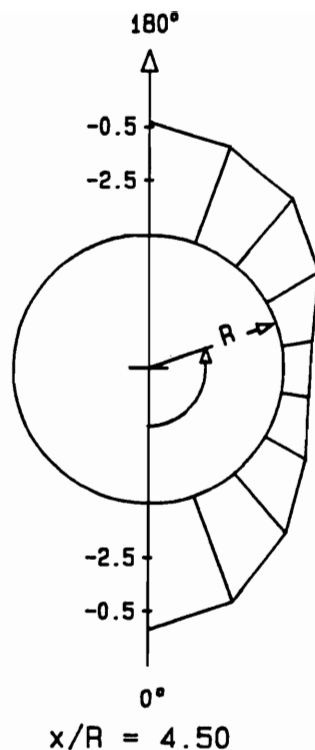
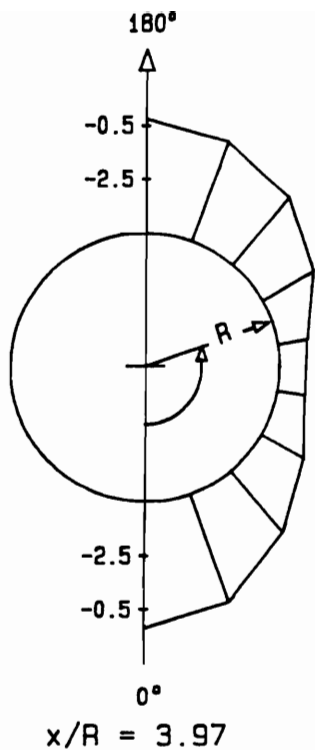


Figure 4.28. Circumferential pressure distributions on a hemisphere-cylinder at $\alpha = 20^\circ$ and $Re = 2.9 \times 10^5$.

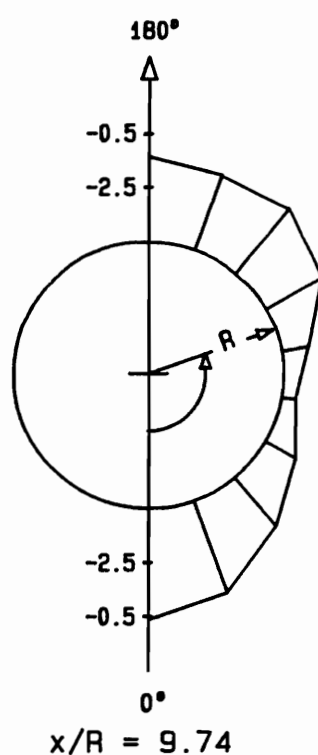
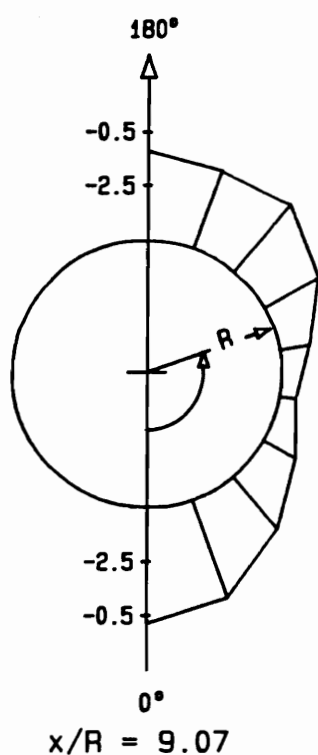
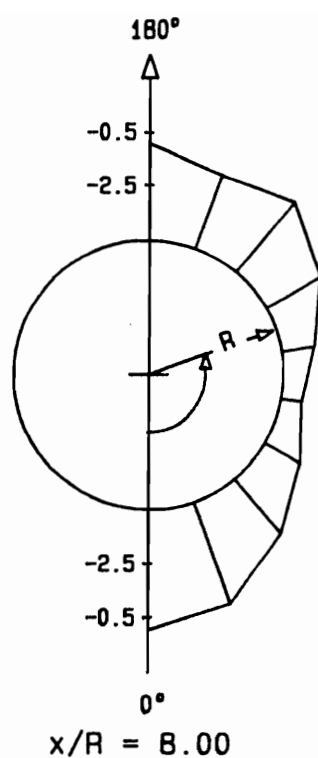
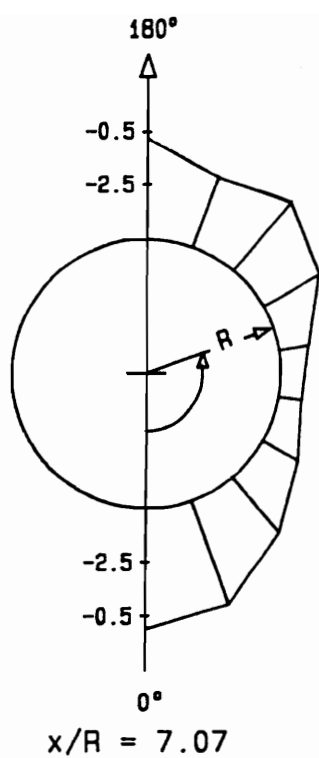


Figure 4.28. Continued.

Axial pressure distributions and a composite of pressure coefficient contours at $\alpha = 20^\circ$ and $Re = 4.2 \times 10^5$ are displayed in Figures 4.29 and 4.30, respectively. The length of the separation bubble is decreased slightly. The circumferential pressure curves displayed in Figures 4.31 and 4.32 indicate three very distinct patterns of pressure distributions downstream of the hemispherical cap. The first is found in the leading region of the model, namely for $1.33 < x/R < 1.49$ (Figure 4.31). In this region, the reduced pressure coefficient starts from values near -1.0 at $\phi = 0^\circ$ and continuously decreases toward $\phi = 180^\circ$. This characteristic resembles two-dimensional lifting surfaces, whereby suction conditions are generated on the leeward side of the body. The transition from the first to the second region is somewhat abrupt and occurs between $x/R = 1.6$ and $x/R = 1.76$. In the second region, the pressure distribution is nearly symmetric around $\phi = 90^\circ$ which is similar to a two-dimensional flow over a circular cylinder. However, the pressure coefficient at $\phi = 0^\circ$ vanishes and even takes on negative values, a clear departure from the case of infinite cylinder in yaw. Further downstream, the value of pressure coefficient at $\phi = 0^\circ$ increases and indeed tends to recover the value of one (Figure 4.32), which signals independence of the local conditions from the structure of the flow near the nose of the body.

The first two regions are nearly inviscid. No significant thickening of the boundary-layer develops, even though the onset of open separation is clearly indicated in the second region, as displayed by the convergence of the skin-friction lines. The effect of the viscosity becomes significant only in the third region, where the imprint of a separated vortex appears in the form of a dip in the pressure distribution. The dips are most pronounced between $x/R = 6.54$ to 8.0 demonstrating the existence of strong leeward vortices (Figure 4.32). However, toward the trailing-edge of the model, the dips become shallower. As mentioned in Chapter 3, this was perhaps due to the leeward

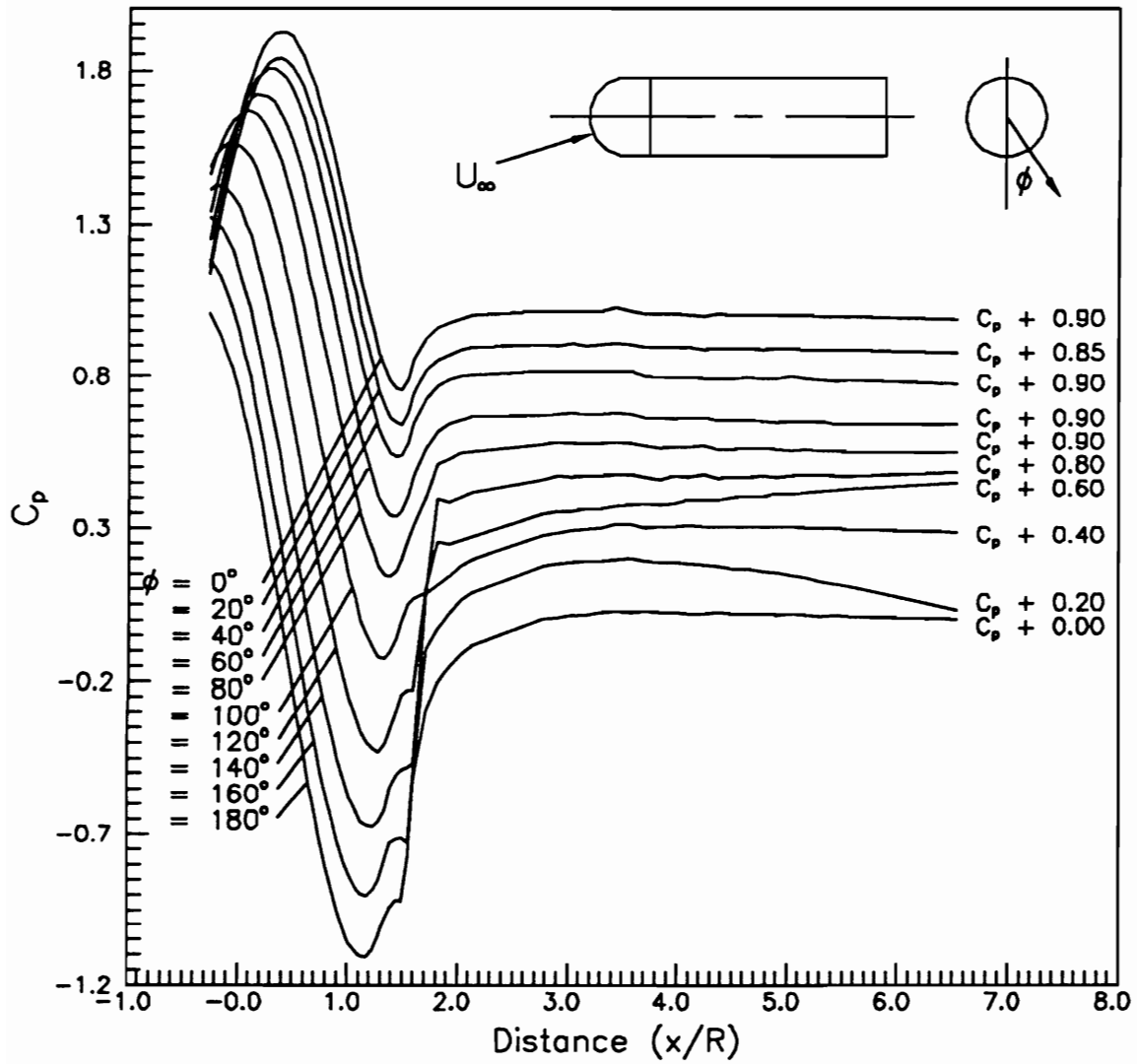


Figure 4.29. Axial pressure distributions on a hemisphere-cylinder at $\alpha = 20^\circ$ and $Re = 4.2 \times 10^5$ with added constants.

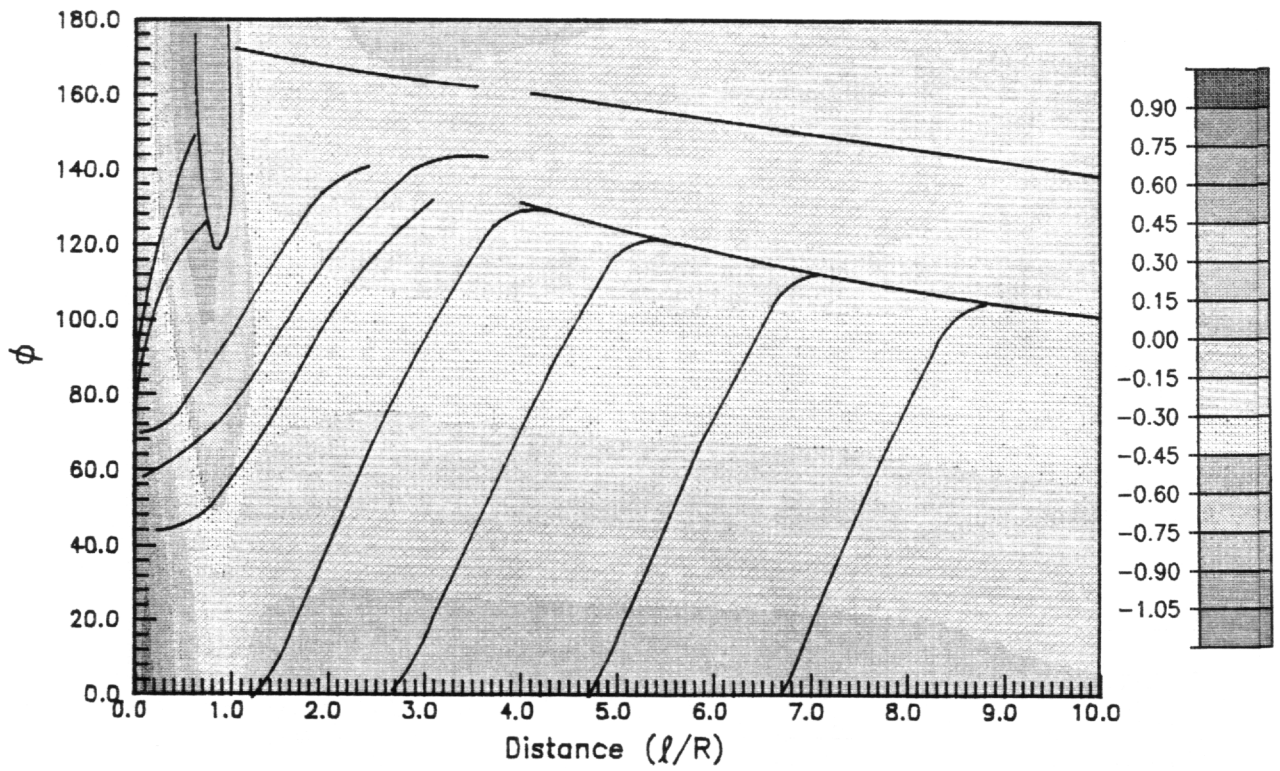


Figure 4.30. Pressure coefficient contours and digitized skin-friction patterns on a hemisphere-cylinder at $\alpha = 20^\circ$ and $Re = 4.2 \times 10^5$.

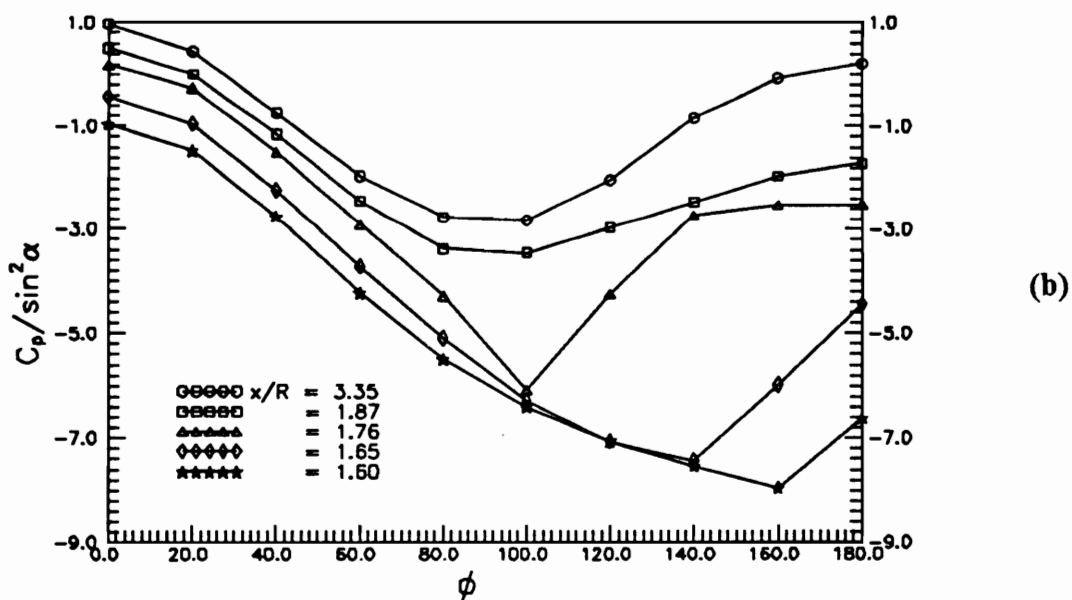
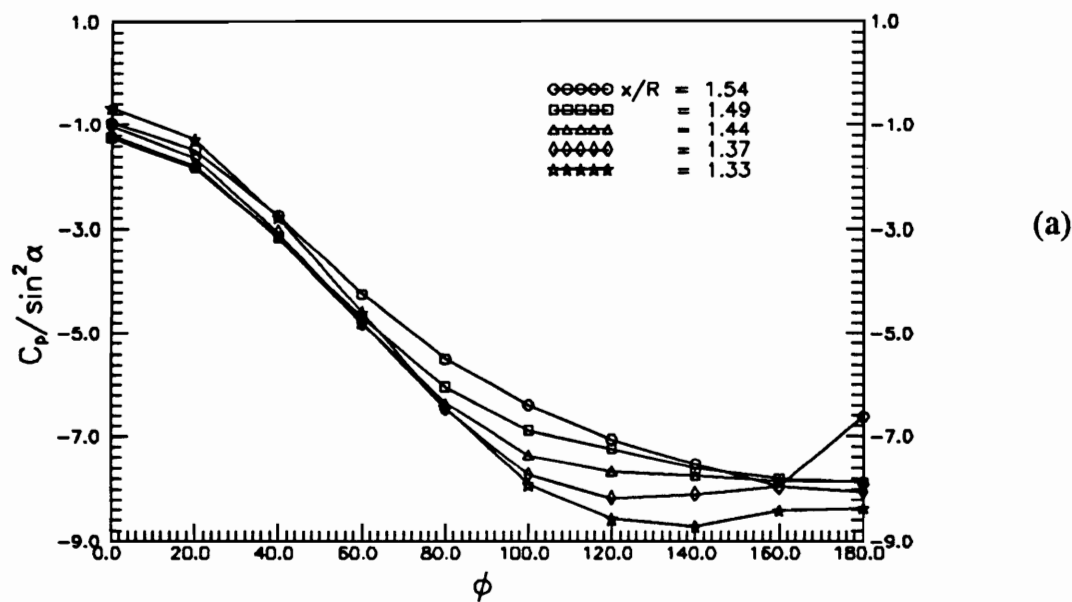


Figure 4.31. Circumferential pressure distributions on a hemisphere-cylinder at $\alpha = 20^\circ$ and $Re = 4.2 \times 10^5$.

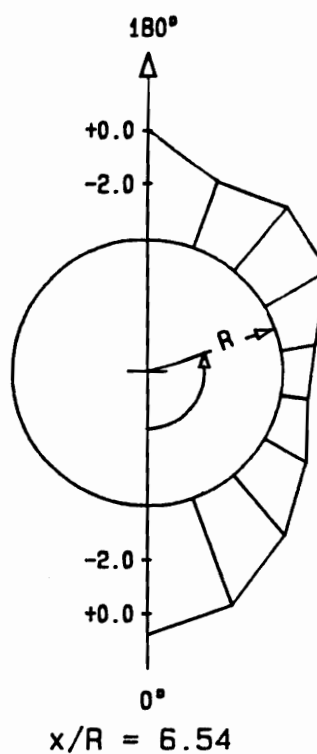
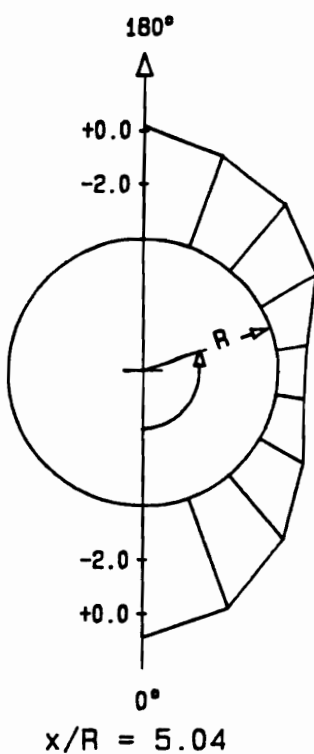
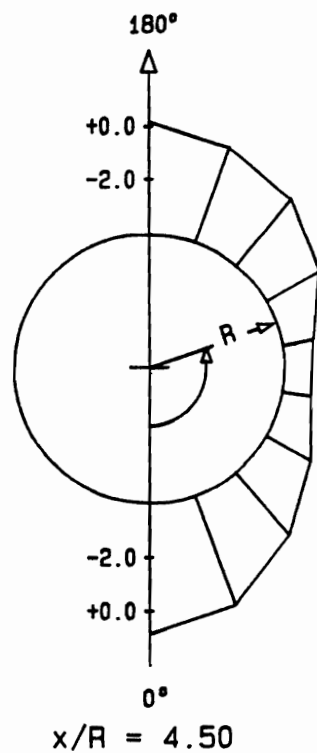
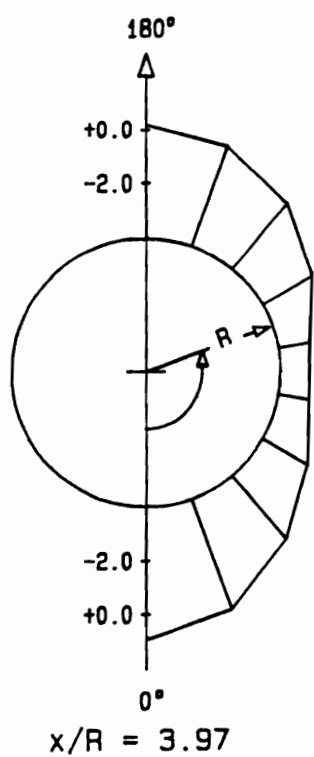


Figure 4.32. Circumferential pressure distributions on a hemisphere-cylinder at $\alpha = 20^\circ$ and $Re = 4.2 \times 10^5$.

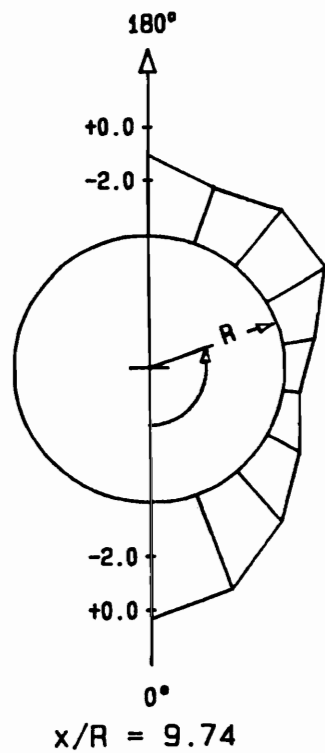
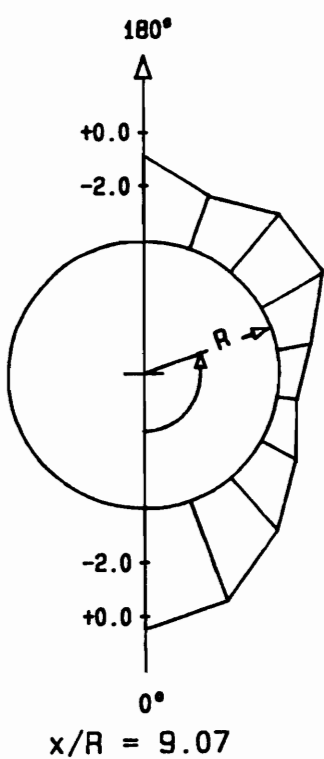
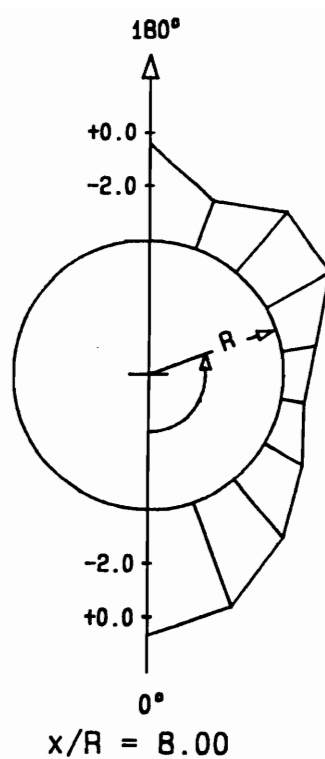
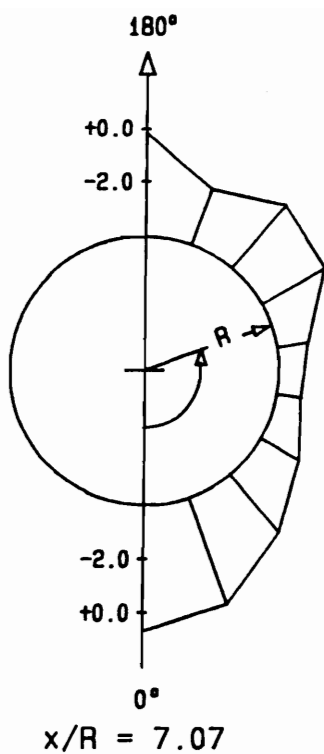


Figure 4.32. Continued.

vortices lifting off from the model's surface near the trailing-edge or perhaps vortex breakdown.

Axial pressure distributions obtained along the leeward meridional for a Reynolds number sweep of $\alpha = 20^\circ$ are presented in Figures 4.33 and 4.34. The separation bubble is once again reduced in length with increasing Reynolds number; although it does not completely disappear. It is interesting to observe that the influence of the Reynolds number on the surface pressure at high Reynolds number flows is apparent, although somewhat localized (only in the region of the separation bubble).

Figures 4.35 - 4.37 and Figures 4.38 - 4.40 display the pressure distributions and pressure coefficient contours for $Re = 2.9 \times 10^5$ and $Re = 4.2 \times 10^5$, respectively, at $\alpha = 30^\circ$. The separation bubble can still be observed in these pressure curves and is isolated to the small region on the top of the model near $x/R = 1.5$. At $Re = 2.9 \times 10^5$, circumferential pressure curves shown in Figure 4.37 do not exhibit any dips although the leeward vortices do exist. At this angle of attack and Reynolds number, the leeward vortices induce very little influences to the surface pressure. At higher Reynolds number, $Re = 4.2 \times 10^5$, leeward vortices become stronger. This results in very pronounced dips displayed by the circumferential pressure curves (Figure 4.40).

Velocity Measurements

To evaluate probe interference with the flow, static pressure distributions of a hemisphere-cylinder were obtained along a meridional plane with the seven-hole probe mounted immediately above the solid surface at different radial locations (Figure 4.3). Pressures along the same line were also measured without the presence of the probe. The effect of the seven-hole probe on the surface pressure is studied. Figure 4.41 displays axial pressure distributions on the model along $\phi = 90^\circ$ and $\alpha = 0^\circ$ with the

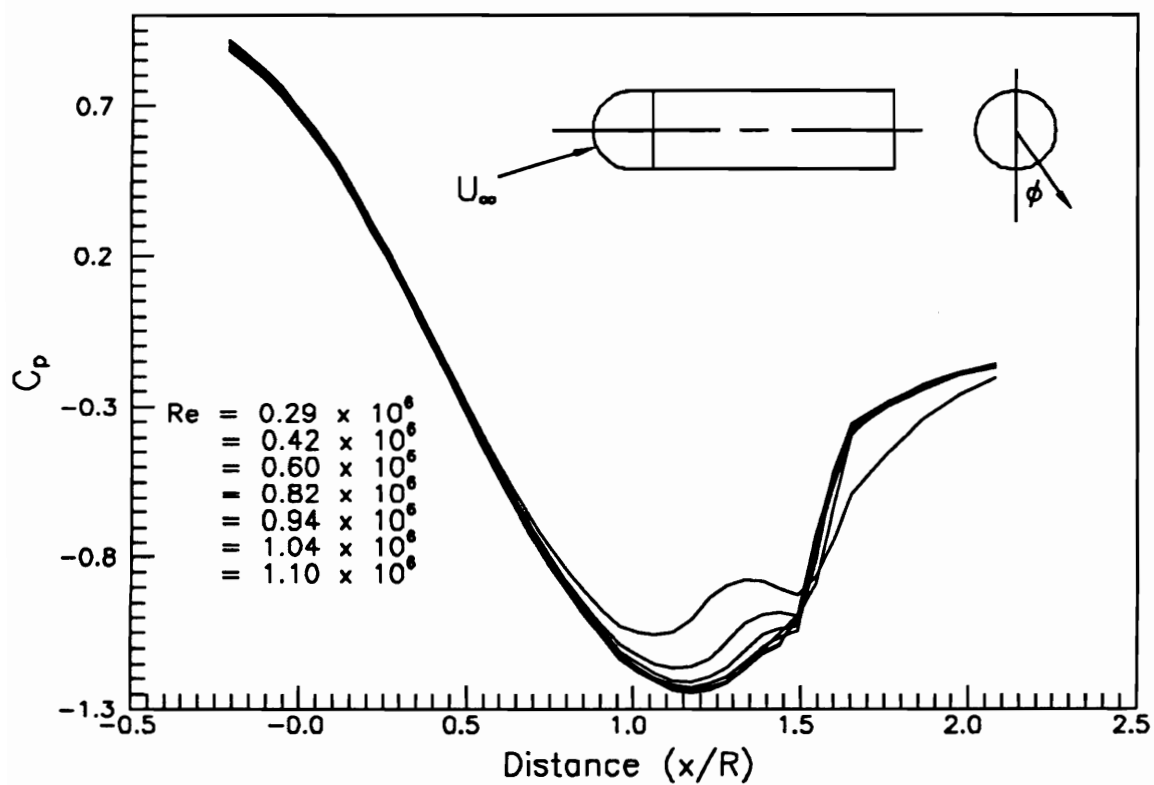


Figure 4.33. Axial pressure distributions on a hemisphere-cylinder at $\alpha = 20^\circ$ and various Reynolds numbers.

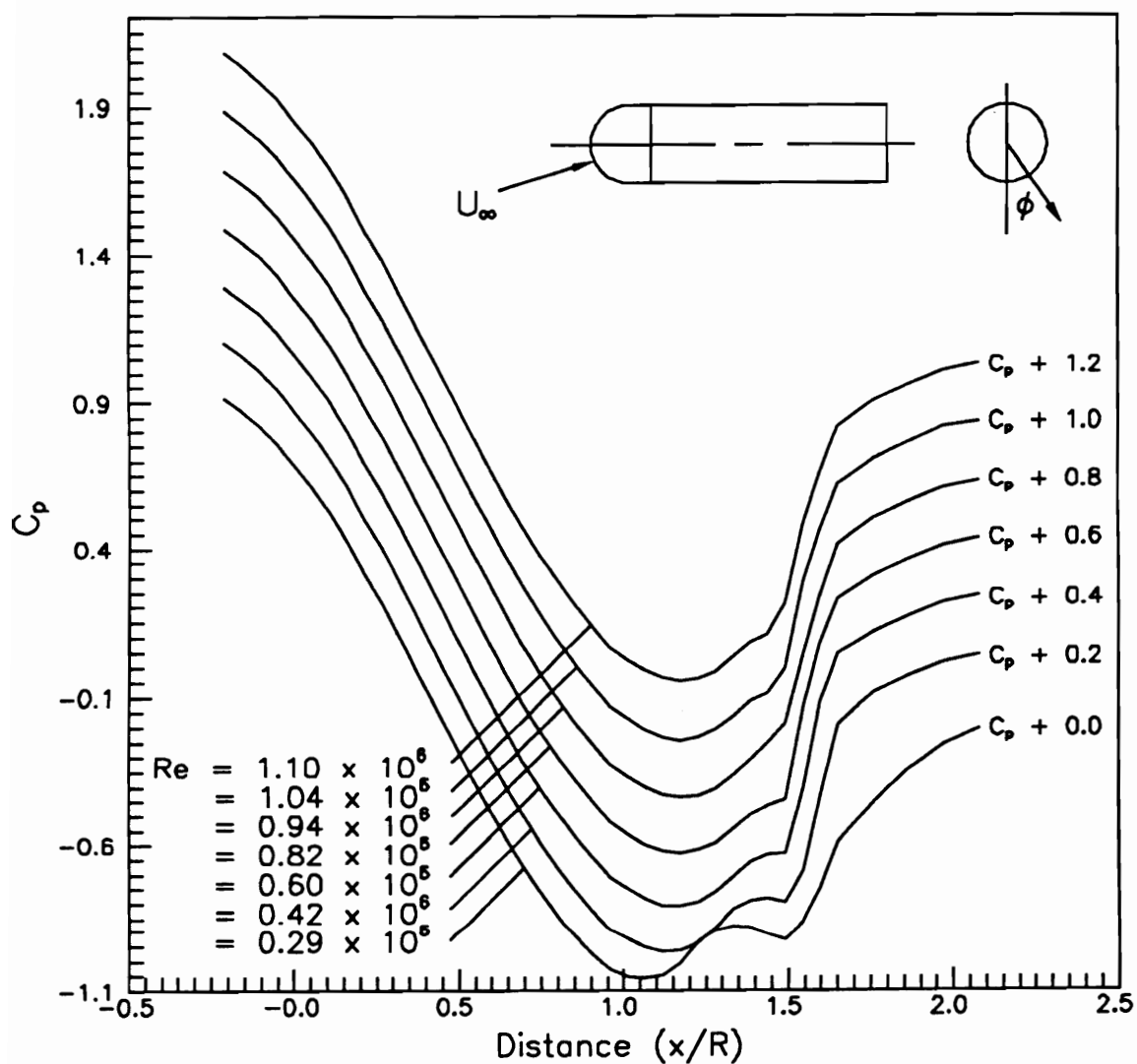


Figure 4.34. Axial pressure distributions on a hemisphere-cylinder at $\alpha = 20^\circ$ and various Reynolds numbers with added constants.

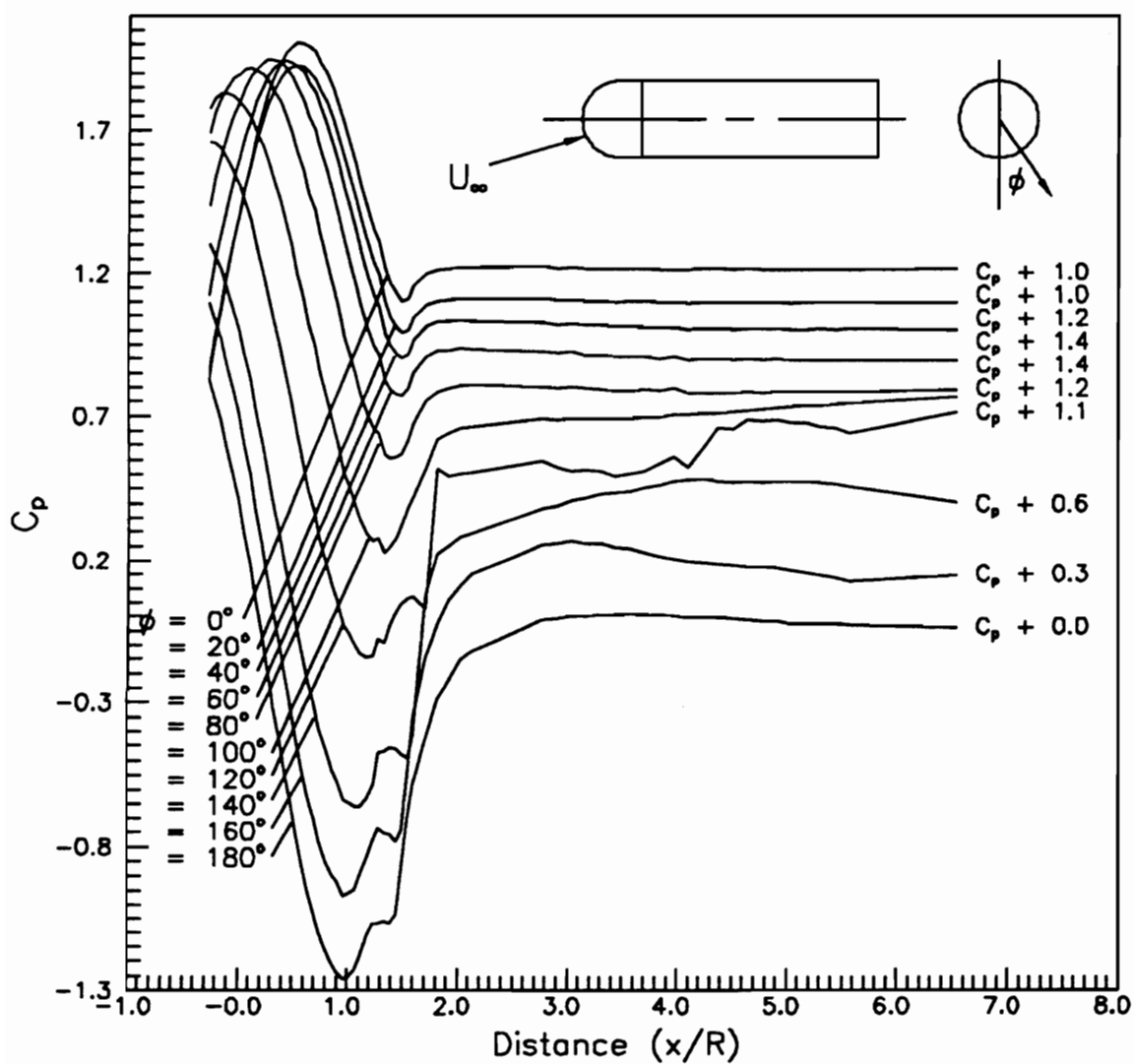


Figure 4.35. Axial pressure distributions on a hemisphere-cylinder at $\alpha = 30^\circ$ and $Re = 2.9 \times 10^5$ with added constants.

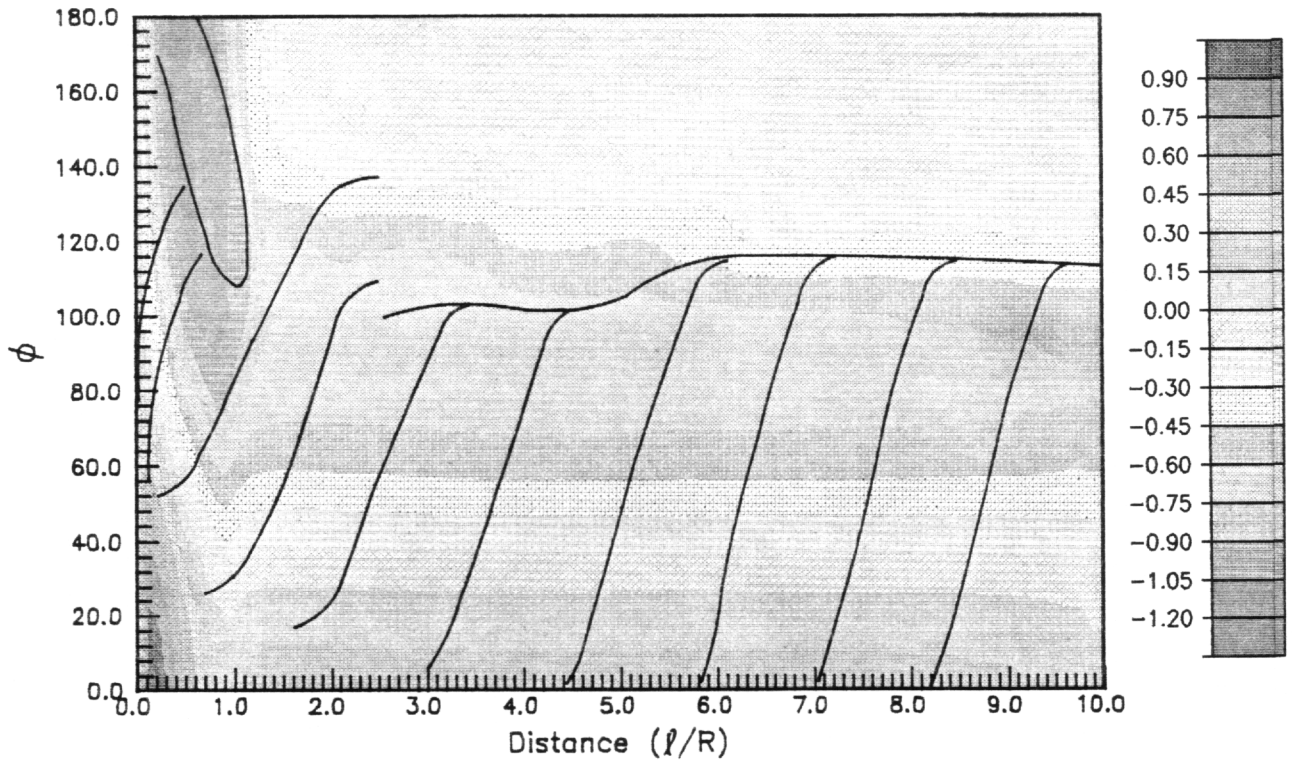


Figure 4.36. Pressure coefficient contours and digitized skin-friction patterns on a hemisphere-cylinder at $\alpha = 30^\circ$ and $Re = 2.9 \times 10^5$.

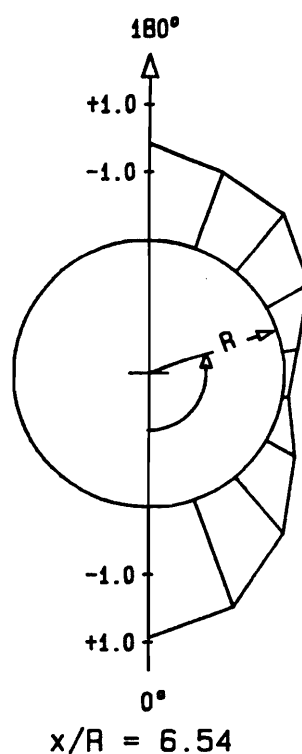
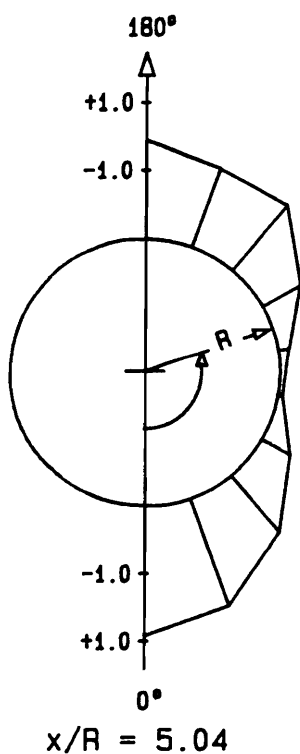
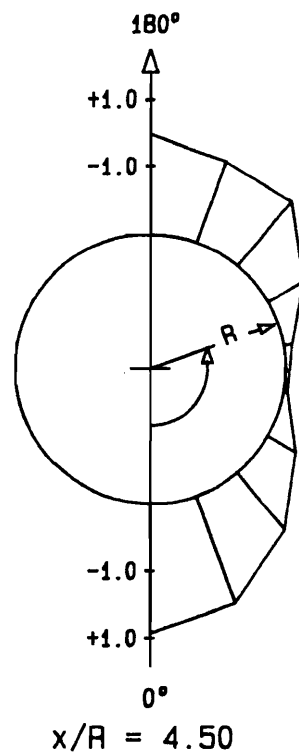
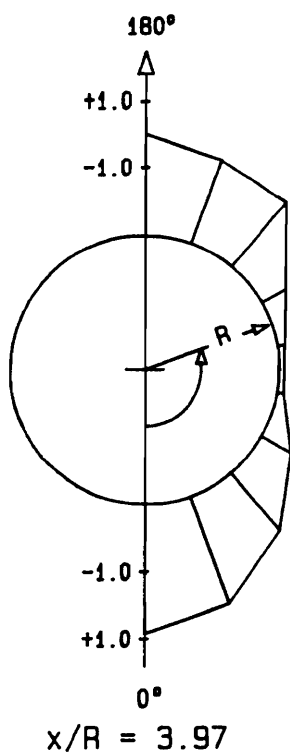


Figure 4.37. Circumferential pressure distributions on a hemisphere-cylinder at $\alpha = 30^\circ$ and $Re = 2.9 \times 10^5$.

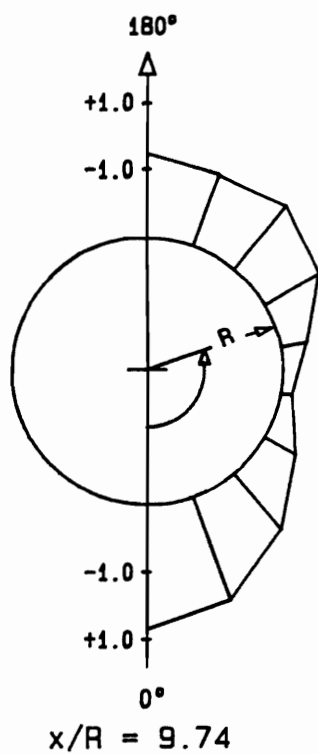
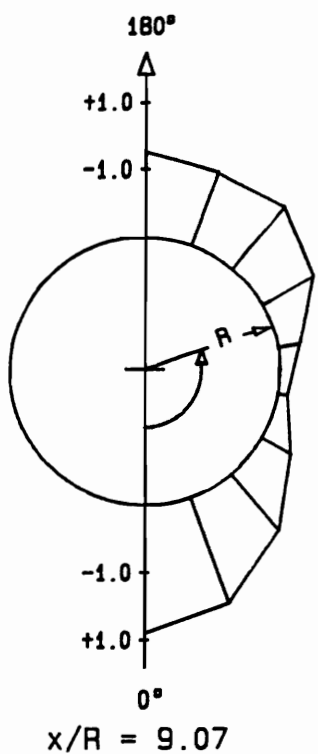
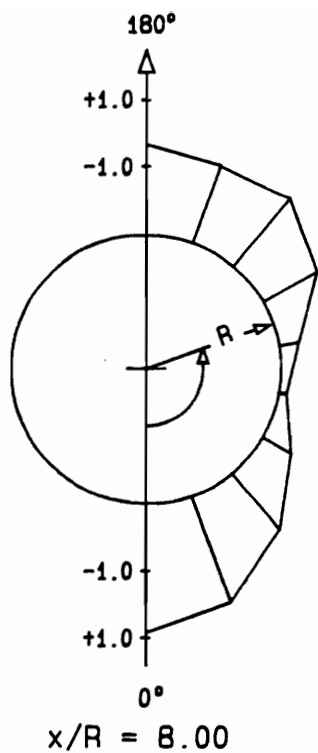
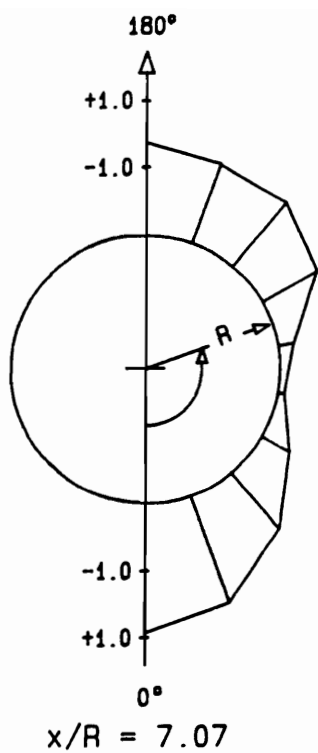


Figure 4.37. Continued.

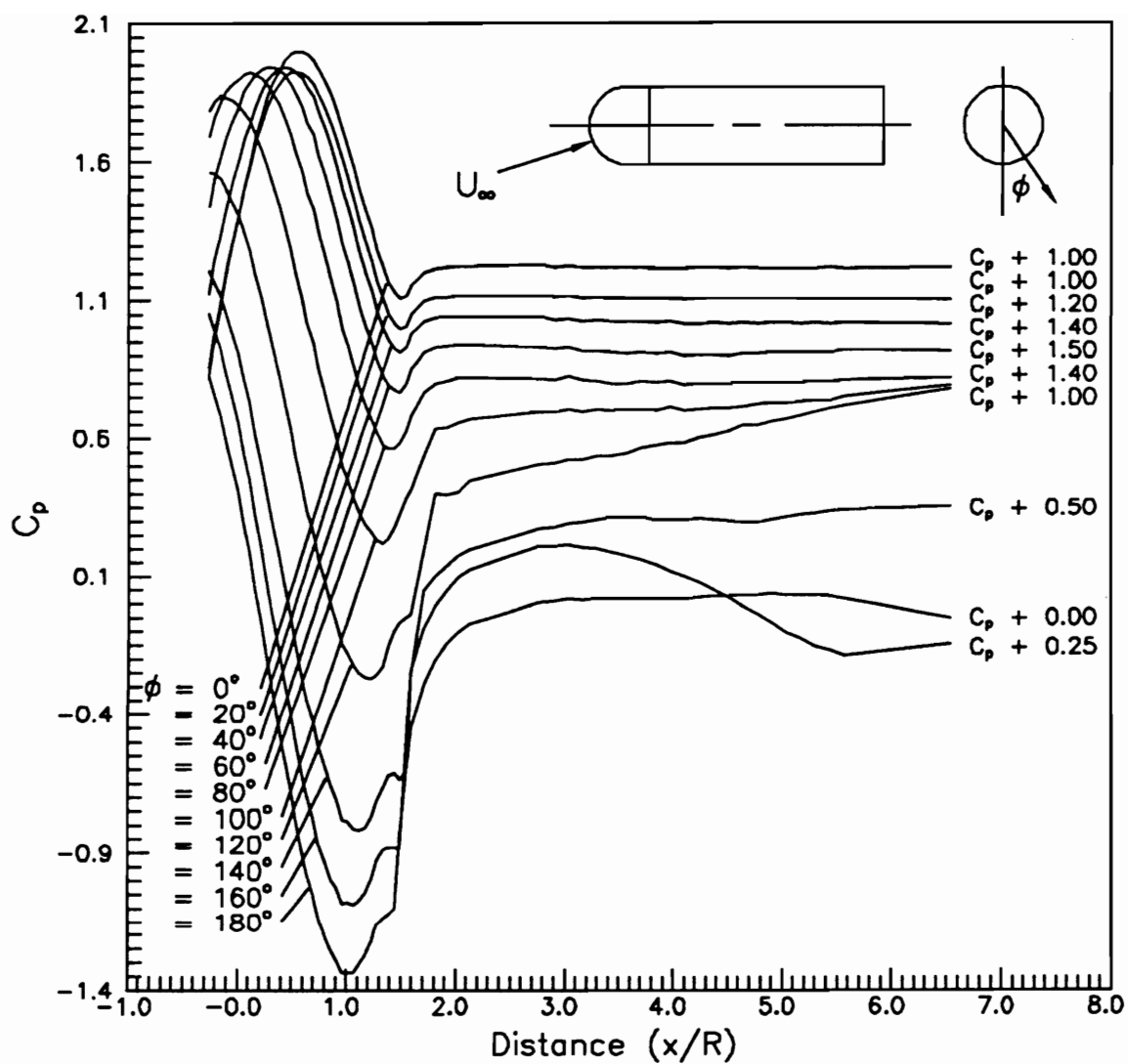


Figure 4.38. Axial pressure distributions on a hemisphere-cylinder at $\alpha = 30^\circ$ and $Re = 4.2 \times 10^5$ with added constants.

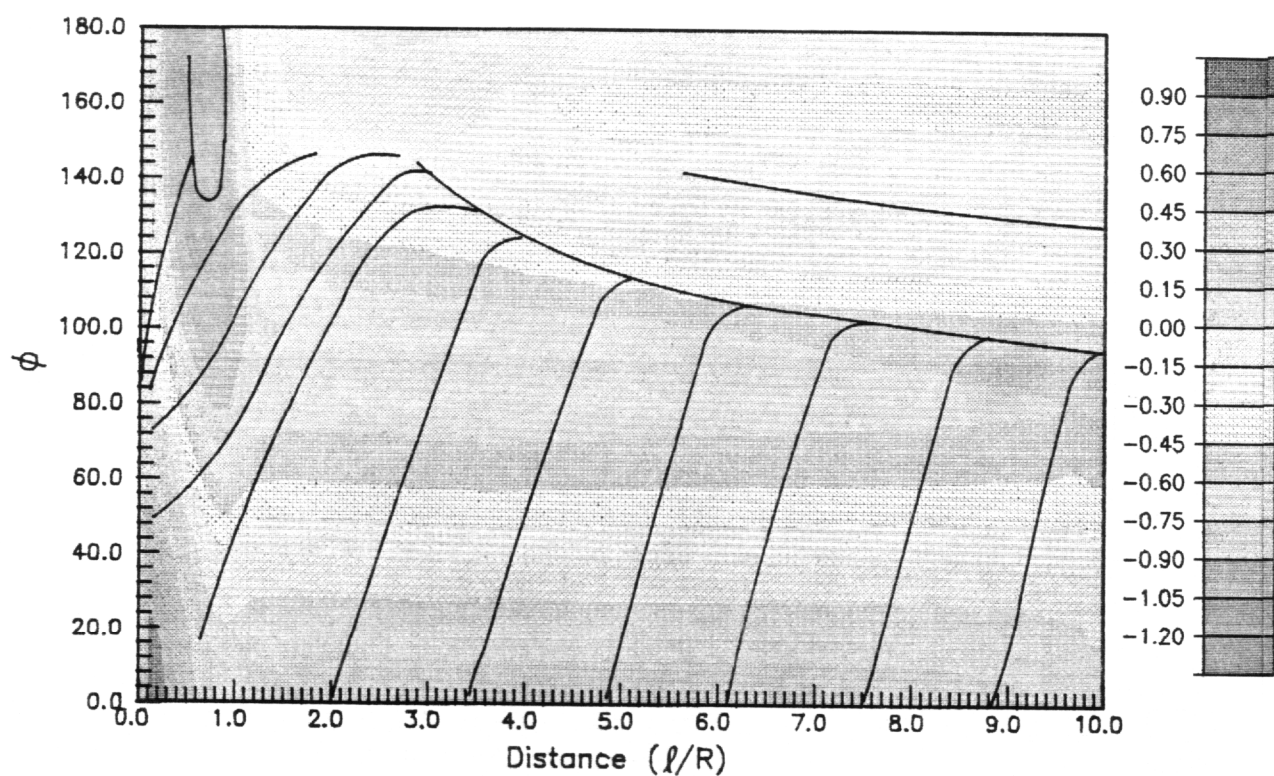


Figure 4.39. Pressure coefficient contours and digitized skin-friction patterns on a hemisphere-cylinder at $\alpha = 30^\circ$ and $Re = 4.2 \times 10^5$.

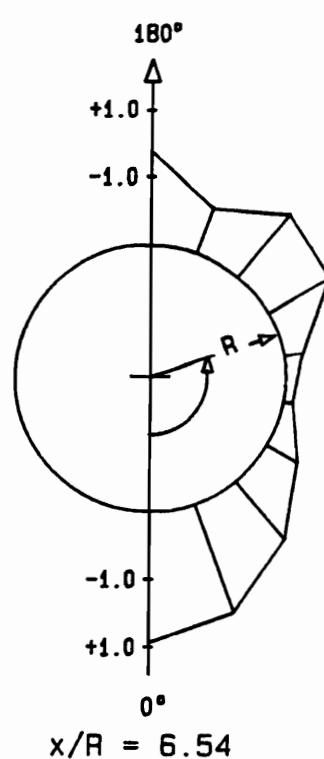
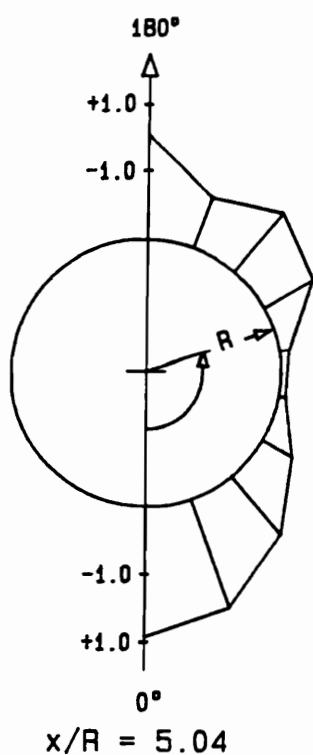
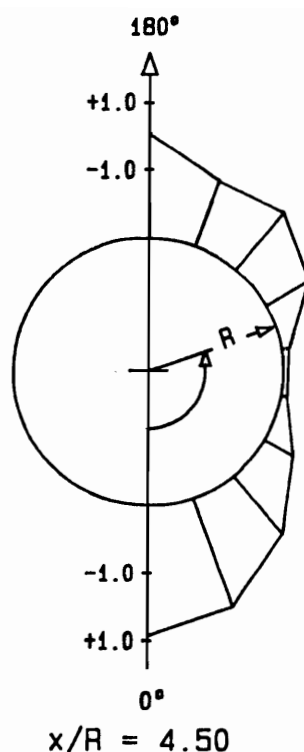
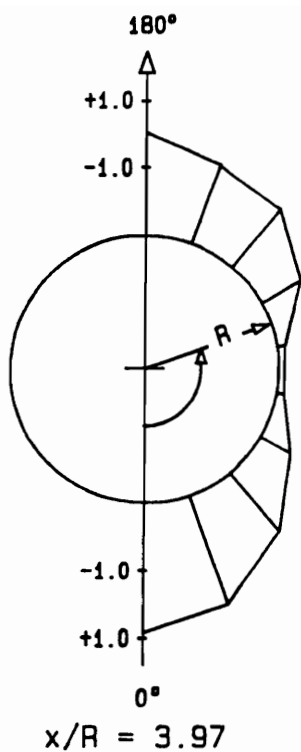


Figure 4.40. Circumferential pressure distributions on a hemisphere-cylinder at $\alpha = 30^\circ$ and $Re = 4.2 \times 10^5$.

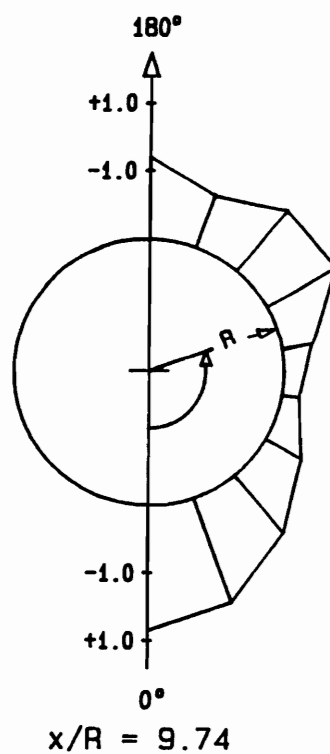
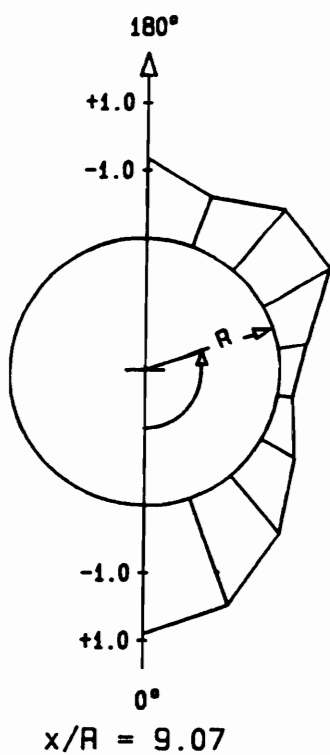
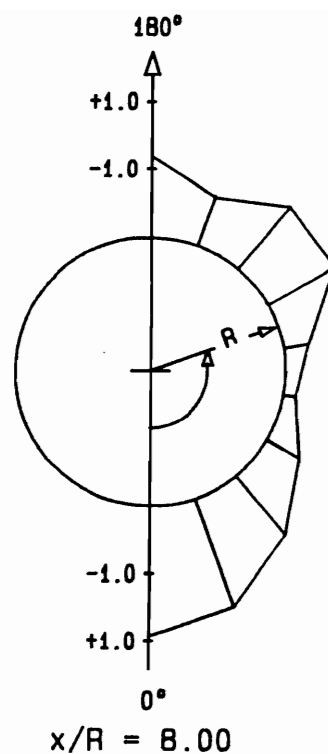
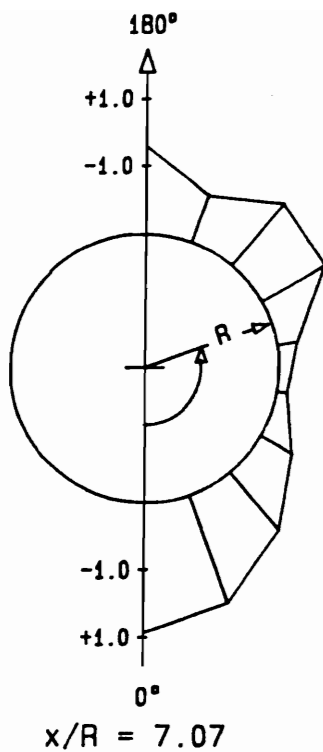


Figure 4.40. Continued.

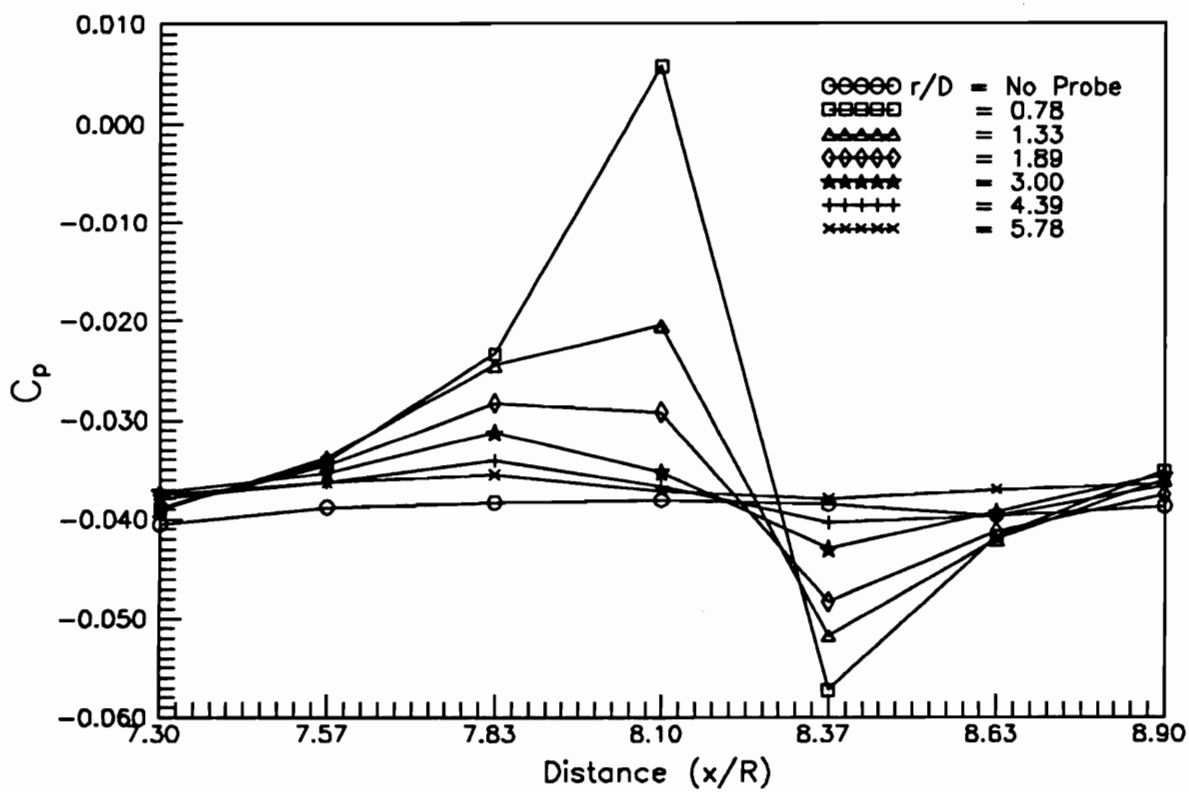


Figure 4.41. Pressure distributions on a hemisphere-cylinder at $\alpha = 0^\circ$ with the seven-hole probe mounted at different radial locations and $\phi = 90^\circ$.

seven-hole probe placed at various radial locations. The tip of the seven-hole probe was at $x/R = 8.1$. The free-stream velocity was 37 ft/sec, corresponding to a Reynolds number of 1.5×10^5 . The symbols r and D in this figure represent the radial distance from the surface of the model to hole#1 of the seven-hole probe and the diameter of the seven-hole probe, respectively. From the figure, it is obvious that when the probe is at about three probe-diameters away from the model's surface, the pressure coefficients are restored to their original values. For $\alpha = 30^\circ$ and $Re = 1.5 \times 10^5$, the probe was positioned outside and inside the vortex at $\phi = 90^\circ$ and 170° , respectively. The probe had a noticeable effect on the surface pressure data only when located at less than two probe-diameters away from the model's surface (Figure 4.42).

The cross-plane velocity vectors obtained with a seven-hole probe at six different axial stations are displayed in Figures 4.43-4.48. These figures show the development of the flow in crossflow plane along the body. The experiments were conducted at an angle of attack $\alpha = 20^\circ$ and $Re = 1.5 \times 10^5$. At $x/R = 5.8$ (Figure 4.43), the leeward vortex is small but clearly visible with the core at approximately $\phi = 165^\circ$. Separation occurs near $\phi = 145^\circ$ and then moves toward $\phi \simeq 130^\circ$ at $x/R = 10.0$. The vortex appears to grow both in size and strength with downstream distance but still forms well beyond $\phi = 90^\circ$. This is perhaps due to the fact that for $\alpha = 20^\circ$, the axial component of the motion is quite dominant and the cross-flow deviates substantially from the two-dimensional case. At $x/R = 8.1$ and 8.4 (Figures 4.45 and 4.46), the primary and secondary separation points are found at $\phi \simeq 120^\circ$ and 145° , respectively. The core of the leeward vortex remains at $\phi \simeq 165^\circ$. There exists another smaller vortex (secondary vortex) in the region between the primary and secondary separation points. It rotates in the same direction as the dominant leeward vortex. The dominant vortex will be referred in the sequel as the primary vortex. Hsieh [1977] reported a possible appearance of three vortices in the wake of a hemisphere-cylinder at an angle of attack. He named

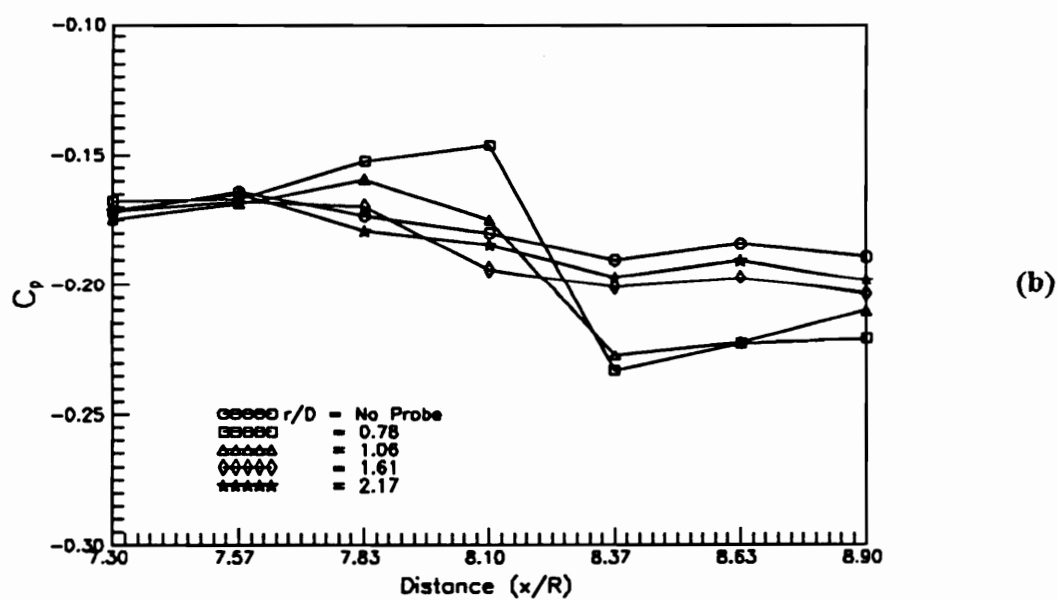
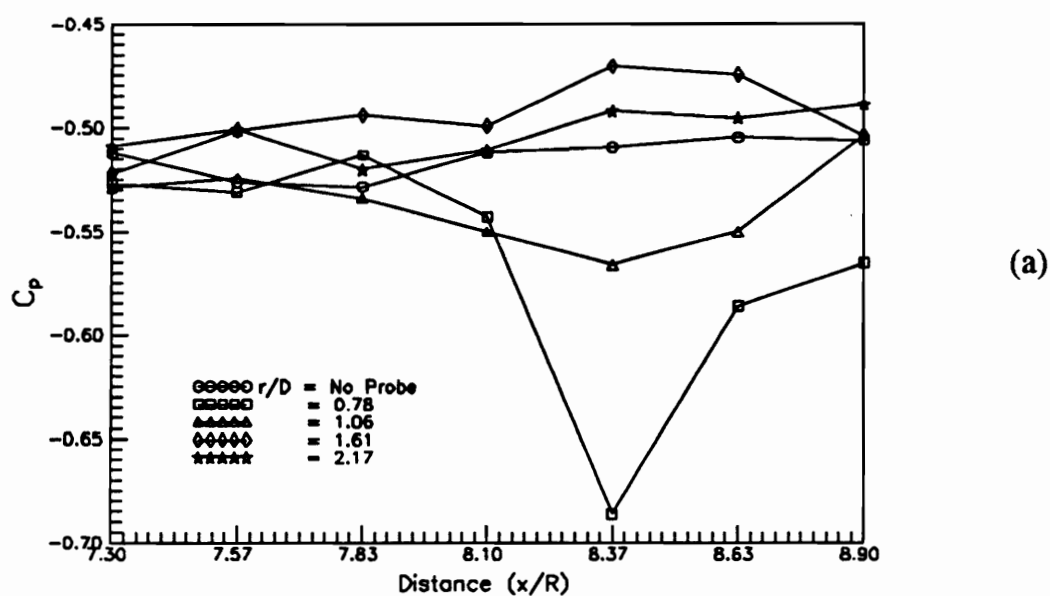


Figure 4.42. Pressure distributions on a hemisphere-cylinder at $\alpha = 30^\circ$ with the seven-hole probe at (a) $\phi = 90^\circ$ (b) $\phi = 170^\circ$.

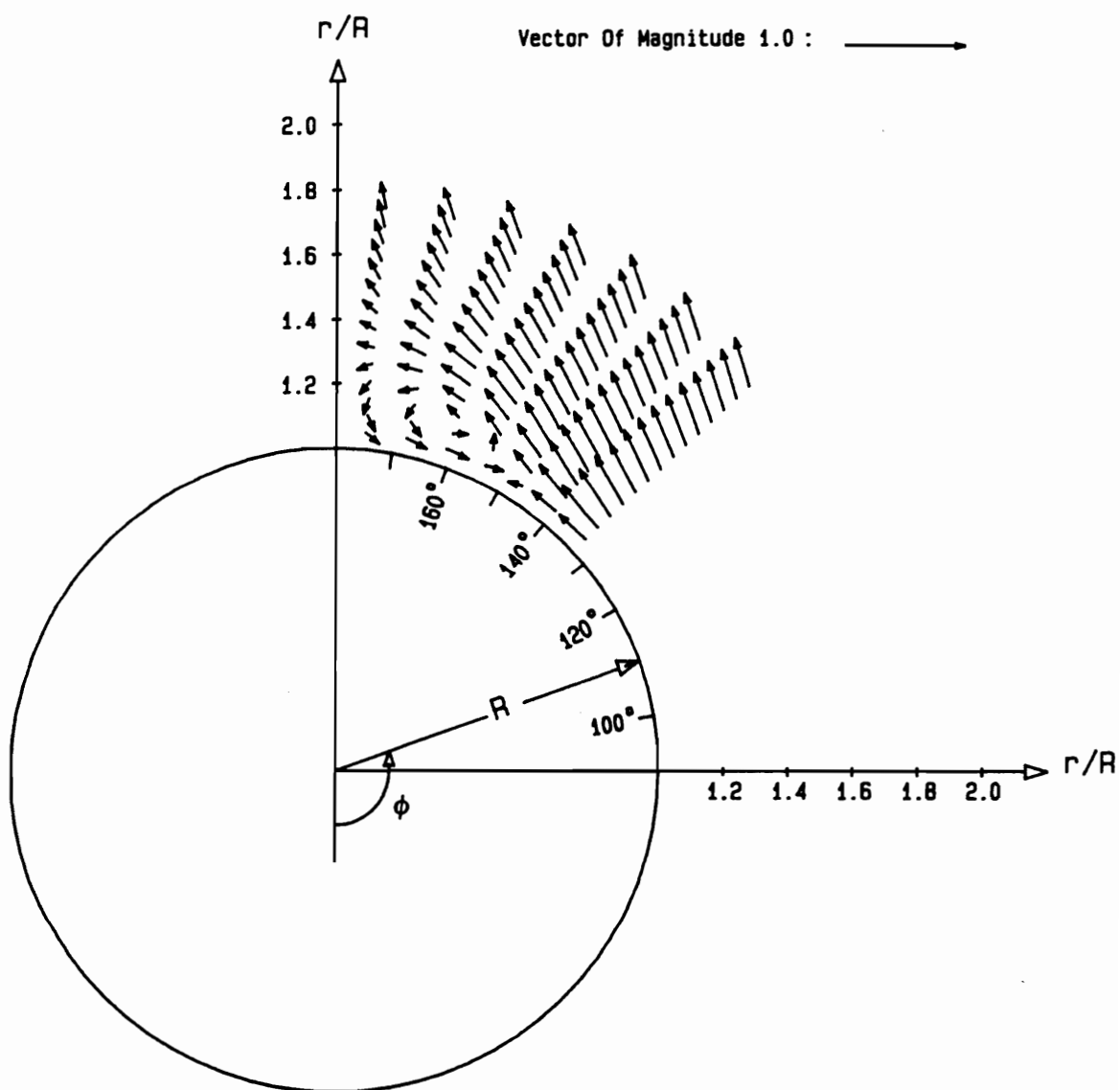


Figure 4.43. Seven-hole probe velocity vector fields along a normal plane at $x/R = 5.8$, $\alpha = 20^\circ$, and $Re = 1.5 \times 10^5$.

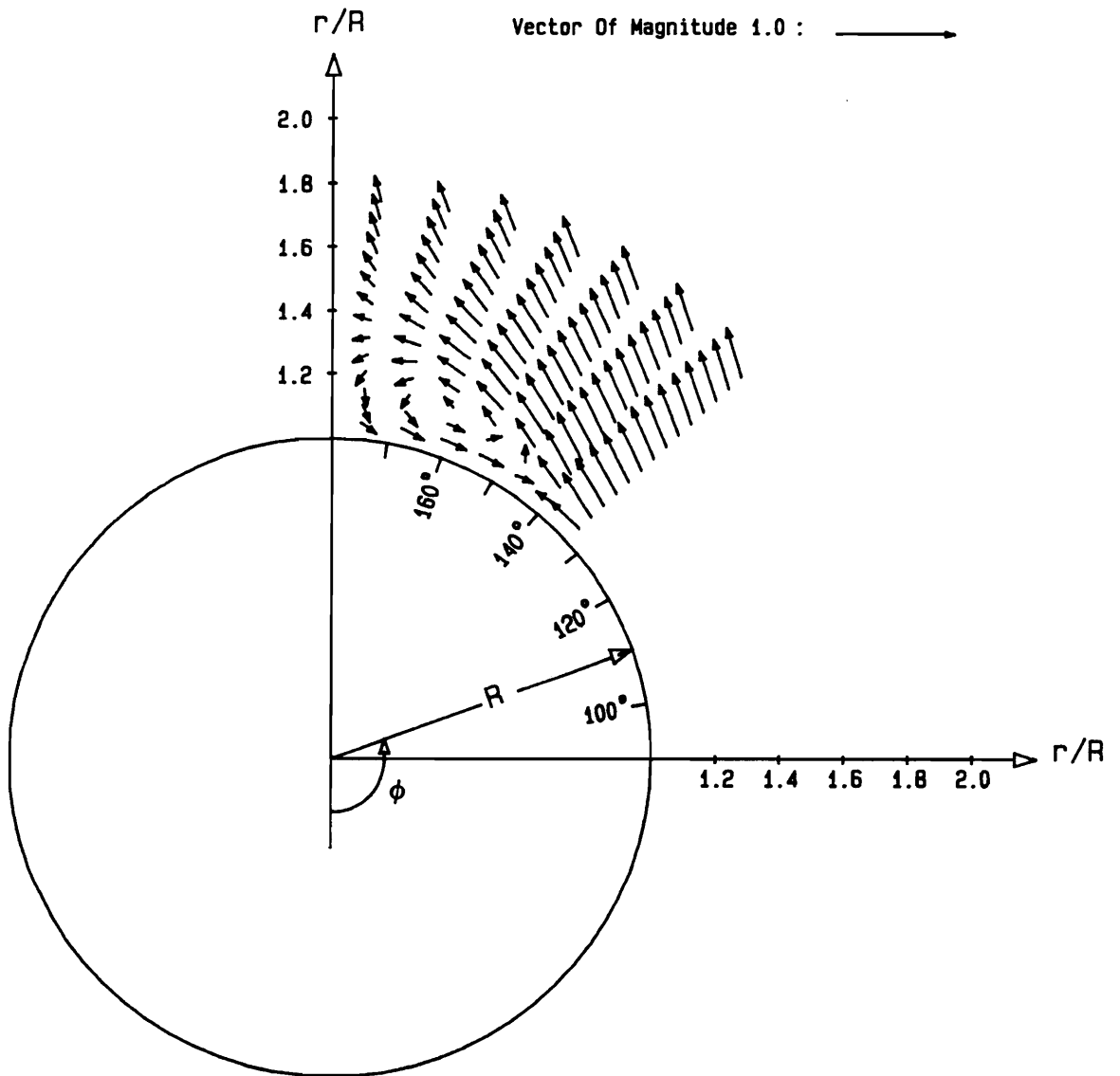


Figure 4.44. Seven-hole probe velocity vector fields along a normal plane at $x/R = 6.1$, $\alpha = 20^\circ$, and $Re = 1.5 \times 10^5$.

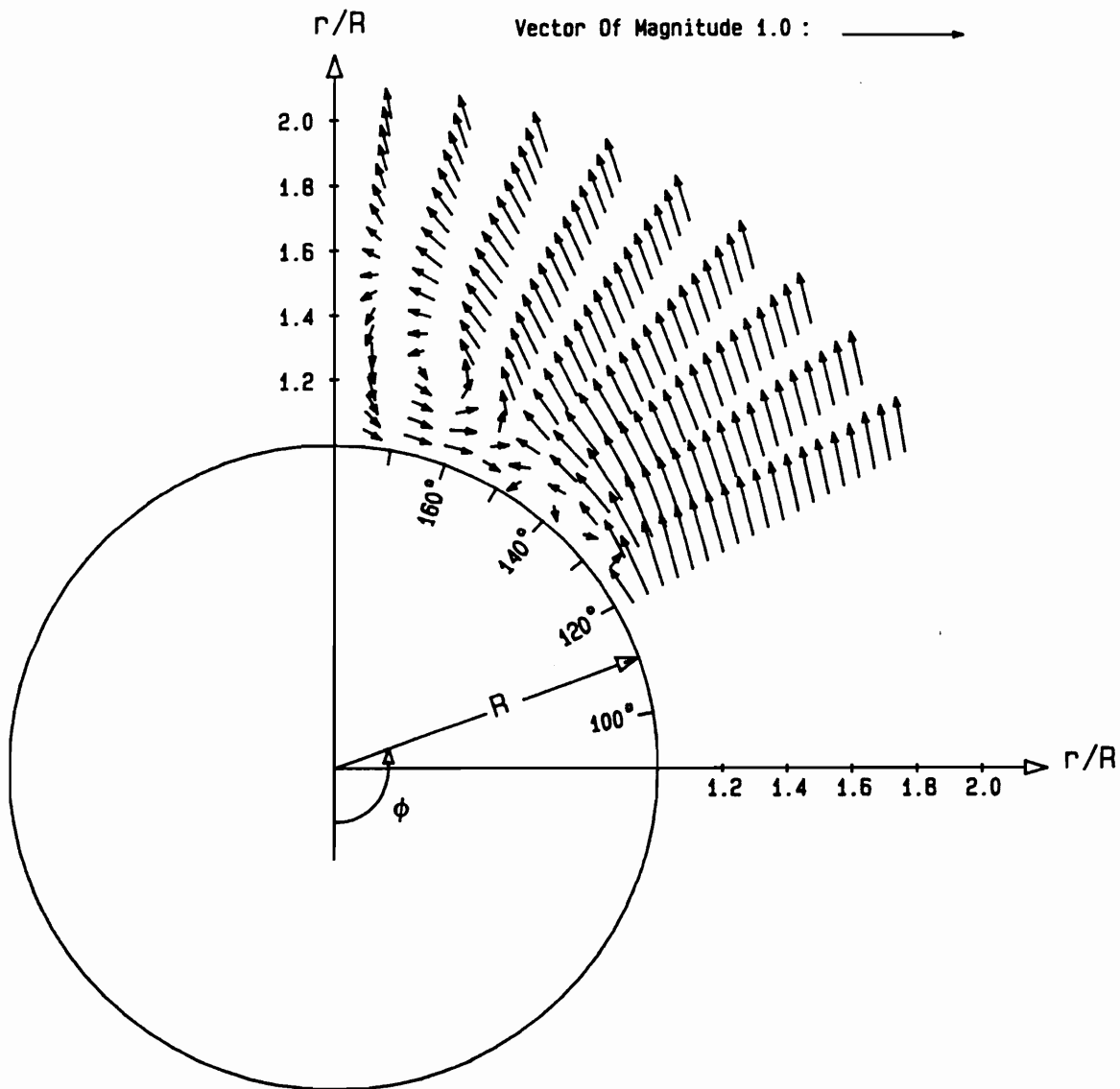


Figure 4.45. Seven-hole probe velocity vector fields along a normal plane at $x/R = 8.1$, $\alpha = 20^\circ$, and $Re = 1.5 \times 10^5$.

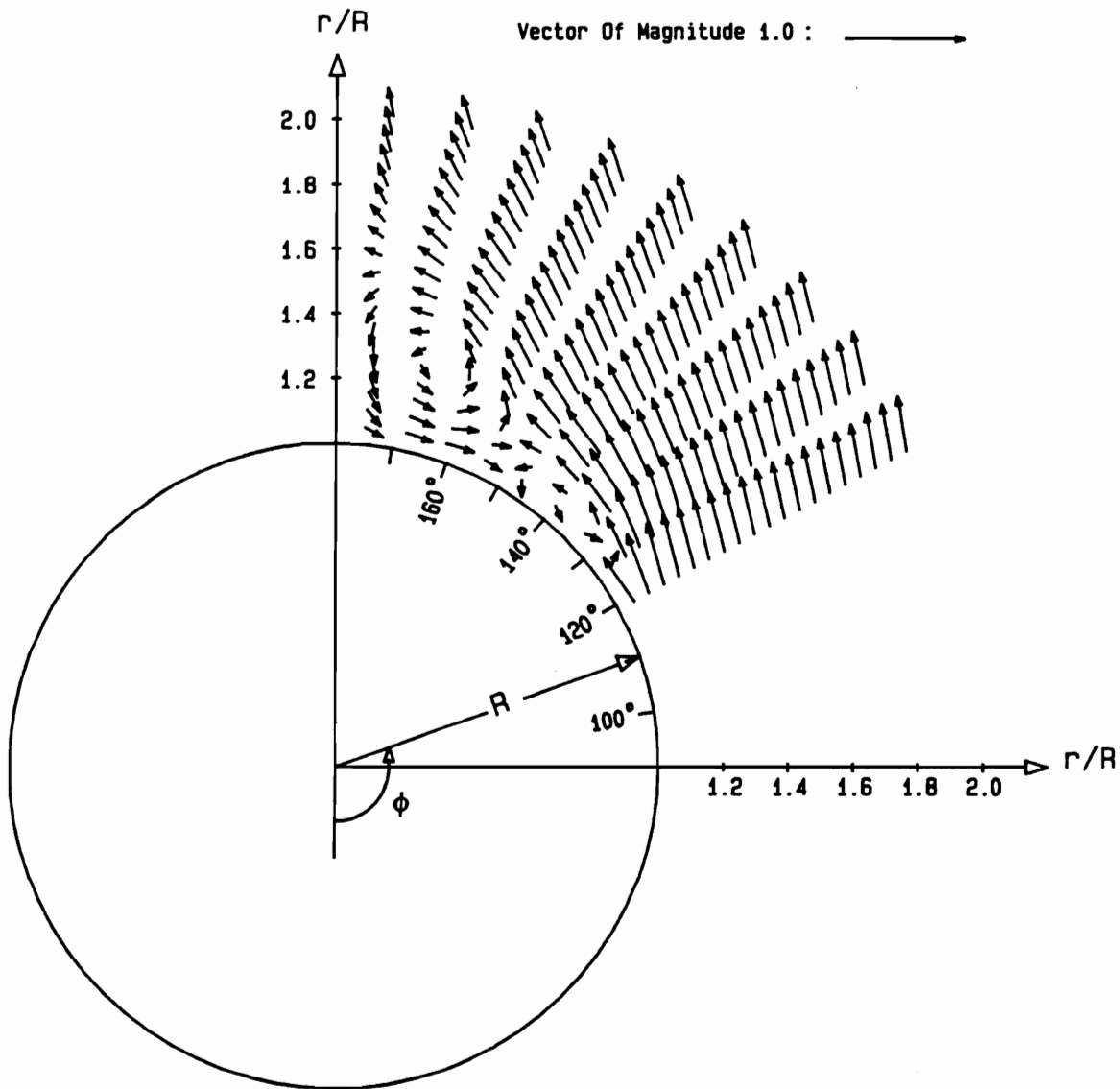


Figure 4.46. Seven-hole probe velocity vector fields along a normal plane at $x/R = 8.4$, $\alpha = 20^\circ$, and $Re = 1.5 \times 10^5$.

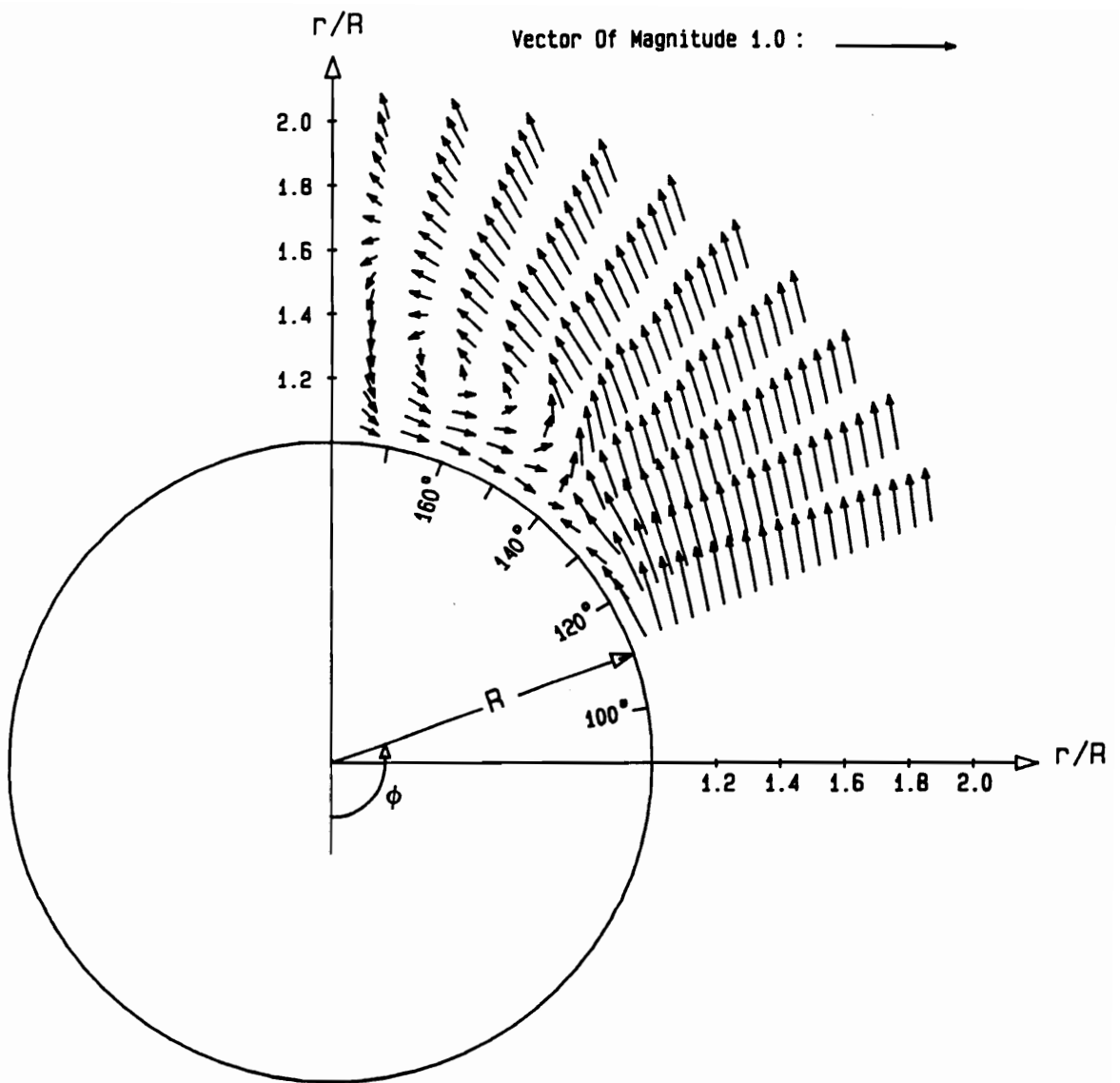


Figure 4.47. Seven-hole probe velocity vector fields along a normal plane at $x/R = 9.7$, $\alpha = 20^\circ$, and $Re = 1.5 \times 10^5$.

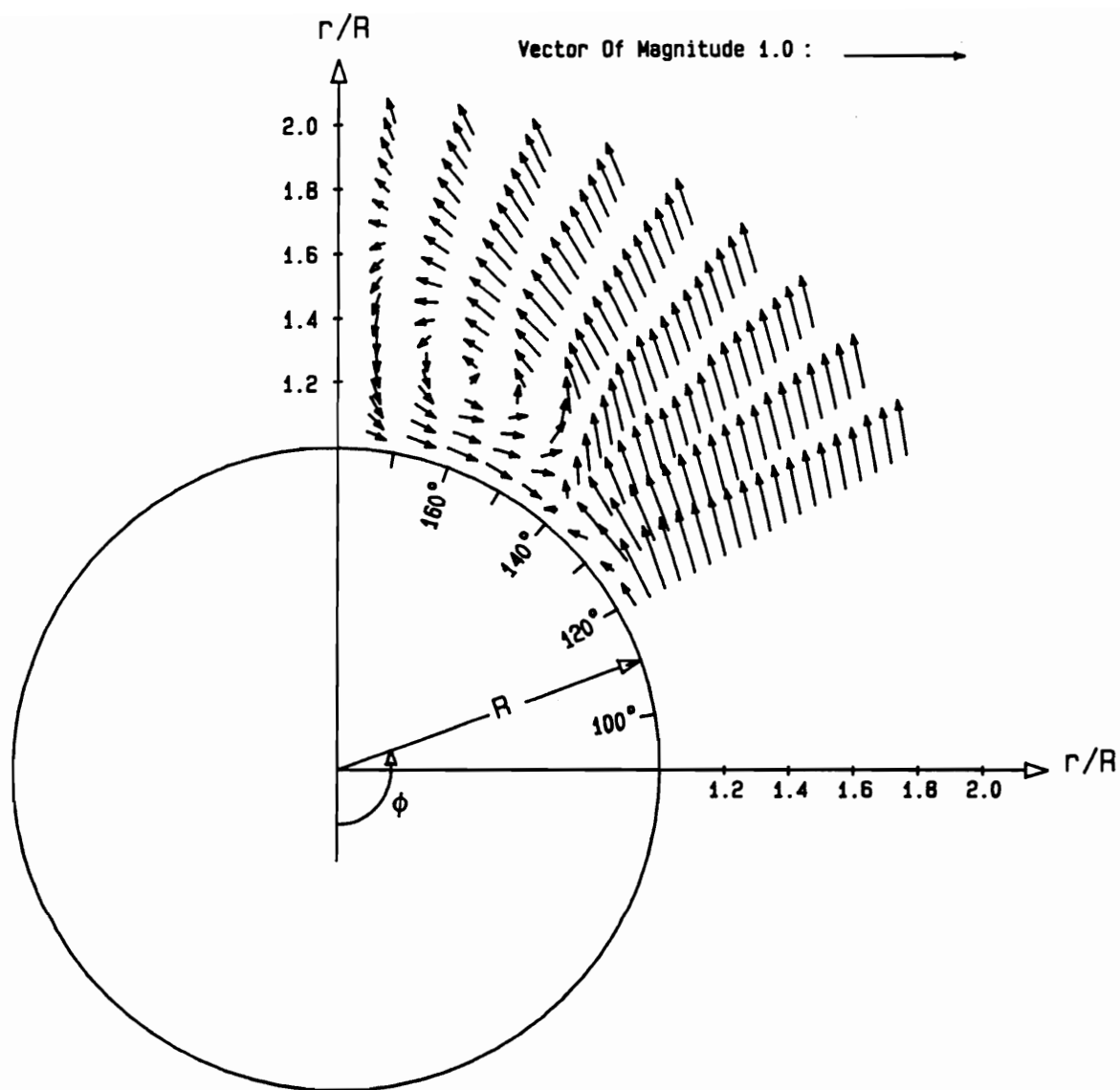


Figure 4.48. Seven-hole probe velocity vector fields along a normal plane at $x/R = 10.0$, $\alpha = 20^\circ$, and $Re = 1.5 \times 10^5$.

these primary, secondary and tertiary vortices (Figure 3.2). The existence of a third vortex proposed by Hsieh is not detected here. At $x/R = 9.7$ and 10.0 (Figures 4.47 and 4.48), the secondary vortex disappears.

Velocity data obtained with a fiber-optic LDV probe and a seven-hole probe under the same conditions are plotted in Figures 4.49-4.54. The purpose is to compare the accuracy of the velocity data taken with the seven-hole probe. At $x/R = 5.8$, data for the circumferential component shown in Figure 4.49 indicates a good agreement away from the vortex and some deviation within the vortex. Apparently, the seven-hole probe registers consistently lower values within the recirculating region. There is little influence in the axial component (Figure 4.50a), except again within the vortex, where the values obtained by the seven-hole probe are lower (Figures 4.50b and 4.50c). At this station, the ratio of the size of the probe to the size of the vortex is quite large, therefore, the probe generates a global interference to the flow. Large errors are registered at every ϕ within the vortex. The differences of 46% and 17% are seen in the V_ϕ and V_z components of velocity, respectively. Insertion of the probe at locations where the vortex is still small and weak may distort the flow and induces some sort of vortex breakdown. At $x/R = 9.7$ and 10.0 (Figures 4.51-4.54), the errors in both axial and circumferential components of velocity are confined to the neighborhood of the shear-layer near the point of separation, $\phi = 140^\circ$. The probe has little effect on the flow within the vortex since the wake had already developed into a strong leeward vortex. For this case, errors involved in seven-hole probe data are probably due to large local velocity gradients in a plane parallel to the axis of the the seven-hole probe. Moreover, the seven-hole probe has a much smaller spatial resolution than the fiber-optic LDV probe, since its effective measuring volume is 4.572 mm compare to 50 microns of the LDV probe.

Similar discrepancies between multiple-hole probes and LDV data for delta wing flows were also reported by Taylor et al. [1987] and Rediniotis et al. [1990]. These au-

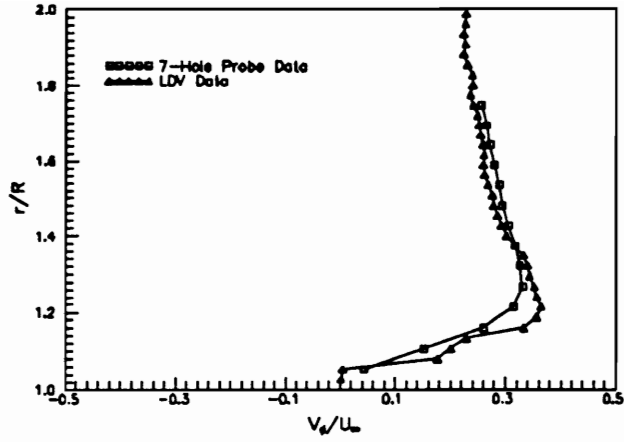
thors reported deviations of LDV and five-hole probe data as high as 40% of each other for all three velocity components in the vicinity of high flow angularities and high velocity gradients (i.e. the vortex core). However, the two techniques agree well in regions of low shear and flow angularity.

Seven-hole probe data at stations $x/R = 5.8, 6.1, 8.1$ and 8.4 are presented in Figures 4.55-4.58, respectively. The experiments were conducted at a Reynolds number of 1.5×10^5 and $\alpha = 30^\circ$. At $x/R = 5.8$ and 6.1 , the cross-flow is strong which causes the boundary-layer to separate at about $\phi = 100^\circ$. Figures 4.55 and 4.56 reveal an area of recirculating flow around $130^\circ \leq \phi \leq 150^\circ$. The vortical structure is not very well organized. Perhaps the whole flow field is affected by the presence of the probe because the size of the vortex at this station is still small. At $x/R = 8.1$ and 8.4 , both primary and secondary vortices are observed (Figures 4.57 and 4.58) and the primary vortex core locates near $\phi = 140^\circ$. The size of these vortices are much bigger than the $\alpha = 20^\circ$ case. Again, a third vortex is not detected along the afterbody of the model at this angle of attack. At station $x/R = 5.8$, the agreement between the two methods outside the recirculating region is acceptable as shown in Figures 4.59a and 4.60a. The profiles of Figures 4.59b and 4.60b on the other hand indicate a violent departure between the two methods of measurement in the vicinity of the vortex core. LDV data show much larger velocity values in the circumferential direction, and therefore a much larger values of vorticities in the vortex.

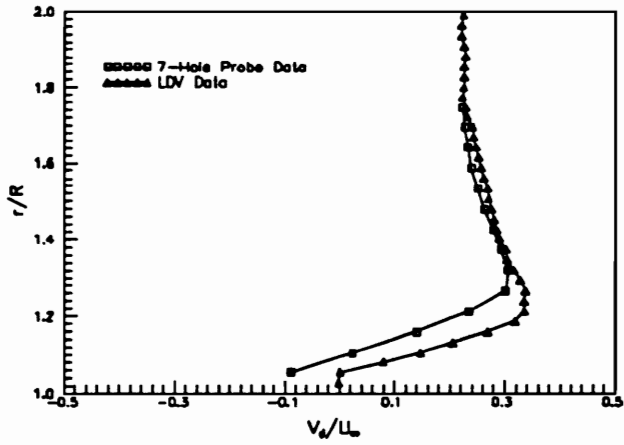
Figure 4.61 displays LDV data taken along $\phi = 160^\circ$, $x/R = 8.1$, for $Re = 1.5 \times 10^5$ with the presence of the seven-hole probe. The probe was mounted at a fixed location, $r/R = 1.2$, $\phi = 160^\circ$, $x/R = 8.15$. It would be more desirable to have the probe moving with the LDV measuring volume instead of keeping it fixed. However, this setup was not possible since there was only one traversing mechanism available at the time. LDV data without the seven-hole probe and the seven-hole probe data at the

same location are also plotted on Figure 4.61. LDV data with the probe consistently register values lower than LDV data without the probe and the seven-hole probe data register the lowest values at all locations inside the vortex. The results also show that the seven-hole probe has a global effect on the flow since the LDV data with the probe indicate that errors are not isolated to regions around the probe.

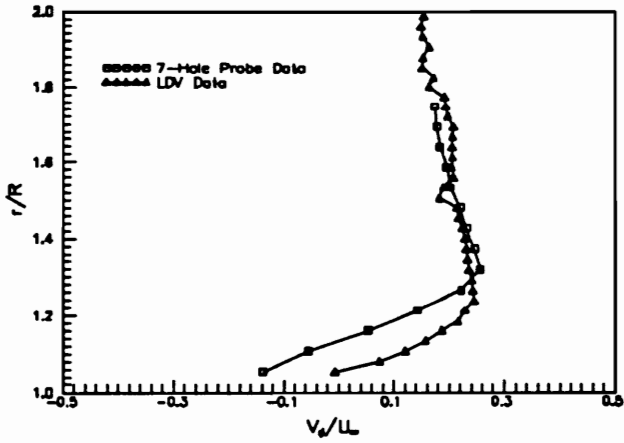
Velocity power spectra in the wake of the hemisphere-cylinder model were obtained by performing a fast-Fourier transformation on the time record of the LDV data. The results did not show any spikes, indicating the absence of any organized unsteady motion. Hot-wire anemometers were also used to detect vortex unsteadiness at $0^\circ \leq \alpha \leq 30^\circ$ and for $Re > 1.5 \times 10^5$. Again, no organized unsteady motion was found. It will be seen later in Chapter 5 that vortex shedding is identified for all angles of attack greater than 15° at Reynolds number of 2.0×10^4 .



(a)

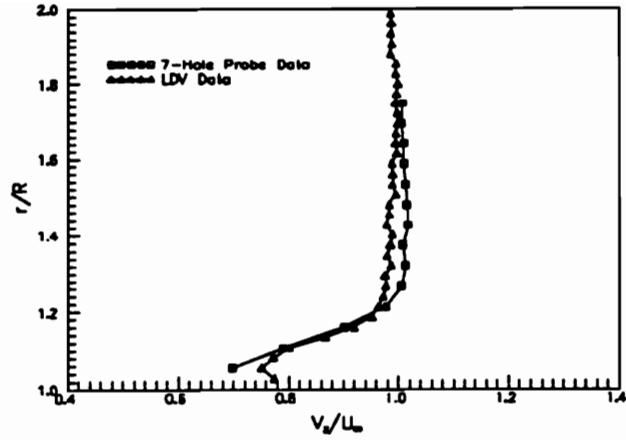


(b)

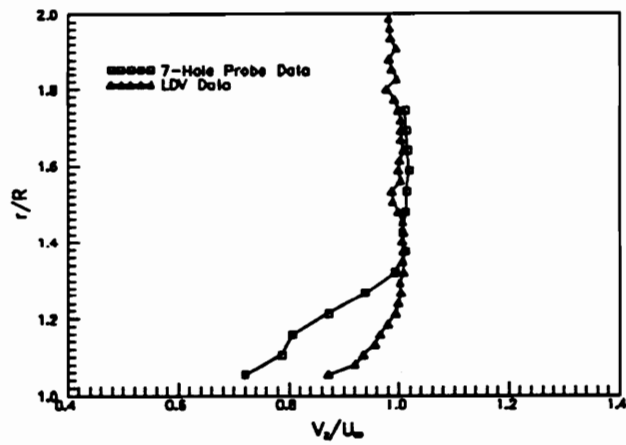


(c)

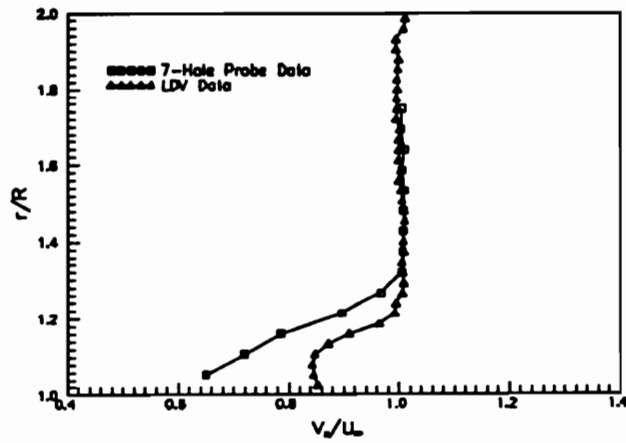
Figure 4.49. LDV and seven-hole probe circumferential velocity profiles at $x/R = 5.8$, $\alpha = 20^\circ$ (a) $\phi = 147^\circ$ (b) $\phi = 154^\circ$ (c) $\phi = 161^\circ$.



(a)

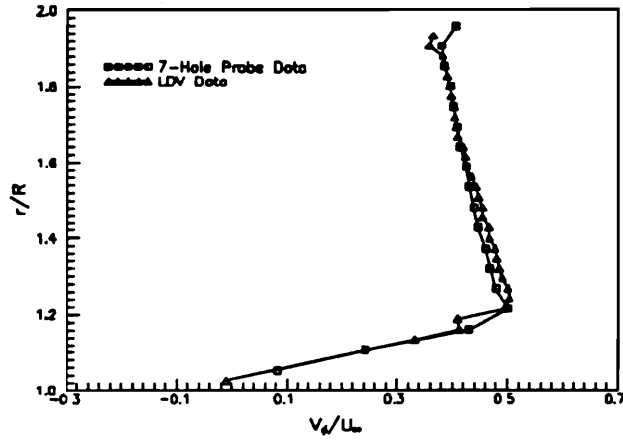


(b)

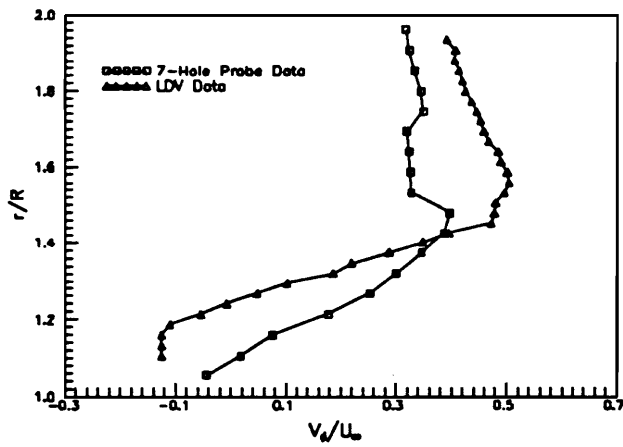


(c)

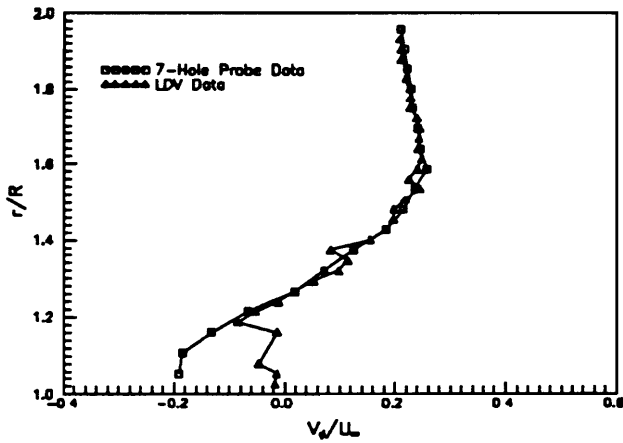
Figure 4.50. LDV and seven-hole probe axial velocity profiles at $x/R = 5.8$, $\alpha = 20^\circ$ (a) $\phi = 147^\circ$ (b) $\phi = 154^\circ$ (c) $\phi = 161^\circ$.



(a)

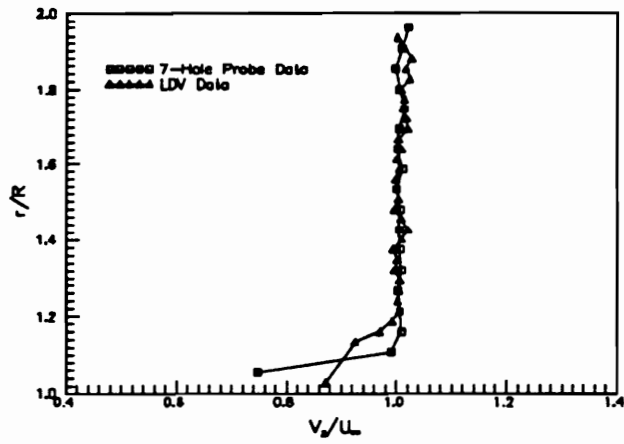


(b)

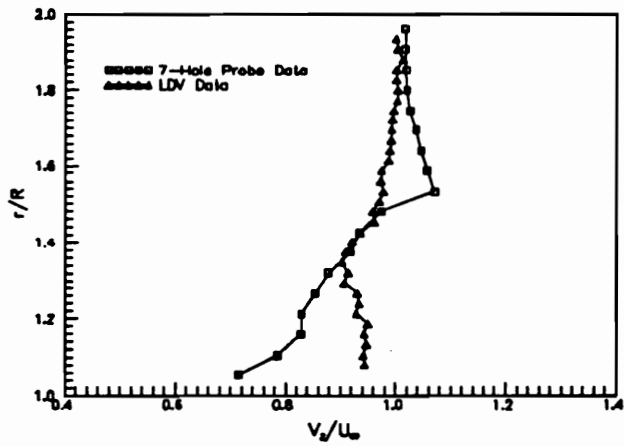


(c)

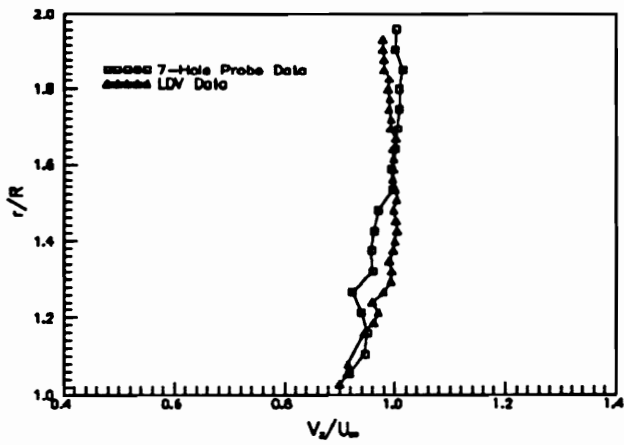
Figure 4.51. LDV and seven-hole probe circumferential velocity profiles at $x/R = 9.7$, $\alpha = 20^\circ$ (a) $\phi = 119^\circ$ (b) $\phi = 140^\circ$ (c) $\phi = 161^\circ$.



(a)

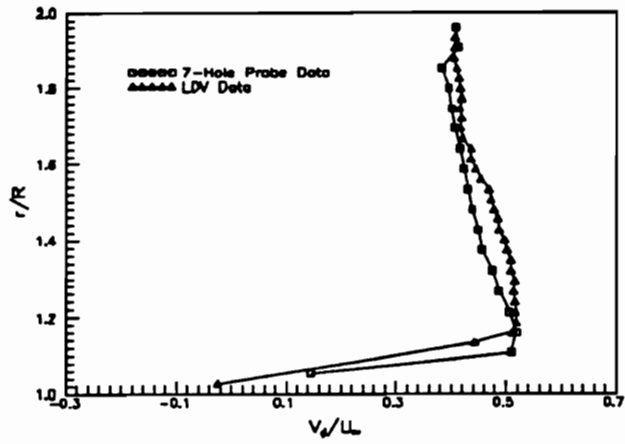


(b)

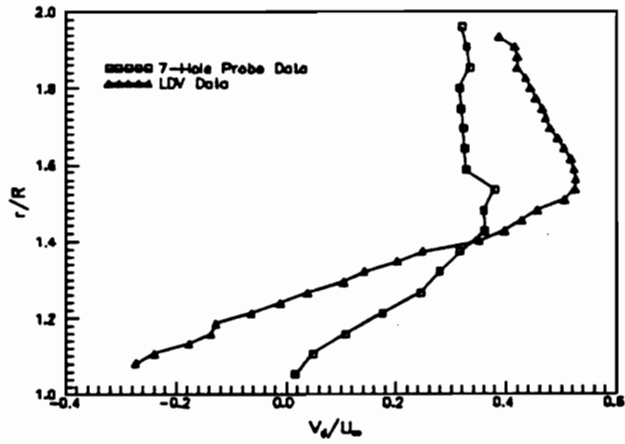


(c)

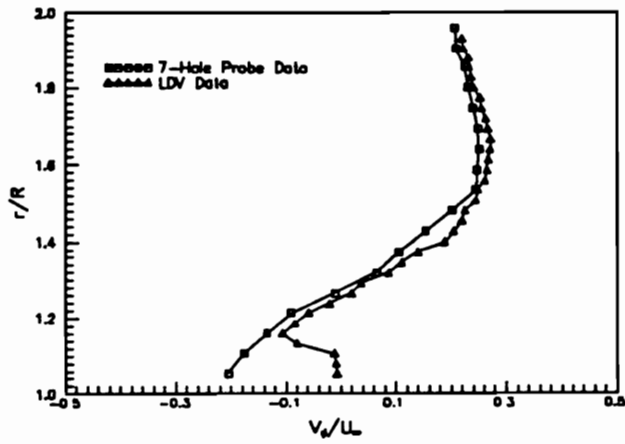
Figure 4.52. LDV and seven-hole probe axial velocity profiles at $x/R = 9.7$, $\alpha = 20^\circ$ (a) $\phi = 119^\circ$ (b) $\phi = 140^\circ$ (c) $\phi = 161^\circ$.



(a)

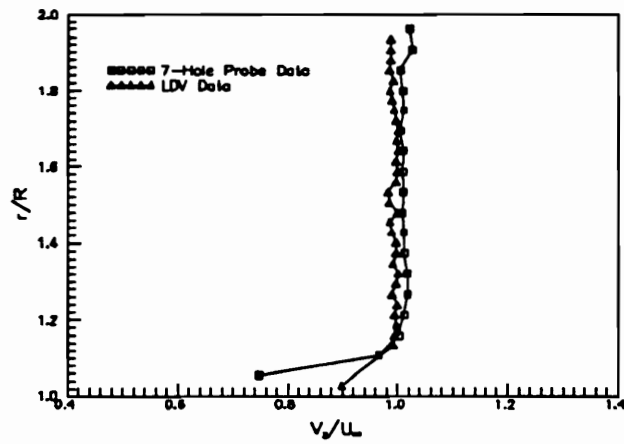


(b)

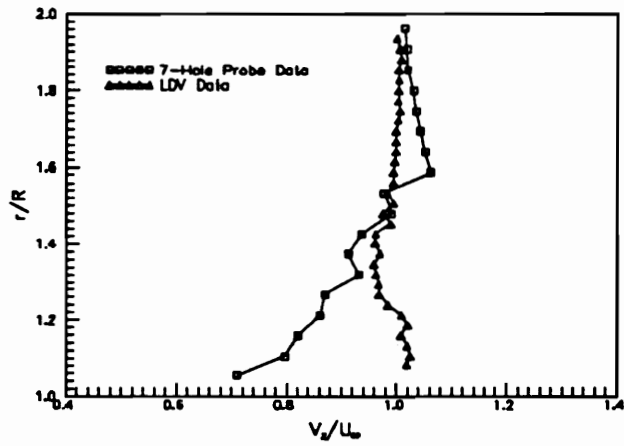


(c)

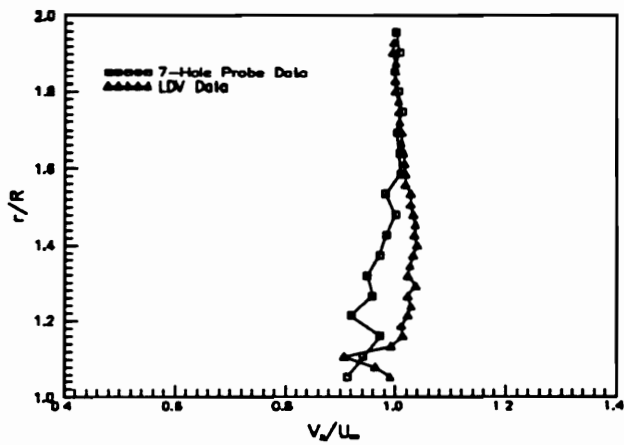
Figure 4.53. LDV and seven-hole probe circumferential velocity profiles at $x/R = 10.0$, $\alpha = 20^\circ$ (a) $\phi = 119^\circ$ (b) $\phi = 140^\circ$ (c) $\phi = 161^\circ$.



(a)



(b)



(c)

Figure 4.54. LDV and seven-hole probe axial velocity profiles at $x/R = 10.0$, $\alpha = 20^\circ$ (a) $\phi = 119^\circ$ (b) $\phi = 140^\circ$ (c) $\phi = 161^\circ$.

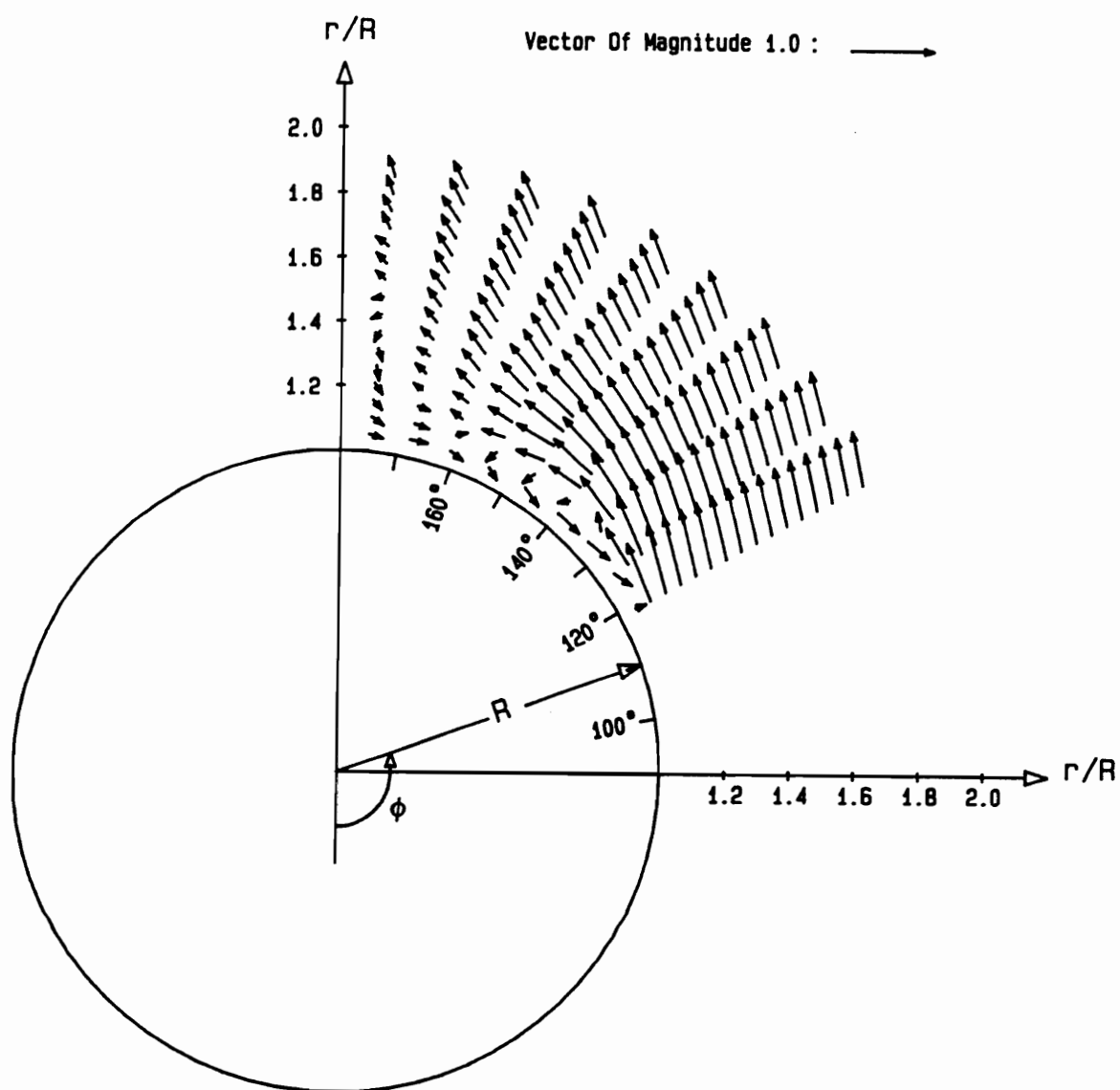


Figure 4.55. Seven-hole probe velocity vector fields along a normal plane at $x/R = 5.8$, $\alpha = 30^\circ$, for $Re = 1.5 \times 10^5$.

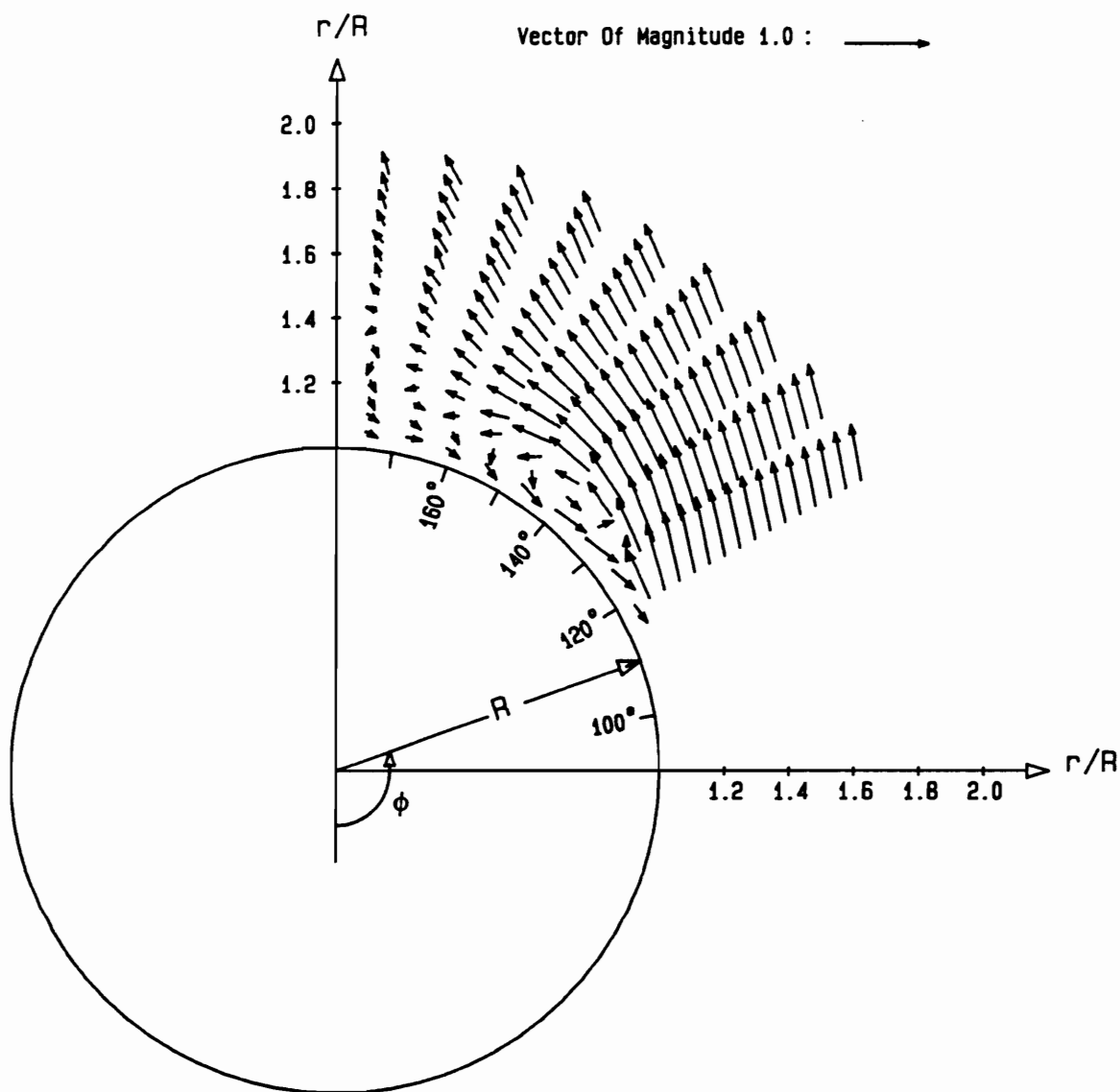


Figure 4.56. Seven-hole probe velocity vector fields along a normal plane at $x/R = 6.1$, $\alpha = 30^\circ$, and $Re = 1.5 \times 10^5$.

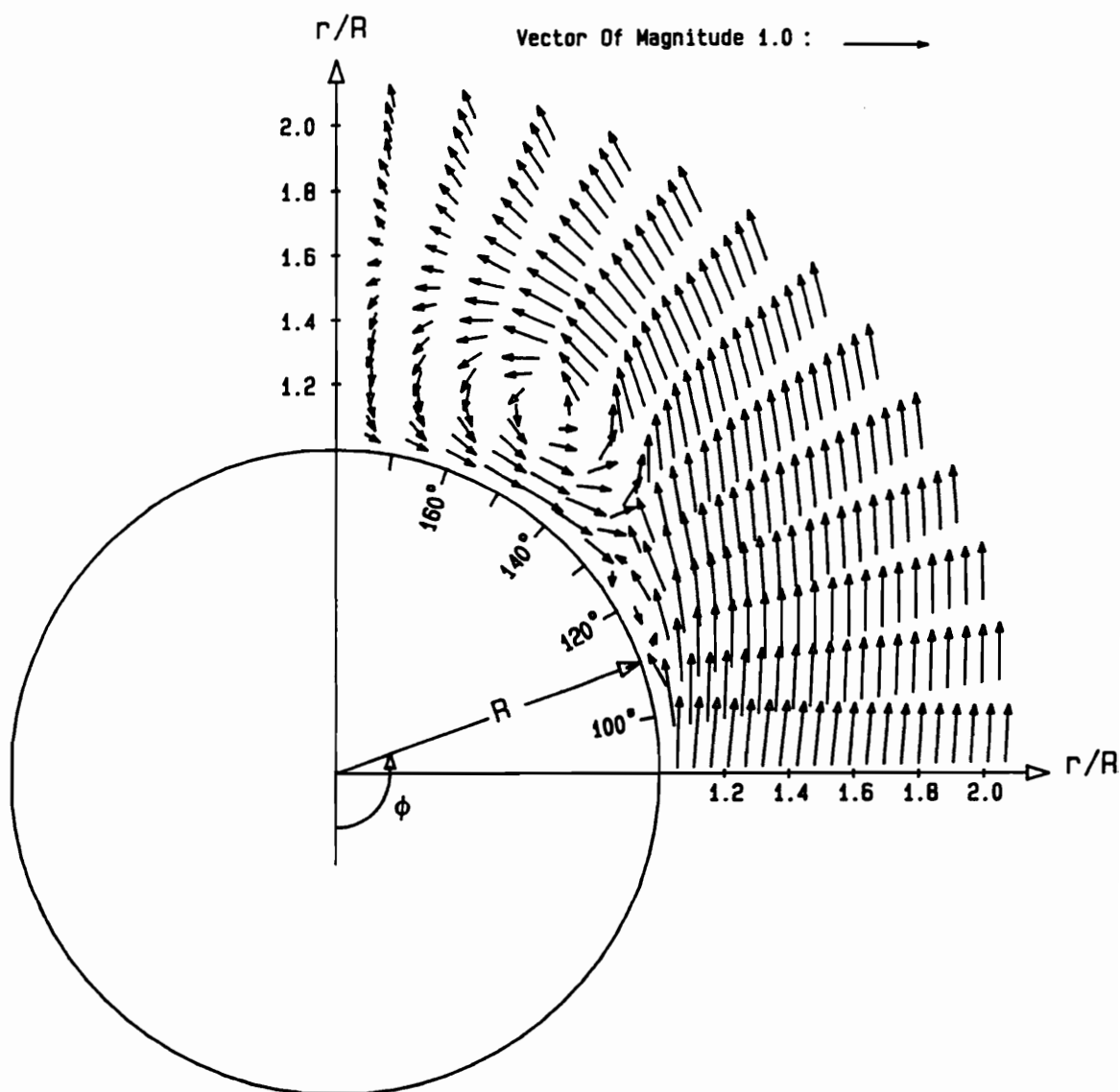


Figure 4.57. Seven-hole probe velocity vector fields along a normal plane at $x/R = 8.1$, $\alpha = 30^\circ$, and $Re = 1.5 \times 10^5$.

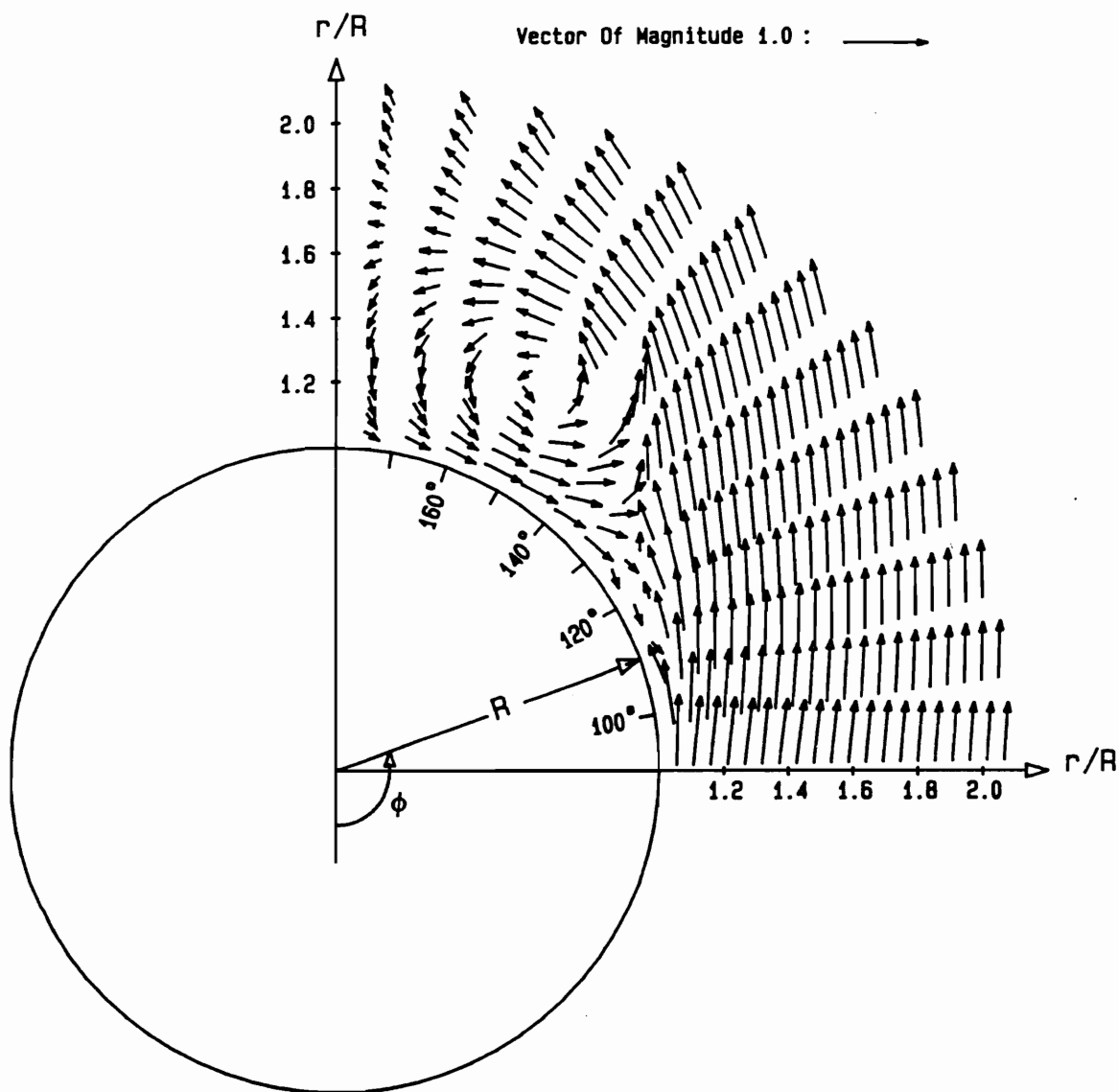


Figure 4.58. Seven-hole probe velocity vector fields along a normal plane at $x/R = 8.4$, $\alpha = 30^\circ$, and $Re = 1.5 \times 10^5$.

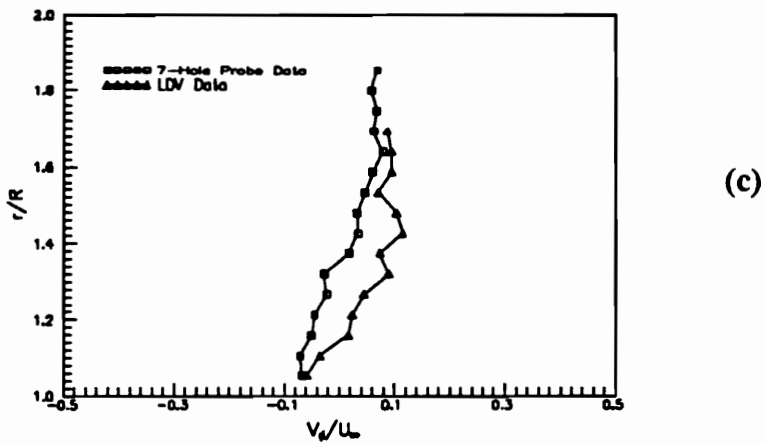
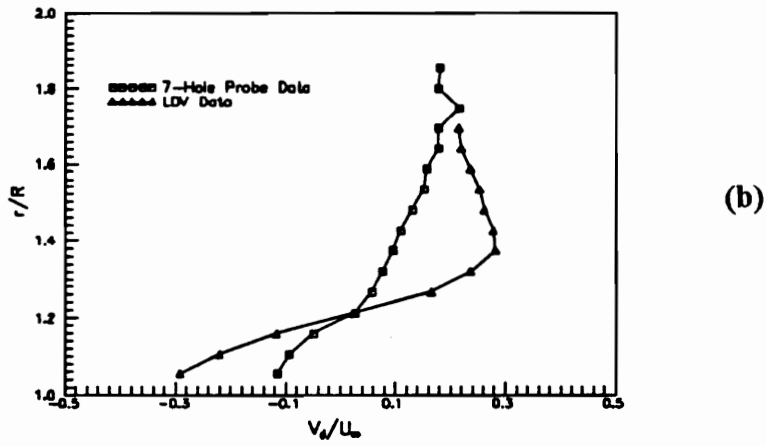
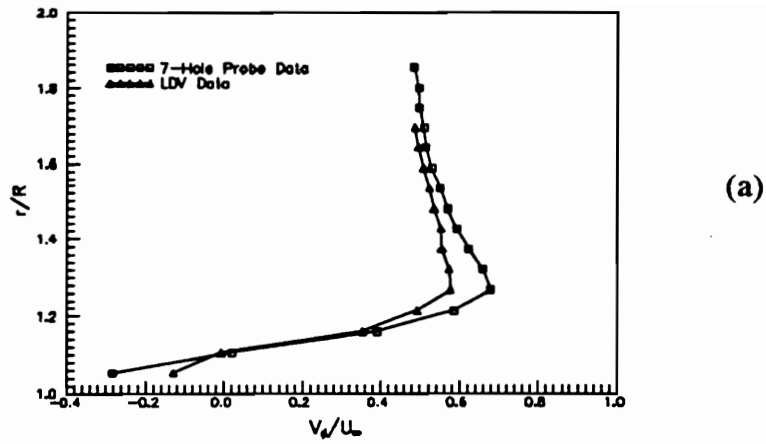
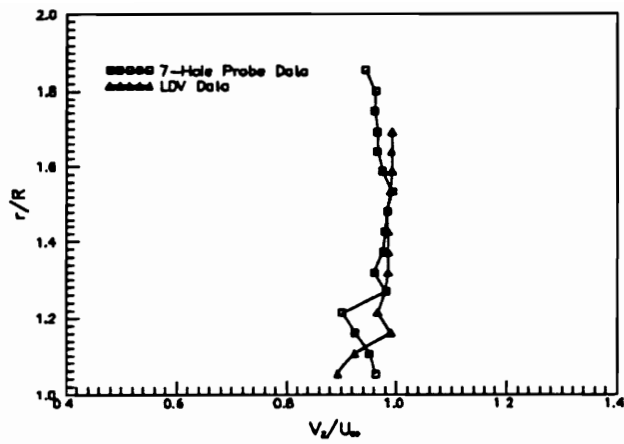
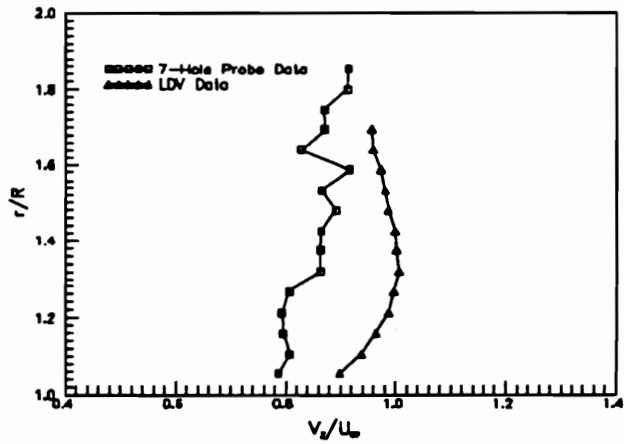


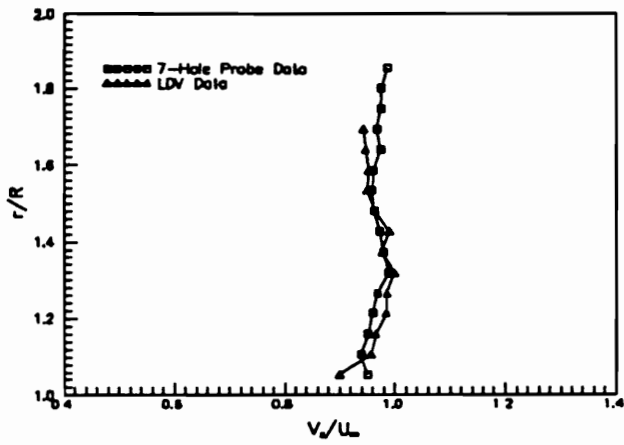
Figure 4.59. LDV and seven-hole probe circumferential velocity profiles at $x/R = 5.8$, $\alpha = 30^\circ$ (a) $\phi = 140^\circ$ (b) $\phi = 168^\circ$ (c) $\phi = 175^\circ$.



(a)



(b)



(c)

Figure 4.60. LDV and seven-hole probe axial velocity profiles at $x/R = 5.8$, $\alpha = 30^\circ$ (a) $\phi = 140^\circ$ (b) $\phi = 168^\circ$ (c) $\phi = 175^\circ$.

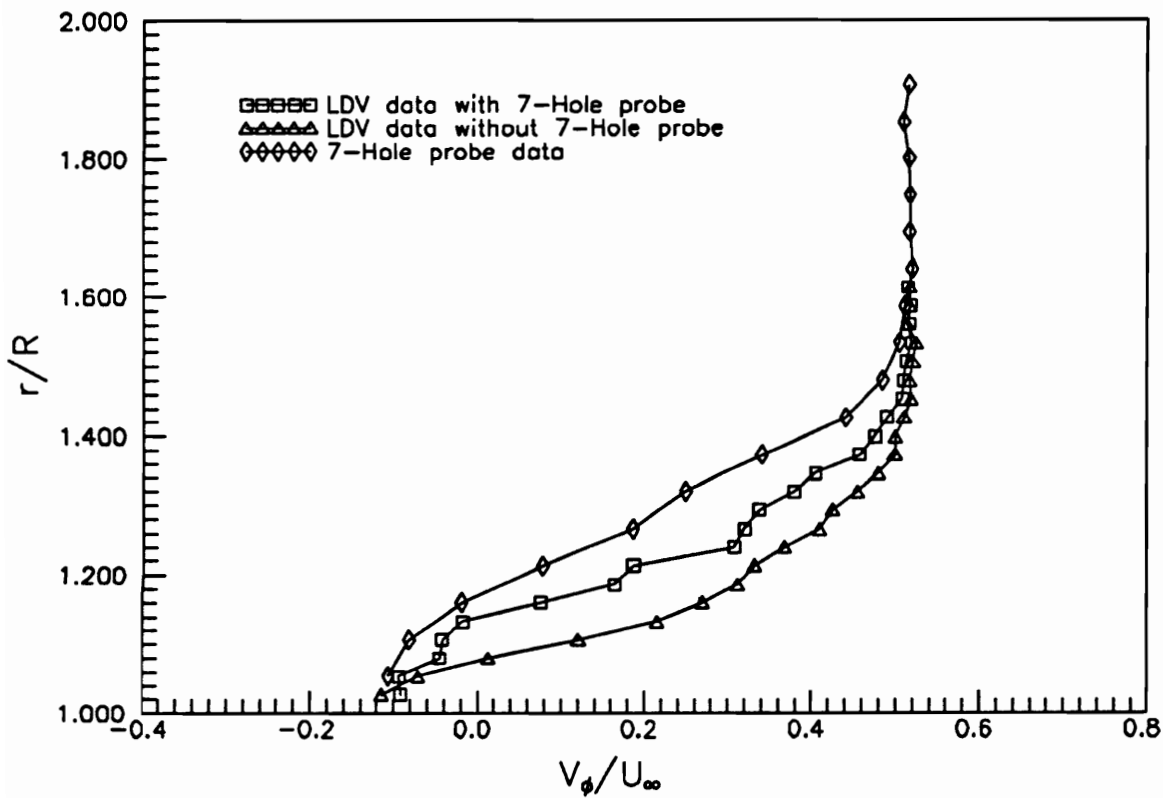


Figure 4.61. LDV and seven-hole probe profiles at $x/R = 8.1$, $\phi = 160^\circ$, $\alpha = 30^\circ$ and $Re = 1.5 \times 10^5$.

Chapter 5: Unsteady Flow

5.1 Introduction

Flows over various axisymmetric bodies, as for example ogive-cylinder, hemisphere-cylinder and prolate spheroid have been studied experimentally by many investigators. References on this literature are included in a recent publication of the present author (Hoang et al., 1990). In most of these studies, a great deal of effort has been focused on the steady field and, generally, the average values are reported. Detailed investigations of the three-dimensional boundary-layers and separation as well as the development of vortical structures have been reported. However, very little attention has been given to the unsteady character of such flows. Ramberg [1983] explored the natural shedding characteristics of slender cylinders with different end conditions for $Re \leq 1000$. Degani and Zilliac [1990] provided evidence that the flow over inclined bodies of revolution is characterized by periodic motions at discrete frequencies, reminiscent of vortex shedding. These types of problems are examined here in greater detail

for flows over a hemisphere-cylinder. The periodic motions of the vortices at $\alpha = 0^\circ$ - 90° for $Re = 2.0 \times 10^4$ are carefully observed.

In the present work, different patterns of vortex shedding are identified for all angles of attack greater than 15° . A new mode of periodic vortex shedding is discovered. This involves a periodic heaving of axial vortices in the direction normal to the free-stream. These phenomena are further complicated by the asymmetry of the vortex patterns which is also described in Chapter 3. Some of our preliminary studies have shown that asymmetric vortical structures too are not steady but engage in periodic organized motions. Vortex shedding over semi-infinite and finite-cylinders with different ends (hemisphere, cone and flat) placed normal to the oncoming flow are also included in this study.

The most common example of periodic vortex shedding is two-dimensional flow over circular cylinders. Such problems have been investigated extensively by researchers interested in flow-induced vibrations, structural mechanics, wind engineering, automobile aerodynamics and others. Practical engineering applications of this configuration include smoke stacks, oil storage tanks, underwater vehicles, antennas and telephone poles, just to name a few. Most of the researchers concentrated their work on measuring static pressure distributions and vortex shedding over infinite cylinders (Gould et al., 1968). Little or no attention was given to the vortex shedding of the wake of a semi-infinite cylinder placed normal to the free-stream. Only in the 1970's, Okamoto and Yagita [1973] looked at the surface pressure distributions for a semi-infinite circular cylinder with varying length-to-diameter ratio, ℓ/D from unity to 12.5. Vortex shedding was recorded for different ℓ/D and Reynolds numbers using hot-wire anemometers. At $Re = 1.31 \times 10^4$ and $\ell/D = 7, 9$ and 12 , vortex shedding near the bottom region of the model occurred at reduced frequencies of 0.15, 0.18 and 0.195, respectively, and decreased gradually toward the tip region. Periodic vortex shedding was detected only up to a

distance of $2D$ from the free end of the cylinder for all cases. The reduced frequency, also known as the Strouhal number is defined as

$$St = \frac{f D}{U_{\infty}} \quad [5.1]$$

where f is the shedding frequency, D is the diameter of the model and U_{∞} is the free-stream velocity.

Farivar [1981] studied the effects of the free end on a semi-infinite circular cylinder on pressure and vortex shedding. Pressure transducers and hot film output connected to an oscilloscope were used to detect vortex shedding. The Strouhal number frequency was measured from the photographs of the signals taken from the oscilloscope. This method is rather inaccurate, especially when the signal is "noisy". At $Re = 7 \times 10^4$ and $\ell/D = 10, 11$ and 12.5 , Farivar detected three distinct regions of vortex shedding along the model each associated with a different frequency. Near the top region of the model, $0.9 \leq z/\ell \leq 1.0$, the Strouhal number was 0.08 . In the middle region, $0.6 \leq z/\ell < 0.9$, the reduced shedding frequency was 0.16 . And along the bottom, $0.05 \leq z/\ell < 0.6$, the Strouhal number was equal to that for a two-dimensional infinite-cylinder ($St = 0.2$). The point $z = 0$ was at the base of the model. The jumps in the frequency along the model indicated that the flow divided itself into separate cells and each cell shed at its own frequency.

Kawamura et al. [1984] examined vortex shedding for a semi-infinite cylinder in the range of $\ell/D = 1$ to 8 . These authors, too, found that for $\ell/D = 8$ the reduced shedding frequency was about 0.18 along the bottom region of the model and gradually decreased toward the tip region. The value of Strouhal number decreased with decreasing ℓ/D . By inspecting the velocity profiles, Kawamura et al. suggested that the flow region near

the free end of the model was dominated by the blow-down flow and thus vortex shedding was suppressed.

Zdrakovich et al. [1989] carried out experiments on finite circular cylinders (two free ends) with length-to-diameter ratios from 2 to 8. A single hot wire, positioned half way between each end, was used to examine the flow. Vortex shedding was detected for four models, $\ell/D = 2, 4, 6$ and 8. However, vortex shedding did not occur at a single frequency but over a range of Strouhal numbers from 0.14 to 0.25. Similar to Zdrakovich et al., Ayoub and Karamcheti [1982] found that vortex shedding near the tip of a cylinder was unstable and intermittent. And the concept of a universal Strouhal number ($St = 0.2$) broke down for a semi-infinite cylinder in regions of highly three-dimensional flow such as near the tip of the model.

Degani and Zilliac [1990] measured the unsteady flowfield of an inclined ogive-cylinder at Reynolds numbers ranging from 17,000 to 35,000. Degani and Zilliac detected vortex shedding, similar to von Karman vortex shedding on a two-dimensional circular-cylinder, at angles of attack greater than 70° along the entire model. The Strouhal number frequency varied with the theoretical curve given by $(0.20 \sin \alpha)$ for angles of attack from 70° to 90° . For $50^\circ < \alpha < 65^\circ$, von Karman vortex shedding was observed at lower Strouhal numbers near the lower portion of the model. Fluctuations at frequencies much higher than von Karman vortex shedding frequency were detected for angles of attack in the range of 30° to 60° . The fluctuations were due to both shear-layer unsteadiness and interaction between the leeward vortices as they curve away from the model and align themselves with the free-stream. The flow was stable for angles of attack less than 30° .

Degani [1991] studied flows around an ogive-cylinder with a splitter plate mounted in the leeward plane of symmetry. The splitter plate was bonded to the model along the full length of the body and extended to the upper wall of the wind tunnel. Both exper-

imental and computational results indicated that the presence of a splitter plate delayed the von Karman vortex shedding. This was due to the splitter plate preventing the vortices from interacting with each other. High frequency fluctuations of shear-layer remained unaffected by the presence of the plate.

5.2 Experimental Setup

The experiments were conducted in the ESM Wind Tunnel and the VPI Stability Wind Tunnel. Two single-wire, DISA type 55D01 constant-temperature anemometers were used in this experiment to detect vortex shedding and heaving. Two electrical output signals, directly proportional to the magnitude of the instantaneous velocity, were processed by an HP3562A dynamic signal analyzer. The output signals could be displayed on both time and frequency domain by the signal analyzer. Phase differences between two signals could also be obtained. A detailed description of the instrument is included in Chapter 2. The traversing mechanisms for the seven-hole probe (see Chapter 3 for the setup) were also used here to traverse the hot wires.

Three different models used in this experiment are shown in Figures 5.1a, 5.1b and 5.1c. Model#1 was a hemisphere-cylinder. It was machined out of aluminum with 13.5 inches in length and 1.65 inches in diameter. Model#2 was a hollow PVC circular cylinder with 10.6 inches in length and 1.32 inch diameter. The top was carefully covered with a flat piece of aluminum to seal the hole. Model#3 was a circular cylinder with a nose cone made out of cardboard and plastic. The model consisted of 15.8 inches in total length and 1.32 inch diameter. The half-angle of the nose cone was 7.1° . The model interior was stuffed with rolled-up papers to strengthen it. All three models could be raised away from the bottom of the wind tunnel. This allowed a conversion from a

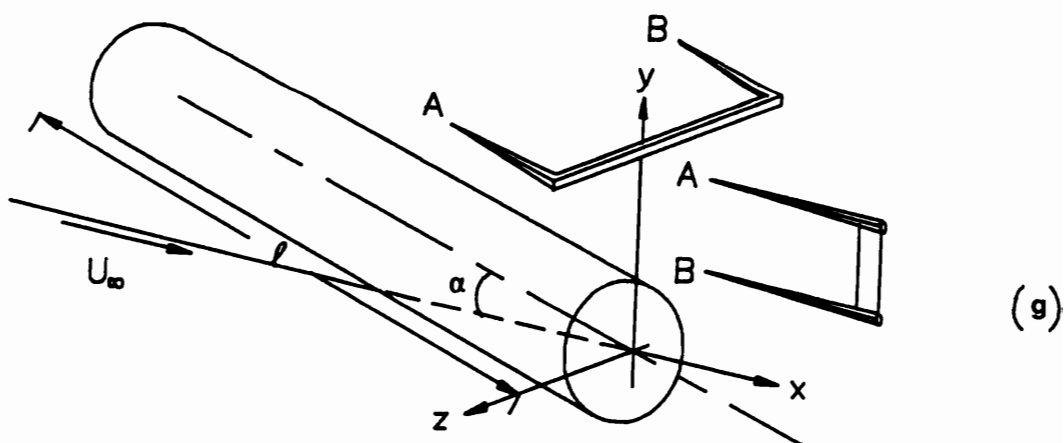
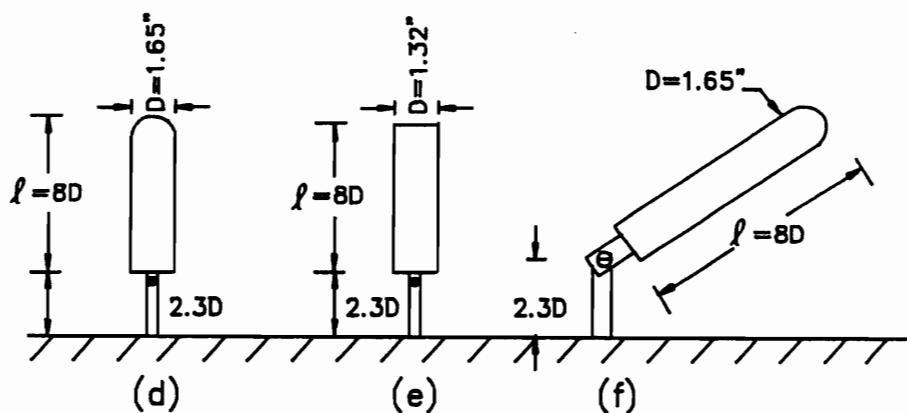
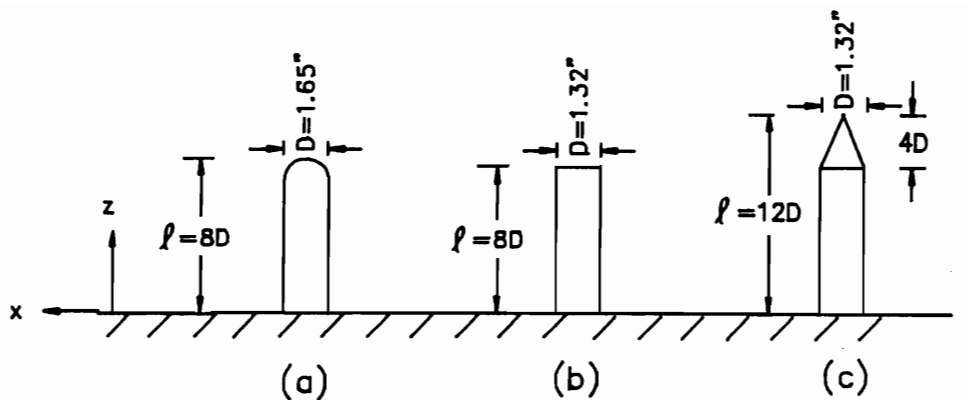


Figure 5.1. (a-f) The position of the models in the wind tunnel (g) definition of coordinates and positioning of the hot wires.

semi-infinite to a finite model (Figures 5.1d, 5.1e and 5.1f). Figure 5.1g displays the definition of coordinates used throughout this chapter.

5.3 Results and Discussion

The main contribution of this chapter is a careful documentation of the periodic oscillations that occur over a hemisphere-cylinder at angles of attack $\alpha = 15^\circ - 90^\circ$. Perhaps more important is the discovery of a different type of vortex shedding. The classical phenomenon in two-dimensional flow over bluff bodies involves the formation and alternate shedding of vortices (Figure 5.2a). In the present research effort, it was observed that as we increase the angle of attack, the vortices over the body of revolution first align their axes with the oncoming stream. They then lock into a periodic heaving motion (Figure 5.2b). This motion could have significant effects on downstream structures. If, for example, vortices are shed off the forebody of an aircraft at large angles of attack, then these heaving vortices could impose a significant periodic motion (fluttering) on the single or twin tails of the aircraft. All of the following cases were tested in both wind tunnels, the ESM Wind Tunnel and the VPI Stability Wind Tunnel, with the same models. The results appear to be identical. This indicates that the blockage effects and the free-stream turbulence level affect very little the unsteady phenomena under investigation.

(i) $\alpha = 90^\circ$ Case

For the problem under consideration here, a limiting case is the model at angle of attack $\alpha = 90^\circ$. Indeed, the first case tested was a 1.68" diameter circular-cylinder

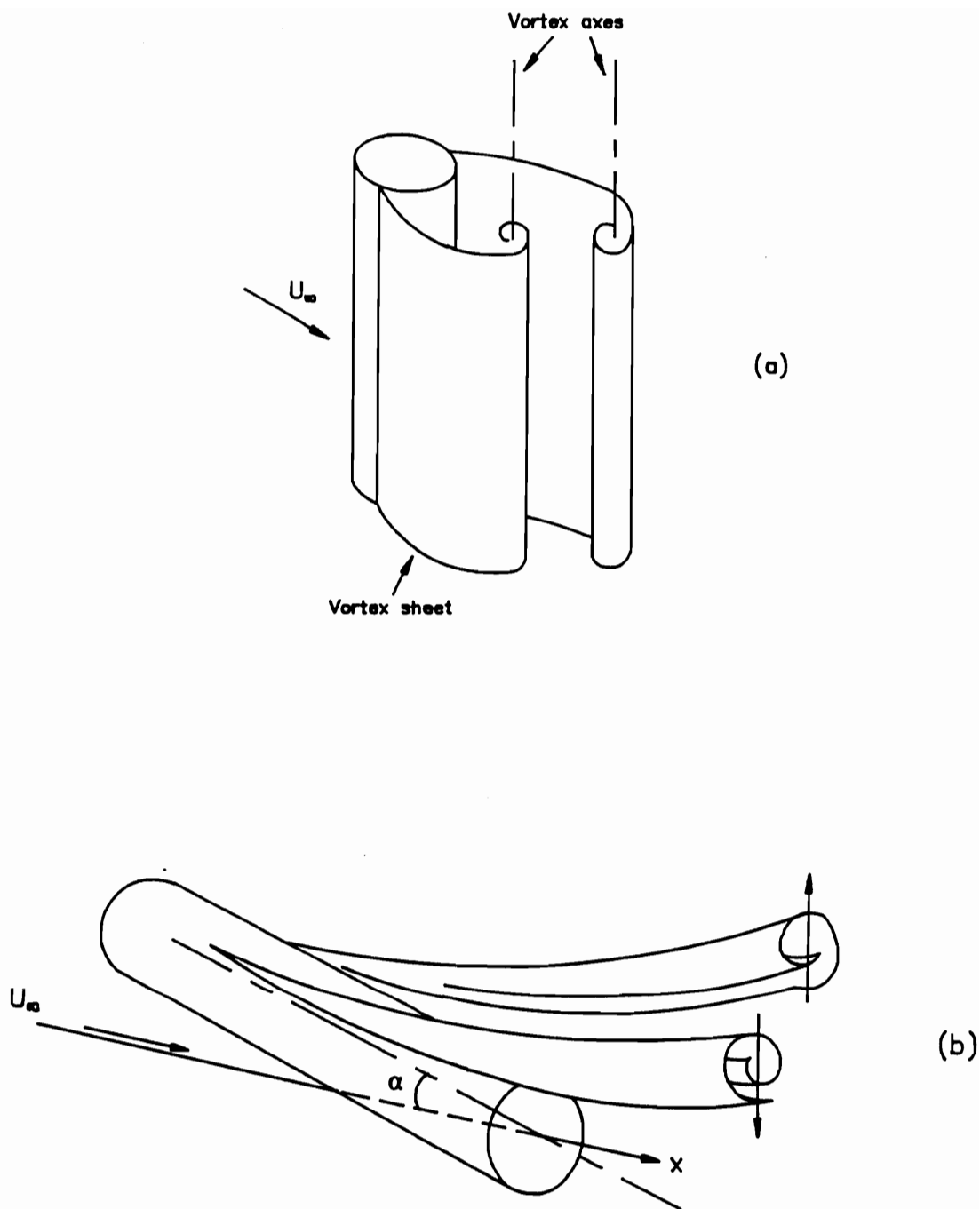
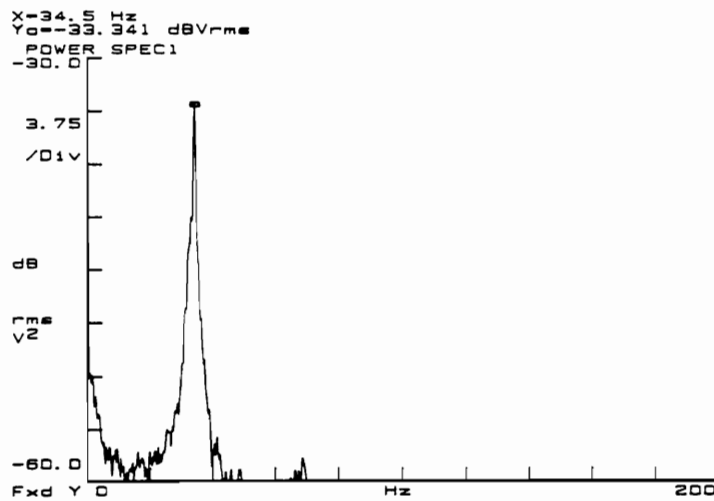


Figure 5.2. (a) Two-dimensional von Karman vortex shedding over an infinite cylinder and (b) periodic motion of the leeward vortices of an inclined hemisphere-cylinder.

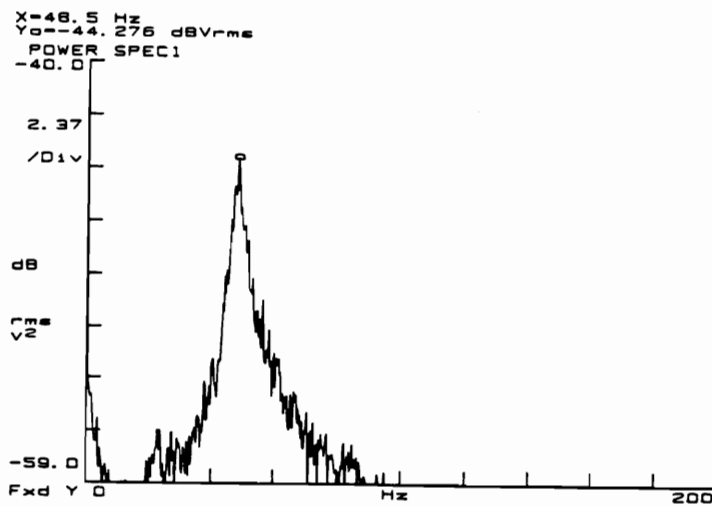
spanning the entire height of the wind tunnel. This represents flow over an 2-D infinite circular-cylinder. Shedding frequency was measured at two different velocities, namely 24.3 ft/sec and 33.8 ft/sec. The corresponding Reynolds numbers were 2.0×10^4 and 3.0×10^4 , respectively. Figure 5.3 displays the velocity power spectra in the wake of the model for these two cases. The Strouhal numbers of 0.2 are measured in agreement with all earlier investigations (Schlichting, 1979). It should be noted that reduced shedding frequency behind an infinite cylinder is equal to 0.2 only in the Reynolds numbers ranging from 1.0×10^3 to 3.0×10^5 . At higher Reynolds numbers, $Re > 3 \times 10^6$, the Strouhal number assumes values around 0.27.

Of greater interest are the cases of semi-infinite and finite circular cylinders at $\alpha = 90^\circ$. Five different geometries tested at a free-stream velocity of 25.1 ft/sec are presented schematically in Figure 5.1a-e. For flows over these configurations, the reduced frequencies of vortex shedding are displayed in Figure 5.4. These are velocity spectra obtained with hot wires in the wake of the model. The open symbols in this figure correspond to cases a, b and c of Figure 5.1, namely models attached to the floor of the tunnel. In the same figure, the filled symbols represent data corresponding to configurations d and e of Figure 5.1. The ordinate represents the elevation at which the data were obtained.

For the semi-infinite circular-cylinder with a hemispherical end, three distinct regions of vortex shedding along the model are detected. Along the bottom region of the model, $0.06 \leq z/\ell \leq 0.7$, the reduced shedding frequency is about 0.17. This value is lower than that for a two-dimensional infinite cylinder. Figure 5.5a shows the cross spectrum of the two hot wires positioned in the wake of the cylinder on each side of the model at an elevation of $z/\ell = 0.3$. In this figure, a peak corresponding to the shedding frequency is evident in the spectrum centered around 31.5 Hz. The phase difference between the two hot wire signals at 31.5 Hz frequency is 175° . Within an experimental



(a)



(b)

Figure 5.3. Velocity power spectra in the wake of an infinite circular-cylinder at free-stream velocities of (a) 24.3 ft/sec and (b) 33.8 ft/sec.

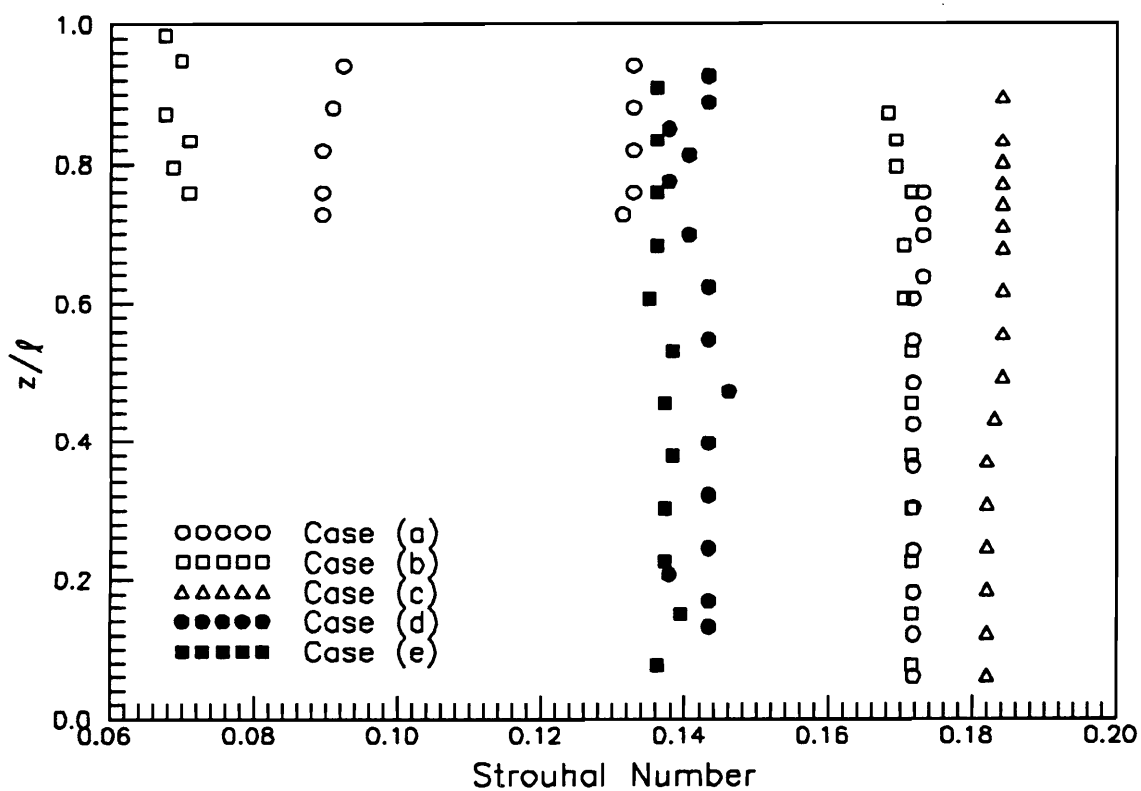
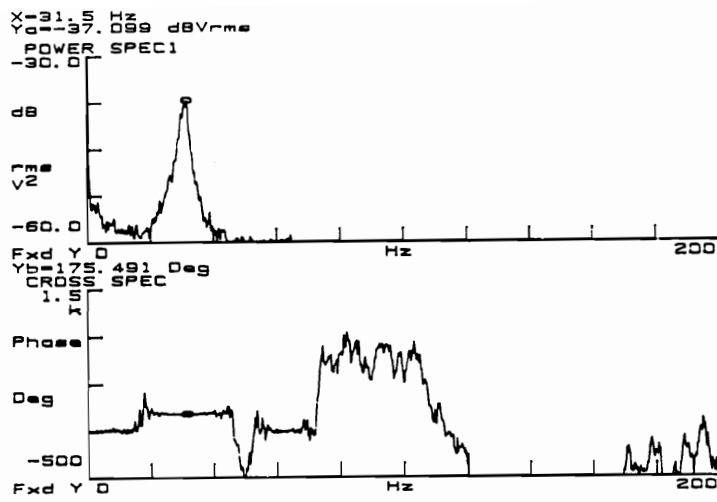
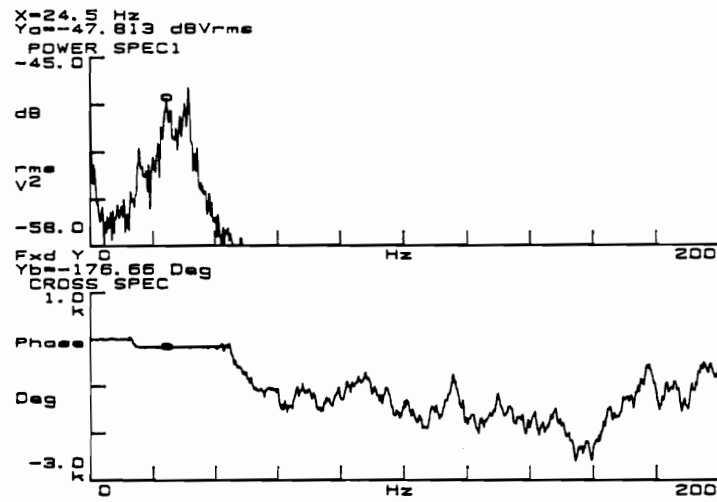


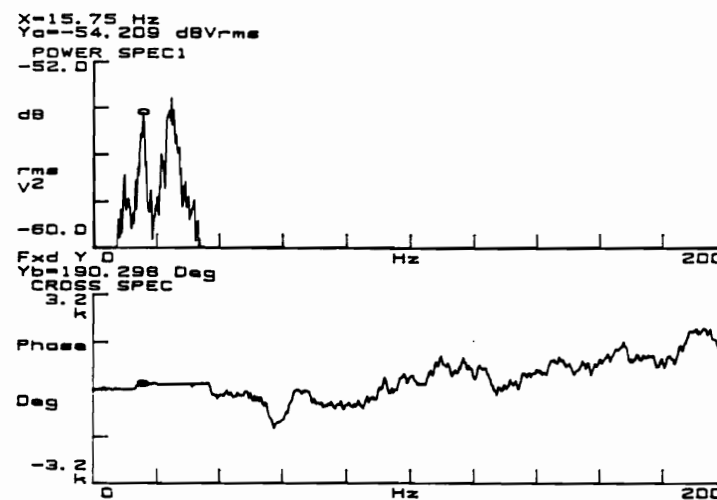
Figure 5.4. The Strouhal number downstream of the models of Figure 5.1 at different elevation from their bottom.



(a)



(b)



(c)

Figure 5.5. Magnitude and phase of cross spectrum of two hot wires positioned in the wake of a semi-infinite hemisphere-cylinder at z/l of (a) 0.3 (b) 0.75 (c) 0.9.

error, this suggests that the vortices are shed alternately. Time records obtained from the hot wires are displayed in Figure 5.6. Again, it appears that the signals are out of phase, a clear indication of alternate vortex shedding. In the middle region of the model, $0.7 < z/\ell \leq 0.78$, three reduced shedding frequencies are observed - 0.17, 0.13 and 0.09 (Figure 5.5b). And near the top region, $0.8 \leq z/\ell \leq 1.0$, the Strouhal numbers are 0.13 and 0.09 (Figure 5.5c). It is obvious that the concept of a universal Strouhal number breaks down for a semi-infinite cylinder not only in regions of highly three-dimensional flow such as near the tip of the model, stated by Ayoub and Karamcheti, but rather along the entire span of the model.

In the case of a semi-infinite circular-cylinder with a flat top, two different vortex shedding frequencies appear along the span of the cylinder. For $0.06 \leq z/\ell \leq 0.75$, the Strouhal number frequency is equal to that for a semi-infinite circular-cylinder with a hemispherical cap, $St = 0.17$ (Figure 5.7a). Two reduced shedding frequencies are detected in the region $0.75 < z/\ell \leq 0.9$ as shown in Figure 5.7b. In this figure, the two peaks are at 38.75 Hz and 15 Hz, corresponding to Strouhal numbers of 0.17 and 0.07, respectively. And near the top region, $0.9 < z/\ell \leq 1.0$, the reduced frequency is found at 0.07 (Figure 5.7c). Similar to Farivar's results, the above data also indicate that the vortices shed in separate cells. In addition, there exist overlapping regions of multiple shedding frequencies.

All investigators had agreed that the tip region of the model is dominated by the blow-down flow and, thus, vortex shedding is suppressed (Farivar, 1981; Ayoub and Karamcheti, 1982; Kawamura et al., 1984; Zdravkovich et al., 1989). Kawamura et al. went a step further to document the velocity profiles in the wake of flat top semi-infinite circular-cylinders. For the model of $\ell/D = 8.0$, the velocity profile in the z -direction assumed a Gaussian distribution. This velocity component was zero at the tip of the model, $z/\ell = 1.0$, and gradually reached a maximum at $z/\ell = 0.75$ and finally approached

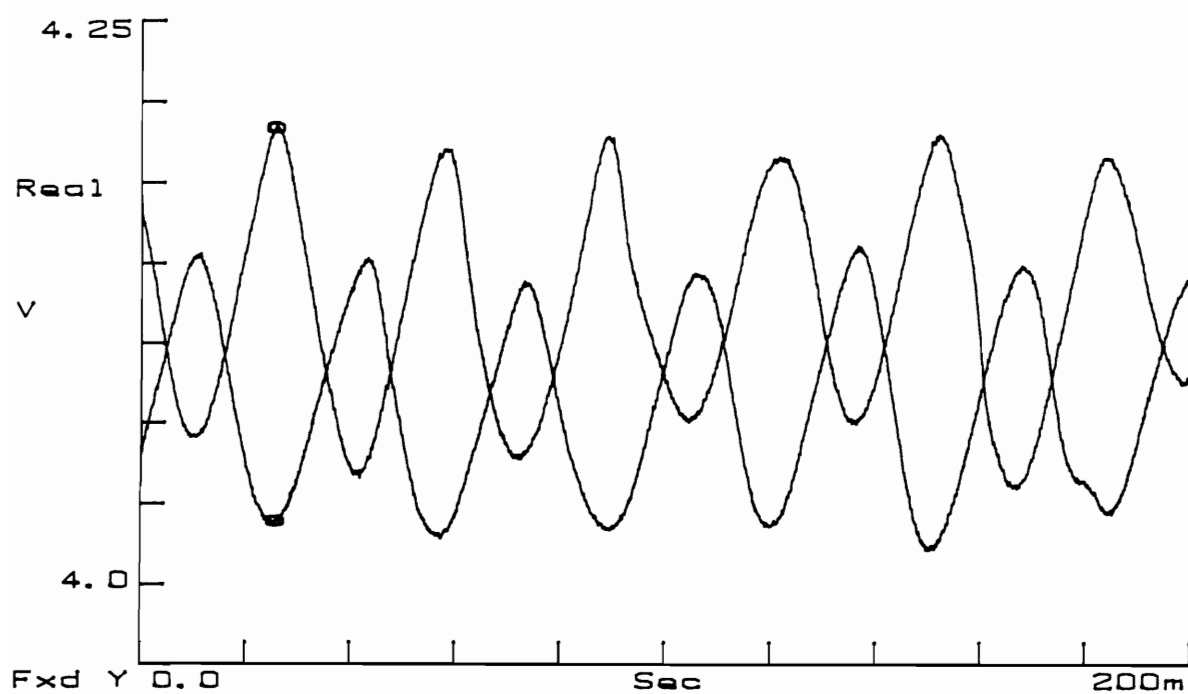
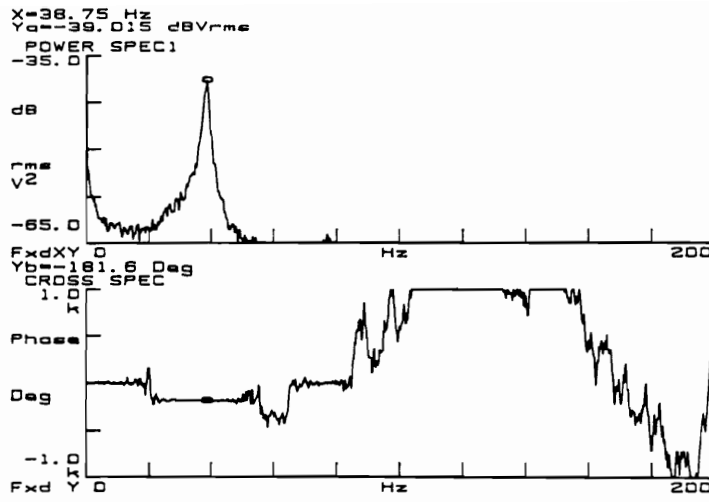
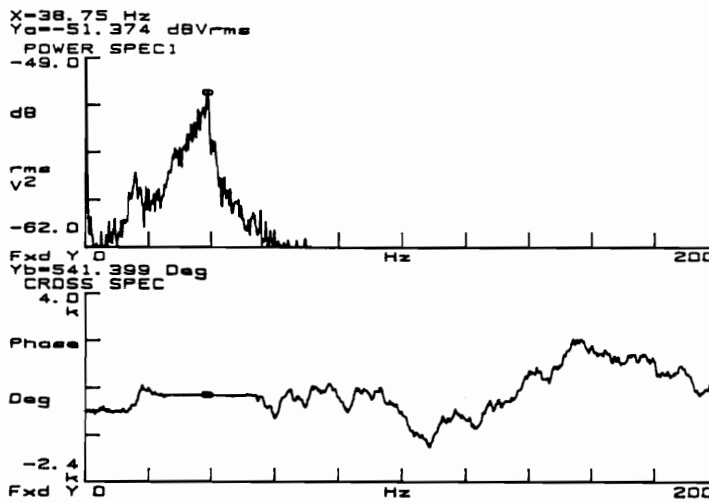


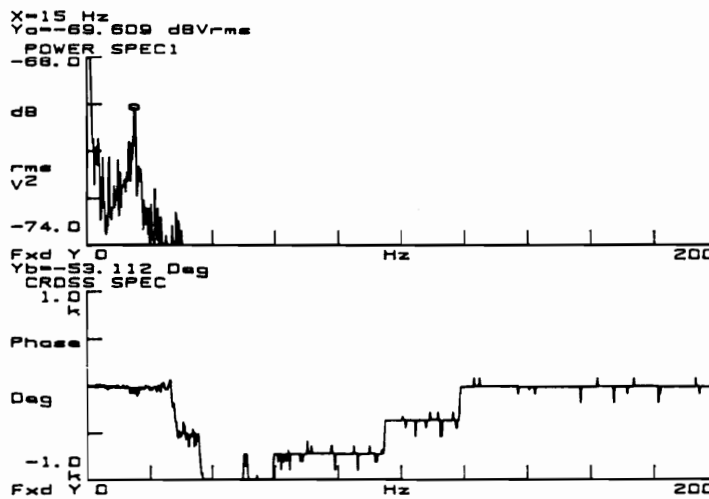
Figure 5.6. Time records obtained with two hot wires positioned in the wake of a semi-infinite hemisphere-cylinder at $z/\ell = 0.3$.



(a)



(b)



(c)

Figure 5.7. Magnitude and phase of cross spectrum of two hot wires positioned in the wake of a semi-infinite flat top cylinder at z/l of (a) 0.5 (b) 0.8 (c) 0.95.

zero at $z/\ell = 0.5$. An interesting observation here is that at the point of maximum downward velocity recorded by Kawamura et al., $z/\ell = 0.75$, the present data indicate that the reduced vortex shedding frequency jumped from 0.07 to 0.17 (Figure 5.4).

Another case tested was the semi-infinite cylinder with a nose cone (Figure 5.1c). Surprisingly, the reduced shedding frequency at the bottom region for this model is slightly higher than the two previous cases - the semi-infinite hemisphere-cylinder and flat top cylinder (Figure 5.4). Figure 5.8 displays the cross spectrum of the hot wire signals in the wake of the model. The vortex shedding frequency occurs at 41.25 Hz. This corresponds to a Strouhal number of 0.18. Along the entire span of the model, only one shedding frequency is detected and vortex shedding disappears in the region $z/\ell > 0.9$.

The semi-infinite hemisphere-cylinder and flat top cylinder were both raised away from the tunnel wall to become finite cylinders (Figures 5.1d and 5.1e). The two free ends shift the reduced shedding frequency to even lower values, $St \approx 0.14$. Only one vortex shedding frequency is detected along the entire span of the models in the region $0.1 \leq z/\ell \leq 0.9$ (Figures 5.9a and 5.9b). For the same finite hemisphere-cylinder model and at $U_\infty = 103.2$ ft/sec, the reduced vortex shedding frequency remains at 0.14 (Figure 5.10).

For the semi-infinite hemisphere-cylinder, a flat plate was mounted at the juncture of the hemisphere and the cylinder to delay the flow over the top of the hemispherical cap from entering the wake (Figure 5.11). Figure 5.12 displays the cross spectrum of the hot wires positioned in the wake of the cylinder with a flat plate. The plate consisted of $4D$ in length and $2D$ in width. The reader is reminded here that the symbol D represents the diameter of the cylinder. In Figure 5.12, the vortex shedding frequency returns to the value of 0.2 which is equal to that for the universal Strouhal number frequency of an infinite cylinder. The width of the flat plate was then reduced to D and

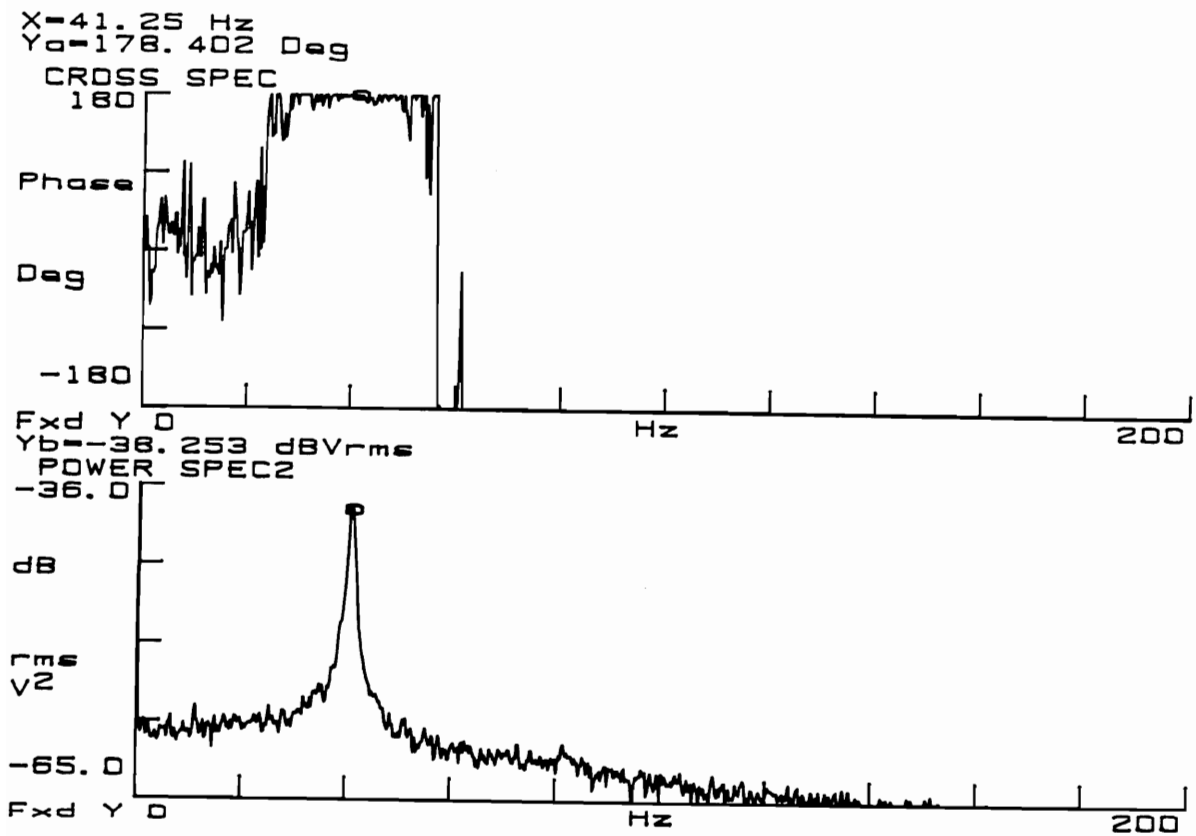
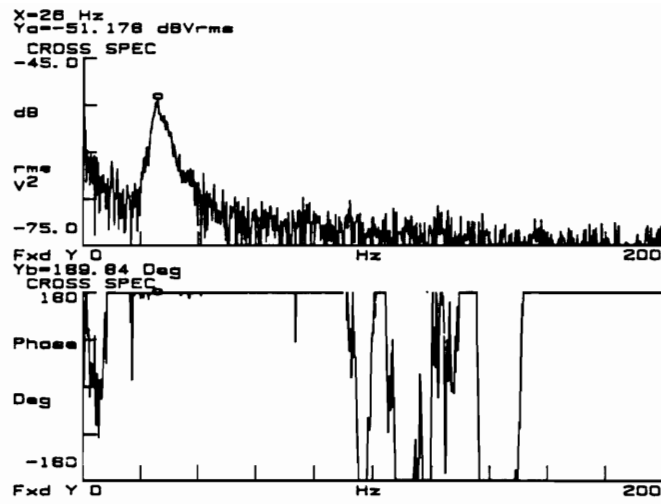
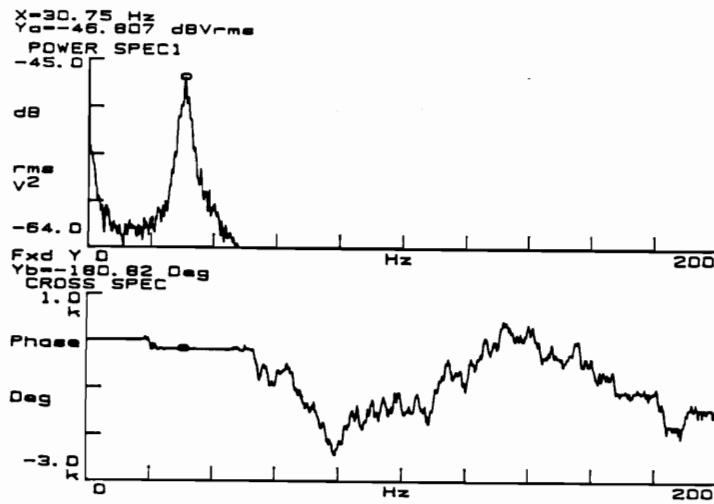


Figure 5.8. Magnitude and phase of cross spectrum of two hot wires positioned in the wake of a semi-infinite nose cone cylinder at $z/\ell = 0.5$.



(a)



(b)

Figure 5.9. Magnitude and phase of cross spectrum of two hot wires positioned at $z/l = 0.5$ in the wake of a finite (a) hemisphere-cylinder (b) flat top cylinder.

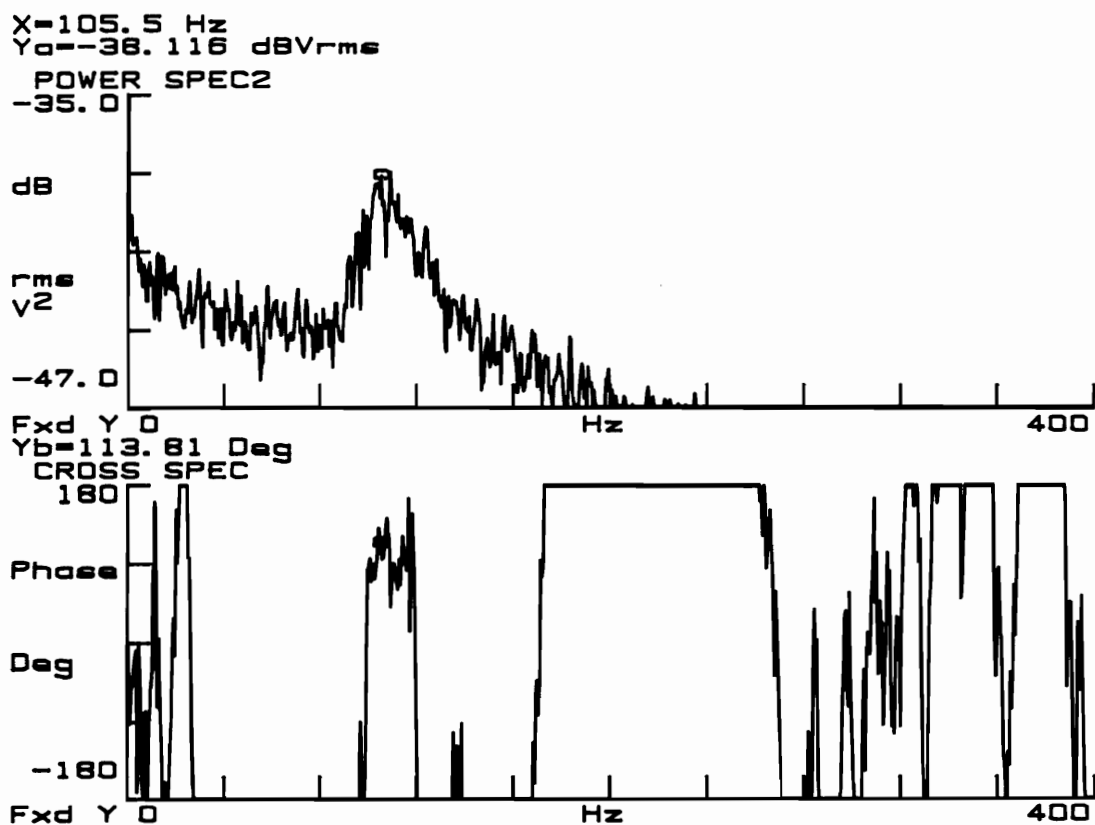


Figure 5.10. Magnitude and phase of cross spectrum of two hot wires positioned in the wake of a finite hemisphere-cylinder at $z/\ell = 0.5$.

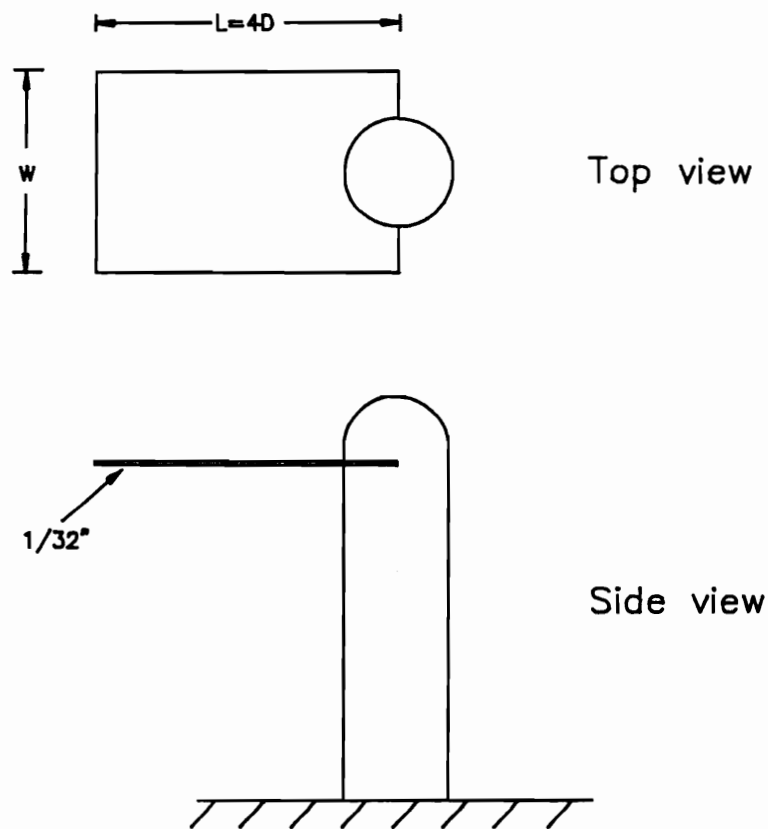


Figure 5.11. The hemisphere-cylinder model with a plate mounted near the top.

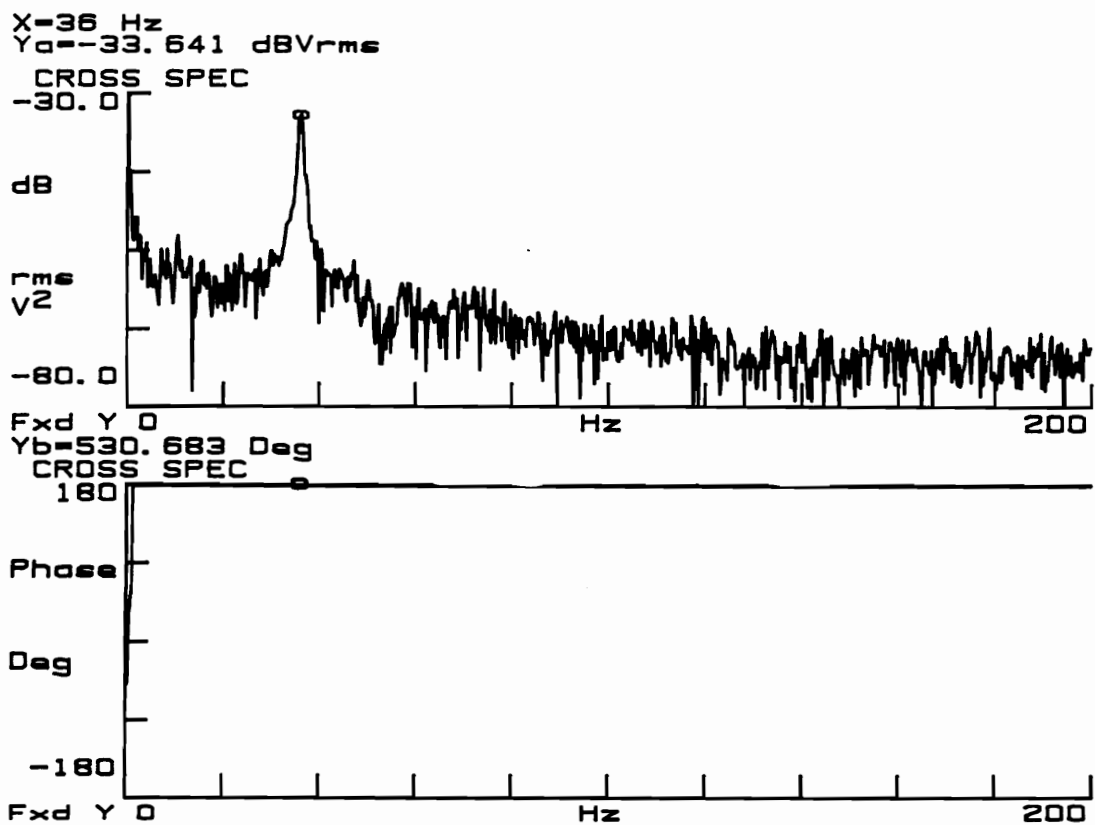


Figure 5.12. Magnitude and phase of cross spectrum of two hot wires positioned in the wake of a semi-infinite hemisphere-cylinder (with a plate mounted near the top) at $z/l = 0.5$.

the length was kept the same at 4D. The reduced vortex shedding frequency remained at 0.2.

(ii) $\alpha = 0^\circ - 85^\circ$ Case

Measurements were then obtained with the model at an angle of attack, namely configuration f in Figure 5.1. For this configuration data were taken by pairs of hot wires positioned either along a vertical or horizontal line, as shown schematically in Figure 5.1g. At first data were obtained with two hot wires symmetrically positioned with respect to the vertical plane xz. Typical velocity power spectra and phase differences are displayed in Figure 5.13. It is interesting to observe that at different angles of attack, distinct and sometimes multiple frequencies of oscillation are detected. For angles of attack $65^\circ \leq \alpha \leq 85^\circ$, shedding occurs at a Strouhal number of about 0.14 along the entire body of the model (Figure 5.13f). Unlike the results presented by Degani and Zilliac for flow over an ogive-cylinder, it appears that the shedding frequency at these angles of attack for a hemisphere-cylinder does not fall on the theoretical curve given by $(0.20 \sin \alpha)$. For the angles of attack ranging from 43° to 65° , vortex shedding is at a Strouhal number of 0.06 near the bottom region of the model (Figure 5.13e). The vortices are heaving at multiple frequencies for angles of attack from 24° to 42° and at a single frequency for $15^\circ \leq \alpha \leq 22^\circ$ (Figures 5.13a-5.13d). No organized unsteady motion is detected for angles of attack less than 15° . Figure 5.14 displays the observed frequencies for all angles of attack tested. Open symbols in this figure represent signals in phase on the two sides of the model and closed symbols represent signals out of phase. Data obtained in the VPI Stability Tunnel with much less free-stream turbulence and negligible blockage are remarkably similar in magnitude to data obtained in the ESM Tunnel.

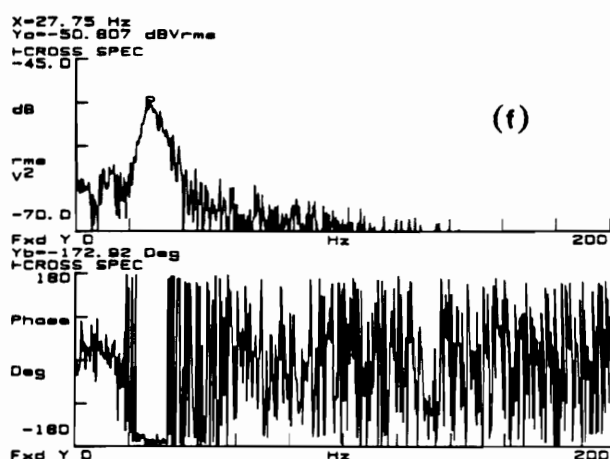
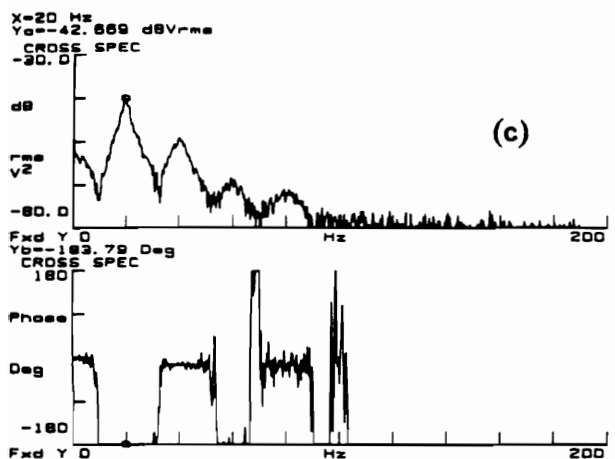
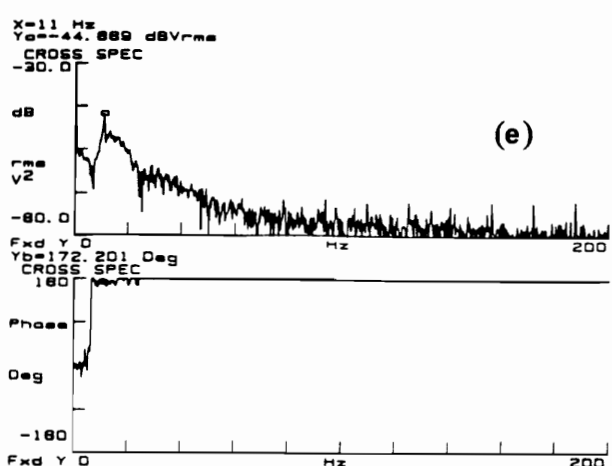
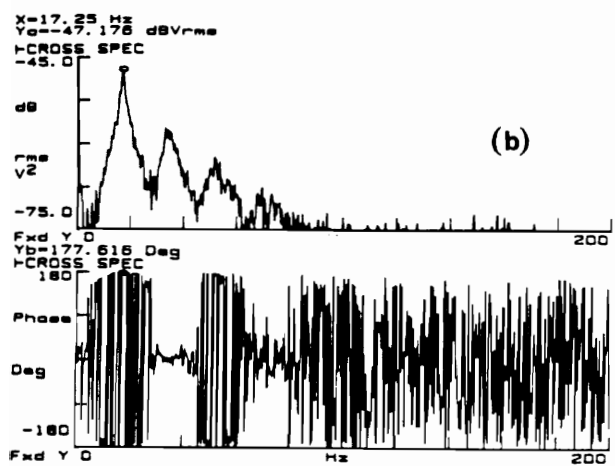
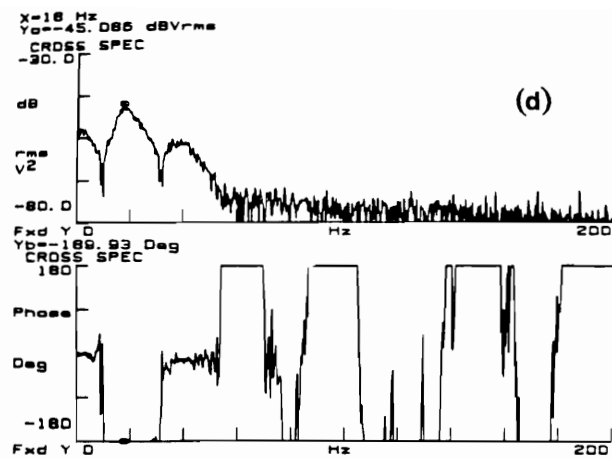
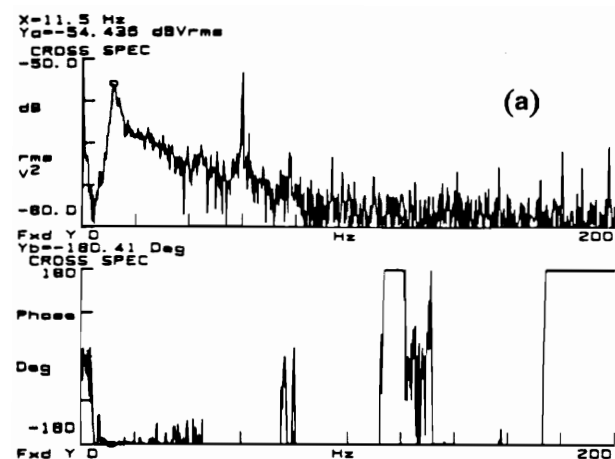


Figure 5.13. Magnitude and phase of cross spectrum of two hot wires when the model at an angle of attack of (a) 20° (b) 25° (c) 30° (d) 40° (e) 45° (f) 80°.

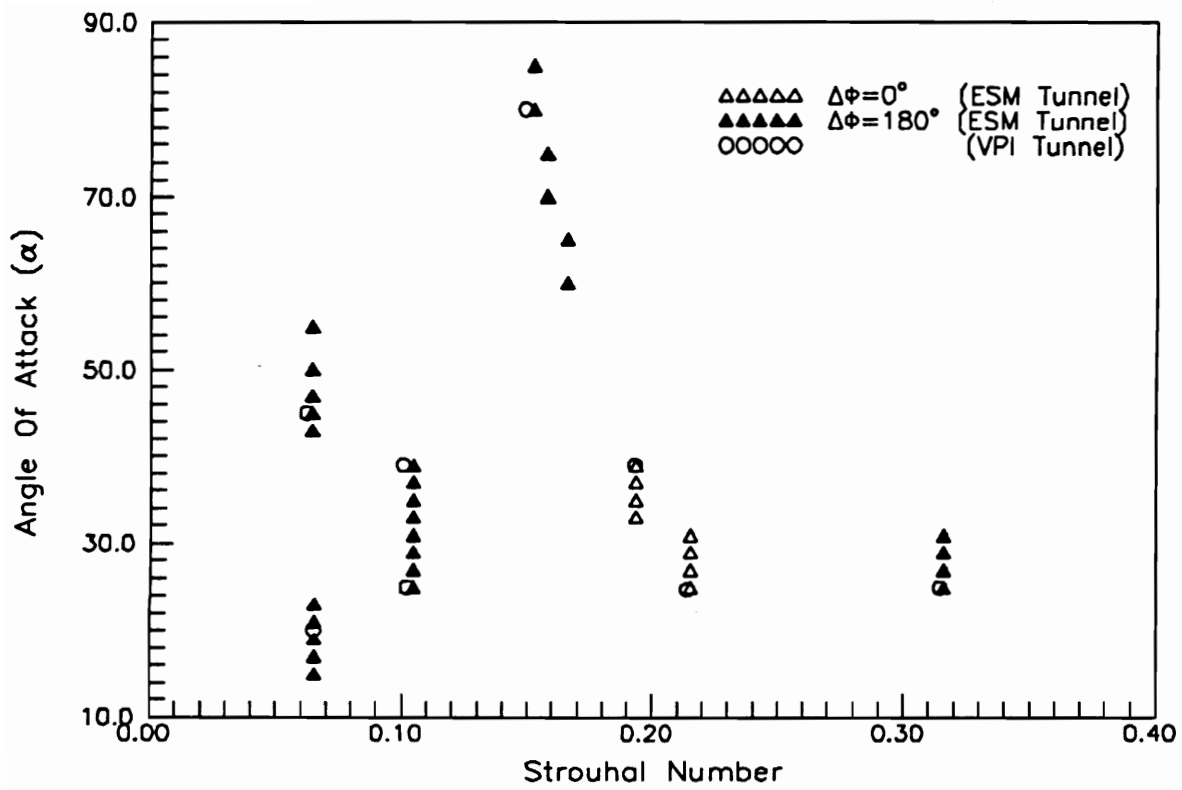


Figure 5.14. Strouhal number obtained at different angles of attack.

Evidence that the vortices engage in a periodic heaving motion were obtained first by a pair of hot wires positioned one above the other, with the model at 25° incidence (Figure 5.1g). The phase difference (only of the first harmonic) of the signals is nearly zero when both hot wires positioned below or above the vortex (Figures 5.15a and 5.15b). On the other hand, the phase difference gradually increases when one hot wire is moved away from the other (Figures 5.15c and 5.15d). Figure 5.15e displays the cross spectrum of the signals when the hot wires are located at different sides of the vortex core along the vertical direction. The hot wire signals are at about 160° out of phase. This indicates that the vortices engage in a periodic heaving motion. Higher harmonics are also present, but it is not possible yet to determine whether they correspond to a different mechanism of vortex heaving. Similar measurements were obtained by pairs of hot wires positioned along a horizontal but on the same side of the symmetry plane. In this case, one wire was kept fixed near the symmetry plane while the other was moved away from the symmetry plane. All data indicate no phase difference which proves the fact that the vortices do not displace in the horizontal direction.

A splitter plate of variable width was mounted on the hemisphere-cylinder model in the leeward plane of symmetry to suppress vortex heaving. The splitter plate was stretched from the juncture of the hemisphere and cylinder to the trailing-edge (Figure 5.16). Flows at three different angles of attack were tested, $\alpha = 20^\circ$, 25° and 40° . Periodic heaving motion vanishes at all three angles of attack when the width of the splitter plate is greater than $0.6D$. For the splitter plate with the width in the range from $0.1D$ to $0.6D$, only the first harmonic of vortex heaving frequency re-appears for all angles of attack. Figures 5.17a, 5.17b and 5.17c display the velocity power spectra for $\alpha = 20^\circ$, 25° and 40° , respectively, with a splitter plate consisted of $W = 0.15D$.

At a higher velocity, $U_\infty = 103.2 \text{ ft/sec}$ ($Re = 8.5 \times 10^4$), vortex unsteadiness in the wake of a hemisphere-cylinder is detected only at two angles of attack $\alpha = 30^\circ$ and 35° .

The cross spectra of the hot wire signals for these two cases are displayed in Figures 5.18a and 5.18b, respectively. For angles of attack $\alpha < 30^\circ$ and $40^\circ \leq \alpha \leq 60^\circ$, the velocity power spectra do not show any identifiable peaks.

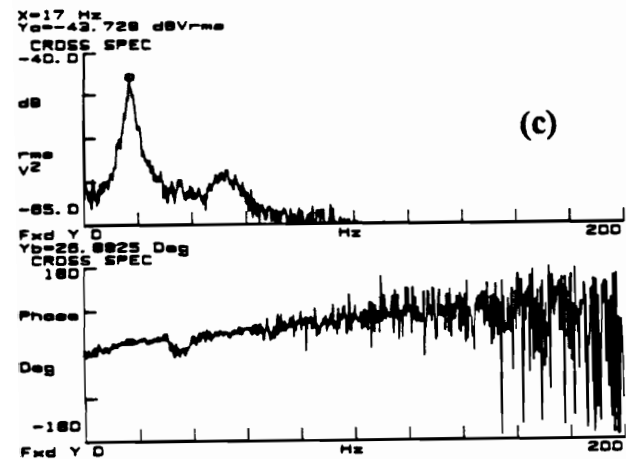
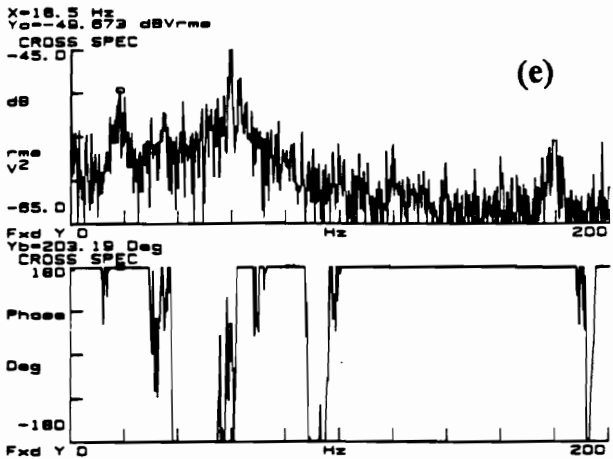
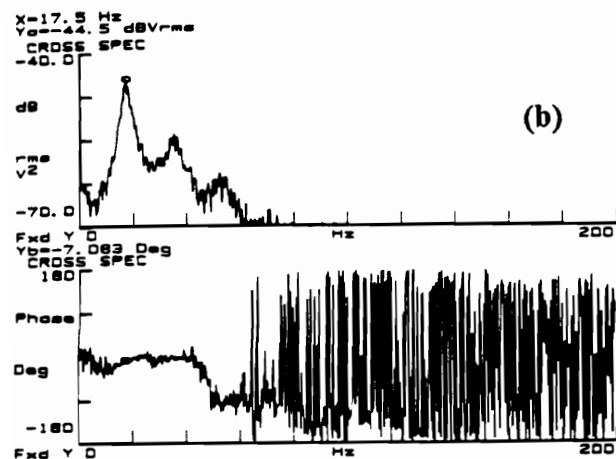
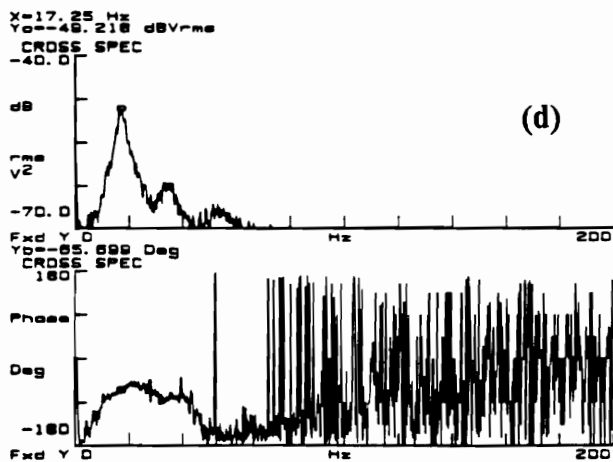
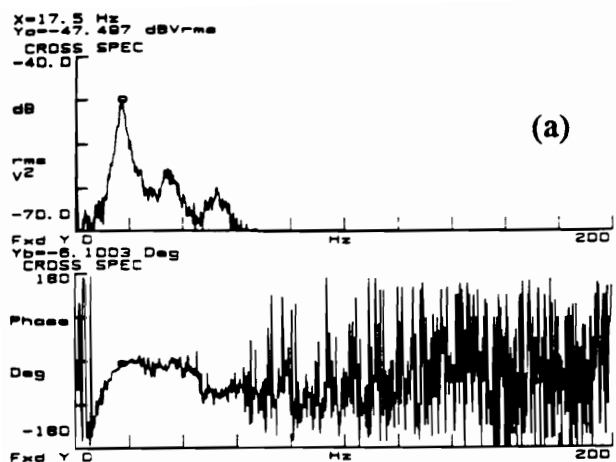


Figure 5.15. Magnitude and phase of cross spectrum of two hot wires at a vertical distance of (a) 0.060D (b) 0.303D (c) 0.606D (d) 0.909D (e) 1.212D from each other.

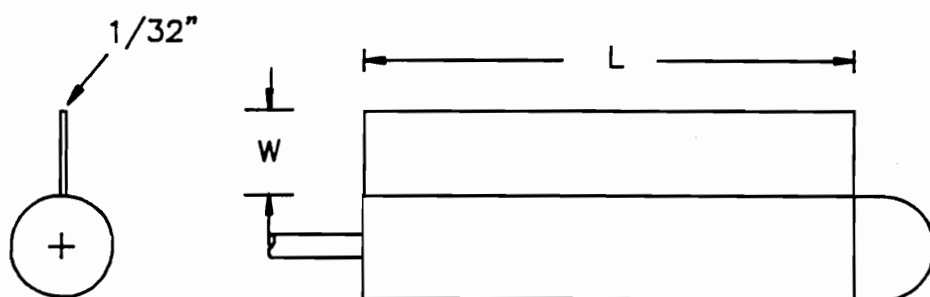
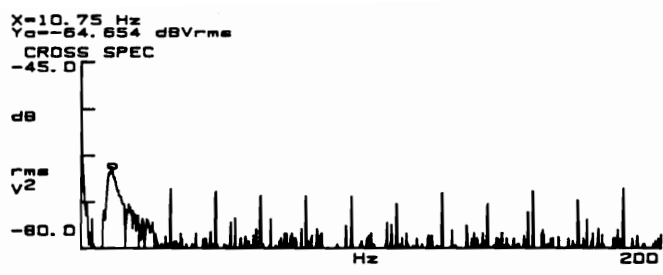
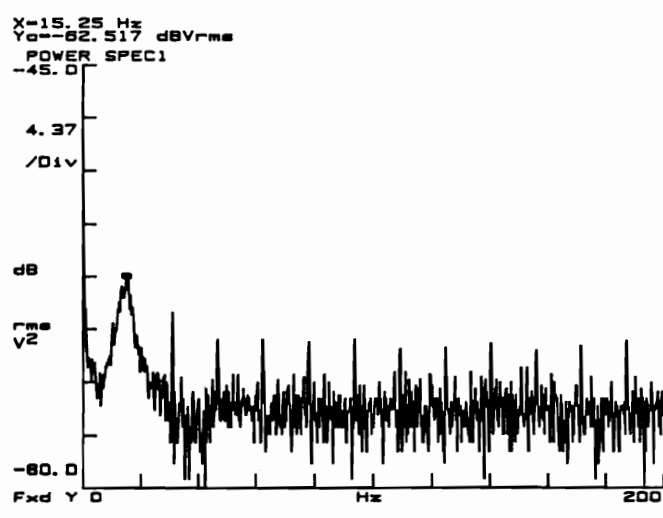


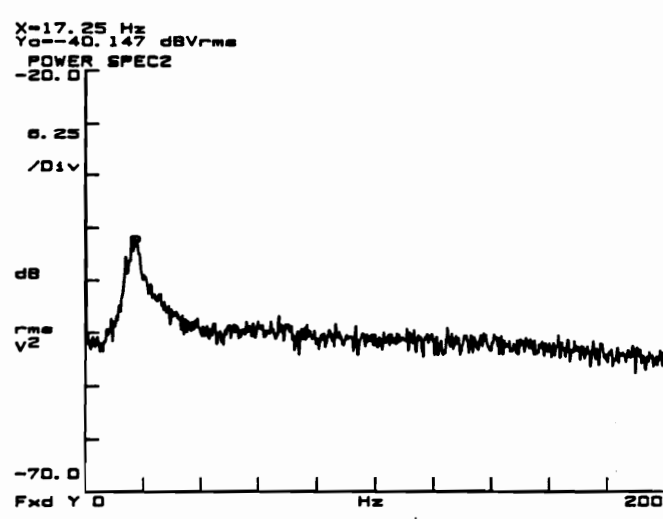
Figure 5.16. The hemisphere-cylinder model with a splitter plate mounted in the leeward plane of symmetry.



(a)

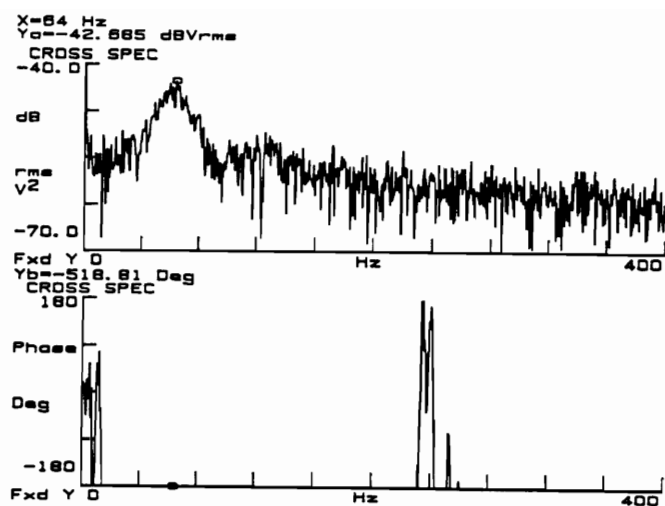


(b)

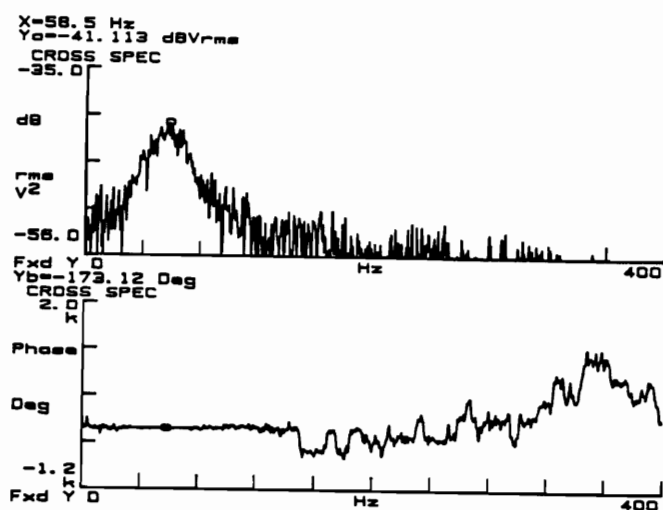


(c)

Figure 5.17. Velocity spectrum of the hot wires positioned in the wake of the hemisphere-cylinder with a splitter plate at α of (a) 20° (b) 25° (c) 40° .



(a)



(b)

Figure 5.18. Magnitude and phase of cross spectrum of the hot wires positioned in the wake of the hemisphere-cylinder at high Re and α of (a) 30° (b) 35° .

Chapter 6: Conclusions and Recommendations

Flow over a hemisphere-cylinder has been studied experimentally in the past with emphasis placed on the separation bubble and the horn vortices. The development and formation of the flowfield along the cylinder afterbody were largely neglected. All of these studies were carried out in the transonic and the low supersonic regimes ($M_\infty = 0.7$ to 2.0). Presently, there are no data available for low Mach number flows. The main goal of this research effort was to fill in this gap. Flow visualization and digitization, pressure sensors, hot-wire anemometry, seven-hole probe measurements and fiber-optic laser-Doppler anemometry were used in a comprehensive attempt to understand the overall flowfield over a hemisphere-cylinder, for a wide range of Reynolds numbers and angles of attack. The main findings of this investigation are as follows.

At low Reynolds number, $Re = 2.7 \times 10^4$, four different separation patterns can be identified with increasing angle of attack. For $\alpha \leq 10^\circ$, a separation bubble forms a complete ring around the model near the juncture of the hemispherical cap and the cylindrical afterbody. Two weak horn vortices begin to appear on the suction side of the model at $\alpha = 10^\circ$. The flow exhibits a closed separation. For $15^\circ \leq \alpha \leq 20^\circ$, the separation bubble is confined to the top of the hemispherical cap. Leeward vortices begin

to develop at $\alpha = 15^\circ$. The sizes of the horn vortices are largest at $\alpha = 20^\circ$. The skin-friction patterns indicate an open-type separation. The flow develops a closed separation pattern with the presence of the horn vortices at angles of attack ranging from 25° to 30° . For incidences greater than 30° , closed separation is still observed; however, the horn vortices vanish. The flow is always symmetrical for all incidences less than 45° .

It has been long established that the pointed nose axisymmetric bodies sustain highly asymmetric wakes for angles of attack greater than 30° . The mechanisms that cause the flow to become asymmetric are presently not well understood. In this study, vortex asymmetry patterns were not found in the wake of a hemisphere-cylinder. It was conjectured by the author that for a sharp-nose axisymmetric body at low angles of attack, $\alpha < 30^\circ$, the leeward vortices originate somewhere downstream, away from nose. Thus, there exist a gap between them. This allows the flow over the apex of the model to enter the gap between the vortices causing a blockage and preventing their interaction. The result is a symmetric flow pattern in the wake. For $\alpha \geq 30^\circ$, the leeward vortices originate at the nose, inhibiting the flow from entering the space between them. The interaction between the vortices becomes very strong and any minute surface perturbations can cause the vortices to assume an asymmetric orientation. For the hemisphere-cylinder, the leeward vortices are never formed at the tip of the nose. Therefore, the leeward vortices do not have a chance to interact with each other until much further downstream. As a result the wake will always be symmetric. However, a relatively small disturbance in the nose region (in front of the separation bubble) results in significant departures from symmetry. The surprising facts are that the total amount of vorticity in the vortices of an asymmetric wake may reach values up to eight times larger than the corresponding symmetric wake. Moreover, one of the vortices always moves closer to the meridional plane and much closer to the surface of the body. The flowfield pattern displays the highest degree of asymmetry when discrete surface pertur-

bations are located at a circumferential position near $\phi = 120^\circ$ and in front of the separation bubble. The effectiveness of the discrete disturbances on the asymmetry pattern decreases with decreasing disturbance size. It is believed that streamwise vorticity generated by the discrete disturbance washes away part of the separation bubble and somehow alters the lines of primary and secondary separation. This creates the asymmetric flow pattern in the wake of the model.

Hot-wire data at low Reynolds numbers indicated that the wake of a hemisphere-cylinder at moderate angles of attack, $15^\circ \leq \alpha \leq 42^\circ$, contains some organized and periodic unsteadiness. This unsteadiness is due to periodic heaving of the vortices which leave the body and align themselves with the free-stream. Higher harmonics are also present, but it is not yet possible to determine whether they correspond to a different mechanism of vortex shedding. At incidences greater than 42° , vortex shedding occurs along the bottom region of the model. However, the dimensionless frequency of shedding is far from the expected value of $(0.20 \sin \alpha)$. In fact, at $\alpha = 90^\circ$, the Strouhal number does not even reach 0.2. When the model is placed normal to the flow with one free end, the vortices shed in separate cells along the spanwise direction. Reduced shedding frequency near the tip region of the model is determined by the shape of the nose. Only one shedding frequency is detected along the model with two free ends placed normal to the flow. The asymmetric vortex structures too are not steady but engage in periodic organized motions. In addition, the free-stream turbulence levels have very little effect on the dynamic characteristics of the flow.

For high-Reynolds number flows, $Re = 0.29 \times 10^6$ and 0.42×10^6 , the skin-friction patterns are clearly different from the low-Reynolds number flows. The separation bubble is smaller at all angles of attack. The horn vortices are hard to detect since they are also small. The flow exhibits closed separation at $\alpha = 0^\circ$ and becomes open separation at incidences greater than 10° . Unlike the low-Reynolds number case, the flow

remains an open-typed separation up to $\alpha = 30^\circ$. Pressure data show that the separation bubble decreases in size with increasing Reynolds number for all angles of attack and at $\alpha = 0^\circ$ and $Re = 1.1 \times 10^6 (M_\infty = 0.26)$, the separation bubble vanishes.

A considerable portion of this research effort was devoted to the refinement of the operation of the seven-hole probe and fiber-optic LDV probe. The comparisons between seven-hole probe and LDV data show that within the core of the vortex, the seven-hole probe induces large errors, especially if the size of the vortex is small compare to that of the probe. It is believed that these errors are due to interference of the probe which effects a global change on the vortex core, reminiscent of vortex break-down. Some evidence also is provided that the seven-hole probe may offer erroneous results in regions of large cross-flow velocity gradients as for example in the free shear-layer immediately following the line of separation. The present data indicate that the vortices developing over the model contain much more vorticity than originally thought. This is because all earlier data were obtained by multiple-hole probes which must have interfered with the flow in the same way.

It was demonstrated here that a fiber-optic LDV probe can be employed successfully inside the model. The most difficult problem with an LDV system centered around seeding. Only a very small amount of seeding particles can get into the vortex cores, even though in the present case separation is open and therefore directly accessible to seed that is coming from upstream. It was also discovered that when the LDV beams are directed from inside the model, flare impares measurements for distances less than about one inch from the wall. The situation was improved by employing high-quality acrylic windows.

The following experimental work is recommended as an extension of this research effort:

1. Employ surface oil flow to detect the the primary and secondary separation lines and the separation bubble for the asymmetric cases.
2. Document the shapes and conditions of asymmetric steady wakes and measure the corresponding static surface pressure distributions.
3. Map out the cross-flow velocity fields along the model to investigate the development of vortex asymmetry.
4. Collect velocity data over a larger domain to include both leeward vortices and then calculate the net circulation gained with the bead positioned at various locations, by virtue of integrals $\Gamma = \iint \Omega \, dA$ or $\Gamma = \int \mathbf{v} \cdot d\mathbf{l}$.
5. Document vortex asymmetry for angles of attack other than 30° .
6. Perform a thorough study of the effect of vortex asymmetry on the unsteady periodic motions of the wake.
7. Map out the temporal correspondence between events in the wake and dynamic pressure distributions on the model for both the symmetric and asymmetric wakes.
8. Computational work should be carried out and compare the results with the data for the hemisphere-cylinder offered here.

References

- Akima, H., "A Method of Bivariate Interpolation and Smooth Surface Fitting for Irregularly Distributed Data Points", ACM Transactions on Mathematical Software 4, Vol. 2, June 1978.
- Ayoub, A. and Karamcheti, K., "An Experiment on the Flow Past a Finite Circular Cylinder at High Subcritical and Supercritical Reynolds Numbers", Journal of Fluid Mechanics, Vol. 118, 1982, pp. 1-26.
- Blottner, F. G. and Ellis, M. A., "Finite-Difference Solution of the Incompressible Three-Dimensional Boundary-Layer Equations for a Blunt Body", Computers and Fluids, Vol. 1, March 1973, pp. 133-158.
- Chapman, G. T., Keener, E. R. and Malcolm, G. N., "Asymmetric Aerodynamic Forces on Aircraft Forebodies at High Angles of Attack - Some Design Guides", AGARD CP-199, November 1975.
- Choi, K. and Simpson, R. L., "Some Mean Velocity, Turbulence and Unsteadiness Characteristics of the VPI & SU Stability Wind Tunnel", Engineering Report, VPI&SU, December 1987.
- Costis, C. E., Hoang, N. T. and Telionis, D. P., "Laminar Separating Flow over a Prolate Spheroid", Journal of Aircraft, Vol. 26, No. 9, September 1989, pp. 810-816.
- Degani, D. and Zilliac, G. G., "Experimental Study of Unsteadiness of The Flow Around Around an Ogive-Cylinder at Incidence", AIAA Paper 88-4330-CP, January 1988 (also accepted to the AIAA Journal April, 1990 issue).
- Degani, D. and Tobak, M., "Numerical, Experimental and Theoretical Study of Convective Instability of Flows Over Pointed Bodies at Incidence", AIAA Paper 91-0291, January 1991.
- Degani, D., "Effect of Geometrical Disturbance of Vortex Asymmetry", AIAA Journal, Vol. 29, No. 4, April 1991, pp. 560-566.

- Degani, D., "Effect of Splitter Plate on Unsteady Flows Around a Body of Revolution", American Institute of Physics, Vol. 3, No. 9, September 1991, pp. 2122-2131.
- Durst, F., Melling, A. and Whitelaw, J. H., "Principles and Practice of Laser-Doppler Velocimetry", Academic Press, 1981.
- Ericsson, L. E., "The Fluid Mechanics of Slender Wing Rock", Journal of Aircraft, Vol. 21, No. 5, January 1984, pp. 332-328.
- Ericsson, L. E. and Redding, J. P., "Asymmetric Vortex Shedding from Bodies of Revolution", Progress in Astronautics and Aeronautics Series, Vol. 19, 1986.
- Ericsson, L. E., "Analytic Prediction of the Maximum Amplitude of Slender Wing Rock", Journal of Aircraft, Vol. 26, No. 1, January 1989, pp. 35-39. Vol. 19, 1986.
- Ericsson, L. E., "Wing Rock Generated by Forebody Vortices", Journal of Aircraft, Vol. 26, No.2, February 1989, pp. 110-116.
- Ericsson, L. E., "Further Analysis of Wing Rock Generated by Forebody Vortices", Journal of Aircraft, Vol. 26, No.12, December 1989, pp. 1098-1104.
- Everett, K. N., Gerner, A. A. and Durston, D. A., "Seven-Hole Cone Probes for High Angle Flow Measurement : Theory and Calibration", AIAA Journal, Vol. 21, No. 7, July 1983, pp. 992-998.
- Farivar, D., "Turbulent Uniform Flow around Cylinder of Finite Length", AIAA Journal, Vol. 19, No. 3, March 1981, pp. 275-181.
- Gallington, R. W., "Measurement of Very Large Flow Angles with Non-Nulling Seven-Hole Probe", Aeronautic Digest - Spring/Summer 1980, USAFA-TR-80-17, USAF Academy, 1980.
- Geissler, W., "Three-Dimensional Laminar Boundary Layer Over a Body of Revolution at Incidence and with Separation", AIAA Journal, Vol. 12, No. 12, 1974, pp. 1743-1745.
- Gould, R. W. F., Rymer, W. G. and Ponsford, P. J., "Wind Tunnel Tests on Chimneys of Circular Section at High Reynolds Numbers", Proceedings Symposium on Wind Effects on Buildings and Structures, Loughborough University (edited by D. J. Johns), Vol. 2, No. 10, 1968.
- Hall, R. M., "Influence of Reynolds Number on Forebody Side Force for 3.5-Diameter Tangent-Ogive Bodies", AIAA Paper 87-2274-CP, August 1987.
- Hall, R. M., Erickson, G. E., Straka, W. A., Peters, S. E., Maines, B. H., Fox, M. C., Hames, J. E. and LeMay, S. P., "Impact of Nose-Probe Chines on the Vortex Flows about the F-16C", AIAA Paper 90-0386, January 1990.
- Han, T. Y. and Patel, V. C., "Flow Separation on a Spheroid at Incidence", Journal of Fluid Mechanics, Vol. 92, 1974, pp. 643-657.

- Hoang, N. T., Telionis, D. P. and Jones, G. S., "The Hemisphere-Cylinder at an Angle of Attack", AIAA Paper 90-0050, January 1990.
- Hoang, N. T., Rediniotis, O. K. and Telionis, D. P., "Separation Over Axisymmetric Bodies at Large Angles of Attack", AIAA Paper 91-0277, January 1991.
- Hoang, N. T. and Telionis, D. P., "The Dynamic Character of the Wake of an Axisymmetric Body at an Angle of Attack", AIAA Paper 91-3268, September 1991.
- Holman, J. P., "Experimental Methods for Engineers", McGraw-Hill Book Company, New York, 1984.
- Hunt, B. L., "Asymmetric Vortex Forces and Wakes on Slender Bodies", AIAA Paper 82-1336, August 1982.
- Hsieh, T., "Flow Field Study About a Hemispherical Cylinder in Transonic and Low Supersonic Mach Number Range", AIAA Paper 75-83, January 1975.
- Hsieh, T., "Low Supersonic, Three-Dimensional Flow About a Hemisphere-Cylinder", AIAA Paper 75-836, June 1975.
- Hsieh, T., "Hemisphere-Cylinder in Low Supersonic Flow", AIAA Journal, Vol. 13, No. 12, December 1975, pp. 1551-1552.
- Hsieh, T. and Wang, K.C., "Concentrated Vortex on the Nose of an Inclined Body of Revolution", AIAA Journal, Vol. 14, No. 5, May 1976, pp. 698-700.
- Hsieh, T., "An Investigation of Separated Flow About a Hemisphere-Cylinder at Incidence in the Mach Number Range from 0.6 to 1.5", AIAA Paper 77-179, January 1977.
- Hsieh, T., "Analysis of Velocity Measurements about a Hemisphere-Cylinder Using a Laser Velocimeter", Journal of Spacecraft and Rockets, Vol. 14, No. 5, May 1977, pp. 280-283.
- Hsieh, T., "Low Supersonic Flow over Hemisphere-Cylinder at Incidence", Journal of Spacecraft and Rockets, Vol. 14, No. 11, November 1977, pp. 662-668.
- Hsieh, T., "Calculation of Viscous, Sonic Flow Over Hemisphere-Cylinder at 19 Deg Incidence - The Capturing of Nose Vortices", AIAA Paper 81-0189, January 1981.
- IMSL Math/Library User's Manual, Softcover Edition, Version 1.0, April 1987.
- Kamemoto, D. Y., "A Study of Seeding Particulates For Laser Velocimetry Applications", Master's Thesis, George Washington University, August 1989.
- Kawamura, T., Hiwada, M., Hibino, T., Mabuchi, I. and Kumada, M., "Flow Around a Circular Cylinder on a Flat Plate", Bulletin of JSME, Vol. 27, No. 232, October 1984, pp. 2142-2151.
- Keener, E. R. and Chapman, G. T., "Similarity in Vortex Asymmetries over Slender Bodies and Wings", AIAA Journal, Vol. 15, No. 9, September 1977, pp. 1370-1372.

Keener, E. R., "Flow Separation Patterns on Symmetric Forebodies", NASA TM 86016, January 1986.

Klopfer, G. H. and Nielsen, J. N., "Basic Studies of Bodies Vortices at High Angles of Attack and Supersonic Speeds", Nielsen Engineering and Research, Inc. Technical Report No. 226, October 1980.

Kreplin, H. P., Vollmers, H. and Meier, H. U., "Measurements of the Wall Shear Stress on an Inclined Prolate Spheroid", Z. Flugwiss Weltraumforschung, Vol. 6, 1982, pp. 248-252.

Malcolm, G. N., Ng, T. T., Lewis, L. C. and Murri, D. G., "Development of Non-Conventional Control Methods for High Angle of Attack Flight Using Vortex Manipulation", AIAA Paper 89-2192, July 1989.

Maskell, E. C., "Flow Separation in Three Dimensions", Royal Aircraft Establishment, Rept. No. Aero 2565, November 1955.

Meade, A. J., and Schiff, L. B., "Experimental Study of Three-Dimensional Separated Flow Surrounding a Hemisphere-Cylinder at Incidence", AIAA Paper 87-2492-CP, August 1987.

Meier, H. U. and Kreplin, H. P., "Experimental Investigations of Boundary Layer Transition and Separation on a Body of Revolution", Z. Flugwiss Weltraumforschung, Vol. 4, 1980, pp. 65-71.

Meier, H. U. and Kreplin, H. P., "Experimental Study of Boundary Layer Velocity Profiles on a Prolate Spheroid at Low Incidence in the Cross-Section $x/L = 0.64$ ", Proceedings 5th USAF-FRG Data Exchange Agreement Meeting, AFFDL-TR-80-3088, 1980, pp. 169-189.

Meier, H. U., Kreplin, H. P. and Vollmers, H., "Velocity Distributions in 3-D Boundary Layers and Vortex Flows on an Inclined Prolate Spheroid", Proceedings 6th USAF-FRG Data Exchange Agreement Meeting, DFVLR-AVA Report IB 22281 CP1, 1981, pp. 202-217.

Moskovitz, C. A., Hall, R. M. and DeJarnette, F. R., "Effects of Nose Bluntness, Roughness and Surface Perturbations on the Asymmetric Flow Past Slender Bodies at Large Angle of Attack", AIAA Paper 89-2236, July 1989.

Ng, T. T., "Effect of a Single Strake on the Forebody Vortex Asymmetry", Journal of Aircraft, Engineering Notes, Vol. 27, 1990, pp. 844-846.

Ng, T. T. and Malcolm, G. N., "Aerodynamic Control Using Forebody Strakes", AIAA Paper 91-0618, January 1991.

Okamoto, T. and Yagita, M., "The Experimental Investigation on the Flow Past a Circular Cylinder of Finite Length Placed Normal to the Plane Surface in a Uniform Stream", Bull. JSME, Vol. 16, No. 95, May 1973, pp. 805-814.

Patel, V. C. and Baek, J. H., "Calculation of Boundary Layers and Separation on a Spheroid at Incident", presented at Numerical and Physical Aspects of Aerodynamic Flows, Long Beach, CA, January 1983.

Patel, V. C. and Choi, D. H., "Calculation of Three-Dimensional Laminar and Turbulent Boundary Layers on Bodies of Revolution at Incidence", in *Turbulent Shear Flows II, Selected Papers from the 2nd Intern. Symp.*, London, edited by L. J. S. Bradbury, F. Durst, B. E. Launder, F. W. Schmidt, J. H. Whitelaw (Springer, New York), 1980, pp. 199-217.

Peake, D. J. and Tobak, M., "Topological Structure of Three-Dimensional Separated Flow", AIAA Paper 81-1260, January 1981.

Ramaprian, B. R., Patel, V. C. and Choi, D. H., "Mean Flow Measurements in the Three-Dimensional Boundary Layer Over a Body of Revolution at Incidence", *Journal of Fluid Mechanics*, Vol. 103, 1981, pp. 479-504.

Ramberg, S. E., "The Effects of Yaw and Finite Length Upon the Vortex Wakes of Stationary and Vibrating Circular Cylinders", *Journal of Fluid Mechanics*, Vol. 128, 1983, pp. 81-107.

Rediniotis, O. K., Hoang, N. T. and Telionis, D. P., "Multi-sensor Investigations of Delta Wing High-Alpha Aerodynamics", AIAA Paper 91-0735, January, 1991.

Richards, B. E., "Measurement of Unsteady Fluid Dynamic Phenomena", Hemisphere Publishing, 1976.

Roos, F. W. and Kegelmann, J. T., "Aerodynamic Characteristics of Three Generic Forebodies at High Angles of Attack", AIAA Paper 91-0275, January 1991.

Schlichting, H., "Boundary-Layer Theory", McGraw-Hill Book Company, New York, Seventh Edition, 1979.

Seegmiller, H. L., "Development of a New Laser-Doppler Velocimeter For The Ames High Reynolds Channel No. II", NASA TM 86772, July 1985.

Seider, G., "Design, Construction and Calibration of Low-Speed Wind Tunnel", Engineering Report, VPI&SU, May 1984.

Shirayama, S. and Kuwahara, K., "Patterns of Three-Dimensional Boundary-Layer Separation", AIAA Paper 87-0461, January 1987.

Stahl, W., "Suppression of Asymmetry of the Vortex Flow Behind a Circular Cone at High Incidence", AIAA Paper 89-3372-CP, August 1989.

Stock, H. W., "Laminar Boundary Layers on Inclined Ellipsoids of Revolution", *Z. Flugwiss Weltraumforschung*, Vol. 4, 1980, pp. 217-224.

Tai, T. C., "Determination of Three-Dimensional Flow Separation by a Streamline Method", AIAA Journal, Vol. 19, 1981, pp. 1264-1271.

Tobak, M., "Topology of Pressure Surfaces in Three-Dimensional Separated Flows", NASA TM 84226, 1987.

Taylor, S. L., Kjelgaard, S. O., Weston, R. P., Thomas, J. L. and Sellers, W. L. III, "Experimental and Computational Study of the Subsonic Flow About a 75° Swept Delta Wing", AIAA Paper 87-2425, August 1987.

Telionis, D. P. and Costis, C. E., "Three-Dimensional Laminar Separation", DTNSRDC Contractors Report, No. DTNSRDC-ASED-CR-04-83, December 1983.

Tobak, M. and Peake, D. J., "Topology of Two-Dimensional and Three-Dimensional Separated Flows", AIAA Paper 79-1480, July 1979.

Tobak, M. and Peake, D. J., "Topology of Three-Dimensional Separated Flows", Annual Review Fluid Mechanics, 1982, 14:61-85.

Tobak, M., Degani, D. and Zilliac, G. G., "Analytical Study of the Origin and Behavior of Asymmetric Vortices", NASA TM 102796, April, 1990.

TSI notes for short courses on data analysis and laser velocimetry, St. Paul, Minnesota, 1987.

Wang, K. C., "Boundary Layers Over a Blunt Body at Low Incidence with Circumferential Reversed Flow", Journal of Fluid Mechanics, Vol. 72, Pt. 1, November 1975, pp. 49-65.

Wang, K. C., "New Developments About Open Separation", AE&EM TR-82-02, San Diego State University, July 1982.

Wardlaw, A. B. and Yanta, W. J., "Multistable Vortex Patterns on Slender, Circular Bodies at High Incidence", AIAA Journal, Vol. 20, No. 4, April 1982, pp. 509-515.

Wardlaw, A. B. and Yanta, W. J., "Asymmetric Flowfield Development of a Slender Body at High Incidence", AIAA Journal, Vol. 22, No. 2, February 1984, pp. 242-249.

Yates, L. A. and Chapman, G. T., "Streamlines, Vorticity Lines and Vorticities", AIAA Paper 91-0731, January 1991

Ying, S. X., Steger, J. L., Schiff, L. B. and Baganoff, D., "Numerical Simulation of Unsteady, Viscous, High-Angle-Of-Attack Flows Using a Partially Flux-Split Algorithm", AIAA Paper 86-2179, June 1986.

Ying, S. X., Schiff, L. B. and Steger, J. L., "A Numerical Study of Three-Dimensional Separated Flow Past a Hemisphere Cylinder", AIAA Paper 87-1207, June 1987.

Zdravkovich, M. M., Brand, V. P., Mathew, G. and Weston, A., "Flow Past Short Circular Cylinders With Two Free Ends", Journal of Fluid Mechanics, Vol. 203, 1989, pp. 557-575.

Zilliac, G. G., "A Computational/Experimental Study of the Flow Around A Body of Revolution Angle of Attack", NASA TM 88329, September 1986.

Zilliac, G. G., "Computational/Experimental Study of the Flowfield on a Body of Revolution at Incidence", AIAA Journal, Vol. 27, No. 8, August 1989, pp. 1008-1016.

Zilliac, G. G., "Calibration of Seven-Hole Pressure Probes For Use in Fluid Flows with Large Angularity", NASA TM 102200, December 1989.

Zilliac, G. G., Degani, D. and Tobak, M., "Asymmetric Vortices on a Slender Body of Revolution", AIAA Paper 90-0388, January 1990.

Appendix: Data Acquisition and Reduction Programs

```
*****
;*
;* WRITTEN BY : NGOC HOANG
;* PURPOSE   : LDV Data Acquisition Program
;*
*****
interrupt_5 equ 5
interrupt_8 equ 8
interrupt_9 equ 9
interrupt_f1 equ 241
interrupt_f2 equ 242
interrupt_f3 equ 243
interrupt_ff equ 255
motor_data segment at 00H
    org     3C4H
    no_pts  dw ?
    message db 40 dup (?)
motor_data ends
rom_bios_data segment at 40H
    org     1AH
    head    dw ?
    tail    dw ?
    buffer  dw 16 dup (?)
    buffer_end label word
rom_bios_data ends
code_seg segment
    assume  cs:code_seg
    org     100h
first: jmp     load_prog
    old_key_int label word
    old_keyboard_int dd ?
prog    proc near
    assume cs:code_seg
    push  ax
    push  bx
    push  cx
    push  dx
    push  di
    push  si
    push  ds
    push  es
    pushf
check_key: call old_keyboard_int
    assume ds:rom_bios_data
```

```

        mov     bx,rom_bios_data
        mov     ds,bx
        mov     bx,tail
        cmp     bx,head
        jne     exit
check_mot: assume ds:motor_data
        mov     bx,motor_data
        mov     ds,bx
        mov     bx,[no_pts]
        cmp     bx,0000h
        je      exit
        dec     bx
        mov     [no_pts],bx
motor_prg: assume ds:motor_data
        mov     bx,motor_data
        mov     ds,bx
        mov     dx,1
        mov     ah,00h
        mov     al,0e3h
        int     14h
        mov     dx,1
        xor     cx,cx
        mov     bx,offset message
        mov     cl,[bx]
        inc     bx
loop1:   mov     al,[bx]
        mov     ah,01h
        int     14h
        mov     ah,02h
        int     14h
        mov     dx,1
        inc     bx
        loop    loop1
        mov     cx,3A98h
delay1:  push    cx
        mov     cx,0104h
delay2:  loop    delay2
        pop     cx
        loop    delay1
begin_TSI: assume ds:rom_bios_data
        mov     bx,rom_bios_data
        mov     ds,bx
        mov     bx,001EH
        mov     [head],bx
        mov     bx,0024H
        mov     [tail],bx
        mov     buffer,3C00H
        mov     buffer[2],3C00H
        mov     buffer[4],1E61H
exit:    pop     es
        pop     ds
        pop     si
        pop     di
        pop     dx
        pop     cx
        pop     bx
        pop     ax
        iret
prog     endp
load_prog proc near
        mov     ah,35H
        mov     al,interrupt_8
        int     21H

```

```

        mov  old_key_int,bx
        mov  old_key_int[2],es
        mov  ah,25H
        lea  dx,prog
        int  21H
        mov  dx,offset load_prog
        int  27H
load_prog endp
code_seg ends
        end  first

```

```

(*****)
(*
(*  WRITTEN BY : NGOC HOANG
(*  PURPOSE   : LDV Data Acquisition Program
(*
(*****)
{$M $4000,0,0}
{$I-}
Program MasterControl;
Uses Crt,Dos;
Type MaxStr = String[80];

(*****)
(*  Procedure Hide_Cursor
(*****)
Procedure Hide_Cursor;
Begin
InLine
( $B4/$01/
  $B5/$01/
  $B1/$00/
  $CD/$10 )
End;

(*****)
(*  Procedure Unhide_Cursor
(*****)
Procedure Unhide_Cursor;
Begin
InLine
( $B4/$01/
  $B5/$0E/
  $B1/$00/
  $CD/$10 )
End;

(*****)
(*  Procedure Remove_Memory
(*****)
Procedure Remove_Memory;
Const
  Clock_IP : Word = $00AA;
  Clock_CS : Word = $0BA2;
Var
  Mem_IP,Mem_CS : Word;
  Regs          : Registers;
Begin
  Mem_IP := MemW[$0000:$0020];
  Mem_CS := MemW[$0000:$0022];
  MemW[$0000:$0020] := Clock_IP;
  MemW[$0000:$0022] := Clock_CS;
  With Regs Do
  Begin
    AH := $49;
    ES := Mem_CS;
  End;
  MsDos(Regs);
End;

(*****)
(*  Procedure Auto_Screen
(*****)

```

```

Procedure Auto_Screen(Auto_Cntp:Integer);
Begin
  Case Auto_Cntp Of
    10 : Begin
      TextBackGround(LightBlue);
      TextColor(Yellow);
      GotoXY(18,10);
      Write(' < R > Run Stepping Motor Program      ');
      TextBackGround(Black);
      TextColor(Yellow);
      GotoXY(18,12);
      Write(' < S > Set-up Data Collecting Procedure ');
      GotoXY(18,14);
      Write(' < C > Start Collecting Data           ');
      GotoXY(18,16);
      Write(' < M > Return To Main Menu              ');
    End;
    12 : Begin
      TextBackGround(LightBlue);
      TextColor(Yellow);
      GotoXY(18,12);
      Write(' < S > Set-up Data Collecting Procedure ');
      TextBackGround(Black);
      TextColor(Yellow);
      GotoXY(18,10);
      Write(' < R > Run Stepping Motor Program      ');
      GotoXY(18,14);
      Write(' < C > Start Collecting Data           ');
      GotoXY(18,16);
      Write(' < M > Return To Main Menu              ');
    End;
    14 : Begin
      TextBackGround(LightBlue);
      TextColor(Yellow);
      GotoXY(18,14);
      Write(' < C > Start Collecting Data           ');
      TextBackGround(Black);
      TextColor(Yellow);
      GotoXY(18,10);
      Write(' < R > Run Stepping Motor Program      ');
      GotoXY(18,12);
      Write(' < S > Set-up Data Collecting Procedure ');
      GotoXY(18,16);
      Write(' < M > Return To Main Menu              ');
    End;
    16 : Begin
      TextBackGround(LightBlue);
      TextColor(Yellow);
      GotoXY(18,16);
      Write(' < M > Return To Main Menu              ');
      TextBackGround(Black);
      TextColor(Yellow);
      GotoXY(18,10);
      Write(' < R > Run Stepping Motor Program      ');
      GotoXY(18,12);
      Write(' < S > Set-up Data Collecting Procedure ');
      GotoXY(18,14);
      Write(' < C > Start Collecting Data           ');
    End;
  End;
End;

```

```

(*****)
(* Procedure Auto_Menu
(*****)
Procedure Auto_Menu(Auto_Cntp:Integer);
Var Incre : Real;
    No_Pts : Integer;
    DataF : Text;
Begin
    ClrScr;
    TextBackground(LightBlue);
    TextColor(Yellow);
    GotoXY(30,4);
    Write(' ');
    GotoXY(30,5);
    Write(' AUTO MENU ');
    GotoXY(30,6);
    Write(' ');
    GotoXY(1,1);
    Write(
    '          CONTROL PROGRAM FOR TSI SOFTWARE',
    ');
    GotoXY(1,25);
    Write(
    ' Arrow Up-Move Up   Arrow Down-Move Down',
    ' Enter-Choose   M-Main Menu ');
    Auto_Screen(Auto_Cntp);
    GotoXY(1,23);
    Write('Increment Of Stepping Motor(in.) : ');
    GotoXY(1,24);
    Write('Number Of Points To Be Collected : ');
    Assign(DataF,'Motor.Dat');
    Reset(DataF);
    If IOresult < > 0 Then
    Begin
        GotoXY(36,23);
        Write('0.00');
        GotoXY(36,24);
        Write(' 0');
    End
    Else
    Begin
        Readln(DataF,Incre);
        Readln(DataF,No_Pts);
        GotoXY(36,23);
        Write(Incre:5:4);
        GotoXY(36,24);
        Write(No_Pts);
        Close(DataF);
    End;
End;

(*****)
(* Procedure Auto_Call
(*****)
Procedure Auto_Call(Var Auto_Cntp:Integer;
    Var Auto_Respl,Auto_Respl2:Char);
Begin
    Repeat
        Auto_Respl := ReadKey;
        Case UpCase(Auto_Respl) Of
            'R' : Begin Auto_Cntp:= 10;Auto_Respl:= #13;End;
            'S' : Begin Auto_Cntp:= 12;Auto_Respl:= #13;End;
            'C' : Begin Auto_Cntp:= 14;Auto_Respl:= #13;End;

```

```

End;
If (Auto_Resp1 = #0) and KeyPressed Then
Begin
  Auto_Resp2 := ReadKey;
  If (Auto_Resp2 = #72) or (Auto_Resp2 = #80) Then
  Begin
    Case Auto_Resp2 Of
      #72 : If Auto_Cntp > 10 Then
        Auto_Cntp := Auto_Cntp - 2;
      Else Auto_Cntp := 16;
      #80 : If Auto_Cntp < 16 Then
        Auto_Cntp := Auto_Cntp + 2;
      Else Auto_Cntp := 10;
    End;
    Auto_Screen(Auto_Cntp);
  End;
End;
Until ((UpCase(Auto_Resp1) = 'M') or (Auto_Resp1 = #13))
  or (UpCase(Auto_Resp1) = 'R') or
  (UpCase(Auto_Resp1) = 'S') or (Auto_Resp1 = 'C'));
End;

(*****
(* Procedure Main_Screen
(*****
Procedure Main_Screen(Main_Cntp: Integer);
Begin
  Case Main_Cntp Of
    10 : Begin
      TextBackground(LightBlue);
      TextColor(Yellow);
      GotoXY(17,10);
      Write(' < I > Initialize The FIND Software ');
      TextBackground(Black);
      TextColor(Yellow);
      GotoXY(17,12);
      Write(' < M > Run The FIND Software Manually ');
      GotoXY(17,14);
      Write(' < A > Run The FIND Software Automatically ');
      GotoXY(17,16);
      Write(' < P > Plot The Velocity Vector Field ');
      GotoXY(17,18);
      Write(' < Q > Quit The Program And Return To DOS ');
    End;
    12 : Begin
      TextBackground(LightBlue);
      TextColor(Yellow);
      GotoXY(17,12);
      Write(' < M > Run The FIND Software Manually ');
      TextBackground(Black);
      TextColor(Yellow);
      GotoXY(17,10);
      Write(' < I > Initialize The FIND Software ');
      GotoXY(17,14);
      Write(' < A > Run The FIND Software Automatically ');
      GotoXY(17,16);
      Write(' < P > Plot The Velocity Vector Field ');
      GotoXY(17,18);
      Write(' < Q > Quit The Program And Return To DOS ');
    End;
    14 : Begin
      TextBackground(LightBlue);
      TextColor(Yellow);

```



```

        GotoXY(17,14);
        Write(' < A > Run The FIND Software Automatically ');
        TextBackGround(Black);
        TextColor(Yellow);
        GotoXY(17,10);
        Write(' < I > Initialize The FIND Software ');
        GotoXY(17,12);
        Write(' < M > Run The FIND Software Manually ');
        GotoXY(17,16);
        Write(' < P > Plot The Velocity Vector Field ');
        GotoXY(17,18);
        Write(' < Q > Quit The Program And Return To DOS ');
    End;
16 : Begin
    TextBackGround(LightBlue);
    TextColor(Yellow);
    GotoXY(17,16);
    Write(' < P > Plot The Velocity Vector Field ');
    TextBackGround(Black);
    TextColor(Yellow);
    GotoXY(17,10);
    Write(' < I > Initialize The FIND Software ');
    GotoXY(17,12);
    Write(' < M > Run The FIND Software Manually ');
    GotoXY(17,14);
    Write(' < A > Run The FIND Software Automatically ');
    GotoXY(17,18);
    Write(' < Q > Quit The Program And Return To DOS ');
    End;
18 : Begin
    TextBackGround(LightBlue);
    TextColor(Yellow);
    GotoXY(17,18);
    Write(' < Q > Quit The Program And Return To DOS ');
    TextBackGround(Black);
    TextColor(Yellow);
    GotoXY(17,10);
    Write(' < I > Initialize The FIND Software ');
    GotoXY(17,12);
    Write(' < M > Run The FIND Software Manually ');
    GotoXY(17,14);
    Write(' < A > Run The FIND Software Automatically ');
    GotoXY(17,16);
    Write(' < P > Plot The Velocity Vector Field ');
    End;
End;
End;

(*****
(*  Procedure Main_Menu
(*****
Procedure Main_Menu(Main_Cntp:Integer);
Begin
    ClrScr;
    TextMode(3);
    TextBackGround(LightBlue);
    TextColor(Yellow);
    GotoXY(30,4);
    Write(' ');
    GotoXY(30,5);
    Write(' MAIN MENU ');
    GotoXY(30,6);
    Write(' ');

```

```

GotoXY(1,1);
Write(
'          CONTROL PROGRAM FOR TSI SOFTWARE',
');
GotoXY(1,25);
Write(
' Arrow Up-Move Up      Arrow Down-Move Down      Enter-Choose',
'   Q-Quit ');
Main_Screen(Main_Cntp);
End;

(*****
(*  Procedure Main_Call
*****
Procedure Main_Call(Var Main_Cntp:Integer;
                    Var Main_Respl,Main_Respl2:Char);
Begin
Repeat
Main_Respl := ReadKey;
Case UpCase(Main_Respl) Of
'I' : Begin Main_Cntp:= 10;Main_Respl:= #13;End;
'M' : Begin Main_Cntp:= 12;Main_Respl:= #13;End;
'A' : Begin Main_Cntp:= 14;Main_Respl:= #13;End;
'P' : Begin Main_Cntp:= 16;Main_Respl:= #13;End;
End;
If (Main_Respl = #0) and KeyPressed Then
Begin
Main_Respl2 := ReadKey;
If (Main_Respl2 = #72) or (Main_Respl2 = #80) Then
Begin
Case Main_Respl2 Of
#72 : If Main_Cntp > 10 Then
Main_Cntp:= Main_Cntp-2
Else Main_Cntp:= 18;
#80 : If Main_Cntp < 18 Then
Main_Cntp:= Main_Cntp + 2
Else Main_Cntp:= 10;
End;
Main_Screen(Main_Cntp);
End;
End;
Until ((UpCase(Main_Respl) = 'Q') or (Main_Respl = #13)
or (UpCase(Main_Respl) = 'I') or (UpCase(Main_Respl) = 'M')
or (Main_Respl = 'P') or (UpCase(Main_Respl) = 'A'));
End;

(*****
(*  Procedure Response
*****
Procedure Response(X,Y : Integer;Var Flag : Boolean);
Begin
GotoXY(22,19);
Write(' Wrong response ... Try Again ',#G);
Delay(1500);
TextBackGround(Black);
TextColor(Yellow);
GotoXY(22,19);
Write('          ');
GotoXY(X,Y);
TextBackGround(LightBlue);
TextColor(Yellow);
Flag := False;
End;

```

```

(*****)
(* Procedure Motor_Dat
(*****)
Procedure Motor_Dat;
Var
  Flag      : Boolean;
  Incre     : Real;
  DataF     : Text;
  No_Pts    : Integer;
Begin
  TextBackGround(LightBlue);
  TextColor(Yellow);
  GotoXY(36,23);
  Write(' ');
  GotoXY(36,23);
  Repeat
    Flag := True;
    Readln(Incre);
    If IOResult < > 0 Then response(36,23,flag);
  Until Flag = True;
  TextBackGround(Black);
  TextColor(Yellow);
  GotoXY(36,23);
  Write(Incre:5:4);
  TextBackGround(LightBlue);
  TextColor(Yellow);
  GotoXY(36,24);
  Write(' ');
  GotoXY(36,24);
  Repeat
    Flag := True;
    Readln(No_Pts);
    If IOResult < > 0 Then response(36,24,flag);
  Until Flag = True;
  TextBackGround(Black);
  TextColor(Yellow);
  GotoXY(36,24);
  Write(No_Pts);
  Assign(DataF,'Motor.Dat');
  Rewrite(DataF);
  Writeln(DataF,Incre);
  Writeln(DataF,No_Pts);
  Close(DataF);
End;

(*****)
(* Procedure Run_Motor
(*****)
Procedure Run_Motor(Out_Motor : MaxStr);
Begin
  InLine(
    $BA/$01/$00/
    $B4/$00/
    $B0/$E3/
    $CD/$14/
    $BA/$01/$00/
    $C5/$76/$04/
    $33/$C9/
    $8A/$0C/
    $46/
    $8A/$04/
    $B4/$01/

```

```

$CD/$14/
$B4/$02/
$CD/$14/
$8A/$D0/
$B4/$02/
$CD/$21/
$BA/$01/$00/
$E2/$EA/
$B9/$98/$3A/
$E2/$FE);
End;

(*****
(* Procedure Get_Data_Motor
(*****
Procedure Get_Data_Motor(Var Out_Motor:MaxStr;Incre:Real;OK:Boolean);
Const Rev_Per_Inch : Real = 40.0;
      Step_Per_Rev  : Real = 12800.0;
      Blank         : string[1] = ' ';
Var Distance_String : MaxStr;
      Flag          : Boolean;
      Distance_Travel : Real;
      s             : String[1];
Begin
  If OK Then
    Begin
      TextBackGround(Black);
      TextColor(Yellow);
      GotoXY(1,22);
      Write('Distance Stepping Motor Will Move(in.) : ');
      TextBackGround(LightBlue);
      TextColor(Yellow);
      GotoXY(43,22);
      Write(' ');
      GotoXY(43,22);
      Repeat
        Flag := True;
        Readln(Distance_Travel);
        If IOResult < > 0 Then response(43,22,flag);
      Until Flag = True
    End
    Else Distance_Travel := Incre;
      Distance_Travel := Distance_Travel*Rev_Per_Inch*Step_Per_Rev;
      str(Distance_Travel:10:2,Distance_String);
      s := Copy(Distance_String,1,1);
      while (s = Blank) Do
        Begin
          Distance_String := Copy(Distance_String,2,79);
          s := Copy(Distance_String,1,1);
        End;
      Out_Motor := 'A1 V5 D'+ Distance_String + ' G ';
      TextBackGround(Black);
      TextColor(Yellow);
End;

(*****
(* Procedure Collect_Data
(*****
Procedure Collect_Data(No_Pts:Integer;Out_Motor:MaxStr);
Var
  Regs      : Registers;
  Pts_Collect : Word;
  Pts_Length : Byte;

```

```

i      : Word;
s      : String[1];
Begin
{ MemW[$0040:$001A] := $001E;
  MemW[$0040:$001C] := $0022;
  MemW[$0040:$001E] := $2166;
  MemW[$0040:$0020] := $1071;
  Exec('c:\command.com',/c drpacq');
  MemW[$0040:$001A] := $001E;
  MemW[$0040:$001C] := $0020;
  MemW[$0040:$001E] := $1400;
  Intr($09,Regs);
  Exec('c:\command.com',/c drpacq');}
Pts_Collect := No_Pts;
Pts_Length := Length(Out_Motor);
MemW[$0000:$03C4] := Pts_Collect;
Mem[$0000:$03C6] := Pts_Length;
For i:= $03C7 to $03C7 + Pts_Length Do
Begin
  s := Copy(Out_Motor,1,1);
  Mem[$0000:i] := Ord(s[1]);
  Out_Motor := Copy(Out_Motor,2,80);
End;
Exec('c:\command.com',/c c:\Tsi\drpacq');
End;

(*****
(*   Procedure Main
(*****
Var
  Main_Cntp,Auto_Cntp   : Integer;
  Main_Respl,Main_Resp2 : Char;
  Auto_Respl,Auto_Resp2 : Char;
  OK                    : Boolean;
  No_Pts                : Integer;
  Regs                  : Registers;
  Out_Motor             : MaxStr;
  Incre                 : Real;
  DataF                 : Text;
  Ans                   : Char;
Begin
  Exec('c:\Dos\command.com',/c c:\Dos\graphics');
  Exec('c:\Dos\command.com',/c c:\Dos\grftabl');
  Exec('c:\Dos\command.com',/c c:\Tsi\vidpop');
  MemW[$0000:$03C4] := $0000;
  Exec('c:\Dos\command.com',/c c:\Tsi\pop');
  Main_Cntp := 10;
  Repeat
    Main_Menu(Main_Cntp);
    Hide_Cursor;
    Main_Call(Main_Cntp,Main_Respl,Main_Resp2);
    If Main_Respl=#13 Then
      Begin
        Case Main_Cntp Of
          10 : Exec('c:\Dos\command.com',/c c:\Tsi\drpacq');
          12 : Exec('c:\Dos\command.com',/c c:\Tsi\drpacq');
          14 : Begin
              Auto_Cntp := 10;
              Repeat
                Auto_Menu(Auto_Cntp);
                Auto_Call(Auto_Cntp,Auto_Respl,Auto_Resp2);
                If Auto_Respl=#13 Then
                  Begin

```

```

Case Auto_Cntp Of
10 : Begin
{
    OK := True;
    Get_Data_Motor(Out_Motor,Incr,OK);
    GotoXY(1,22);
    Write('Motor is moving... ');
    GotoXY(1,30);
    Write(' String sent to motor is : ');
    Run_Motor(Out_Motor);
    Delay(2000); }
    Exec('c:\Dos\command.com','/c c:\Tsi\motor');
End;
12 : Motor_Dat;
14 : Begin
    OK := False;
    Assign(DataF,'Motor.Dat');
    Reset(DataF);
    If IOresult < > 0 Then
    Begin
        TextBackGround(LightBlue);
        TextColor(Yellow);
        GotoXY(16,19);
        Write('      Cannot find MOTOR.DAT file',
            ' ... ');
        GotoXY(16,20);
        Write(' Use the previous option to create',
            ' this file ',cG);
        Delay(4000);
        TextBackGround(Black);
        TextColor(Yellow);
    End
    Else
    Begin
        Readln(DataF,Incr);
        Readln(DataF,No_Pts);
        Get_Data_Motor(Out_Motor,Incr,OK);
        Collect_Data(No_Pts,Out_Motor);
        Close(DataF);
    End;
    Auto_Menu(Auto_Cntp);
End;
16 : Begin End;
End;
End;
Until (UpCase(Auto_Respl) = 'M')or(Auto_Cntp=16);
End;
16 : Begin
    ClrScr;
    Repeat
        Write(' Reduce LDV raw data or plot? (R or P) : ');
        Readln(Ans);
    Until (UpCase(Ans)='R')or(UpCase(Ans)='P');
    Case UpCase(Ans) Of
        'R' : Exec('c:\Dos\command.com','/c c:\Tsi\trans');
        'P' : Exec('c:\Dos\command.com','/c c:\Tsi\ldv');
    End;
End;
End;
18 : Begin
    Unhide_Cursor;
    Remove_Memory;
    TextMode(3);
    TextBackGround(Black);
    TextColor(White);

```

```
        ClrScr;
        Exit;
    End;
End;
End;
Until UpCase(Main_Respl) = 'Q';
UnHide_Cursor;
Remove_Memory;
TextMode(3);
TextBackGround(Black);
TextColor(White);
ClrScr;
End.
```

```

10 '*****
11 '*'
20 '* WRITTEN BY : NGOC HOANG
30 '* PURPOSE : LDV Data Acquisition Program
50 '*'
51 '*****
60 Color 14,0,0
70 Cls
80 Key Off
90 Open "COM2:9600,N,8,1,RS,DS,CD" AS #1
100 Locate 5,25
101 Print chr$(201);
102 For i = 1 to 26
103 Print chr$(205);
104 Next i
105 Print chr$(187)
110 Locate 6,25 : Print chr$(186);" STEPPING MOTOR PROGRAM ";chr$(186)
120 Locate 7,25 :
121 Print chr$(200);
122 For i = 1 to 26
123 Print chr$(205);
124 Next i
125 Print chr$(188)
130 Locate 15,12 : Print "Distance the motor moved (in.) : 0"
140 Locate 13,12 : Print "Velocity is set at 10 rev/sec"
150 Locate 14,12 : Print "Acceleration is set at 5 rev/sec/sec"
160 Locate 1,1
161 Print chr$(201);
162 For i = 1 to 78
163 Print chr$(205);
164 Next i
165 Print chr$(187)
180 Locate 2,1
190 Print chr$(186);" ";
191 Print "CHECK TO SEE IF THE STEPPING MOTOR RESPONDS";
192 Print " ";chr$(186)
200 Locate 3,1
201 Print chr$(200);
202 For i = 1 to 78
203 Print chr$(205);
204 Next i
205 Print chr$(188)
220 Posi = 0
230 Locate 16,12
240 Input "Enter distance to be moved (in.) : ",Dis
250 Rev = Dis*40!*12800!
260 Posi = Posi + Dis
270 Locate 15,46 : Print "
280 Locate 15,45 : Print USING "-###.#####";Posi
290 Locate 16,46 : Print "
300 A$ = Str$(Rev)
310 S$ = Mid$(A$,1,1)
320 IF S$="." THEN 350
330 A$ = Mid$(A$,2)
340 IF Rev=0 THEN 380
350 Comad$ = "A1 V5 D"+A$+" G "
360 Print #1,Comad$
370 Goto 230
380 Locate 17,12
390 Input "Enter increment of stepping motor(in.) : ",Dis
400 Rev = Dis*40!*12800!
410 A$ = Str$(Rev)
420 S$ = Mid$(A$,1,1)

```



```
430 AS = Mid$(AS,2)
440 Comad$ = "A1 V5 D"+AS+" G "
450 Print #1,Comad$
460 Comad$ = "A1 V5 D-"+AS+" G "
470 Print #1,Comad$
480 Screen 0,1
490 Color 15,0
500 Cls
510 End
```

```

(*****)
(*
(* WRITTEN BY : NGOC HOANG
(* PURPOSE   : Controls the Velmex stepping motor
(*
(*****)
{$M $4000,0,0}
{$I-}
Program Velmex_Motor;
Uses Crt,Dos;
Type MotorStr = String[100];
Var Str      : MotorStr;
    a        : Char;
    PortInFo  : Byte;
    PortNumber : Word;
    Distance  : Real;
    No_Velmex,No_Compu : Integer;
    i,j       : Integer;

(*****)
(* Procedure InitializePort
(*****)
Procedure InitializePort;
Var Regs : Registers;
Begin
    With Regs Do
        Begin
            AH := $00;
            AL := PortInFo;
            DX := PortNumber;
        End;
        Intr($14,Regs);
    End;

(*****)
(* Procedure ReceiveChar
(*****)
Procedure ReceiveChar;
Var Regs : Registers;
    RPrompt : Boolean;
Begin
    RPrompt := False;
    While RPrompt Do
        Begin
            With Regs Do
                Begin
                    AH := $02;
                    DL := PortNumber;
                End;
                Intr($14,Regs);
                RPrompt := False = (Chr(Regs.AL) = 'c');
            End;
        End;

(*****)
(* Procedure SendChar
(*****)
Procedure SendChar (OutPutChar : Char);
Var Regs : Registers;
Begin
    With Regs Do
        Begin
            AH := $01;

```

```

    AL := Ord(OutPutChar);
    DX := PortNumber;
End;
Intr($14,Regs);
End;

(*****
(* Procedure MoveVelmexMotor
*****
Procedure MoveVelmexMotor (Str:MotorStr;StrLgth:Integer);
Var Regs : Registers;
    i : Integer;
Begin
    For i := 1 To StrLgth Do
        Begin
            With Regs Do
                Begin
                    AH := $01;
                    AL := Ord(Str[i]);
                    DX := PortNumber;
                End;
                Intr($14,Regs);
            End;
        End;
    End;

(*****
(* Procedure Serial_Talk
*****
Procedure Serial_Talk;
Var ClearPort : Byte;
    Data_Ready,Parity_Error,Framing_Error : Boolean;
Begin
    ClearPort := Ord('S');
    ClearPort := Port[$3F8];
    Repeat ClearPort:= Port[$3F8] Until ClearPort=Ord('G');
End;

(*****
(* Procedure Main
*****
Begin
    ClrScr;
    PortInFo := $83;
    PortNumber := $0000;
    InitializePort;
    No_Compu := 40;
    No_Velmex := 25;
    For i:= 1 To No_Velmex Do
        Begin
            For j:= 1 To No_Compu Do
                Begin
                    Exec('c:\dos\command.com','/c seven');
                    Exec('c:\dos\command.com','/c mot1');
                    Delay(1000);
                End;
                Exec('c:\dos\command.com','/c mot2');
                Delay(10000);
                Exec('c:\dos\command.com','/c mot2');
                Delay(10000);
                Exec('c:\dos\command.com','/c mot2');
                Delay(10000);
                Exec('c:\dos\command.com','/c mot2');
                Delay(10000);
            End;
        End;
    End;
End;

```

```
ReceiveChar;  
SendChar('E');  
Str := 'C1 = 0.01:V1 = 1000:R1 = 2:I1 = -2.54:@' + Chr(13);  
MoveVelmexMotor(Str,Length(Str));  
ReceiveChar;  
Delay(2000);  
SendChar('&');  
Delay(10000);  
End;  
End.
```

```

SLARGE
$DECLARE
$DEBUG
C*****
C*
C* WRITTEN BY : NGOC HOANG
C* PURPOSE   : LDV Data Reduction Program
C*
C*****
  Program Transfer
  Character*1  Ans
  Character*60 Fname,Fblank
  Character*10 NumberType
  Character*64 FTemp
  Character*70 OutFi
  Integer Mode,TBD,Kpts,Unit,Fnum,i,j,k,l,Start
  Real BlueShift,GreenShift,Temp,Distance,Incre
  NumberType = '0123456789'
c  Write(*,'(a26\)' ) ' Continuity ? (Y or N) : '
c  Read(*,'(a1)' ) Ans
c  If ((Ans.EQ.'Y').or.(Ans.EQ.'y')) Then
c    Call CONTINUITY( )
c    Goto 300
c  EndIf
  Write(*,'(a24\)' ) ' Input number of file : '
  Read(*,'(i3)' ) Fnum
  Write(*,'(a38\)' ) ' Input name of file (w/o extension) : '
  Read(*,'(a60)' ) Fname
  Do 200 i = 1,60
    If (Fname(60:60).EQ.' ') Then
      Fblank = ' ' // Fname(1:59)
      Fname = Fblank
    EndIf
200 Continue
  Write(*,'(a24\)' ) ' Starting file number : '
  Read(*,'(i3)' ) Start
  Write(*,'(a28\)' ) ' Name of output data file : '
  Read(*,'(a70)' ) OutFi
  open(Unit = 8,file = OutFi,status = 'new')
  Write(8,'(a61)' ) 'Distance(in.)      Velocity(Blue)      Ve
> locity(Green)'
  Write(*,'(a25\)' ) ' Total Distance travel : '
  Read(*,*) Distance
  Write(*,'(a24\)' ) ' Incremental Distance : '
  Read(*,*) Incre
  Distance = Distance + Incre
  Fnum = Fnum + Start-1
  Do 100 i = Start,Fnum
    Distance = Distance - Incre
    j = i/10 + 1
    l = i / 10
    Temp = ((Float(i)/10.0) - Float(l))*10.0
    k = Temp + 1
    FTemp = Fname // '.R' // NumberType(j:j) // NumberType(k:k)
    Write(*,'(1x,a64)' ) FTemp
    open(Unit = 6,file = FTemp,access = 'sequential')
    Call rdfhdr(Mode,TBD,Kpts,BlueShift,GreenShift)
    Close (Unit = 6)
    open(Unit = 6,file = FTemp,access = 'direct',Recl = 840)
    Call RawDat(Mode,TBD,Kpts,BlueShift,GreenShift,Distance)
    Close (Unit = 6)
100 Continue

```

```

      Close (Unit = 8)
300  Continue
      End

```

```

C*****

```

```

C* SUBROUTINE RDFHDR :

```

```

C*****

```

```

      Subroutine rdfhdr(Mode,TBD,Kpts,BlueShift,GreenShift)
      Integer Mode,TBD,Kpts,i
      Real BlueShift,GreenShift
      Character*20 Dummy
      Character*20 drparr(153)
      Do 100 i = 1,5
100  Read(6,'(a20)') Dummy
      Read(6,'(i1)') Mode
      Read(6,'(a20)') Dummy
      Read(6,'(i1)') TBD
      Read(6,'(a20)') Dummy
      Read(6,'(i2)') Kpts
      Do 200 i = 11,27
200  Read(6,'(a20)') Dummy
      Read(6,'(f3.1)') BlueShift
      Read(6,'(f3.1)') GreenShift
      c If (Mode.EQ.1) Write(*,*) ' Random Mode is on'
      c If (Mode.EQ.0) Write(*,*) ' Coincidence Mode is on'
      c If (TBD.EQ.1) Write(*,*) ' TBD is on'
      c If (TBD.EQ.0) Write(*,*) ' TBD is off'
      c Write(*,'(1x,a27,i2)') ' Number of data K-points : ',Kpts
      c Write(*,'(1x,a32,f10.4,a4)') ' Frequency shift IFA#1 (Blue) : ',
      c *BlueShift,' MHz'
      c Write(*,'(1x,a32,f10.4,a4)') ' Frequency shift IFA#2 (Green): '
      c *GreenShift,' MHz'
      Return
      End

```

```

C*****

```

```

C* SUBROUTINE RAWDAT

```

```

C*****

```

```

      Subroutine RawDat(Mode,TBD,Kpts,BlueShift,GreenShift,Distance)
      Integer Mode,TBD,Kpts,RecNum,NowPDP,TotalRec,NumRec,NumPts
      Real BlueShift,GreenShift,Distance
      if ((Mode.EQ.1).And.(TBD.EQ.0)) NowPDP = 2
      If ((Mode.EQ.1).And.(TBD.EQ.1)) NowPDP = 3
      If ((Mode.EQ.0).And.(TBD.EQ.0)) NowPDP = 4
      If ((Mode.EQ.0).And.(TBD.EQ.1)) NowPDP = 5
      NumRec = Kpts*1024*NowPDP/420
      TotalRec = NumPts*1024*NowPDP/420
      If(NumRec.Ne.TotalRec) NumRec = NumRec + 1
      NumRec = NumRec + 4
      If ((Mode.EQ.1).And.(TBD.EQ.0))
      > Call RANDOM(BlueShift,GreenShift,TBD,NumRec,Distance)
      If ((Mode.EQ.1).And.(TBD.EQ.1))
      > Call RANDOM(BlueShift,GreenShift,TBD,NumRec,Distance)
      If ((Mode.EQ.0).And.(TBD.EQ.0))
      > Call COINCI(BlueShift,GreenShift,TBD,NumRec,Distance)
      If ((Mode.EQ.0).And.(TBD.EQ.1))
      > Call COINCI(BlueShift,GreenShift,TBD,NumRec,Distance)
      Return
      End

```

```

C*****

```

```

C* SUBROUTINE CHAUVENET

```

```

C*****

```

```

      Subroutine Chauvenet(AveVel,Velocity,NoPts)
      Integer NoPts,i

```

```

Real*8 AveVel,Velocity(4000),Deviation(4000),AcceptDev,StdDev
Real*8 TotalVel,Cnt
StdDev = 0.0D0
Cnt = 0.0D0
TotalVel = 0.0D0
If (NoPts.LE.3) AcceptDev = 1.38
If (NoPts.EQ.4) AcceptDev = 1.54
If (NoPts.EQ.5) AcceptDev = 1.65
If (NoPts.EQ.6) AcceptDev = 1.73
If ((NoPts.GT.6).And.(NoPts.LT.10)) AcceptDev = 1.80
If ((NoPts.GE.10).And.(NoPts.LT.15)) AcceptDev = 1.96
If ((NoPts.GE.15).And.(NoPts.LT.25)) AcceptDev = 2.13
If ((NoPts.GE.25).And.(NoPts.LT.50)) AcceptDev = 2.33
If ((NoPts.GE.50).And.(NoPts.LT.100)) AcceptDev = 2.57
If ((NoPts.GE.100).And.(NoPts.LT.300)) AcceptDev = 2.81
If ((NoPts.GE.300).And.(NoPts.LT.500)) AcceptDev = 3.14
If ((NoPts.GE.500).And.(NoPts.LT.1000)) AcceptDev = 3.29
If (NoPts.GE.1000) AcceptDev = 3.48
Do 100 i=1,NoPts
  StdDev = StdDev + (Velocity(i)-AveVel)**2.0
  Deviation(i) = ABS(Velocity(i)-AveVel)
100 Continue
StdDev = dsqrt(1.0/Float(NoPts-1)*StdDev)
Do 200 i=1,NoPts
If ((Deviation(i)/StdDev).LT.AcceptDev) Then
  TotalVel = TotalVel + Velocity(i)
  Cnt = Cnt + 1.0D0
EndIf
200 Continue
AveVel = TotalVel/Cnt
Return
End
C*****
C* SUBROUTINE RANDOM
C*****
Subroutine RANDOM(BlueShift,GreenShift,TBD,NumRec,Distance)
Integer i,j,k,l,TBD,NumRec,Cnt1,Cnt0
Integer*2 Model,TBD1,ID1,Cycle1,Man1,Exp1
Integer*2 Mode0,TBD0,ID0,Cycle0,Man0,Exp0
Integer*2 ID,Buffer(420)
Real BlueShift,GreenShift,Distance
Real*8 Dop0,Dop1,BlueFS,GreenFS,VelBlue(4000),VelGreen(4000)
Real*8 AveBlue,AveGreen
Cnt1 = 0
Cnt0 = 0
BlueFS = 3.55D0
GreenFS = 3.72D0
j = 420
If (TBD.EQ.0) k = 2
If (TBD.EQ.1) k = 3
Do 90 l=5,NumRec
Write(*,'(a20,i4)') ' Record number = ',l
Read(6,Rec=1) (Buffer(i),i=1,420)
Do 100 i=1,j,k
If (Buffer(i).EQ.0) Then
  NumRec=1
  Goto 100
EndIf
c
c Calculating TBD in microsecond
If (TBD.EQ.1) Then
  Man = iand(Buffer(i+2),16#0FFF)
  Exp = ishift(Buffer(i+2),-12)

```

```

    TotalTBD = Man*(2**Exp)
EndIf
C
ID = ishft(Buffer(i),-8)
If ((iand(ID,16#000F).Ne.16#0001).And.
(iand(ID,16#000F).Ne.16#0000)) Then
    Write(*,(1x,a26)) ' ID number must be 1 or 0 '
    Write(*,(1x,a16)) ' Check data file '
    Stop
EndIf
If (iand(ID,16#000F).EQ.16#0001) Goto 200
If (iand(ID,16#000F).EQ.16#0000) Goto 300
C
C Velocity for IFA#1 (Green Light)
C Wavelength from this channel must be 514.5 nano meter
C Fringe spacing from this channel must be 5.01 micro meter
C
200 Cycle1 = iand(Buffer(i),16#000F)
ID1 = ishft(Buffer(i),-8)
Mode1 = ishft(Buffer(i),-14)
TBD1 = ishft(Buffer(i),-15)
Man1 = iand(Buffer(i+1),16#0FFF)
Exp1 = ishft(Buffer(i+1),-12)
If (Cycle1.Ne.16#0008) Then
    Write(*,*)
    Write(*,(1x,a27)) ' Number of Cycles must be 8 '
    Write(*,(1x,a16)) ' Check data file '
    Write(*,(1x,a19,i4)) ' Number of Cycle = ',Cycle1
    Stop
EndIf
Cnt1 = Cnt1 + 1
Dop1 = Float(Man1)*(2.0**(Exp1-2))
Dop1 = 8.0/Dop1*1000.0-GreenShift
VelGreen(Cnt1) = GreenFS*Dop1
Write(8,7) TotalTBD, VelGreen(Cnt1), ' 1 '
7 Format(1x,f20.5,5x,f10.5,2x,a9)
Goto 100
C
C Write(*,(1x,i4)) Cycle1
C Write(*,(1x,i4)) ID1
C Write(*,(1x,i4)) Mode1
C Write(*,(1x,i4)) TBD1
C Write(*,(1x,i4)) Man1
C Write(*,(1x,i4)) Exp1
C Write(*,*) VelGreen
C
C Velocity for IFA#0 (Blue Light)
C Wavelength from this channel must be 488.0 nano meter
C Fringe spacing from this channel must be 4.68 micro meter
C
300 Cycle0 = iand(Buffer(i),16#000F)
ID0 = ishft(Buffer(i),-8)
Mode0 = ishft(Buffer(i),-14)
TBD0 = ishft(Buffer(i),-15)
Man0 = iand(Buffer(i+1),16#0FFF)
Exp0 = ishft(Buffer(i+1),-12)
If (Cycle0.Ne.16#0008) Then
    Write(*,(1x,a27)) ' Number of Cycles must be 8 '
    Write(*,(1x,a16)) ' Check data file '
    Write(*,(1x,a19,i4)) ' Number of Cycle = ',Cycle0
    Stop
EndIf
Cnt0 = Cnt0 + 1

```



```

Dop0 = Float(Man0)*(2.0**(Exp0-2))
Dop0 = 8.0/Dop0*1000.0-BlueShift
VelBlue(Cnt0) = BlueFS*Dop0
Write(8,7) TotalTBD, VelBlue(Cnt0), ' 0'
C
C Write(*,'(1x,i4)') Cycle0
C Write(*,'(1x,i4)') ID0
C Write(*,'(1x,i4)') Mode0
C Write(*,'(1x,i4)') TBD0
C Write(*,'(1x,i4)') Man0
C Write(*,'(1x,i4)') Exp0
C Write(*,*) VelBlue
C Write(*,*)
100 Continue
90 Continue
AveBlue = 0.0D0
AveGreen = 0.0D0
If (Cnt0.Ne.0) Then
  Do 500 i = 1, Cnt0
500 AveBlue = AveBlue + VelBlue(i)
  AveBlue = AveBlue/Float(Cnt0)
  Call Chauvenet(AveBlue, VelBlue, Cnt0)
Else
  Write(*,'(a31)') ' No data points for blue beams'
  AveBlue = 9999.0D0
EndIf
If (Cnt1.Ne.0) Then
  Do 600 i = 1, Cnt1
600 AveGreen = AveGreen + VelGreen(i)
  AveGreen = AveGreen/Float(Cnt1)
  Call Chauvenet(AveGreen, VelGreen, Cnt1)
Else
  Write(*,'(a32)') ' No data points for green beams'
  AveGreen = 9999.0D0
EndIf
Write(*,*)
Write(8,700) ' Velocity of IFA#1 (Blue) = ', AveBlue, ' m/s'
Write(8,700) ' Velocity of IFA#2 (Green) = ', AveGreen, ' m/s'
700 Format(1x,a29,f10.5,a4)
800 Format(1x,1p,e10.4,5x,e20.10,5x,e20.10)
Return
End
C*****
C* SUBROUTINE COINCI
C*****
Subroutine COINCI(BlueShift, GreenShift, TBD, NumRec, Distance)
Integer i, j, k, l, TBD, NumRec, Cnt1, Cnt0
Integer*2 Model, TBD1, ID1, Cycle1, Man1, Exp1
Integer*2 Mode0, TBD0, ID0, Cycle0, Man0, Exp0
Integer*2 ID, Buffer(420)
Integer*2 Man, Exp
Real BlueShift, GreenShift, Distance, TotalTBD
Real*8 Dop0, Dop1, BlueFS, GreenFS, VelBlue(4000), VelGreen(4000)
Real*8 AveBlue, AveGreen
Cnt1 = 0
Cnt0 = 0
BlueFS = 3.55D0
GreenFS = 3.72D0
j = 420
If (TBD.EQ.0) k = 4
If (TBD.EQ.1) k = 5
do 90 l = 5, NumRec
Write(*,'(a20,i4)') ' Record number = ', l

```

```

Read(6,Rec=1) (Buffer(i),i=1,420)
Do 100 i=1,j,k
If (Buffer(i).EQ.0) Then
    NumRec=1
    Goto 100
EndIf
C
C    Calculating TBD in microsecond
C
If (TBD.EQ.1) Then
    Man = iand(Buffer(i+4),16#0FFF)
    Exp = ishft(Buffer(i+4),-12)
    TotalTBD = Man*(2**Exp)
EndIf
C
C
C    Velocity for IFA#1 (Green Light)
C    Wavelength from this channel must be 514.5 nano meter
C    Fringe spacing from this channel must be 5.01 micro meter
C
Cycle1 = iand(Buffer(i),16#000F)
ID1 = ishft(Buffer(i),-8)
Model = ishft(Buffer(i),-14)
TBD1 = ishft(Buffer(i),-15)
Man1 = iand(Buffer(i+1),16#0FFF)
Exp1 = ishft(Buffer(i+1),-12)
If (Cycle1.Ne.16#0008) Then
    Write*,'(1x,a27)' ' Number of Cycles must be 8'
    Write*,'(1x,a16)' ' Check data file'
    Write*,'(1x,a19,i4)' ' Number of Cycle = ',Cycle1
    Stop
EndIf
If (ID1.Ne.16#0001) Then
    Write*,'(1x,a27)' ' ID number must be 1'
    Write*,'(1x,a16)' ' Check data file'
    Write*,'(1x,a13,i4)' ' ID number = ',ID1
    Stop
EndIf
Cnt1 = Cnt1 + 1
Dop1 = Float(Man1)*(2.0**(Exp1-2))
Dop1 = 8.0/Dop1*1000.0-GreenShift
VelGreen(Cnt1) = GreenFS*Dop1
C
C    Write*,'(1x,i4)' Cycle1
C    Write*,'(1x,i4)' ID1
C    Write*,'(1x,i4)' Model
C    Write*,'(1x,i4)' TBD1
C    Write*,'(1x,i4)' Man1
C    Write*,'(1x,i4)' Exp1
C    Write*,'*' VelGreen
C
C
C    Velocity for IFA#0 (Blue Light)
C    Wavelength from this channel must be 488.0 nano meter
C    Fringe spacing from this channel must be 4.68 micro meter
C
Cycle0 = iand(Buffer(i+2),16#000F)
ID0 = ishft(Buffer(i+2),-8)
Mode0 = ishft(Buffer(i+2),-14)
TBD0 = ishft(Buffer(i+2),-15)
Man0 = iand(Buffer(i+3),16#0FFF)
Exp0 = ishft(Buffer(i+3),-12)
If (Cycle0.Ne.16#0008) Then

```

```

        Write(*,'(1x,a27)') ' Number of Cycles must be 8'
        Write(*,'(1x,a16)') ' Check data file'
        Write(*,'(1x,a19,i4)') ' Number of Cycle = ',Cycle0
        Stop
    EndIf
    If (ID0.Ne.16#0000) Then
        Write(*,'(1x,a27)') ' ID number must be 0'
        Write(*,'(1x,a16)') ' Check data file'
        Write(*,'(1x,a13,i4)') ' ID number = ',ID0
        Stop
    EndIf
    Cnt0 = Cnt0 + 1
    Dop0 = Float(Man0)*(2.0**(Exp0-2))
    Dop0 = 8.0/Dop0*1000.0-BlueShift
    VelBlue(Cnt0) = BlueFS*Dop0
C
C   Write(*,'(1x,i4)') Cycle0
C   Write(*,'(1x,i4)') ID0
C   Write(*,'(1x,i4)') Mode0
C   Write(*,'(1x,i4)') TBD0
C   Write(*,'(1x,i4)') Man0
C   Write(*,'(1x,i4)') Exp0
C   Write(*,*) VelBlue
C   Write(*,*)
    Write(8,7) TotalTBD, VelBlue(Cnt0), VelGreen(Cnt1)
7   Format(1x,f20.5,5x,f10.5,5x,f10.5)
100  Continue
90   Continue
    AveBlue = 0.0D0
    AveGreen = 0.0D0
    If (Cnt0.Ne.0) Then
        Do 500 i=1,Cnt0
500   AveBlue = AveBlue + VelBlue(i)
        AveBlue = AveBlue/Float(Cnt0)
        Call Chauvenet(AveBlue, VelBlue, Cnt0)
    Else
        Write(*,'(a31)') ' No data points for blue beams'
        AveBlue = 9999.0D0
    EndIf
    If (Cnt1.Ne.0) Then
        Do 600 i=1,Cnt1
600   AveGreen = AveGreen + VelGreen(i)
        AveGreen = AveGreen/Float(Cnt1)
        Call Chauvenet(AveGreen, VelGreen, Cnt1)
    Else
        Write(*,'(a32)') ' No data points for green beams'
        AveGreen = 9999.0D0
    EndIf
    Write(8,*)
    Write(8,700) ' Velocity of IFA#1 (Blue) = ',AveBlue,' m/s'
    Write(8,700) ' Velocity of IFA#2 (Green) = ',AveGreen,' m/s'
700  Format(1x,a29,f10.5,a4)
800  Format(1x,f10.4,5x,f20.10,5x,f20.10)
    Return
End

```

```

(*****)
(*
(* WRITTEN BY : NGOC HOANG
(* PURPOSE   : Takes pressure data in the ESM Wind Tunnel
(*
(*****)
Program pressure;
{$I PCLDEFS.TP}
{$I PCLERRS.PAS}
Const External_Amplifier : real = 100.0;
Type Voltage_Type = array [0..15] of real;
      Static_Type = array [1..48] of real;
Var Voltage           : Voltage_Type;
    Gain,Number_Of_Scans : integer;
    Start_Channel,End_Channel : integer;
    Port_Begin,Port_End   : integer;
    DA_Channel,No_Pts,i   : integer;
    DA_Out_Voltage        : real;
    Density,Viscosity      : real;
    Dynamic_Pressure       : real;
    FreeStream_Velocity    : real;
    Static_Pressure        : Static_Type;
    fname                  : string[70];
    outf                   : text;
    ans                    : char;

(*****)
(* Procedure AD_Routine
(*****)
procedure AD_Routine(var Voltage:Voltage_Type;Start_Channel:integer;
                    End_Channel:integer;Number_Of_Scans:integer;
                    Gain:integer);
var ADvalue,status,Timing_source : integer;
    Error_Value                   : word;
    Requested_Frequency           : word;
    Number_of_Ticks               : word;
    Total_Number_Scans            : word;
    range,NOC                     : real;
    LSB,scaled_LSB,scaled_LOW     : real;
    High_Volt,Low_Volt            : real;
    Analog_Data_Array             : array[0..10000] of integer;
    i,j                           : integer;
begin
    Timing_Source := 0;
    Requested_Frequency := 1;
    Number_of_Ticks := 4000 div Requested_Frequency;
    Total_Number_Scans := (End_Channel+1-Start_Channel)*Number_Of_Scans;
    Error_Value := 0;
    High_Volt := +10.0;
    Low_Volt := -10.0;
    range := High_Volt - Low_Volt;
    NOC := 4096.0;
    LSB := range/NOC;
    scaled_LSB := LSB/Gain;
    scaled_LOW := Low_Volt/Gain;
    for i:=0 to 10000 do Analog_Data_Array[i] := 0;
    for i:=0 to 15 do Voltage[i] := 0.0;
    status := SetErrorControlWord(Error_Value);
    status := SetupAdc(Timing_Source,Start_Channel,End_Channel,Gain);
    status := GetDtError(Error_Value);
    If Error_Value < > 0 then
    begin
        writeln(' Illegal Channels or gain specified ...');
    end
end

```

```

        writeln(' Check program ...          ');
        writeln(Error_value);
        halt;
    end;
    status := Initialize;
    status := SetClockDivider(Number_Of_Ticks);
    status := DisableSystemClock;
    status := SelectBoard(1);
    status := ADcSeries(Total_Number_Scans,Analog_Data_Array[0]);
    status := EnableSystemClock;
    status := GetDtError(Error_Value);
    If Error_Value < > 0 then
    begin
        writeln(' Error during acquisition ...');
        writeln(' Check program ...          ');
        writeln(Error_value);
        halt;
    end;
    status := Terminate;
    for j:= 0 to End_Channel do
    begin
        i := j;
        while i <= (Total_Number_Scans-1)
        begin
            Voltage[j] := Voltage[j] + (Analog_Data_Array[i]*
            scaled_LSB) + scaled_LOW;
            i := i + (End_channel + 1);
        end;
        Voltage[j] := Voltage[j]/Number_Of_Scans;
    end;
end;

(*****
(* Procedure DA_Routine
(*****
procedure DA_Routine(DA_Out_Voltage:real;DA_Channel:integer);
var High_Volt,Low_Volt,range,NOC,CPV : real;
    Analog_Value,status              : integer;
begin
    High_Volt := +10.0;
    Low_Volt  := -10.0;
    range     := High_volt - Low_Volt;
    NOC       := 4096.0;
    CPV       := NOC/range;
    Analog_Value := Trunc((DA_Out_Voltage - Low_Volt) * CPV);
    status := DAcValue(DA_Channel,Analog_Value);
end;

(*****
(* Procedure Measure_Dynamic_Pressure
(*****
procedure Measure_Dynamic_Pressure(var Dynamic_Pressure:real;
    var FreeStream_Velocity:real;
    Density:real);
var Gain,Start_Channel,End_Channel,Number_Of_Scans : integer;
    Specific_Weight_Water,Inch_Of_Water              : real;
    Reynolds_Number,Diameter_Model                    : real;
    ans                                                : char;
begin
    (* Check with the manometer
    Specific_Weight_Water := 56.1;
    Inch_Of_Water := 0.16/12.0;
    Dynamic_Pressure := Specific_Weight_Water*Inch_Of_Water;

```

```

FreeStream_Velocity := Sqrt(2.0*Dynamic_Pressure/Density);
writeln(' Free Stream Velocity from the manometer is : ',
        FreeStream_Velocity:10:5, ' ft/sec');  *)
Diameter_Model := 1.15625/12.0;
Gain := 1;
Start_Channel := 0;
End_Channel := 0;
Number_Of_Scans := 300;
repeat
  AD_Routine(Voltage,Start_Channel,End_Channel,Number_Of_Scans,Gain);
  Voltage[0] := Voltage[0]/External_Amplifier;
  Dynamic_Pressure := Voltage[0]*10.0;
  Dynamic_Pressure := Dynamic_Pressure*2.78496;
  FreeStream_Velocity := Sqrt(ABS(2.0*Dynamic_Pressure/Density));
  Reynolds_Number := FreeStream_Velocity*Diameter_Model*Density/
  Viscosity;
  writeln(' Free Stream Velocity is : ',FreeStream_Velocity:10:5
  , ' ft/sec');
  writeln(' Reynolds Number is      : ',Reynolds_Number:10:5);
  writeln(' Change speed of tunnel ...');
  write (' Otherwise hit N : ');
  readln(ans);
until upcase(ans)='N';
end;

(*****
(* Procedure Measure_Static_Pressure
*****
)
procedure Measure_Static_Pressure(var Static_Pressure : Static_Type;
        Port_Begin:integer;Port_End:integer);
var Gain,Start_Channel,End_Channel,
    Number_Of_Scans,DA_Channel,i : integer;
    DA_Out_Voltage : real;
    Voltage        : Voltage_type;
begin
  writeln;
  for i:= Port_Begin to Port_End do
    begin
      DA_Channel := 0;
      DA_Out_Voltage := 5.0;
      DA_Routine(DA_Out_Voltage,DA_Channel);
      Delay(500);
      DA_Out_Voltage := 0.0;
      DA_Routine(DA_Out_Voltage,DA_Channel);
      Delay(3000);
      Gain := 1;
      Start_Channel := 0;
      End_Channel := 0;
      Number_Of_Scans := 300;
      AD_Routine(Voltage,Start_Channel,End_Channel,Number_Of_Scans,Gain);
      Static_Pressure[i] := Voltage[0]*10.0*2.78496/External_Amplifier;
      write(i, ' ');
    end;
    DA_Channel := 1;
    DA_Out_Voltage := 5.0;
    DA_Routine(DA_Out_Voltage,DA_Channel);
    Delay(500);
    DA_Out_Voltage := 0.0;
    DA_Routine(DA_Out_Voltage,DA_Channel);
  end;

(*****
(* Procedure Viscosity_Density
*****
)

```

```

(*****)
procedure Viscosity_Density(var Viscosity:real;var Density:real);
var Musubo,Tsubo,S,Temperature : real;
    P,R,T          : real;
begin
(* Sutherland's Law *)
    Musubo := 0.1716*(0.0020886/1000.0);
    Tsubo := 491.6;
    S := 199;
    T := 459.0 + 70.0;
    Temperature := Exp(1.5*ln(T/Tsubo));
    Viscosity := Musubo*Temperature*(Tsubo + S)/(T + S);
(* Perfect Gas *)
    P := 2116.8;
    R := 1715.0;
    Density := P/R/T;
end;

(*****)
(* Procedure Plot
(*****)
procedure Plot_Pressure(Static_Pressure : Static_Type;No_Pts:integer);
const MaxX : integer = 600;
    MinX : integer = 20;
    MinY : integer = 30;
    MaxY : integer = 180;
var OrigX,OrigY : integer;
    DivX,DivY : integer;
    x,y,i,xo,yo : integer;
    X_Coord : array[1..32] of real;
    Radius : real;

begin
    Radius := (1.0 + (5.0/32.0))/2.0;
    X_Coord[1] := -3.0*0.0625-0.09375;
    for i:= 2 to 4 do X_Coord[i] := X_Coord[i-1] + 0.0625;
    for i:= 5 to 6 do X_Coord[i] := X_Coord[i-1] + 0.09375;
    for i:= 7 to 9 do X_Coord[i] := X_Coord[i-1] + 0.0625;
    for i:= 10 to 11 do X_Coord[i] := X_Coord[i-1] + 0.15625;
    for i:= 12 to 27 do X_Coord[i] := X_Coord[i-1] + 0.078125;
    X_Coord[28] := X_Coord[27] + (3.0/32.0);
    X_Coord[29] := X_Coord[28] + (7.0/32.0);
    X_Coord[30] := X_Coord[29] + (11.0/32.0);
    X_Coord[31] := X_Coord[30] + (18.0/32.0);
    X_Coord[32] := X_Coord[31] + (19.0/32.0);
    for i:= 1 to 32 do X_Coord[i] := X_Coord[i]/Radius;
    for i:= 1 to 32 do writeln(outf,X_Coord[i]:10:6,' ',
        Static_Pressure[i]:10:8);
    for i:= 1 to 32 do X_Coord[i] := X_Coord[i]/X_Coord[32];
    OrigX := 50;
    DivX := MaxX-50;
    OrigY := (MaxY + MinY) div 2;
    DivY := (OrigY - 40);
    HiRes;
    HiResColor(White);
    Draw(0,2,639,2,white);
    Draw(639,2,639,199,White);
    Draw(637,2,637,199,white);
    Draw(639,199,0,199,White);
    Draw(0,2,0,199,White);
    Draw(2,2,2,199,white);
    Draw(2,20,637,20,white);
    GotoXY(17,2);write('Pressure Coefficient over Hemisphere-Cylinder');

```

```

Draw(MinX,OrigY,MaxX,OrigY,white);
Draw(50,MinY,50,MaxY,white);
Draw(51,MinY,51,MaxY,white);
Draw(45,40,55,40,white);
GotoXY(2,6);write(' 1.0');
Draw(45,170,55,170,white);
GotoXY(2,22);write(' -1.0');
for i:= 2 to No_Pts do
begin
  Draw(round(X_Coord[i-1]*DivX) + 50,OrigY-round(
    Static_Pressure[i-1]*DivY),round(X_Coord[i]*DivX) + 50,
    OrigY-round(Static_Pressure[i]*DivY),white);
end;
repeat until keypressed;
TextMode;
TextColor(White);
end;

(*****)
(* Procedure Menu
(*****)
Procedure Menu;
Var i : integer;
begin
  clrscr;
  write(' ');
  write(chr(201));for i:= 1 to 46 do write(chr(205));
  write(chr(187));writeln;
  write(' ');
  writeln(chr(186),' STATIC PRESSURE MEASUREMENT OVER HEMIS-CYN ',
  chr(186)); write(' ');
  write(chr(200));for i:= 1 to 46 do write(chr(205));
  write(chr(188));writeln;
  writeln('      1) Place the switch of the signal conditioner');
  writeln('          in position Z, and adjust front panel ZERO');
  writeln('          control for a meter reading of zero. ');
  writeln('      2) Place the switch of the signal conditioner');
  writeln('          in position S, and adjust front panel SPAN');
  writeln('          control until the meter reads CAL number. ');
  writeln('      3) Place the switch of the signal conditioner');
  writeln('          in position X.1. Adjust front panel ZERO');
  writeln('          control until the meter reads zero. ');
  writeln('      4) Place the total pressure end of the pitot');
  writeln('          tube to port#0 of the SCANI-VALVE. ');
  writeln('      5) Hook the static pressure end of the pitot');
  writeln('          to the reference pressure port of the');
  writeln('          BAROCEL(P2). ');
  writeln('      6) Have the model ready with all the pressure');
  writeln('          ports hook-up to the SCANI-VALVE starting');
  writeln('          from port#1');
  writeln('      7) Hook the output signal of the conditioner');
  writeln('          to channel#0 of the A/D board');
  write('      8) Hit any key when ready... ');
  repeat until keypressed;
end;

(*****)
(* Procedure main
(*****)
begin
  write(' Do you want to align the model with the flow(Y or N) ? ');
  readln(ans);
  while (upcase(ans)='Y') do

```



```

begin
  Port_Begin := 1;
  Port_End := 6;
  Measure_Static_Pressure(Static_Pressure,Port_Begin,Port_End);
  writeln;
  writeln('P[4] = ',Static_Pressure[4]);
  writeln('P[5] = ',Static_Pressure[5]);
  writeln('P[6] = ',Static_Pressure[6]);
  writeln;
  write(' Do you want to align the model with the flow(Y or N) ? ');
  readln(ans);
end;
Port_Begin := 1;
Port_End := 32;
Viscosity_Density(Viscosity,Density);
TextMode;
TextColor(White);
writeln;writeln;
repeat
  clrscr;
  write(' Name of output file : ');
  readln(fname);
  assign(outf,fname);
  rewrite(outf);
  Measure_Dynamic_Pressure(Dynamic_Pressure,FreeStream_Velocity,
  Density);
  Measure_Static_Pressure(Static_Pressure,Port_Begin,Port_End);
  for i:= 1 to 32 do Static_Pressure[i]:= Static_Pressure[i]/
  Dynamic_Pressure;
  No_Pts := 32;
  Plot_Pressure(Static_Pressure,No_Pts);
  close(outf);
  write(' Do you want another run? (Y or N) : ');
  readln(ans);
until upcase(ans)='N';
end.

```

```

1  *****
2  '*'
3  '*  WRITTEN BY : NGOC HOANG
4  '*  PURPOSE   : Takes pressure data in the VPI Wind Tunnel
5  '*'
6  *****
10 MASS STORAGE IS :INTERNAL,4,1
20 DIM P(48),CLEAR_CRT$(2),MESS$(80),FNAMES$(80)
30 INPUT INPUT NAME OF DATA FILE:,FNAMES$
40 CREATE ASCII FNAMES,10
50 ASSIGNDATA TO FNAMES
60 CLEAR_CRT$=CHR$(255)&CHR$(75)
70 GCLEAR
80 GINIT
90 GRAPHICS OFF
100 OUTPUT 2;CLEAR_CRT$;
110 INPUT MESSAGE OF THIS RUN,MESS$
120 OUTPUTDATA;MESS$
130 PRINT MESS$
140 INPUT ENTER FIRST PRESSURE PORT,NPR1
150 PRINT FIRST PRESSURE PORT = ;NPR1
160 INPUT ENTER LAST PRESSURE PORT,NPR2
170 PRINT LAST PRESSURE PORT = ;NPR2
180 INPUT ENTER NUMBER OF SCANS PER READING,SCN
190 PRINT NUMBER OF SCANS PER READING;SCN
200 NPR=NPR2-NPR1+1
210 PSCALE=.01678      ! SCALE TO CONVERT VOLTAGE TO PRESSURE
220 PSF=0              ! FREE STREAM PRESSURE
230 QD=0               ! DYNAMIC PRESSURE
240 TEMP=0             ! TEMPERATURE
250 DENS=0             ! DENSITY
260 VEL=0              ! VELOCITY
270 VISC=0             ! VISCOSITY
280 FOR N=1 TO 50
290 CALL ADVANCE(1)
300 WAIT .1
310 NEXT N
320 FOR N=1 TO 48
330 P(N)=0
340 NEXT N
350 GINIT
360 GRAPHICS ON
370 MOVE 0,40
380 IDRAW 120,0
390 WAIT 5
400 CALL PRESS(PINIT,SCN,PSCALE)
401 PINIT=0.
410 CALL ADVANCE(2)
420 FOR N=1 TO NPR
430 CALL CONDITIONS(PST,Q,T,RO,V,MU)
440 CALL PRESS(P(N),SCN,PSCALE)
450 P(N)=P(N)-PINIT
460 PFS=PFS+PST
470 QD=QD+Q
480 TEMP=TEMP+T
490 DENS=DENS+RO
500 VELO=VELO+V
510 VISC=VISC+MU
520 CALL ADVANCE(1)
530 MOVE 2.5*(NPR1+N-1),40
540 IDRAW 0,P(N)/QD*N*5/.036095
550 NEXT N
560 FOR N=1 TO 50-NPR

```

```

570 CALL ADVANCE(1)
580 WAIT .1
590 NEXT N
600 PFS = PFS/NPR
610 TEMP = TEMP/NPR
620 DENS = DENS/NPR
630 VELO = VELO/NPR
640 VISC = VISC/NPR
650 REY = REY/NPR
660 QD = QD/NPR
670 OUTPUT 701;
680 OUTPUT 701;
690 OUTPUT 701;MESS$
710 OUTPUT 701;TEMPERATURE ;INT(TEMP*10)/10-459,DEG. F
720 OUTPUT 701;DYNAMIC PRESSURE ;INT(QD*100)/100,IN H2O
730 OUTPUT 701;VELOCITY ;INT(VELO*10)/10,FT/SEC
750 OUTPUT 701;VISCOSITY ;INT(VISC*10000000000)/10000000000
770 OUTPUT 701;
860 OUTPUT 701;SURFACE PRESSURES
880 OUTPUT 701;= = = = =
890 OUTPUT 701;
900 FOR N=1 TO 48
910 OUTPUT 701;NPR1 + N-1; ;P(N); ;P(N)
920 NEXT N
930 OUTPUT 701;
940 OUTPUT 701;
950 DUMP GRAPHICS
960 OUTPUTDATA;INT(PFS*10)/10
970 OUTPUTDATA;INT(TEMP*10)/10-459
980 OUTPUTDATA;INT(QD*100)/100
990 OUTPUTDATA;INT(VELO*10)/10
1000 OUTPUTDATA;INT(DENS*10000)/10000
1010 OUTPUTDATA;INT(VISC*10000000000)/10000000000
1030 FOR N=1 TO 48
1040 OUTPUTDATA;P(N);P(N)/QD/.036095
1050 NEXT N
1060 INPUT DO YOU WANT TO MAKE ANOTHER MEASUREMENT,ANS$
1070 IF ANS$=Y THEN GOTO 30
1080 IF ANS$=Y THEN GOTO 30
1090 GCLEAR
1100 GRAPHICS OFF
1110 OUTPUT 2;CLEAR CRTS;
1120 ASSIGNDATA TO *
1130 MASS STORAGE IS :INTERNAL,4,0
1140 STOP
1150 END
1160 ! ***** ADVANCE SUBROUTINE *****
1170 SUB ADVANCE(P)
1180 OUTPUT 716;B3
1190 OUTPUT 716;B4
1200 OUTPUT 716;A3
1210 IF P=2 THEN OUTPUT 716;A4
1220 WAIT .15
1230 OUTPUT 716;B3
1240 OUTPUT 716;B4
1250 SUBEND
1260 ! ***** CONDITIONS SUBROUTINE *****
1270 SUB CONDITIONS(P,QD,T,DENS,VELO,VISC)
1280 OUTPUT 709;01
1290 P=0
1300 WAIT .3
1310 FOR N=1 TO 3
1320 TRIGGER 722

```

```

1330 ENTER 722;PRESS
1340 P = P + PRESS
1350 NEXT N
1360 P = P/3
1370 OUTPUT 709;02
1380 T = 0
1390 WAIT .3
1400 FOR N = 1 TO 3
1410 TRIGGER 722
1420 ENTER 722;TEMP
1430 T = T + TEMP
1440 NEXT N
1450 T = T/3
1460 OUTPUT 709;09
1470 QD = 0
1480 WAIT .3
1490 FOR N = 1 TO 3
1500 TRIGGER 722
1510 ENTER 722;Q
1520 QD = QD + Q
1530 NEXT N
1540 QD = QD/3
1550 P = 707.3 * P
1560 T = 459 + 100 * T * 1.798 / .1
1570 DENS = P / 1716 / T
1580 VELO = SQR(ABS(104 * QD / DENS))
1.5 / (T + 198.6) / 1.E + 8
1600 QD = 10 * QD
1610 SUBEND
1620 ! ***** SUBROUTINE PRESS *****
1630 SUB PRESS(P,S,PSCALE)
1640 OUTPUT 709;35
1650 P = 0
1660 WAIT 1
1670 FOR N = 1 TO S
1680 TRIGGER 722
1690 ENTER 722;PRESS
1700 P = P + PRESS
1710 NEXT N
1720 P = (P/S)/PSCALE
1730 SUBEND

```

```

(*****)
(*
(* WRITTEN BY : NGOC HOANG
(* Calibration and data acquisition program for the 7-hole probe
(*
(*****)
Program Seven_Hole_Probe;
{$I PCLDEFS.TP}
{$I PCLERRS.PAS}
Const Amplifier_Gain : real = 100.0;
Type Voltage_Type = array [0..15] of real;
    Static_Type = array [1..48] of real;
    Augmented_Matrix = array [1..15,1..16] of real;
    K_Matrix = array [1..15] of real;
Var Region,i : integer;
    Density,Viscosity,Dynamic_Pressure,FreeStream_Velocity : real;
    At,As,Bc,Br : real;
    Qprime,By,Bp : real;
    B : K_Matrix;
    P : Static_Type;
    u,v,w : real;
    Temp_Press,T : real;
    Ind_c,Ind_cc : array [1..7] of integer;
    infltemp,outf : text;
    fname : string[70];

(*****)
(* Procedure AD_Routine
(*****)
procedure AD_Routine(var Voltage:Voltage_Type;Start_Channel:integer;
    End_Channel:integer;Number_Of_Scans:integer;
    Gain:integer);
var ADvalue,status,Timing_source : integer;
    Error_Value : word;
    Requested_Frequency : word;
    Number_of_Ticks : word;
    Total_Number_Scans : word;
    range,NOC : real;
    LSB,scaled_LSB,scaled_LOW : real;
    High_Volt,Low_Volt : real;
    Analog_Data_Array : array[0..10000] of integer;
    i,j : integer;
begin
    Timing_Source := 0;
    Requested_Frequency := 1;
    Number_of_Ticks := 2000 div Requested_Frequency;
    Total_Number_Scans := (End_Channel+1-Start_Channel)*Number_Of_Scans;
    Error_Value := 0;
    High_Volt := +10.0;
    Low_Volt := -10.0;
    range := High_Volt - Low_Volt;
    NOC := 4096.0;
    LSB := range/NOC;
    scaled_LSB := LSB/Gain;
    scaled_LOW := Low_Volt/Gain;
    for i:=0 to 10000 do Analog_Data_Array[i] := 0;
    for i:=0 to 15 do Voltage[i] := 0.0;
    status := SetErrorControlWord(Error_Value);
    status := SetupAdc(Timing_Source,Start_Channel,End_Channel,Gain);
    status := GetDtError(Error_Value);
    If Error_Value < > 0 then
    begin
        writeln(' Illegal Channels or gain specified ...');
    end
end

```

```

        writeln(' Check program ...          ');
        writeln(Error_value);
        halt;
    end;
    status := Initialize;
    status := SetClockDivider(Number_Of_Ticks);
    status := DisableSystemClock;
    status := SelectBoard(1);
    status := ADcSeries(Total_Number_Scans,Analog_Data_Array[0]);
    status := EnableSystemClock;
    status := GetDtError(Error_Value);
    If Error_Value < > 0 then
    begin
        writeln(' Error during acquisition ...');
        writeln(' Check program ...          ');
        writeln(Error_value);
        halt;
    end;
    status := Terminate;
    for j:= 0 to End_Channel do
    begin
        i := j;
        while i <= (Total_Number_Scans-1)
        begin
            Voltage[j] := Voltage[j] + (Analog_Data_Array[i]*
            scaled_LSB) + scaled_LOW;
            i := i + (End_channel + 1);
        end;
        Voltage[j] := Voltage[j]/Number_Of_Scans;
    end;
end;

(*****)
(* Procedure DA_Routine
(*****)
procedure DA_Routine(DA_Out_Voltage:real;DA_Channel:integer);
var High_Volt,Low_Volt,range,NOC,CPV : real;
    Analog_Value,status              : integer;
begin
    High_Volt := +10.0;
    Low_Volt  := -10.0;
    range     := High_volt - Low_Volt;
    NOC       := 4096.0;
    CPV       := NOC/range;
    Analog_Value := Trunc((DA_Out_Voltage - Low_Volt) * CPV);
    status := DAcValue(DA_Channel,Analog_Value);
end;

(*****)
(* Procedure Measure_Dynamic_Pressure
(*****)
procedure Measure_Dynamic_Pressure(var Dynamic_Pressure:real;
    var FreeStream_Velocity:real;
    Density : real ; Viscosity : real);
var Gain,Start_Channel,End_Channel,Number_Of_Scans : integer;
    Specific_Weight_Water,Inch_Of_Water              : real;
    Reynolds_Number,Diameter_Probe                   : real;
    Voltage                                           : Voltage_type;
    ans                                              : char;
begin
    (* write(' Enter reading from manometer (in. of water) : ');
    readln(Inch_Of_Water);
    Specific_Weight_Water := 56.1;

```

```

Inch_Of_Water := Inch_Of_Water/12.0;
Dynamic_Pressure := Specific_Weight_Water*Inch_Of_Water;
FreeStream_Velocity := Sqrt(2.0*Dynamic_Pressure/Density);
writeln(' Free Stream Velocity from the manometer is : ',
    FreeStream_Velocity:15:10, ' ft/sec');
Diameter_Probe := 3.0/16.0/12.0; *)
Gain := 1;
Start_Channel := 0;
End_Channel := 0;
Number_Of_Scans := 300;
(* repeat *)
    AD_Routine(Voltage,Start_Channel,End_Channel,Number_Of_Scans,Gain);
    Dynamic_Pressure := Voltage[0]*10.0;
    Dynamic_Pressure := Dynamic_Pressure*2.78496;
    Dynamic_Pressure := Dynamic_Pressure/Amplifier_Gain;
    FreeStream_Velocity := Sqrt(ABS(2.0*Dynamic_Pressure/Density));
(* Reynolds_Number := FreeStream_Velocity*
    Diameter_Probe*Density/Viscosity; *)
    writeln(' Free Stream Velocity is : ',
        FreeStream_Velocity:15:10, ' ft/sec');
(* writeln(' Reynolds Number is      : ',
    Reynolds_Number:15:10; *)
(* write(' Need to change the speed of the tunnel(Y or N) ? : ');
    readln(ans);
    if (upcase(ans)='Y') then
        begin
            write(' Adjust the speed of tunnel now. Hit a key when done');
            repeat until keypressed;
            writeln;
        end;
    until upcase(ans)='N'; *)
end;

(*****
*) Procedure Measure_Static_Pressure
(*****
procedure Measure_Static_Pressure(var P : Static_Type);
var port_begin,port_end,i : integer;
    Gain,Start_Channel,End_Channel,Number_Of_Scans,DA_Channel : integer;
    DA_Out_Voltage : real;
    Voltage : Voltage_type;
begin
    port_begin := 1;
    port_end := 7;
    writeln;
    for i:= port_begin to port_end do
        begin
            DA_Channel := 0;
            DA_Out_Voltage := 5.0;
            DA_Routine(DA_Out_Voltage,DA_Channel);
            Delay(500);
            DA_Out_Voltage := 0.0;
            DA_Routine(DA_Out_Voltage,DA_Channel);
            Delay(2000);
            Gain := 1;
            Start_Channel := 0;
            End_Channel := 0;
            Number_Of_Scans := 300;
            AD_Routine(Voltage,Start_Channel,End_Channel,Number_Of_Scans,Gain);
            P[i] := Voltage[0]*10.0*2.78496/Amplifier_Gain;
            write(i, ' ');
        end;
    writeln;

```

```

    DA_Channel := 1;
    DA_Out_Voltage := 5.0;
    DA_Routine(DA_Out_Voltage, DA_Channel);
    Delay(500);
    DA_Out_Voltage := 0.0;
    DA_Routine(DA_Out_Voltage, DA_Channel);
end;

(*****)
(* Procedure Viscosity_Density
(*****)
procedure Viscosity_Density(var Viscosity : real ;
                             var Density : real ; T : real);
var Musubo, Tsubo, S, Temperature : real;
    P, R : real;
begin
    (* Sutherland's Law *)
    Musubo := 0.1716*(0.0020886/1000.0);
    Tsubo := 491.6;
    S := 199;
    T := T + 459.0;
    Temperature := Exp(1.5*ln(T/Tsubo));
    Viscosity := Musubo*Temperature*(Tsubo + S)/(T + S);
    (* Perfect Gas *)
    P := 2116.8;
    R := 1715.0;
    Density := P/R/T ;
end;

(*****)
(* Procedure B_Matrix
(*****)
procedure B_Matrix(Bc:real;Br:real;var B:K_Matrix);
begin
    B[1] := 1.0;
    B[2] := Bc;
    B[3] := Br;
    B[4] := Bc*Bc;
    B[5] := Bc*Br;
    B[6] := Br*Br;
    B[7] := Bc*Bc*Bc;
    B[8] := Bc*Bc*Br;
    B[9] := Bc*Br*Br;
    B[10] := Br*Br*Br;
    B[11] := Bc*Bc*Bc*Bc;
    B[12] := Bc*Bc*Bc*Br;
    B[13] := Bc*Bc*Br*Br;
    B[14] := Bc*Br*Br*Br;
    B[15] := Br*Br*Br*Br;
end;

(*****)
(* Procedure Gaussian
(*****)
Procedure Gaussian(n:integer;a:Augmented_Matrix;var x:K_Matrix);
Var i,j,k,p : integer;
    m,temp : real;
begin
    for i:= 1 to n-1 do
        begin
            p := i;
            while (a[p,i] = 0) do p := p + 1;
            if (p > n) then

```



```

begin
  write('No unique solution exists');
  exit;
end;
if (p < > i) then
  for k := 1 to n+1 do
  begin
    temp := a[p,k];
    a[p,k] := a[i,k];
    a[i,k] := temp;
  end;
  for j := i+1 to n do
  begin
    m := a[j,i]/a[i,i];
    for k := 1 to n+1 do a[j,k] := a[j,k] - m*a[i,k];
  end;
end;
if (a[n,n]=0) then
begin
  write('No unique solution exists');
  exit;
end;
x[n] := a[n,n+1]/a[n,n];
temp := 0.0;
i := n-1;
repeat
  for j := i+1 to n do temp := temp + a[i,j]*x[j];
  x[i] := (a[i,n+1] - temp)/a[i,i];
  i := i - 1;
  temp := 0.0;
until i=0;
end;

(*****)
(* Procedure Calibration_p_y
(*****)
Procedure Calibration_p_y;
Var Density,Viscosity,Dynamic_Pressure,FreeStream_Velocity : real;
    Beta,Alpha,Qprime,At,As,By,Bp : K_Matrix;
    K_Beta,K_Alpha,K_At,K_As : K_Matrix;
    T : real;
    P : Static_Type;
    i,n,j : integer;
    fname : string[70];
    outf : text;
    outfo : text;
    ans : char;
    a : Augmented_Matrix;
begin
  Viscosity_Density(Viscosity,Density,T);
  n := 10;
  clrscr;
  writeln(' Beginning calibration process for region #1');
  write(' Do you want to reset the position of the probe (Y or N) ? ');
  readln(ans);
  while (upcase(ans)='Y') do
  begin
    Measure_Dynamic_Pressure(Dynamic_Pressure,FreeStream_Velocity,
      Density,Viscosity);
    Measure_Static_Pressure(P);
    writeln;
    for i:= 1 to 7 do writeln('P['i,'] = ',P[i]:20:8);
    write(' Do you want to reset the probe (Y or N) ? ');

```

```

    readln(ans);
end;
write(' Enter name of file (read): ');
readln(fname);
assign(outf,fname);
reset(outf);
write(' Enter name of file (write): ');
readln(fname);
assign(outfo,fname);
rewrite(outfo);
for i:= 1 to n do
begin
    writeln(' Number of times : ',i);
    write(' Enter the angle 'chr(225),' : ');readln(outf,Beta[i]);
    write(Beta[i]);
    write(' Enter the angle 'chr(224),' : ');readln(outf,Alpha[i]);
    write(Alpha[i]);
    readln(outf,P[1]);
    readln(outf,P[2]);
    readln(outf,P[3]);
    readln(outf,P[4]);
    readln(outf,P[5]);
    readln(outf,P[6]);
    readln(outf,P[7]);
    readln(outf,Dynamic_Pressure);
    write(P[1]);
    write(P[2]);
    write(P[3]);
    write(P[4]);
    write(P[5]);
    write(P[6]);
    write(P[7]);
    write(Dynamic_Pressure);
(* Measure_Dynamic_Pressure(Dynamic_Pressure,FreeStream_Velocity,
    Density,Viscosity);
    Measure_Static_Pressure(P); *)
    Qprime[i] := P[1] - (P[2] + P[3] + P[4] + P[5] + P[6] + P[7])/6.0;
    At[i] := (P[1]-Dynamic_Pressure)/Qprime[i];
    As[i] := P[1]/Qprime[i];
    By[i] := (P[2]-P[3])/Qprime[i];
    Bp[i] := ((P[4] + P[6])/2.0 - (P[5] + P[7])/2.0)/Qprime[i];
    a[i,1] := 1.0;
    a[i,2] := By[i];
    a[i,3] := Bp[i];
    a[i,4] := By[i]*By[i];
    a[i,5] := By[i]*Bp[i];
    a[i,6] := Bp[i]*Bp[i];
    a[i,7] := By[i]*By[i]*By[i];
    a[i,8] := By[i]*By[i]*Bp[i];
    a[i,9] := By[i]*Bp[i]*Bp[i];
    a[i,10] := Bp[i]*Bp[i]*Bp[i];
(* a[i,11] := By[i]*By[i]*By[i]*By[i];
    a[i,12] := By[i]*By[i]*By[i]*Bp[i];
    a[i,13] := By[i]*By[i]*Bp[i]*Bp[i];
    a[i,14] := By[i]*Bp[i]*Bp[i]*Bp[i];
    a[i,15] := Bp[i]*Bp[i]*Bp[i]*Bp[i]; *)
(* writeln(outf,'Beta := ',Beta[i]:10:3);
    writeln(outf,'Alpha := ',Alpha[i]:10:3);
    for j := 1 to 7 do writeln(outf,'P['j,'] := ',P[j]:20:8,');
    for j := 1 to 7 do writeln('P['j,'] = ',P[j]:20:8);
    writeln(outf,'Dynamic Pressure := ',Dynamic_Pressure:20:8);
    writeln(outf); *)
end;

```

```

for i:= 1 to n do a[i,n+1] := Beta[i];
Gaussian(n,a,K_Beta);
for i:= 1 to n do writeln(outfo,'K_Beta['i,'] := ',
K_Beta[i]:20:8,';');
for i:= 1 to n do a[i,n+1] := Alpha[i];
Gaussian(n,a,K_Alpha);
for i:= 1 to n do writeln(outfo,'K_Alpha['i,'] := ',
K_Alpha[i]:20:8,';');
for i:= 1 to n do a[i,n+1] := At[i];
Gaussian(n,a,K_At);
for i:= 1 to n do writeln(outfo,'K_At['i,'] := ',K_At[i]:20:8,';');
for i:= 1 to n do a[i,n+1] := As[i];
Gaussian(n,a,K_As);
for i:= 1 to n do writeln(outfo,'K_As['i,'] := ',K_As[i]:20:8,';');
close(outfo);
close(outfo);
end;

(*****
(* Procedure Calibration_c_r
(*****
Procedure Calibration_c_r;
Var Density,Viscosity,Dynamic_Pressure,FreeStream_Velocity : real;
    Theta,Phi,Qprime,At,As,Bc,Br : array [1..15] of real;
    K_Theta,K_Phi,K_At,K_As : K_Matrix;
    T : real;
    P : Static_Type;
    i,n,j : integer;
    fname : string[70];
    outf : text;
    ans : char;
    a : Augmented_Matrix;
begin
    Viscosity_Density(Viscosity,Density,T);
    n := 15;
    clrscr;
    writeln(' Beginning calibration process for region #2-#7');
    write(' Do you want to reset the probe (Y or N) ? ');
    readln(ans);
    while (upcase(ans) = 'Y') do
    begin
        Measure_Dynamic_Pressure(Dynamic_Pressure,FreeStream_Velocity,
            Density,Viscosity);
        Measure_Static_Pressure(P);
        writeln;
        for i:= 1 to 7 do writeln('P['i,'] = ',P[i]:20:8);
        write(' Do you want to reset the probe (Y or N) ? ');
        readln(ans);
    end;
    write(' Enter name of file : ');readln(fname);
    assign(outf,fname);
    rewrite(outf);
    for i:= 1 to 15 do
    begin
        write(' Enter the angle 'chr(233),' : ');readln(Theta[i]);
        write(' Enter the angle 'chr(237),' : ');readln(Phi[i]);
        Measure_Dynamic_Pressure(Dynamic_Pressure,FreeStream_Velocity,
            Density,Viscosity);
        Measure_Static_Pressure(P);
        Qprime[i] := P[1] - (P[2] + P[3] + P[4] + P[5] + P[6] + P[7])/6.0;
        At[i] := (P[1]-Dynamic_Pressure)/Qprime[i];
        As[i] := P[1]/Qprime[i];
        Bc[i] := (P[2]-P[3])/Qprime[i];

```

```

Br[i] := ((P[5] + P[7])/2.0 - (P[4] + P[6])/2.0)/Qprime[i];
a[i,1] := 1.0;
a[i,2] := Bc[i];
a[i,3] := Br[i];
a[i,4] := Bc[i]*Bc[i];
a[i,5] := Bc[i]*Br[i];
a[i,6] := Br[i]*Br[i];
a[i,7] := Bc[i]*Bc[i]*Bc[i];
a[i,8] := Bc[i]*Bc[i]*Br[i];
a[i,9] := Bc[i]*Br[i]*Br[i];
a[i,10] := Br[i]*Br[i]*Br[i];
writeln(outf,Theta = ',Theta[i]:10:3);
writeln(outf,Phi = ',Phi[i]:10:3);
for j := 1 to 7 do writeln(outf,P['j,'] = ',P[j]:20:8);
writeln(outf,'Dynamic Pressure = ',Dynamic_Pressure:20:8);
writeln(outf);
end;
for i:= 1 to n do a[i,16] := Theta[i];
Gaussian(n,a,K_Theta);
for i:= 1 to n do writeln(outf,'K_Theta['i,'] := ',
K_Theta[i]:20:8,',');
for i:= 1 to n do a[i,16] := Phi[i];
Gaussian(n,a,K_Phi);
for i:= 1 to n do writeln(outf,'K_Phi['i,'] := ',
K_Phi[i]:20:8,',');
for i:= 1 to n do a[i,16] := At[i];
Gaussian(n,a,K_At);
for i:= 1 to n do writeln(outf,'K_At['i,'] := ',K_At[i]:20:8,',');
for i:= 1 to n do a[i,16] := As[i];
Gaussian(n,a,K_As);
for i:= 1 to n do writeln(outf,'K_As['i,'] := ',K_As[i]:20:8,',');
close(outf);
end;

(*****
(* Procedure Velocity_Theta_Phi
(*****
Procedure Velocity_Theta_Phi(Pt : real ; Ps : real ; q : real ;
    Var Alpha : real ; Var Beta : real; Var
    Theta : real ; Var Phi : real ;
    Density : real ; Var Vinf : real ;
    Var u : real ; Var v : real ; Var w : real);
begin
    q := Pt-Ps;
    Theta := Theta*Pi/180.0;
    Phi := Phi*Pi/180.0;
    Vinf := Sqrt(abs(2.0*q/Density));
    u := Vinf*cos(Theta);
    v := Vinf*sin(Theta)*cos(Phi);
    w := Vinf*sin(Theta)*sin(Phi);
    writeln(outf,' Flow is in region 2-7 ');
    writeln(outf,Theta*180.0/Pi:15:10,'    (' ,chr(233),' degree)');
    writeln(outf,Phi*180.0/Pi:15:10,'    (' ,chr(232),' degree)');
    writeln(outf,Vinf:15:10,'    (Calculated Local Velocity ft/sec)');
    writeln(outf,u:15:10,'    (u ft/sec)');
    writeln(outf,v:15:10,'    (v ft/sec)');
    writeln(outf,w:15:10,'    (w ft/sec)');
    writeln(outf);
end;

(*****
(* Procedure Region_1

```

```

(*****)
Procedure Region_1(B:K_Matrix;P:Static_Type;Qprime:real;Density:real;
var u:real;var v:real;var w:real);
Var K_Beta,K_Alpha,K_At,K_As,Temp_B : K_Matrix;
At,As,Pt,Ps,q,Vinf,Alpha,Beta,Phi,Theta,By,Bp : real;
i : integer;
begin
  {SI k-1-all.pas}
  Alpha := 0.0;
  Beta := 0.0;
  By := (P[2]-P[3])/Qprime;
  Bp := ((P[4]+P[6])/2.0 - (P[5]+P[7])/2.0)/Qprime;
  B_Matrix(By,Bp,Temp_B);
  for i:= 1 to 15 do
  begin
    Beta := Beta + K_Beta[i]*Temp_B[i];
    Alpha := Alpha + K_Alpha[i]*Temp_B[i];
  end;
  Beta := Beta*Pi/180.0;
  Alpha := Alpha*Pi/180.0;
  Phi := arctan(sin(abs(Alpha))/(sin(abs(Beta))/cos(abs(Beta))));
  Phi := Phi*180.0/Pi;
  if((P[3]>P[2]) and (P[4]>P[5])) then
  begin
    if(Phi<45.0) then
    begin
      (* It is in region 1-1 *)
      {SI k-1-1.pas }
    end;
    if(Phi>45.0) then
    begin
      (* It is in region 1-2 *)
      {SI k-1-2.pas }
    end;
  end;
  if((P[3]<P[2]) and (P[6]>P[7])) then
  begin
    if(Phi>45.0) then
    begin
      (* It is in region 1-3 *)
      {SI k-1-3.pas }
    end;
    if(Phi<45.0) then
    begin
      (* It is in region 1-4 *)
      {SI k-1-4.pas }
    end;
  end;
  if((P[3]<P[2]) and (P[6]<P[7])) then
  begin
    if(Phi<45.0) then
    begin
      (* It is in region 1-5 *)
      {SI k-1-5.pas }
    end;
    if(Phi>45.0) then
    begin
      (* It is in region 1-6 *)
      {SI k-1-6.pas }
    end;
  end;
  if((P[3]>P[2]) and (P[4]<P[5])) then
  begin

```

```

if(Phi > 45.0) then
begin
  (* It is in region 1-7 *)
  {SI k-1-7.pas }
end;
if(Phi < 45.0) then
begin
  (* It is in region 1-8 *)
  {SI k-1-8.pas }
end;
end;
Alpha := 0.0;
Beta := 0.0;
At := 0.0;
As := 0.0;
for i:= 1 to 10 do
begin
  Beta := Beta + K_Beta[i]*B[i];
  Alpha := Alpha + K_Alpha[i]*B[i];
  At := At + K_At[i]*B[i];
  As := As + K_As[i]*B[i];
end;
Beta := Beta*Pi/180.0;
Alpha := Alpha*Pi/180.0;
Pt := P[1]-At*Qprime;
Ps := P[1]-As*Qprime;
q := Pt-Ps;
Vinf := Sqrt(abs(2.0*q/Density));
u := Vinf*cos(Alpha)*cos(Beta);
v := Vinf*sin(Beta);
w := Vinf*sin(Alpha)*cos(Beta);
writeln(outf,' Flow is in region 1 ');
writeln(outf,Alpha*180.0/Pi:15:10,' (',chr(224),' degree)');
writeln(outf,Beta*180.0/Pi:15:10,' (',chr(225),' degree)');
writeln(outf,Vinf:15:10,' (Calculated Local Velocity ft/sec)');
writeln(outf,u:15:10,' (u ft/sec)');
writeln(outf,v:15:10,' (v ft/sec)');
writeln(outf,w:15:10,' (w ft/sec)');
writeln(outf);
end;

(*****
(* Procedure Region_2
*****
Procedure Region_2(B:K_Matrix;P:Static_Type;Qprime:real;Density:real;
  var u:real;var v:real;var w:real);
Var K_Theta,K_Phi,K_At,K_As : K_Matrix;
  At,As,Pt,Ps,q,Vinf,Alpha,Beta,Phi,Theta : real;
  i : integer;
begin
  If (P[7]> P[6]) then
  begin
    (* It is in region 2-1 *)
    {SI k-2-1.pas }
  end
  else
  begin
    (* It is in region 2-2 *)
    {SI k-2-2.pas }
  end;
  end;
  Phi := 0.0;
  Theta := 0.0;
  At := 0.0;

```

```

As := 0.0;
for i:= 1 to 10 do
begin
  Theta := Theta + K_Theta[i]*B[i];
  Phi := Phi + K_Phi[i]*B[i];
  At := At + K_At[i]*B[i];
  As := As + K_As[i]*B[i];
end;
Pt := P[2]-At*Qprime;
Ps := P[2]-As*Qprime;
Velocity_Theta_Phi(Pt,Ps,q,Alpha,Beta,Theta,Phi,Density,Vinf,u,v,w);
end;

(*****
(* Procedure Region_3
(*****
Procedure Region_3(B:K_Matrix;P:Static_Type;Qprime:real;Density:real;
  var u:real;var v:real;var w:real);
Var K_Theta,K_Phi,K_At,K_As : K_Matrix;
  At,As,Pt,Ps,q,Vinf,Alpha,Beta,Phi,Theta : real;
  i : integer;
begin
  If (P[4]>P[5]) then
  begin
    (* It is in region 3-1 *)
    {$I k-3-1.pas }
  end
  else
  begin
    (* It is in region 3-2 *)
    {$I k-3-2.pas }
  end;
  Phi := 0.0;
  Theta := 0.0;
  At := 0.0;
  As := 0.0;
  for i:= 1 to 10 do
  begin
    Theta := Theta + K_Theta[i]*B[i];
    Phi := Phi + K_Phi[i]*B[i];
    At := At + K_At[i]*B[i];
    As := As + K_As[i]*B[i];
  end;
  Pt := P[3]-At*Qprime;
  Ps := P[3]-As*Qprime;
  Velocity_Theta_Phi(Pt,Ps,q,Alpha,Beta,Theta,Phi,Density,Vinf,u,v,w);
end;

(*****
(* Procedure Region_4
(*****
Procedure Region_4(B:K_Matrix;P:Static_Type;Qprime:real;Density:real;
  var u:real;var v:real;var w:real);
Var K_Theta,K_Phi,K_At,K_As : K_Matrix;
  At,As,Pt,Ps,q,Vinf,Alpha,Beta,Phi,Theta : real;
  i : integer;
begin
  If (P[6]>P[3]) then
  begin
    (* It is in region 4-1 *)
    {$I k-4-1.pas }
  end
  else

```

```

begin
  (* It is in region 4-2 *)
  {SI k-4-2.pas }
end;
Phi := 0.0;
Theta := 0.0;
At := 0.0;
As := 0.0;
for i:= 1 to 10 do
begin
  Theta := Theta + K_Theta[i]*B[i];
  Phi := Phi + K_Phi[i]*B[i];
  At := At + K_At[i]*B[i];
  As := As + K_As[i]*B[i];
end;
Pt := P[4]-At*Qprime;
Ps := P[4]-As*Qprime;
Velocity_Theta_Phi(Pt,Ps,q,Alpha,Beta,Theta,Phi,Density,Vinf,u,v,w);
end;

(*****)
(* Procedure Region_5
(*****
Procedure Region_5(B:K_Matrix;P:Static_Type;Qprime:real;Density:real;
  var u:real;var v:real;var w:real);
Var K_Theta,K_Phi,K_At,K_As : K_Matrix;
  At,As,Pt,Ps,q,Vinf,Alpha,Beta,Phi,Theta : real;
  i : integer;
begin
  If (P[3]>P[7]) then
  begin
    (* It is in region 5-1 *)
    {SI k-5-1.pas }
  end
  else
  begin
    (* It is in region 5-2 *)
    {SI k-5-2.pas }
  end;
  Phi := 0.0;
  Theta := 0.0;
  At := 0.0;
  As := 0.0;
  for i:= 1 to 10 do
  begin
    Theta := Theta + K_Theta[i]*B[i];
    Phi := Phi + K_Phi[i]*B[i];
    At := At + K_At[i]*B[i];
    As := As + K_As[i]*B[i];
  end;
  Pt := P[5]-At*Qprime;
  Ps := P[5]-As*Qprime;
  Velocity_Theta_Phi(Pt,Ps,q,Alpha,Beta,Theta,Phi,Density,Vinf,u,v,w);
end;

(*****)
(* Procedure Region_6
(*****
Procedure Region_6(B:K_Matrix;P:Static_Type;Qprime:real;Density:real;
  var u:real;var v:real;var w:real);
Var K_Theta,K_Phi,K_At,K_As : K_Matrix;
  At,As,Pt,Ps,q,Vinf,Alpha,Beta,Phi,Theta : real;

```



```

i : integer;
begin
  If (P[2] > P[4]) then
    begin
      (* It is in region 6-1 *)
      {SI k-6-1.pas }
    end
  else
    begin
      (* It is in region 6-2 *)
      {SI k-6-2.pas }
    end;
  Phi := 0.0;
  Theta := 0.0;
  At := 0.0;
  As := 0.0;
  for i:= 1 to 10 do
    begin
      Theta := Theta + K_Theta[i]*B[i];
      Phi := Phi + K_Phi[i]*B[i];
      At := At + K_At[i]*B[i];
      As := As + K_As[i]*B[i];
    end;
  Pt := P[6]-At*Qprime;
  Ps := P[6]-As*Qprime;
  Velocity_Theta_Phi(Pt,Ps,q,Alpha,Beta,Theta,Phi,Density,Vinf,u,v,w);
end;

(*****)
(* Procedure Region_7
(*****)
Procedure Region_7(B:K_Matrix;P:Static_Type;Qprime:real;Density:real;
  var u:real;var v:real;var w:real);
Var K_Theta,K_Phi,K_At,K_As : K_Matrix;
  At,As,Pt,Ps,q,Vinf,Alpha,Beta,Phi,Theta : real;
  i : integer;
begin
  If (P[5] > P[2]) then
    begin
      (* It is in region 7-1 *)
      {SI k-7-1.pas }
    end
  else
    begin
      (* It is in region 7-2 *)
      {SI k-7-2.pas }
    end;
  Phi := 0.0;
  Theta := 0.0;
  At := 0.0;
  As := 0.0;
  for i:= 1 to 10 do
    begin
      Theta := Theta + K_Theta[i]*B[i];
      Phi := Phi + K_Phi[i]*B[i];
      At := At + K_At[i]*B[i];
      As := As + K_As[i]*B[i];
    end;
  Pt := P[7]-At*Qprime;
  Ps := P[7]-As*Qprime;
  Velocity_Theta_Phi(Pt,Ps,q,Alpha,Beta,Theta,Phi,Density,Vinf,u,v,w);
end;

```

```

(*****)
(* Procedure main
(*****)
begin
(* repeat
  write(' What region do you want to calibrate (1-7) ? ');
  readln(Region);
  case region of
    1 : Calibration_p_y;
    2..7 : Calibration_c_r;
  end;
  write(' Do you want to calibrate another region (Y or N) ? ');
  readln(Ans);
  until upcase(Ans) = 'N';*)
Ind_c[2] := 6;
Ind_cc[2] := 7;
Ind_c[3] := 5;
Ind_cc[3] := 4;
Ind_c[4] := 3;
Ind_cc[4] := 6;
Ind_c[5] := 7;
Ind_cc[5] := 3;
Ind_c[6] := 4;
Ind_cc[6] := 2;
Ind_c[7] := 2;
Ind_cc[7] := 5;
assign(inftemp,'temp');
reset(inftemp);
readln(inftemp,fname);
assign(outf,fname);
append(outf);
TextMode;
TextColor(White);
clrscr;
T := 70.0;
Viscosity_Density(Viscosity,Density,T);
Measure_Dynamic_Pressure(Dynamic_Pressure,FreeStream_Velocity,
                          Density,Viscosity);
Measure_Static_Pressure(P);
Temp_Press := P[1];
Region := 1;
for i:= 2 to 7 do
begin
  If (P[i]>Temp_Press) then
  begin
    Region := i;
    Temp_Press := P[i];
    Qprime := P[i] - (P[Ind_c[i]] + P[Ind_cc[i]])/2.0;
    if Qprime < > 0.0 then
    begin
      Bc := (P[i]-P[1])/Qprime;
      Br := (P[Ind_cc[i]]-P[Ind_c[i]])/Qprime;
      B_Matrix(Bc,Br,B);
    end;
  end;
end;
if (Region = 1) then
begin
  Qprime := P[1] - (P[2] + P[3] + P[4] + P[5] + P[6] + P[7])/6.0;
  if Qprime < > 0.0 then
  begin
    By := (P[2]-P[3])/Qprime;
    Bp := ((P[4] + P[6])/2.0 - (P[5] + P[7])/2.0)/Qprime;
  end;
end;

```

```

    B_Matrix(By,Bp,B);
end;
end;
writeln(outf,T:15:10,' (Temperature ',chr(248),'F)');
writeln(outf,Density:15:10,
' (Density lb-sec',chr(253),'ft**4)');
writeln(outf,Viscosity:15:10,
' (Viscosity lb-sec/ft',chr(253),'');
writeln(outf,Dynamic_Pressure:15:10,
' (Dynamic Pressure lb/ft',chr(253),'');
writeln(outf,FreeStream_Velocity:15:10,
' (Pitot Tube Freestream Velocity ft/sec)');
writeln(outf,P[1]:15:10,' (P[1] lb/ft',chr(253),'');
writeln(outf,P[2]:15:10,' (P[2] lb/ft',chr(253),'');
writeln(outf,P[3]:15:10,' (P[3] lb/ft',chr(253),'');
writeln(outf,P[4]:15:10,' (P[4] lb/ft',chr(253),'');
writeln(outf,P[5]:15:10,' (P[5] lb/ft',chr(253),'');
writeln(outf,P[6]:15:10,' (P[6] lb/ft',chr(253),'');
writeln(outf,P[7]:15:10,' (P[7] lb/ft',chr(253),'');
if Qprime = 0.0 then
begin
    writeln('Qprime = 0.0');
    writeln(outf,'Qprime = 0.0');
    writeln(outf,' 0.0 ('',chr(224),' degree)');
    writeln(outf,' 0.0 ('',chr(225),' degree)');
    writeln(outf,' 0.0 (Calculated Local Velocity ft/sec)');
    writeln(outf,' 0.0 (u ft/sec)');
    writeln(outf,' 0.0 (v ft/sec)');
    writeln(outf,' 0.0 (w ft/sec)');
    writeln(outf);
    close(outf)
end
else
begin
    case Region of
        1 : Region_1(B,P,Qprime,Density,u,v,w);
        2 : Region_2(B,P,Qprime,Density,u,v,w);
        3 : Region_3(B,P,Qprime,Density,u,v,w);
        4 : Region_4(B,P,Qprime,Density,u,v,w);
        5 : Region_5(B,P,Qprime,Density,u,v,w);
        6 : Region_6(B,P,Qprime,Density,u,v,w);
        7 : Region_7(B,P,Qprime,Density,u,v,w);
    end
end;
close(outf);
end.

```

Vita

Personal

Born: January 20, 1962
Place: Hue, Vietnam

Education

Ph.D. (1991) - VPI&SU
M.S. (1989) - VPI&SU
B.S. (1984) - VPI&SU


Ngoc Hoang